

Copyright
by
Amanda Lea Heiderman
2012

The Dissertation Committee for Amanda Lea Heiderman
certifies that this is the approved version of the following dissertation:

**Exploring the Limits of Star Formation from the
Extreme Environment of Galaxy Interactions to the
Milky Way**

Committee:

Neal J. Evans II, Supervisor

Karl Gebhardt, Supervisor

Milos Milosavljevic

Gary Hill

Daniela Calzetti

Casey Papovich

**Exploring the Limits of Star Formation from the
Extreme Environment of Galaxy Interactions to the
Milky Way**

by

Amanda Lea Heiderman, B.A., M.A.

DISSERTATION

Presented to the Faculty of the Graduate School of
The University of Texas at Austin
in Partial Fulfillment
of the Requirements
for the Degree of

DOCTOR OF PHILOSOPHY

THE UNIVERSITY OF TEXAS AT AUSTIN

December 2012

Dedicated to my parents, Lonnie and Frank, for their unconditional support
and always believing in me.

Acknowledgments

I have been very fortunate to cross paths with many amazing and supportive individuals who helped guide me on my path to obtain my doctorate and beyond.

Firstly, I would like to thank my community college Professors Robert Collier, Michael Sady, and Edward Kingham. These three individuals were the first people outside of my family to believe in my capabilities and not only did they push me to exceed the limitations I placed on myself as a high school student, but also mentored and guided me to transfer and obtain a Bachelors degree. I cannot thank them enough for their continual support to this day.

Words cannot express how grateful I am to my two dissertation advisors, Dr. Neal Evans and Dr. Karl Gebhardt, for taking me as their student despite having a full fleet of students in tow and other insane duties such as leading a gianormous dark energy survey or departmental chair duties on top of their normal teaching and research load. I thank them for allowing me the independence and scientific freedom to develop a portion of my thesis project and for journeying with me into new scientific territory. My thesis work would not have gone as far as it has without them constantly challenging me to not just do things well, but do them better. I would not be the scientist I am today without these two individuals.

I also would like to thank and specially acknowledge my dissertation committee members: Dr. Milos Milosavljevic, Dr. Gary Hill, Dr. Daniela Calzetti, and Dr. Casey Papovich for their time and help shaping my thesis into its final form.

I would also like to acknowledge the support and guidance of Dr. Carl Heiles for believing in my capabilities and pushing me to do my best during my undergraduate work at Berkeley, Dr. Kelsey Johnson for being an amazing female scientist role model, preparing me for entrance into graduate school, and mentoring me throughout graduate school, Dr. Megan Gray for being an great role model and unbeknownst to her taught me a lot on how to lead a large team of researchers through thick and thin, Dr. Shardha Jogee for teaching me how to be a respectable scientist, Dr. Casey Papovich for his constant encouragement and push to develop my own research program for my thesis project, Dr. Kurtis Williams for devoting his precious time to teach me how to develop a scientific research project from the ground up, Dr. Daniel Jaffe for his encouragement and constantly nudging me to keep moving forward.

Last but by far not the least I acknowledge the support of parents Frank and Lonnie, brother Danny, my extended family: Claudia, Mary Ann, Don, Jake, Mike, Jeff, Mitzi, and Tim, as well as my good friends and fellow graduate students and postdocs who have supported me, taught me many new things, and helped me to be the best scientist I can be during my undergraduate and graduate years: Miranda Dunham, Casey Deen, Irina Marinova, John Graham, Violet Yeager, Alicia Lanz, Amanda Bayless, Bi-Qing For,

Amanda Bauer, Liliana Lopez, Jami Brumfield, Ximena Cid, John Barentine, Tim Weinzirl, Colleen Schwartz, Candace Gray, Hyo Jeong Kim, Michael Dunham, Julie Comerford, Jeremy Murphy, Joel Green, Maverick, Michael Cooper, Remco van den Bosch, Peter Yoachim, Andrea Urban, Mubdi Rahman, Timothy Davis, Guillermo Blanc, and Joshua Adams.

Exploring the Limits of Star Formation from the Extreme Environment of Galaxy Interactions to the Milky Way

Amanda Lea Heiderman, Ph.D.
The University of Texas at Austin, 2012

Supervisors: Neal J. Evans II
Karl Gebhardt

In this thesis, I explore the rate at which molecular gas is converted to stars through detailed studies of a sample of molecular clouds in the Milky Way, IFU spatially resolved observations of gas-rich nearby interacting galaxies, as well as the environmental dependence of star formation and galaxy morphology in a galaxy supercluster. This thesis is composed of three individual projects that investigate nearby star formation within the local 500 pc of our Sun, to neighboring extreme star forming environments of interacting starburst galaxies, and finally studying how star formation varies with galaxy morphology in a galaxy supercluster at $z \sim 0.165$.

I discuss the relation between the star formation rate (SFR) and molecular gas surface densities (e.g., Schmidt-Kennicutt relation) in Galactic star forming regions and find there is a discrepancy between my study and extragalactic relations. The discrepancy is attributed to extragalactic measurements that are averaged over large $\gtrsim \text{kpc}$ scales and include star forming molecular gas (above some threshold) and molecular gas that is not dense enough

to form stars. I find a steep increase in the Galactic SFR-gas surface density relation indicative of a threshold for efficient star formation that is best fit to a broken power law with a linear slope above $129 \text{ M}_{\odot} \text{ pc}^{-2}$.

I introduce the VIRUS-P Investigation of the eXtreme ENviroments of Starbursts (VIXENS) project which is a survey of interacting is a large integral field unit survey of nearby infrared bright ($L_{IR} > 3 \times 10^{10} L_{\odot}$) interacting/starburst galaxies. The main goal of VIXENS is to investigate the relation between star formation and gas content on spatially resolved scales of $\sim 0.1\text{-}1 \text{ kpc}$ in the extreme star forming environments of interacting/starburst galaxies. The VIXENS sample is composed of systems in a range interaction stages with morphological signatures from early phase (close pairs) to late stage mergers (single system with multiple nuclei), SFRs, and gas surface densities.

I highlight the first results from the VIXENS survey in the late interaction phase galaxy merger Arp 299. I find 1.3 kpc regions in Arp 299 to lie along the SFR-gas surface density relation found for mergers at high redshift, but this relation is highly dependent on the CO to molecular hydrogen (H_2) conversion factor. I find evidence for a Galactic CO-to- H_2 conversion factor using metallicity and dust temperature measurements, which would place 1.3 kpc regions in the Arp 299 merger in between the high redshift and Kennicutt-Schmidt relations. Comparing the SFR to dense gas surface densities as traced by HCN and HCO^+ , I find an agreement between the spatially resolved measurements and that found on global scales in spirals and (ultra)luminous in-

frared galaxies.

Finally, I present an investigation of the influence of environment on frequency, distribution, color, and star formation properties of galaxy mergers and non-interacting galaxies in the Abell 901/902 supercluster at $z \sim 0.165$. I find galaxy mergers be preferentially blue in color and have an enhanced SFR by a factor of ~ 2 compared to non-interacting galaxies. This result may be due to a decrease in galaxy velocity dispersion in the cluster outskirts, favoring galaxy-galaxy interactions, or to interacting galaxies that are part of groups or field galaxies being accreted along cosmological filaments by the clusters. I compare to N -body simulations of groups and field galaxies accreting onto the clusters and find the fraction of mergers are similar to that predicated at group overdensities. I find the SFR of galaxies in the supercluster to be depressed compared to field galaxies in both the core and cluster outskirts, suggesting that an environmental process such as ram pressure stripping is effective throughout the cluster. The results of a modest SFR enhancement and a low merger fraction culminate in my finding that mergers contribute only a small fraction (between 10% and 15%) of the total SFR density of the Abell 901/902 clusters.

Table of Contents

Acknowledgments	v
Abstract	viii
List of Tables	xiv
List of Figures	xvi
Chapter 1. Introduction	1
Chapter 2. The Star Formation Rate and Gas Surface Density Relation in the Milky Way: Implications for Extragalactic Studies	11
2.1 Introduction and Motivation	12
2.2 Low-mass Star Forming Regions from <i>Spitzer</i> c2d and Gould's Belt Surveys	17
2.2.1 Estimating Σ_{gas} from Extinction Maps	18
2.2.2 Estimating Star Formation Rates from YSO Counts . .	23
2.2.3 Estimating Σ_{gas} and Σ_{SFR} for the Youngest YSOs as a Function of A_V	27
2.2.3.1 MISidentified YSOs from SED FITS (MISFITS)	28
2.2.4 Results: The Youngest YSOs as a Function of Σ_{gas} . . .	35
2.3 Why are Galactic SFR-gas Relations different from Extragalactic Relations?	41
2.3.1 The use of CO versus A_V to determine Σ_{gas}	42
2.3.2 Do High-mass and Low-mass Star Forming Regions Behave Differently?	55
2.3.2.1 Star Formation Threshold	65
2.3.3 Does the Lack of Resolution in Extragalactic Studies Explain the Discrepancy in Σ_{SFR} ?	69
2.4 Comparison to High Redshift Mergers	73
2.5 Summary and Conclusions	73

Chapter 3. The VIRUS-P Investigation of the eXtreme Environments of Starbursts (VIXENS) Survey	79
3.1 VIXENS Project Motivation	79
3.2 VIXENS Survey Description	81
 Chapter 4. Extreme Star Formation in Arp 299 from VIXENS: Constraints on the Spatially Resolved SFR–Gas Relations in a Nearby Merger	 89
4.1 Introduction and Motivation	91
4.2 The VIRUS-P Investigation of the eXtreme ENvironments of Starbursts (VIXENS) Survey	95
4.3 Observations	98
4.3.1 IFU Data Reduction and Emission Line Flux Measurements	99
4.3.1.1 Data Reduction, Flux Calibration, Astrometry, and Final Data Products	99
4.3.2 Ancillary Data	103
4.3.2.1 Molecular Gas Maps	103
4.3.3 Neutral Hydrogen Map	104
4.3.3.1 <i>Spitzer</i> 24 μ m Data	104
4.3.3.2 <i>HST</i> NICMOS Pa α Data	105
4.4 Data Analysis	105
4.4.1 Emission Line Flux Measurements	105
4.4.2 Molecular Gas Surface Density Measurements	110
4.5 Extinction	118
4.6 Star Formation Rates and Surface Density Measurements . . .	126
4.7 Active Galactic Nuclei Activity in Arp 299	127
4.8 Results	135
4.8.1 Comparison of Global SFRs	135
4.8.2 Region–by–Region Comparison of SFRs	137
4.8.3 SFR–Gas Surface Density Relation in Nuclear Regions .	142
4.8.4 Spatially Resolved SFR–Gas Surface Density Relation .	147
4.8.5 Spatially Resolved SFR–Dense Gas Surface Density Relation	150
4.8.6 Spatially Resolved SFR–HI Gas Surface Density Relation	151

4.8.6.1	Variation of CO-to-H ₂ Conversion Factor with Metallicity, IRAS F_{60}/F_{100} Flux Ratio, and Dust Temperature	155
4.9	Comparison to Galactic Star Forming Regions	165
4.10	Summary	166
Chapter 5. Interacting Galaxies in the A901/902 Supercluster with STAGES		173
5.1	Introduction and Motivation	174
5.2	The A901/902 Supercluster: Dataset and Sample Selection . .	178
5.3	Methodology and Analysis	181
5.3.1	Galaxy Mergers in this study	181
5.3.2	Visual classification of mergers and non-interacting galaxies	184
5.3.3	Tests on the Visual Classes	198
5.3.4	CAS: Quantitative method for capturing interacting galaxies	202
5.4	Results and Discussion	204
5.4.1	Merger fraction in A901/902 from visual classification . .	204
5.4.2	Frequency of mergers in A901/902 from CAS	209
5.4.3	Distribution of mergers	213
5.4.4	What accounts for the distribution of mergers?	219
5.4.5	Comparison with groups and clusters at different epochs	227
5.4.6	Galaxies on the blue cloud and red sample	232
5.4.7	Star formation properties of interacting galaxies	236
5.5	The Morphology-Density relation in A901/02	242
5.6	The depression of star formation in A901/902 cluster galaxies .	245
5.7	Summary and Conclusions	247
Chapter 6. Summary		255
Bibliography		262
Index		288
Vita		289

List of Tables

2.1	Measured Quantities for Clouds.	22
2.2	Properties of Suspicious YSOs and MISFITS	31
2.2	Properties of Suspicious YSOs and MISFITS	32
2.2	Properties of Suspicious YSOs and MISFITS	33
2.2	Properties of Suspicious YSOs and MISFITS	34
2.3	Measured Quantities for Clouds in A_V Contours	38
2.3	Measured Quantities for Clouds in A_V Contours	39
2.3	Measured Quantities for Clouds in A_V Contours	40
2.4	A_V , ^{12}CO , and ^{13}CO Masses and Σ_{gas} for Per and Oph Clouds	44
2.5	A_V , ^{12}CO , and ^{13}CO Masses and Σ_{gas} for Per and Oph Clouds in A_V Contours	46
2.6	Massive Clumps $\text{HCN } J=(1-0)$	60
3.1	Interacting Galaxy Sample. Columns are: (1) ARP or VV Peculiar Galaxy identifier. (2) Right Ascension (J2000). (3) Declination (J2000). (4) Interaction state: 1= early-interaction (close pairs, tidal tails or bridges), 2= mid-interaction (galaxies share common body or envelope, faint tidal debris, double nuclei), 3= late-interaction (spheroidal or unknown morphology, arcs, shells, ripples). (5) IR SFR derived from IRAS fluxes following the method used in Kewley (2002). (6) Estimated H_2 gas surface densities. (7) Comments and availability of archival data: S= Spitzer $24\mu\text{m}$, G= GALEX FUV, CO= CO map, HI= HI map, and environment of interacting systems: P = isolated pair, Gr = group, Trp = triplet, Cl = cluster.	87
3.2	VIXENS Observing Runs	88
4.1	Global Star Formation Rates	96
4.2	Star formation and Gas Surface Densities in Regions A, B1, C, and C'	114
5.1	Visual Classification Results for the sample of bright intermediate-mass ($M_* \geq 10^9 M_\odot$) galaxies	187

5.2	Visual Classification of Mergers in the Sample of Bright Intermediate-mass ($M_* \geq 10^9 M_\odot$) galaxies	189
5.2	Visual Classification of Mergers in the Sample of Bright Intermediate-mass ($M_* \geq 10^9 M_\odot$) galaxies	190
5.3	Merger fraction for different mass cuts	207
5.4	Visual Classes of Galaxies Satisfying the CAS Criterion ($A > 0.35$ and $A > S$)	209
5.5	Comparison of Projected Galaxy Number Densities n and σ_{gal}	215
5.6	Properties in Core, Outer Region, and Outskirt of A901/902 Clusters	218
5.7	Visual Classes of Galaxies on the Blue Cloud and Red Sample	235

List of Figures

1.1	Diagram illustrating the overall idea of this work which is to investigate the present day SFR–Gas surface density ($\Sigma_{\text{SFR}}\text{--}\Sigma_{\text{gas}}$) scaling relations in interacting galaxies and ‘normal’ galaxies (e.g., spirals, dwarfs) in different environments as a function of redshift (z), as well as compare this to star forming regions in the Milky Way ($z=0$). Connecting SFR–Gas scaling relations across all star formation regimes will allow us to better understand if there exists a universal star formation law that could describe the relation between gas and star formation throughout cosmic time.	9
2.1	Σ_{SFR} is shown versus the Σ_{gas} for c2d and GB clouds (cyan squares) and the Gutermuth et al. (2011) cloud sample (orange squares). All cloud Σ_{gas} are measured above $A_V > 2$ (or the cloud completeness limit, see §Section 2.2.1). We also include an estimate for the Taurus molecular cloud (black square) which includes YSO counts from Rebull et al. (2010) and an $A_V > 2$ gas mass from Pineda et al. (2010). Extragalactic observed relations are shown for the sample of Kennicutt (1998b) and Bigiel et al. (2008) (blue solid and red lines, respectively). . .	25
2.2	An example of the Σ_{gas} measurement method in the Perseus molecular cloud from the c2d survey. The grayscale image is the extinction map with black contours ranging from 2–29 in intervals of 4.5 mag The yellow filled circles are Flat SED sources and the red filled circles are Class I sources. Sources that have an open star correspond to suspicious YSOs (MISFITS) that were observed in $\text{HCO}^+ J=3\text{--}2$ at the CSO and were not detected. We measure the Σ_{gas} from each map in each contour of extinction. Contours are spaced in intervals wider than the extinction map beam size of $270''$. To estimate SFR, we count the YSOs in corresponding contour levels (§Section 2.2.2). . .	29

2.3	Gas surface densities measured from extinction maps and SFRs estimated from Class I (green stars) and Flat SED (magenta stars) YSO number counts in c2d and Gould's belt clouds are shown. For contour levels that do not contain any YSOs, we calculate an upper limit for that region using one YSO (open inverted triangles). Extragalactic observed relations are shown for the sample of Kennicutt (1998b) and Bigiel et al. (2008) (blue solid and red lines, respectively).	37
2.4	top panels: ^{12}CO integrated intensity versus visual extinction (A_V) for Per (left) and Oph (right). The standard X_{CO} -factor fit from Bloemen et al. (1986) is shown by the dashed grey lines (§Section 2.3.1). bottom panels: ^{13}CO column densities versus visual extinction (A_V) for Per (left) and Oph (right). The average H_2 -to- ^{13}CO abundance ratio from the literature is shown by the grey dashed lines (§Section 2.3.1).	48
2.5	The ratio of H_2 gas surface densities from CO compare to that estimated from A_V maps (Σ_{gas}). The cyan squares and circles are points for the Oph and Per clouds, respectively. The filled green (^{13}CO) and yellow (^{12}CO) squares (Oph) and circles (Per) are measurements in evenly spaced contour intervals of A_V . The dashed horizontal green and yellow lines are the average of ^{13}CO and ^{12}CO contour points. If CO traces the mass we find using extinction maps, we would expect the ratio of CO/A_V to be of order unity as shown by the solid black line.	53
2.6	Σ_{gas} and Σ_{SFR} are show for the sample of massive dense clumps from the survey of Wu et al. (2010). Gas surface densities are measured from the $\text{HCN } J=1-0$ maps and SFRs are estimated from the total IR luminosity, using the extragalactic prescription from Kennicutt (1998b). The relation between SFR and dense gas from Wu et al. (2005) is shown (grey solid line) and is extrapolated to lower Σ_{gas} . We make a cut at $L_{\text{IR}} > 10^{4.5} L_{\odot}$, below which the clumps are not massive enough to sample the IMF and lie off a the linear relation (§Section 2.3.2).	59
2.7	Comparison of Galactic total c2d and GB clouds, YSOs, and massive clumps to extragalactic relations. SFR and gas surfaces densities for the total c2d and GB clouds (cyan squares), c2d Class I and Flat SED YSOs (green and magenta stars), and $L_{\text{IR}} > 10^{4.5} L_{\odot}$ massive clumps (yellow diamonds) are shown. The range of gas surface densities for the spirals and circum-nuclear starburst galaxies in the Kennicutt (1998b) sample are denoted by the grey horizontal lines. The grey shaded region denotes the range for Σ_{th} of $129 \pm 14 M_{\odot} \text{ pc}^{-2}$	61

2.8	Comparison of massive, dense clumps with $L_{\text{IR}} > 10^{4.5} L_{\odot}$ to extragalactic relations (Kennicutt (1998b), Bigiel et al. (2008), and Krumholz et al. (2009), blue, red, and orange lines, respectively). The relation between SFR and dense gas from Wu et al. (2005) is also shown (grey solid line).	63
2.9	The ratio of Σ_{SFR} and Σ_{gas} compared to Σ_{gas} for low and high-mass star forming regions. We find a steep fall off in $\Sigma_{\text{SFR}}/\Sigma_{\text{gas}}$ in the range of $\Sigma_{\text{gas}} \sim 100\text{--}200 M_{\odot} \text{ pc}^{-2}$. We denote this steep fall off as a star forming threshold, Σ_{th} , between active star forming regions and inactive regions.	64
2.10	We fit Class I and Flat SED YSOs (green stars) and massive clumps (yellow diamonds) to a broken power law (§Section 2.3.2) and obtain an estimate for the star forming threshold, Σ_{th} , of $129 \pm 14 M_{\odot} \text{ pc}^{-2}$ (grey shaded region). The slope changes from 4.6 below Σ_{th} to 1.1 above Σ_{th}	67
2.11	I compare clumps, clouds, and YSOs to the relation found for high redshift mergers by Daddi et al. (2010) (see also Genzel et al. (2010)). I find Galactic clumps and YSOs above the star forming threshold (Σ_{th} ; grey line) to lie around the relation for high redshift mergers which suggests the bulk of gas in mergers traces star forming clouds.	74
3.1	SDSS RGB (i,r,g) images of the VIXENS interacting galaxy sample. The white boxes show the VIRUS-P IFU field of view ($1.7' \times 1.7'$) and the yellow lines indicate a scale of 10 kpc. The range of total molecular hydrogen gas surface densities estimated from CO maps and SFRs from IRAS are shown. . . .	82
3.2	Late interaction phase galaxy merger Arp 299 VIRUS-P linearly interpolated IFU maps based on the discrete values at each fiber position of (a) 4600Å-6800Å integrated stellar flux, (b) H α flux overlaid with CO(2-1) and H I integrated intensity map contours in intervals of $1\text{--}\sigma_{\text{rms}}$ and beam sizes from the CO(2-1) (black) and H I (red) maps, (c) stellar velocity field, and (d) H α velocity field.	86

4.1	RGB image of interpolated $H\alpha$ flux map based on discrete values at each IFU fiber position (red), archival <i>HST</i> 814W image (green), <i>Spitzer</i> $24\mu\text{m}$ image (blue), and contours of <i>HST</i> $\text{Pa}\alpha$ emission (yellow; note coordinates are offset see Alonso-Herrero et al. (2000)). The two main separate components of the Arp 299 merger IC 694 and NGC 3690 and individual nuclei (A and B1) and star forming complexes (C, and C' are indicated. Also shown is a possible stellar cluster associated with a peak in both $H\alpha$ and HI	97
4.2	Spectrum of fiber 354 with a high $A/N = 100$ in the Arp 299 data cube. The observed spectrum and 1σ uncertainties are shown in blue and the yellow envelope, respectively. The best fit stellar plus emission line spectrum is shown by the orange solid line and the dotted green line shows the stellar component of the fit without the emission lines. The vertical yellow bands are masked regions around sky line residuals.	108
4.3	Spectrum of fiber 633 with a low $A/N = 7$ in the Arp 299 RSS file. The observed spectrum and 1σ uncertainties are shown in blue and the yellow envelope, respectively. The best fit stellar plus emission line spectrum is shown by the orange solid line and the dotted green line shows the stellar component of the fit without the emission lines. The vertical yellow bands are masked regions around sky line residuals.	109
4.4	$H\alpha$ ionized gas velocity field. AGN contaminated regions are marked with black cross (X-ray) and stars (IFU).	116
4.5	$H\alpha$ ionized gas velocity field. AGN contaminated regions are marked with black cross (X-ray) and stars (IFU)	117
4.6	Extinction corrected $H\alpha$ versus $\text{Pa}\alpha$ fluxes measured in $6''$ size apertures in the nuclear regions in Arp 299.	121
4.7	Histogram of the extinction corrected $H\alpha/\text{Pa}\alpha$ flux ratio. The dashed line indicates the intrinsic $H\alpha/\text{Pa}\alpha$ line ratio of 7.58 from case B recombination line theory.	122
4.8	Visual extinction map (A_V) from the Balmer decrement ($H\beta/H\alpha$) line ratio in IFU fiber sized regions assuming a foreground dust screen model, and a mean interstellar extinction law from Draine (2003).	123
4.9	Visual extinctions for IFU fiber sized regions with a $S/N > 5$ from the Balmer decrement ($H\beta/H\alpha$) line ratio, a foreground dust screen model, and a Galactic extinction law from Draine (2003).	124
4.10	Extinction corrected fiber to fiber $H\alpha$ map of Arp 299 with the locations of nuclear regions A, B1, C, and C' indicated. . . .	125

- 4.11 **Top:** BPT diagram showing Kewley et al. (2001) extreme starburst classification line (red solid line) and errors (red diagonal line region), the pure star formation classification line from Kauffmann et al. (2003) (blue solid line), and the Ho et al. (1997) classification schemes (black dashed lines). White star points indicated regions that were selected by all three BPT diagrams, boxed points indicate regions selected by two or more BPT diagrams, and crosses mark regions within a $6''$ radius of the X-ray selected AGN from (Ballo et al. 2004). The solid yellow star shows the integrated ratio for the system. **Bottom:** The AGN selected regions (star and boxed points) are overlaid on an fiber-by-fiber $[\text{NII}]/\text{H}\alpha$ flux map. 131
- 4.12 **Top:** BPT diagram showing Kewley et al. (2001) extreme starburst classification line (red solid line) and errors (red diagonal line region), the Kewley et al. (2006) Seyfert-LINER line (blue and solid diagonal lines), and the Ho et al. (1997) classification schemes (black dashed lines). White star points indicated regions that were selected by all three BPT diagrams, boxed points indicate regions selected by two or more BPT diagrams, and crosses mark regions within a $6''$ radius of the X-ray selected AGN from (Ballo et al. 2004). The solid yellow star shows the integrated ratio for the system. **Bottom:** The AGN selected regions (star and boxed points) are overlaid on an fiber-by-fiber $[\text{SII}]/\text{H}\alpha$ flux map. 132
- 4.13 **Top:** BPT diagram showing Kewley et al. (2001) extreme starburst classification line (red solid line) and errors (red diagonal line region), the Kewley et al. (2006) Seyfert-LINER line (blue and solid diagonal lines), and the Ho et al. (1997) classification schemes (black dashed lines). White star points indicated regions that were selected by all three BPT diagrams, boxed points indicate regions selected by two or more BPT diagrams, and crosses mark regions within a $6''$ radius of the X-ray selected AGN from (Ballo et al. 2004). The solid yellow star shows the integrated ratio for the system. **Bottom:** The AGN selected regions (star and boxed points) are overlaid on an fiber-by-fiber $[\text{OI}]/\text{H}\alpha$ flux map. 133
- 4.14 Interpolated $\text{H}\alpha$ flux map based on discrete values at each IFU fiber position overlaid with H I (red) contours and contours starting at 2σ above the noise level and increase intervals of 2σ ... $\text{H}\alpha$ flux map overlaid with $\text{CO} J = 2 \rightarrow 1$ (blue) $\text{CO} J = 3 \rightarrow 2$ (white) contours starting at 2σ above the noise level and increase... Map beam sizes are shown in the top left corner. AGN contaminated regions are marked with black cross (X-ray) and stars (IFU). 136

4.15	Top: Comparison of extinction corrected $H\alpha$ and $24\mu\text{m}$ SFRs measured on scales of $24\mu\text{m}$ resolution ($6''$). Potential AGN contaminated points are denoted by stars and open squares. The colors represent the ratio of $\text{SFR}[H\alpha + 24\mu\text{m}] / \text{SFR}[H\alpha]$ shown in the bottom panel. The dark blue points represent where there is a roughly linear relation between the $H\alpha + 24\mu\text{m}$ and $H\alpha$ based SFRs. The solid black line is a linear relation at a SFR of 0.01. Bottom: The ratio of $H\alpha + 24\mu\text{m}$ to extinction corrected $H\alpha$ SFRs measured on scales of $24\mu\text{m}$ resolution ($6''$). AGN contaminated regions are marked with black cross (X-ray) and stars (IFU).	139
4.16	$\Sigma_{\text{SFR}}[H\alpha + 24\mu\text{m}]$ map where circles indicated 1.3 kpc scales and $H\alpha$ line fluxes have $A/N \geq 4$	141
4.17	Interpolated $H\alpha$ flux map based on discrete values at each IFU fiber position overlaid with $\text{HCN}(1-0)$ (cyan) contours and $\text{HCO}^+(1-0)$ contours (white) starting at 2σ above the noise level and increase intervals of 2σ . Map beam sizes are shown in the top left corner. AGN contaminated regions are marked with black cross (X-ray) and stars (IFU).	144
4.18	SFR–Mol gas surface density measurements of the nuclear regions of Arp 299 using $\text{CO}J = 2 \rightarrow 1$ and $\text{CO}J = 3 \rightarrow 2$ on scales of 1.3 kpc. The mass (M_{Mol}) is calculated using the same aperture area ($3''$ in radius). Lines indicate extragalactic relations on disk-averaged scales for spirals and starbursts (blue line; Kennicutt 1998b) and high- z mergers (green line; Daddi et al. 2010), as well as in 1 kpc regions in spirals and dwarf galaxies (red line; Bigiel et al. 2011).	145
4.19	SFR–Dense gas surface density measurements of the nuclear regions of Arp 299 using $\text{HCN}(1-0)$ and $\text{HCO}^+(1-0)$ on scales of 1.3 kpc. The mass (M_{Dense}) is calculated using the same aperture area ($3''$ in radius). The yellow line indicates the SFR–Dense gas relation on disk-averaged scales for spirals and (U)LIRGs (Gao & Solomon 2004b).	146

4.20	Spatially resolved SFR–Mol gas surface density relations from measurements at each IFU fiber position with CO J =2–1 coverage with data convolved to the 6'' 24 μ m resolution (scales of 1.3 kpc). The mass (M_{Mol}) is calculated using the same aperture area (3'' in radius). The dotted vertical line is the sensitivity limit of the CO J = 2 \rightarrow 1 map. Large yellow star is the integrated value for Arp 299. Lines indicate extragalactic relations on disk-averaged scales for spirals and starbursts (blue line; Kennicutt (1998b)) and high- z mergers (green line; Daddi et al. (2010)), as well as in 1 kpc regions in spirals and dwarf galaxies (red line; Bigiel et al. (2011)). AGN contaminated regions are marked with boxes from IFU line fluxes and black crosses (X-ray).	148
4.21	Spatially resolved SFR–Mol gas surface density relations from measurements at each IFU fiber position with CO J =3–2 coverage with data convolved to the 6'' 24 μ m resolution (scales of 1.3 kpc). The mass (M_{Mol}) is calculated using the same aperture area (3'' in radius). The dotted vertical line is the sensitivity limit of the CO J = 2 \rightarrow 1 map. Large yellow star is the integrated value for Arp 299. Lines indicate extragalactic relations on disk-averaged scales for spirals and starbursts (blue line; Kennicutt (1998b)) and high- z mergers (green line; Daddi et al. (2010)), as well as in 1 kpc regions in spirals and dwarf galaxies (red line; Bigiel et al. (2011)). AGN contaminated regions are marked with boxes from IFU line fluxes.	149
4.22	Spatially resolved SFR–Dense gas surface density relations from measurements at using HCN(1–0) and HCO $^+$ (1–0) each IFU fiber position with data convolved to the 6'' 24 μ m resolution (scales of 1.3 kpc). The mass (M_{Dense}) is calculated using the same aperture area (3'' in radius). The dotted vertical line is the sensitivity limit of the HCN J = 1 \rightarrow 0 and HCO $^+$ J = 1 \rightarrow 0 maps. The large cyan and purple stars are the integrated value of HCN J = 1 \rightarrow 0 and HCO $^+$ J = 1 \rightarrow 0 for Arp 299. The yellow line indicates the SFR–Dense gas relation on disk-averaged scales for spirals and (U)LIRGs (Gao & Solomon 2004b). . . .	152
4.23	Interpolated H α flux map based on discrete values at each IFU fiber position overlaid with H I (red) contours and contours starting at 2σ above the noise level and increase intervals of 2σ . The two main separate components of the Arp 299 merger IC 694 and NGC 3690 and individual nuclei (A, B1, and B2) and star forming complexes (C, and C') are indicated. AGN contaminated regions are marked with black cross (X-ray) and stars (IFU).	154

4.24	Spatially resolved SFR–HI gas surface density relation from measurements with data convolved to the HI map resolution on scales of 4.7 kpc in the outer regions of Arp 299. The mass (M_{HI}) is calculated using the same aperture area (11'' in radius). Regions for the outer disks in normal spiral and dwarf galaxies on scales of 0.6-1 kpc are shown as orange and purple circles, respectively from Bigiel et al. (2010).	156
4.25	Metallicity map of Arp 299 using the N2 calibration from Pettini & Pagel (2004) and fiber [NII]/H α line ratios.	158
4.26	Metallicity dependent CO–to–H ₂ conversion factor, $\alpha_{\text{CO}}(Z')$, from Narayanan et al. (2012) on scales of 1.3 kpc corresponding to the resolution of 24 μ m PSF for CO $J = 2 \rightarrow 1$ (solid black line) and CO $J = 3 \rightarrow 2$ (dotted black line). The commonly use single value starburst conversion factor (Downes & Solomon 1998) and Galactic conversion factor from (Bloemen et al. 1986) are shown by the dashed black lines.	160
4.27	Spatial distribution of the metallicity dependent CO–to–H ₂ conversion factor, $\alpha_{\text{CO}}(Z')$, from Narayanan et al. (2012) on scales of 1.3 kpc corresponding to the resolution of 24 μ m PSF derived using CO $J = 2 \rightarrow 1$ line intensities.	161
4.28	Spatial distribution of the metallicity dependent CO–to–H ₂ conversion factor, $\alpha_{\text{CO}}(Z')$, from Narayanan et al. (2012) on scales of 1.3 kpc corresponding to the resolution of 24 μ m PSF derived using CO $J = 3 \rightarrow 2$ line intensities.	162
4.29	Spatially resolved SFR–Mol gas surface density relations from measurements at each IFU fiber position with CO $J = 2 \rightarrow 1$ coverage using a metallicity dependent conversion factor ($\alpha_{\text{CO}}(Z')$) from Narayanan et al. (2012) on scales of 1.3 kpc. The mass (M_{Mol}) is calculated using the same aperture area (3'' in radius). The dotted vertical line is the sensitivity limit of the CO $J = 2 \rightarrow 1$ map. Large yellow star is the integrated value for Arp 299. Lines indicate extragalactic relations on disk-averaged scales for spirals and starbursts (blue line; Kennicutt (1998b)) and high-z mergers (green line; Daddi et al. (2010)), as well as in 1 kpc regions in spirals and dwarf galaxies (red line; Bigiel et al. (2011)) AGN contaminated regions are marked with boxes from IFU line fluxes and black crosses (X-ray).	163

4.30 Spatially resolved SFR–Mol surface density relations from measurements at each IFU fiber position with $\text{CO}J = 3 \rightarrow 2$ coverage using a metallicity dependent conversion factor ($\alpha_{\text{CO}}(Z')$) from Narayanan et al. (2012) on scales of 1.3 kpc. The mass (M_{Mol}) is calculated using the same aperture area ($3''$ in radius). The dotted vertical line is the sensitivity limit of the $\text{CO}J = 2 \rightarrow 1$ map. Large yellow star is the integrated value for Arp 299. Lines indicate extragalactic relations on disk-averaged scales for spirals and starbursts (blue line; Kennicutt (1998b)) and high- z mergers (green line; Daddi et al. (2010)), as well as in 1 kpc regions in spirals and dwarf galaxies (red line; Bigiel et al. (2011)). AGN contaminated regions are marked with boxes from IFU line fluxes. 164

5.1 **Top panel:** Apparent R -band magnitude (R_{Vega}), absolute visual magnitude (M_V), and stellar mass (M_*) distributions of the full A901/902 supercluster sample ($R_{\text{Vega}} \leq 24$; 1983 galaxies). **Middle panel:** Same as the top panel, but showing the properties of the sample of 893 intermediate mass galaxies ($M_* \geq 10^9 M_\odot$). **Bottom panel:** Same as the middle panel, but only showing the properties of the 24 galaxies, which are part of the 20 morphologically distorted mergers identified among the sample (see §Section 5.3.2 and Table 5.2 for details). These 20 mergers are labeled with a starred identification number in Table 5.2 and are Cases 1–13, 16–18, 20, 24, 34, 35 in Table 5.2. For the four mergers of type 2b (which are close pairs resolved by COMBO-17) we plot the properties of the eight individual galaxies making up the pair, thus resulting in a total of 24 galaxies. Each pair has a galaxy of mass $M_* \geq 10^9 M_\odot$ and a second galaxy that may be of any mass. 182

5.2 In our visual classification scheme (§Section 5.3.2), systems are classified as Mergers, or Non-interacting. The mergers are subdivided into three groups called Type 1, Type 2a, and Type 2b. Mergers of Type 1 appear, in the ACS F606W image, as a single morphologically distorted remnant, rather than two individually recognizable galaxies. The remnant hosts strong *externally triggered* morphological distortions similar to those seen in simulations of mergers of mass ratio $> 1/10$, such as tidal tails, shells, ripples, warps, strongly asymmetric tidal debris, double nuclei inside a common envelope, or a ‘train-wreck’ morphology. In contrast, mergers of type 2a and 2b appear in ACS images as a very close ($d < 10$ kpc) overlapping pair of two recognizable galaxies. Mergers of type 2b are resolved into two separate galaxies by the ground-based COMBO-17 data, while mergers of type 2a are not. Since some of these type 2a and 2b systems could be due to chance line-of-sight superposition, we conservatively consider for the final analysis only those pairs where at least one member is morphologically distorted (see Table 5.2 and Figure 5.3 for details). Non-interacting systems are subdivided into Irr-1 and Symmetric systems. Irr-1 exhibit *internally triggered* asymmetries, due to star formation typically on scales of a few hundred parsecs. Symmetric systems include galaxies, which are relatively undistorted and are not part of the very close pairs that constitute the mergers of Types 2a and 2b. 186

5.3	ACS images of systems visually classified as mergers of type 1 and <i>potential</i> mergers of type 2a and 2b, respectively (§Section 5.3.2). White horizontal bars denote a scale of 1'' or 2.8 kpc at $z \sim 0.165$. Top panel: The 13 distorted remnants classified as type 1 mergers hosts strong <i>externally triggered</i> morphological distortions similar to those seen in simulations of mergers of mass ratio $> 1/10$, such as tidal tails (e.g., 10, 11), shells, ripples, warps, asymmetric tidal debris and distortions (e.g., 5,6,8,9), double nuclei inside a common envelope, or a ‘train-wreck’ morphology (7, 10–12). The type 1 mergers can be divided into major mergers (7, 10–12), minor mergers (Cases 8,9,13), and ambiguous ‘major or minor’ mergers (1-6; §Section 5.3.2. Middle & Lower panels: The 23 potential mergers of type 2a and 2b shown here include both real and projection very close ($d < 10$ kpc) pairs. The 7 likely real pairs (16–18, 20, 24, 34, 35) are denoted with a starred identification number and contain at least one galaxy with morphological distortions indicative of a galaxy-galaxy interaction. In the final analysis, only the 13 distorted mergers of Type 1 and the 7 distorted mergers of types 2a and 2b are used Type 2b pairs are resolved by COMBO-17 data into two galaxies with separate redshifts and stellar masses, and their stellar mass ratio (listed in Table 5.2) is used to divide Type 2b mergers into major mergers (20–22, 24–26, 28, 29, 23, 34) and minor mergers (19, 23, 27, 30, 31, 33, 35, 36). For the Type 2a pairs, which are unresolved by COMBO-17, the ACS-based luminosity ratio (Table 5.2) of the pair members is used to divide them into major (16, 18) and minor (14, 15, 17) mergers.	188
5.4	The ratio ($N_{\text{obs}}/N_{\text{mc}}$) for pairs of different projected separations d , where N_{obs} and N_{mc} are the number of pairs measured in the observations and random pairs from the Monte Carlo simulations, respectively. See §Section 5.3.2 for details. The four panels represent the mean, median, minimum and maximum distribution as labeled. At smaller separations of $d < 50$ kpc, ($N_{\text{obs}}/N_{\text{mc}}$) is above 1, suggesting that random chance superposition cannot fully account for all the observed pairs.	196
5.5	ACS F606W images of some of the systems visually classified as Non-interacting Symmetric (Cases 1-6) and Non-interacting Irr-1 (Cases 7-12). See §Section 5.3.2 for details.	199

5.6	The results of running CAS on the sample of bright ($R_{\text{Vega}} \leq 24$) intermediate-mass ($M_* \geq 10^9 M_\odot$) systems are shown. Galaxies with different visual classes (Merger, Non-interacting Irr-1, and Non-interacting Symmetric) are shown in the CAS A vs. S plane. We only plot here the 20 distorted mergers of types 1, 2a, and 2b in Table 5.2. The 18 galaxies satisfying the CAS merger criterion ($A > S$ and $A > 0.35$) lie on the upper left corner of the diagram. The CAS merger criterion recovers 11 of the 20 ($61\% \pm 20\%$) of the galaxies visually classified as a merger. Furthermore, there is a significant level of contamination: 7/18 ($39\% \pm 14\%$) of the systems picked up by the CAS criterion are visually classified as Non-interacting Irr-1 and Non-interacting Symmetric.	210
5.7	The top panel shows examples of mergers missed by the CAS merger criterion ($A > S$ and $A > 0.35$). Features of these systems include double nuclei, tidal bridges, and tidal debris. The lower panel show some non-interacting contaminants picked up by the CAS merger criterion, due to small-scale asymmetries from SF, strong patchy dust lanes, and the absence of a clear center, all leading to a larger A value.	212
5.8	The azimuthally averaged projected number density n of bright ($R_{\text{Vega}} \leq 24$) intermediate-mass ($M_* \geq 10^9 M_\odot$) galaxies in the sample is shown as a function of clustocentric radius which is shown for each cluster A901a/b and A902. We consider the cluster core to be at $R \leq 0.25$ Mpc, as this is the region where the projected number density n rises very steeply. We refer to the region which is located at $0.25 \text{ Mpc} < R \leq 1.2 \text{ Mpc}$ between the cluster core and the cluster virial radius as the outer region of the cluster. The region outside the virial radius ($1.2 \text{ Mpc} < R \leq 2.0 \text{ Mpc}$) is referred to as the outskirts region of the cluster. The core, outer region, and outskirts region are labeled.	214

- 5.9 The distribution of visually-classified mergers (coded as yellow diamonds, circles, and crosses) among the final sample of bright ($R_{\text{Vega}} \leq 24$) intermediate-mass ($M_* \geq 10^9 M_\odot$ galaxies) is shown, overlaid on the ICM density map (yellow-orange scale). We only plot here the final sample of 20 distorted mergers, shown with starred identification numbers in Table 5.2. Following Heymans et al. (2008) we show DM masses in terms of the signal-to-noise of the weak lensing detection. The cyan and green contours enclose roughly $6h^{-1}10^{13}M_\odot$ and $3.5h^{-1}10^{13}M_\odot$ for A901a and A901b, and roughly $3h^{-1}10^{13}M_\odot$ and $1.5h^{-1}10^{13}M_\odot$ for the lower mass A902 and South West Group (SWG). The different symbols represent major mergers (circles), minor mergers (diamonds), and ambiguous major or minor merger cases (crosses), identified in §Section 5.3.2. All mergers are located in the outer region and outskirts of each cluster ($0.25 \text{ Mpc} < R \leq 2 \text{ Mpc}$). 217
- 5.10 For mergers and non-interacting galaxies, the minimum distance to the nearest cluster center (A901a, A901b, A902) is plotted against the values of various local environmental parameters, such as the local galaxy surface density (Σ_{10}) (**top left**), the local DM mass surface density (κ) (**middle left**), and the relative local ICM density (**bottom left**). The panels on the right-hand side show the number of mergers and non-interacting galaxies which are found at different for each parameter. Mergers lie in the outer region and outskirts of the cluster ($0.25 \text{ Mpc} < R \leq 2 \text{ Mpc}$) and are associated with low values of κ and intermediate values of Σ_{10} , and ICM density. 220
- 5.11 Local velocity dispersion profiles for A901a, b and A902 clusters, and associated SWG from kinematic modeling using the ~ 420 2dF redshifts (Gray et al. in preparation). The central galaxy velocity dispersion within the cores ($R < 0.25 \text{ Mpc}$) of A901a,b and A902 typically range from 700 to 1000 km s^{-1} . Outside the cluster core, in the outer region ($0.25 \text{ Mpc} < R \leq 1.2 \text{ Mpc}$), the small number statistics leads to large error bars on the galaxy velocity dispersion, making it not viable to determine whether it remains high or drops. 222

- 5.12 Comparison of the observed and theoretically predicted number density of mergers (**top panel**) and fraction of mergers (**lower panel**), §Section 5.4.4. The solid curve shows the *predicted model* number density of mergers ($n(\delta^G)$) and the fraction of mergers ($f(\delta^G)$) as a function of local overdensity (δ^G), in the N -body simulations of the STAGES A901/902 supercluster. Typical values of δ^G are ~ 10 -100 for group overdensities, ~ 200 at the cluster virial radius, and $\gtrsim 1000$ in core of rich clusters. In the models, as field and group galaxies fall into a cluster along filaments, the bulk flow enhances the galaxy density and causes galaxies to have small relative velocities, thus leading to a high probability for mergers at typical group overdensities. Closer to the cluster core, model galaxies show large random motions, producing a sharp drop in the probability of mergers. The three dashed lines show the *observed* number density (n_{merge}) and fraction (f_{merge}) of mergers in three different regions of the A901/902 clusters: the core, the outer region, and the outskirts. A stellar mass cut of $M > 10^9 M_\odot$ is applied to both model and data. The points at which the three dashed lines cross or approach the solid curve tell us the typical overdensities at which we expect to find such merger fraction or merger number densities in the simulations. It can be seen that the low merger density seen in the core region (green dashed line) of the cluster correspond to those expected at typical cluster core overdensities. On the other hand, the larger merger fraction we observe between the cluster core and outer region ($0.25 \text{ Mpc} < R \leq 2 \text{ Mpc}$; blue dashed line) is close to those seen in typical *group overdensities*, in agreement with the scenario of cluster growth via accretion of group and/or field galaxies. . . 224
- 5.13 Comparisons of our observed fraction of mergers among intermediate mass systems in the A901/902 clusters (large filled solid circle) with the results from other studies of clusters and groups. Filled circles are for cluster data points of intermediate luminosity ($L < L^*$ and/or $M = 10^9$ to a few $\times 10^{10} M_\odot$), and include the following studies in order of increasing redshift: this study of A901/902 (most systems have $M_V \sim -19$ to -22 and $M_* = 10^9$ to a few $\times 10^{10} M_\odot$); Couch et al. 1998 ($L < 2L^*$), Oemler et al. 1997; lower limit of f for $M_V < -19$), Dressler et al. 1994 ($M_V < -18.5$). The van Dokkum et al. (1999) point at $z = 0.83$ (open circle) is for a cluster sample of luminous ($M_B \sim -22$ and $L \sim 2L^*$) galaxies. The group point (filled square) is from McIntosh et al. (2008) for galaxy masses above $5 \times 10^{10} M_\odot$. The Hickson compact group point (open triangle), from Zepf (1993), is for galaxies of luminosities $L \leq L^*$ 229

- 5.14 **Left:** the rest-frame $U - V$ color is plotted against the minimum distance from the nearest cluster center, for systems of different visual classes (Merger, Non-interacting Irr-1, and Non-interacting Symmetric). We only consider here the 20 distorted mergers in Table 5.2, split into 13 mergers of type 1, 3 mergers of type 2a, and 4 mergers of type 2b. For mergers of type 2b, which are resolved into two galaxies with separate COMBO-17 colors, we plot the average $U - V$ color of the galaxies in the pair. **Right:** the rest-frame $U - V$ color is plotted against stellar masses. The black solid lines separate the blue cloud and red sample. For $M \geq 10^9 M_\odot$ systems, we find that $80\% \pm 18\%$ (16/20) of mergers lie on the blue cloud, compared to (294/866) or $34\% \pm 7\%$ of the non-interacting galaxies. Thus, mergers and interacting galaxies are preferentially blue compared to non-interacting galaxies. 234
- 5.15 **Bottom panel:** The UV-based SFR is plotted against stellar mass for the sample of 886 bright intermediate-mass ($M_* \geq 10^9 M_\odot$) visually classifiable systems. Systems are coded according to their visual classes: Merger, Non-interacting Irr-1, and Non-interacting Symmetric. We only consider here the 20 distorted mergers in Table 5.2. **Top panel:** The average UV-based SFR is plotted against stellar mass for galaxies of different visual classes. For the few mergers galaxies present (orange line), the average SFR_{UV} is enhanced by at most an average factor of ~ 2 compared to the Non-interacting Symmetric galaxies (purple line) and to all Non-interacting galaxies (i.e Symmetric + Irr-1; black line). No enhancement is seen with respect to the Non-interacting Irr-1 galaxies (green line). 239

- 5.16 **Bottom panel:** the UV+IR-based SFR is plotted against stellar mass for the sample of bright intermediate-mass ($M_* \geq 10^9 M_\odot$) systems. Galaxies are coded according to their visual classes: Merger, Non-interacting Irr-1, and Non-interacting Symmetric. We only consider here the 20 distorted mergers in Table 5.2. For galaxies that were observed and detected at $24\mu\text{m}$, the UV+IR-based SFR is plotted as stars. For galaxies that were observed but undetected at $24\mu\text{m}$, we use the detection limit as an upper limit for the UV+IR-based SFR, and plot this limit as inverted triangles. **Middle panel:** the average UV+IR-based SFR is plotted against stellar mass for galaxies of different visual classes. We include galaxies with a $24\mu\text{m}$ detection, as well as those with only upper limits on the $24\mu\text{m}$ flux. **Top panel:** same as middle panel, except that we only include galaxies with a $24\mu\text{m}$ detection and exclude those with upper limits. In both top and middle panels, we find that for the few mergers present (orange line), the average $\text{SFR}_{\text{UV+IR}}$ is typically enhanced by only a factor of ~ 1.5 compared to the Non-interacting Symmetric galaxies (purple line) and to all Non-interacting galaxies (i.e Symmetric + Irr-1; black line). 240
- 5.17 We revisit the morphology-density relation by overplotting the distribution of bright ($M_V \leq -18$) smooth (gas-poor) galaxies (black crosses) and clumpy (gas-rich) galaxies (white crosses) on the ICM density. Smooth (gas-poor) galaxies populate the highest density regions. 243
- 5.18 The morphology-density relation as a function of local galaxy surface density (Σ_{10}). Smooth, bulge-dominated galaxies are found to lie preferentially at higher Σ_{10} compared to clumpy, gas-rich galaxies. 244
- 5.19 **(a)** The UV+IR based SFR ($\text{SFR}_{\text{UV+IR}}$) is plotted versus clustocentric radius R . Each galaxy is assigned to the cluster closest to it, and R is measured from the center of that cluster. **(b)** The UV based SFR (SFR_{UV}) is shown versus clustocentric radius R . **(c)** $\text{SFR}_{\text{UV+IR}}$ is shown against the local relative ICM density. The inverted triangles denote upper limits to the $\text{SFR}_{\text{UV+IR}}$ and apply to galaxies where there was no $24\mu\text{m}$ detection. **(d)** The variation of $\text{SFR}_{\text{UV+IR}}$ as a function of local galaxy surface density (Σ_{10}). The horizontal dashed line marks the median SFR value for field galaxies. 248

Chapter 1

Introduction

A detailed understanding of the rate at which molecular gas is converted into stars is an essential prerequisite for models of galaxy formation and evolution. In fact this rate, and the parameters that cause it to vary are currently ill constrained, leading to large uncertainties in theoretical models of galaxy formation. This presents an observational need for a robust determination of the relation between star formation rate (SFR) and the amount of available dense molecular gas. The focus of this thesis is to explore the evolution of the rate at which molecular gas is converted into stars through detailed studies of a large sample of molecular clouds in the Milky Way, IFU spatially resolved observations of gas-rich nearby interacting galaxies, as well as the environmental dependence of star formation in a galaxy supercluster.

Understanding how physical processes in the interstellar medium (ISM) control star formation is an important prerequisite to understanding galaxy evolution. A robust measurement of the relation between the star formation rate surface density (Σ_{SFR}) and the surface density of cold gas (Σ_{gas}) is of vital importance for input into theoretical models of galaxy evolution.

The idea that there should be a relation between the density of star

formation and gas density was first proposed by Schmidt (1959). Schmidt investigated this relation, now known as the “Schmidt law”, assuming that it should be in the form of a power law and suggested that the density of star formation was proportional to gas density squared. Kennicutt (1998b) measured the global or disk-averaged Schmidt law in a sample of spiral and starburst galaxies using the projected star formation and Σ_{gas} in the form:

$$\Sigma_{\text{SFR}} \propto \Sigma_{\text{gas}}^N, \quad (1.1)$$

where N is the power law index. The global SFR and Σ_{gas} measurements for the sample of galaxies in Kennicutt (1998b) were fitted to a power law with $N=1.4$, which is known as in the “Kennicutt–Schmidt law” :

$$\Sigma_{\text{SFR}} = (2.5 \pm 0.7) \times 10^{-4} \left(\frac{\Sigma_{\text{gas}}}{1 M_{\odot} \text{ pc}^{-2}} \right)^{1.4 \pm 0.15} (M_{\odot} \text{ yr}^{-1} \text{ kpc}^{-2}). \quad (1.2)$$

While this relation is previously been called the “Kennicutt–Schmidt law”, I refrain from calling this a “law” and instead refer to it as a SFR–gas relation since it is only an assumption that there is *only one relation* that regulates how gas forms stars. There have been many observational studies of SFR–gas relations on either global scales (Kennicutt 1989, 1998b) or using either radial (Martin & Kennicutt 2001; Wong & Blitz 2002; Boissier et al. 2003; Heyer et al. 2004; Komugi et al. 2005; Schuster et al. 2007) or point–by–point measurements (Kuno et al. 1995; Zhang et al. 2001) that find values

of N ranging from 1–2. Recently, this proposed SFR–gas relation has been studied on \sim kpc scales in nearby spiral galaxies where a deviation from the Kennicutt–Schmidt power law index is found (Kennicutt et al. 2007; Thilker et al. 2007; Bigiel et al. 2008; Braun et al. 2009; Blanc et al. 2009; Verley et al. 2010; Rahman et al. 2012) on spatially resolved scales of \sim 0.2–2 kpc. It is evident that sensitivity of N to systematic variations in methodology e.g., data spatial resolution (Calzetti et al. 2012), SFR tracers, power law fitting method (Shetty et al. 2012), accounts for some of the differences in the derived star formation power law index, but the underlying physical reasons for the variations in the SFR–gas relations remain an open, challenging question.

Measurements made in these studies, however, are limited to hundred parsec scales or more and are not directly comparable to the size of individual molecular clouds or dense clumps where stars form. While these studies have all looked at the extragalactic SFR–gas relation, there has been little work until recently investigating this relation locally in the Milky Way.

Surveys of nearby molecular clouds in the Milky Way using *Spitzer* imaging have provided large statistical samples of young stellar object (YSO) candidates (e.g., Evans et al. (2009); Forbrich et al. (2009); Rebull et al. (2010)). These surveys have allowed us to directly count the number of low–mass stars that are forming and estimate SFRs. These data also allow us to trace the low–mass star formation regime essentially invisible to tracers, such as emission in $H\alpha$, ultraviolet, far–infrared (FIR), and singly ionized oxygen, used to establish extragalactic SFR–gas relations. Since these tracers only

probe the rate at which massive stars form, a stellar Initial Mass Function (IMF), extrapolating down to low stellar masses, must be assumed to obtain a SFR. Thus, these SFR estimates are very sensitive to the IMF slope and distribution on the low-mass end.

Evans et al. (2009) compared extragalactic observed SFR–gas relations to total molecular cloud measurements from the *Spitzer* c2d survey. They found that Galactic clouds lie above the SFR–gas relations predicted by extragalactic work (Bigiel et al. 2008; Kennicutt 1998b) and lie slightly above the extrapolated relation from a study of massive dense clumps (Wu et al. 2005):

$$\text{SFR} \sim 1.2 \times 10^{-8} \left(\frac{M_{\text{dense}}}{M_{\odot}} \right) (M_{\odot} \text{ yr}^{-1}). \quad (1.3)$$

This result suggests that studying SFR–gas relations in our Galaxy may be useful for interpreting star formation observed in nearby and high- z galaxies. On the high-mass end of the spectrum, a large survey of massive dense clumps (Wu et al. 2005, 2010), provides a sample that can be directly compared to extragalactic star formation tracers. A better understanding of the SFR–gas relation in the Milky Way can serve as a foundation for interpreting the SFR and relation to gas content in external galaxies with different morphologies at both low and high- z .

Measuring the spatially resolved star formation efficiency in nearby starburst/ interacting galaxies has direct implication at high redshifts, where

such galaxies play an increasing role in the total SFR density (Le Floc'h et al. 2005). Recent work by Genzel et al. (2010) and Daddi et al. (2010) found a bimodal relationship between the SFR and gas surface densities for high redshift merging galaxies and normal disk galaxies (Figure 3). The high redshift mergers from Genzel et al. (2010) lie along the same relation as Galactic low and high mass star forming regions from Heiderman et al. (2010), suggestive that the bulk of gas in merging systems traces star forming gas. While starburst and interacting galaxies are a relatively rarity in the low- z universe, they are the dominant mode of star formation in the distant universe. Understanding the physics of star formation in these systems is therefore paramount. This motivates the observational requirement to study the star formation efficiency in starburst/interacting galaxies.

While some work on the integrated emission SFR-gas relation in extreme star forming environments has been done (Gao & Solomon 2004a,b), such as those in local (ultra)luminous infrared (IR) galaxies, (U)LIRGs, (Sanders & Mirabel 1996) there has been little work done studying the spatially resolved relation between the SFR and gas surface densities in extreme environments such as the triggered starbursts in interacting galaxies. The VIXENS observational program (Chapter 4.2) will provide the required constraints on theoretical models for galaxy evolution as well as provide a comparison sample to multiwavelength observational studies of high- z interacting galaxies.

On global scales, the total IR SFR correlates with gas content measured from CO luminosities (e.g., Sanders & Mirabel 1996). However, extreme

star forming environments like that in local (U)LIRGs, lie above the classical Kennicutt-Schmidt relation (Genzel et al. 2010; Daddi et al. 2010). With critical densities ~ 100 -300 times larger than CO, the $\text{HCN } J = 1 \rightarrow 0$ line traces dense gas better than CO and is found to have a tighter, linear correlation between the IR SFR over two orders of magnitude in luminosity from normal spirals to (U)LIRGs (Gao & Solomon 2004b), as well as on smaller scales in massive star forming regions (Wu et al. 2005). Furthermore, it has been shown that starbursting IR luminous systems exhibit enhanced dense $\text{HCN } J = 1 \rightarrow 0$ gas luminosity compared to CO gas at moderate density (Juneau et al. 2009). This may be due to the gas inflow produced by the gravitational tidal torques into the nuclear region. Alternatively it may be due to an increase in gas velocity dispersion during the interaction, triggering the formation of star forming clouds with densities $\gtrsim 10^4 \text{ cm}^{-3}$ (Gao & Solomon 2004a) far outside the nuclei as predicted in recent theoretical simulations (Bournaud et al. 2010).

The ‘burst’ mode of star formation was first seen by Larson & Tinsley (1978) when they compared a sample of interacting/peculiar galaxies to normal non-interacting galaxies. They found that galaxy dynamics in the form of close tidal interactions between galaxies caused these bursts in star formation. Galaxies in dense environments (e.g., groups, clusters) likely have been impacted by this burst mode as they rapidly form stars and transform via interactions into spheroidal systems. Conversely, continuous star formation is likely responsible in shaping the growth of disk galaxies. This is a commonly accepted theme in current bottom-up cold dark matter (CDM) as-

sembly paradigm of galaxy evolution (e.g., Cole et al. (2000); Steinmetz & Navarro (2002)). However, it is still unclear how and to what extent environmental processes effect the star formation process internal to galaxies. There is strong observational evidence that the internal properties of galaxies depend on their local environment (e.g., morphology density relation Dressler 1980) where late-type star forming galaxies may be transformed to early-type passive galaxies after being accreted onto a group or cluster. Several differences have been observed between galaxies in the field and those in the rich cluster environment, but the physical drivers behind these variations are still under investigation.

Most evidence for galaxy evolution in dense environments leads to environment processes that transform the morphology of galaxies over a period of time. Ram-pressure stripping of gas in a galaxies' disk from the intracluster medium (ICM) (Gunn & Gott 1972; Larson et al. 1980; Quilis et al. 2000; Balogh & Morris 2000), for example, can quench the star formation process over a period of ~ 100 Myr in cluster cores to a slow $\sim \text{Gyr}$ in cluster outskirts (Section 5.6). Other processes such as the cumulative effect of weak galaxy interactions over time (galaxy harassment, Moore et al. 1996) or the tidal field of the cluster potential (Gnedin 2003) likely also play a role. Current evidence suggests that slow preprocessing of galaxies via galaxy-galaxy interactions in groups accreting onto clusters likely impact the shape of a galaxy before entering the cluster environment (Heiderman et al. 2009). This preprocessing likely impacts the amount and extent of star formation in a galaxy (e.g. through

galaxy-galaxy interactions) before cluster processes morph the system into its final quiescent stage.

Discriminating between how various environments (field, groups, and clusters) influence the star formation in galaxies throughout time is also a key step toward developing a coherent picture of galaxy evolution (Fig. 1.1). Probing the variation in the SFR–Gas relations in different galaxy types and environments, as well as locally in our own Milky Way is important for understanding underlying physical mechanisms. Connecting scaling relations across all star formation regimes (e.g. from molecular clouds forming clumps and cores to the secular change in disk galaxies to starbursts in interacting galaxies and finally the more quiescent ellipticals) will allow us to better understand if there exists a universal SFR–Gas relation that could describe the process of star formation throughout cosmic time.

In Chapter 2, I investigate the relation between SFR and gas surface densities in Galactic star forming regions using a sample of young stellar objects (YSOs) and massive dense clumps. The YSO sample allow us to probe the regime of low-mass star formation essentially invisible to tracers of high-mass star formation used to establish extragalactic SFR-gas relations. Chapter 4.2 presents the VIRUS-P Investigation of the eXtreme Environments of Starbursts (VIXENS) survey, sample of interacting galaxies, and integral field unit observations. I discuss the survey motivation, sample selection, observations, and in brief, data reduction and analysis. In Chapter 4 I investigate the relationship between star formation and gas content in late interaction phase

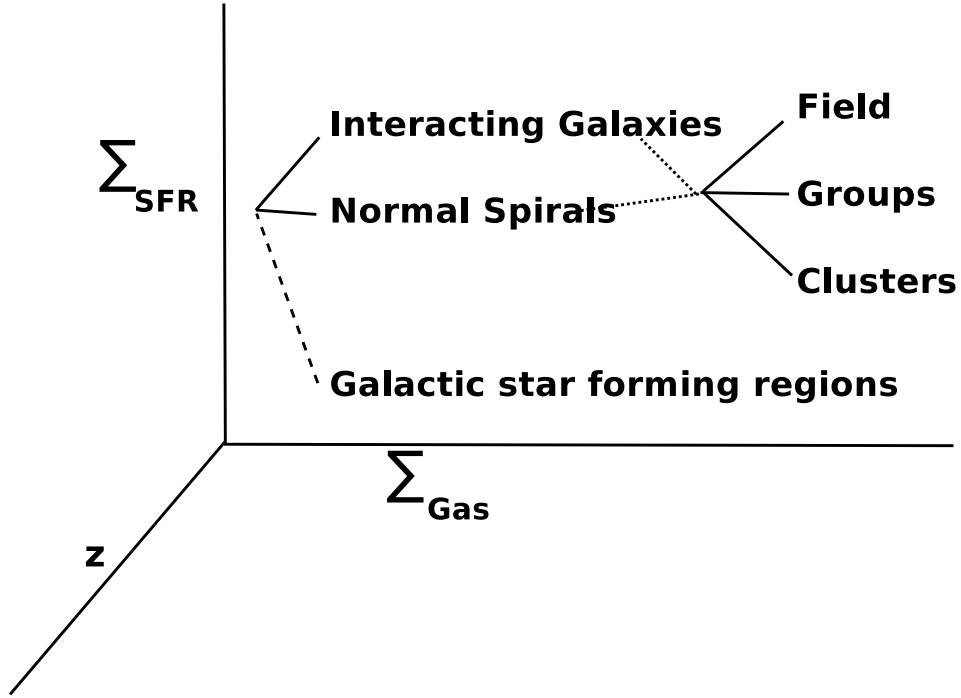


Figure 1.1 Diagram illustrating the overall idea of this work which is to investigate the present day SFR–Gas surface density ($\Sigma_{\text{SFR}}\text{--}\Sigma_{\text{gas}}$) scaling relations in interacting galaxies and ‘normal’ galaxies (e.g., spirals, dwarfs) in different environments as a function of redshift (z), as well as compare this to star forming regions in the Milky Way ($z=0$). Connecting SFR–Gas scaling relations across all star formation regimes will allow us to better understand if there exists a universal star formation law that could describe the relation between gas and star formation throughout cosmic time.

galaxy merger Arp 299 from the VIXENS integral field unit (IFU) survey. I present an investigation of galaxy mergers and the influence of environment in the Abell 901/902 supercluster at $z \sim 0.165$ in Chapter 5. Finally, I provide a comprehensive summary of this work in Chapter 6.

Chapter 2

The Star Formation Rate and Gas Surface Density Relation in the Milky Way: Implications for Extragalactic Studies

I investigate the relation between star formation rate (SFR) and gas surface densities in Galactic star forming regions using a sample of young stellar objects (YSOs) and massive dense clumps. The YSO sample consists of objects located in 20 large molecular clouds from the *Spitzer* cores to disks (c2d) and Gould’s Belt (GB) surveys. These data allow us to probe the regime of low-mass star formation essentially invisible to tracers of high-mass star formation used to establish extragalactic SFR-gas relations. I estimate the gas surface density (Σ_{gas}) from extinction (A_V) maps and YSO SFR surface densities (Σ_{SFR}) from the number of YSOs, assuming a mean mass and lifetime. I also divide the clouds into evenly spaced contour levels of A_V , counting only Class I and Flat SED YSOs, which have not yet migrated from their birthplace. For a sample of massive star forming clumps, I derive SFRs from the total infrared luminosity and use HCN gas maps to estimate gas surface densities. I find that c2d and GB clouds lie above the extragalactic SFR-gas relations (e.g., Kennicutt–Schmidt Law) by factors up to 17. Cloud regions with high Σ_{gas} lie above extragalactic relations up to a factor of 54 and overlap with

high-mass star forming regions. I use ^{12}CO and ^{13}CO gas maps of the Perseus and Ophiuchus clouds from the COMPLETE survey to estimate gas surface densities and compare to measurements from A_V maps. I find that ^{13}CO , with the standard conversions to total gas, underestimates the A_V -based mass by factors of $\sim 4\text{--}5$. ^{12}CO may underestimate the total gas mass at $\Sigma_{\text{gas}} \gtrsim 200 M_{\odot} \text{ pc}^{-2}$ by $\gtrsim 30\%$; however, this small difference in mass estimates does not explain the large discrepancy between Galactic and extragalactic relations. I find evidence for a threshold of star formation (Σ_{th}) at $129 \pm 14 M_{\odot} \text{ pc}^{-2}$. At $\Sigma_{\text{gas}} > \Sigma_{\text{th}}$, the Galactic SFR-gas relation is linear. A possible reason for the difference between Galactic and extragalactic relations is that much of Σ_{gas} is below Σ_{th} in extragalactic studies, which detect all the CO-emitting gas. If the Kennicutt-Schmidt relation ($\Sigma_{\text{SFR}} \propto \Sigma_{\text{gas}}^{1.4}$) and a linear relation between dense gas and star formation is assumed, the fraction of dense star forming gas (f_{dense}) increases as $\sim \Sigma_{\text{gas}}^{0.4}$. When Σ_{gas} reaches $\sim 300 \Sigma_{\text{th}}$, the fraction of dense gas is ~ 1 , creating a maximal starburst.

2.1 Introduction and Motivation

Understanding how physical processes in the interstellar medium (ISM) control star formation is an important prerequisite to understanding galaxy evolution. A robust measurement of the relation between the star formation rate surface density (Σ_{SFR}) and the surface density of cold gas (Σ_{gas}) is of vital importance for input into theoretical models of galaxy evolution.

The idea that there should be a relation between the density of star

formation and gas density was first proposed by Schmidt (1959). Schmidt investigated this relation, now known as the “Schmidt law”, assuming that it should be in the form of a power law and suggested that the density of star formation was proportional to gas density squared. Kennicutt (1998b) measured the global or disk-averaged Schmidt law in a sample of spiral and starburst galaxies using the projected star formation and gas surface densities (Σ_{gas}) in the form:

$$\Sigma_{\text{SFR}} \propto \Sigma_{\text{gas}}^N, \quad (2.1)$$

where N is the power law index. The global SFR and Σ_{gas} measurements for the sample of galaxies in Kennicutt (1998b) were fitted to a power law with $N=1.4$, which is known as in the “Kennicutt–Schmidt law” :

$$\Sigma_{\text{SFR}} = (2.5 \pm 0.7) \times 10^{-4} \left(\frac{\Sigma_{\text{gas}}}{1 M_{\odot} \text{ pc}^{-2}} \right)^{1.4 \pm 0.15} (M_{\odot} \text{ yr}^{-1} \text{ kpc}^{-2}). \quad (2.2)$$

Since it is only an assumption that there is *only one relation* that regulates how gas is forming stars, we refrain from calling this a “law” and instead refer to it as a SFR–gas relation, or as the Kennicutt–Schmidt relation when referring to equation 2 specifically. Several authors (Larson 1992; Elmegreen 1994; Wong & Blitz 2002; Krumholz & Tan 2007) argue that there is a simple explanation for the Kennicutt–Schmidt relation: if the SFR is proportional to the gas mass divided by the time it takes to convert the gas into stars and if we

take this timescale to be the free-fall time, then $t_{ff} \propto \rho_{\text{gas}}^{-0.5}$ and $\dot{\rho}_{\text{SFR}} \propto \rho_{\text{gas}}^{1.5}$. Taking the scale height to be constant, $\rho \propto \Sigma$, and this in turn gives the Kennicutt-Schmidt relation (to the extent that $1.4 \pm 0.15 = 1.5$). A variety of observational methods have been used to investigate this relation in different types of galaxies and on different scales.

There have been many observational studies of SFR–gas relations on either global scales (Kennicutt 1989, 1998b) or using either radial (Martin & Kennicutt 2001; Wong & Blitz 2002; Boissier et al. 2003; Heyer et al. 2004; Komugi et al. 2005; Schuster et al. 2007) or point-by-point measurements (Kuno et al. 1995; Zhang et al. 2001) that find values of N ranging from 1–2. Recently, there have been studies that measure star formation and gas content of galaxies on spatially resolved scales of ~ 0.2 –2 kpc. These studies have found power law indices of $N \approx 0.8 - 1.6$ (Kennicutt et al. 2007; Thilker et al. 2007; Bigiel et al. 2008; Braun et al. 2009; Blanc et al. 2009; Verley et al. 2010). The study by Bigiel et al. (2008) used a sample of 18 nearby galaxies to derive a spatially resolved relation on ~ 750 pc scales. They found a linear relation between Σ_{SFR} and the molecular gas surface density over a range of 3–50 $M_{\odot} \text{pc}^{-2}$:

$$\Sigma_{\text{SFR}} = 10^{-2.1 \pm 0.2} \left(\frac{\Sigma_{\text{H}_2}}{10 M_{\odot} \text{pc}^{-2}} \right)^{1.0 \pm 0.2} (M_{\odot} \text{yr}^{-1} \text{kpc}^{-2}). \quad (2.3)$$

Other spatially resolved studies were based on measurements done in a single galaxy on scales of ~ 100 –500 pc: M51 (Kennicutt et al. 2007; Blanc

et al. 2009), NGC 7331 (Thilker et al. 2007), M31 (Braun et al. 2009), and M33 (Verley et al. 2010). Since the global study of Kennicutt (1998b) and spatially resolved study of Bigiel et al. (2008) obtain results for large samples of galaxies, we use these studies as a baseline for comparison to this work. It is evident that sensitivity of N to systematic variations in methodology (e.g., data spatial resolution, SFR tracers, power law fitting method) accounts for some of the differences in the derived star formation power law index, but the underlying physical reasons for the variations in the SFR–gas relations remain an open, challenging question.

Krumholz et al. (2009) revisited the SFR–gas relation, considering the dependence on atomic and molecular components of Σ_{gas} , metallicity, and clumping of the gas. Their analysis produces a SF–gas relation that rises steeply at low Σ_{gas} , where the gas is mostly atomic, is nearly linear in the regime where normal spiral galaxies are found (Kennicutt et al. 2007; Bigiel et al. 2008; Blanc et al. 2009), and increases superlinearly above $85 M_{\odot} \text{ pc}^{-2}$. Measurements made in these studies, however, are limited to hundred parsec scales or more and are not directly comparable to the size of individual molecular clouds or dense clumps where stars form. While these studies have all looked at the extragalactic SFR–gas relation, there has been little work until recently investigating this relation locally in the Milky Way.

Surveys of nearby molecular clouds in the Milky Way using *Spitzer* imaging have provided large statistical samples of young stellar object (YSO) candidates (e.g., Allen et al. 2010, in preparation, Evans et al. (2009), For-

brich et al. (2009), Rebull et al. (2010)). These surveys have allowed us to directly count the number of low-mass stars that are forming and estimate SFRs. These data also allow us to trace the low-mass star formation regime essentially invisible to tracers, such as emission in $H\alpha$, ultraviolet, far-infrared (FIR), and singly ionized oxygen, used to establish extragalactic SFR-gas relations. Since these tracers only probe the rate at which massive stars form, a stellar Initial Mass Function (IMF), extrapolating down to low stellar masses, must be assumed to obtain a SFR. Thus, these SFR estimates are very sensitive to the IMF slope and distribution on the low-mass end.

Evans et al. (2009) compared extragalactic observed SFR-gas relations to total molecular cloud measurements from the *Spitzer* c2d survey. They found that Galactic clouds lie above the SFR-gas relations predicted by extragalactic work (Bigiel et al. 2008; Kennicutt 1998b) and lie slightly above the extrapolated relation from a study of massive dense clumps (Wu et al. 2005):

$$\text{SFR} \sim 1.2 \times 10^{-8} \left(\frac{M_{\text{dense}}}{M_{\odot}} \right) (M_{\odot} \text{ yr}^{-1}). \quad (2.4)$$

This result suggests that studying SFR-gas relations in our Galaxy may be useful for interpreting star formation observed in nearby and high- z galaxies. On the high-mass end of the spectrum, a large survey of massive dense clumps by Wu et al. (2010), provides a sample that can be directly compared to extragalactic star formation tracers.

In this work, I extend the comparison by Evans et al. (2009) by combining the 7 c2d clouds and 13 clouds from the GB survey. Regions of high-mass star formation from a survey of ~ 50 massive dense Galactic clumps from Wu et al. (2010) provide an extension to high-mass star formation regions. The layout of this paper is organized as follows. I discuss low-mass star formation in the c2d and GB clouds and describe how Σ_{gas} is derived from extinction maps and estimate SFR surface densities (Σ_{SFR}) by YSO counts in Sections 2.2.1 and 2.2.2, respectively. In Section 2.2.3, we separate clouds into evenly spaced contour intervals of Σ_{gas} , measuring the Σ_{SFR} and Σ_{gas} in these intervals. Section 2.3 discusses the differences between Galactic and extragalactic gas and SFR surface density relations. A_V and CO measurements of Σ_{gas} are compared in Section 2.3.1. I investigate whether massive star forming regions behave differently from low-mass star forming regions in Section 2.3.2. The effects of averaging over whole galaxies (kpc scales), including both star forming gas and diffuse molecular gas, on the SFR–gas relation measured in extragalactic studies are discussed in Section 2.3.3. Finally, I summarize the results in Section 6.

2.2 Low-mass Star Forming Regions from *Spitzer* c2d and Gould’s Belt Surveys

The cores to disks (c2d) Legacy project included 5 large clouds: Serpens (Ser), Perseus (Per), Chamaeleon II (Cha II), Ophiuchus (Oph), and Lupus (Lup) (Evans et al. 2009). Because the Lup ‘cloud’ is really composed of

several separate clouds, we divide them in this study by name: Lup I, III, and IV, and obtain a total of 7 clouds. The Gould’s Belt (GB) Legacy project (Allen et al. 2010, in preparation) includes 13 large clouds: IC 5146E and IC 5146NW (Harvey et al. 2008), Corona Australis (CrA), Scorpius (Sco), Auriga (Aur), Auriga North (AurN), Serpens-Aquila (Ser-Aqu), Musca (Mus), Cepheus (Cep) (Kirk et al. 2009), Cha I and III, and Lup V and VI. These 20 clouds span a large range of masses, areas, and number of YSOs (see Table 3.1). The term “large” was used in the c2d study to distinguish them from the sample of small clouds and cores that were biased toward regions known to have dense gas (Evans et al. 2003). The “large” clouds are thus suitable for statistical analyses, such as those presented here, but they are actually small compared to the Orion cloud or many clouds in the inner Galaxy.

2.2.1 Estimating Σ_{gas} from Extinction Maps

We derive cloud masses ($M_{\text{gas,cloud}}$) and mean surface densities ($\Sigma_{\text{gas,cloud}}$) from the extinction maps, which were produced from a combination of 2MASS and *Spitzer* data, ranging from $1.25\mu\text{m}$ to $24\mu\text{m}$. In this wavelength range, the spectral energy distributions (SEDs) of sources classified as stars provide measurements of the visual extinction (A_V) along lines of sight through the clouds (Evans et al. 2007; Huard et al. 2010). Line-of-sight extinctions were determined by fitting the SEDs, adopting the Weingartner & Draine (2001) extinction law with $R_V=A_V/E(B-V)=5.5$. Extinction maps were constructed by convolving these line-of-sight measures with uniformly spaced Gaussian

beams. The c2d team observed “off-cloud fields” for four of the molecular clouds: Chamaeleon, Perseus, Ophiuchus, and Lupus. The line-of-sight extinction measurements from these off-cloud fields suggested A_V calibration offsets of 1–2 magnitudes; therefore, in constructing the maps for these four clouds, Evans et al. (2007) subtracted these calibration offsets. Since no off-cloud field had been observed for Serpens, they used a weighted mean of the A_V calibration offsets to correct the calibration of their Serpens extinction maps. No off-cloud fields were observed for the GB survey. Further analysis of the fitting of the line-of-sight extinctions demonstrates that the inferred calibration offsets strongly depend on which wavebands had detections (Huard et al. 2010). For example, sources with only near-infrared (2MASS) detections may suggest no calibration offset, while sources with only mid-infrared (*Spitzer*) detections show greater calibration offsets, perhaps as high as 2–3 magnitudes. This finding suggests that the Weingartner & Draine (2001) extinction law does not accurately characterize the reddening through the full range 1.25–24 μm spectral range. For if it did, the inferred A_V calibration offsets should be independent of the detected wavebands. For this reason, the extinction maps delivered by the GB survey make use of the catalogued line-of-sight extinctions with no correction for potential calibration offsets, and, for consistency, they suggest that the previously adopted A_V calibration “offsets” of 1–2 magnitudes be added to the c2d extinction maps (Huard et al. 2010). After revising accordingly the extinctions in the clouds mapped by c2d, we find that the gas masses, and thus the cloud surface densities, are

$\sim 20\text{--}30\%$ greater than those previously published by Evans et al. (2009). The extinction maps used in this study probe to higher A_V (up to 40 mag) than some previous studies (e.g., Pineda et al. (2008); Lombardi et al. (2008, 2010)) due to the inclusion of both 2MASS and mid-IR *Spitzer* data.

In order to compute the $M_{\text{gas,cloud}}$, we chose extinction maps with $270''$ beams for all clouds. We base this choice on the best resolution map available for Ophiuchus, which is limited in resolution due to a large extended region of high extinction with relatively few background stars detected. $M_{\text{gas,cloud}}$ and $\Sigma_{\text{gas,cloud}}$ were calculated by summing up extinction map measurements and converting to the column density using the relation $N_{\text{H}}/A_V = (1.086C_{\text{ext}}(V))^{-1} = 1.37 \times 10^{21} \text{ cm}^{-2} \text{ mag}^{-1}$ (Draine 2003) for a Weingartner & Draine (2001) $R_V=5.5$ extinction law, where $C_{\text{ext}}(V) = 6.715 \times 10^{-22} \text{ cm}^2/\text{H}$ from the on-line tables¹, using equation 2.5 and 2.6, respectively. The uncertainties in $M_{\text{gas,cloud}}$ are computed from maps of extinction uncertainty, which account for the statistical photometric uncertainties, but not systematic uncertainties in using the extinction law calibration.

We compute $M_{\text{gas,cloud}}$ by summing up all pixels ($\sum A_V$) above $A_V = 2$ in all clouds except for Serpens and Ophiuchus which are covered by the c2d survey completely down to $A_V = 6$ and 3, respectively. $M_{\text{gas,cloud}}$ is then:

¹Tables available at <http://www.astro.princeton.edu/~draine/dust/dustmix.html>

$$\begin{aligned}
M_{\text{gas,cloud}} &= \mu m_{\text{H}} (1.086 C_{\text{ext}}(V))^{-1} \times \sum A_V \times A_{\text{pixel}} \\
&\approx 1.58 \times 10^{-36} \times \sum \left(\frac{A_V}{\text{mag}} \right) \times \left(\frac{A_{\text{pixel}}}{\text{cm}^2} \right) (M_{\odot})
\end{aligned} \tag{2.5}$$

where the mean molecular weight (μ) is 1.37, the total number of hydrogen atoms is $N(\text{H}) \equiv N(\text{HI}) + 2N(\text{H}_2)$, and we assume a standard molecular cloud composition of 63% hydrogen, 36% helium, and 1% dust, m_{H} is the mass of hydrogen in grams, the area of a pixel in square cm (A_{pixel}) in the extinction map is $(\pi/180/3600)^2 D(\text{cm})^2 R('')^2$, where $R('')$ is the pixel size in arcseconds, and A_{cloud} is the area of the cloud measured in square pc. We divide $M_{\text{gas,cloud}}$ by the area to obtain $\Sigma_{\text{gas,cloud}}$ for each cloud:

$$\Sigma_{\text{gas,cloud}} = \left(\frac{M_{\text{gas,cloud}}}{M_{\odot}} \right) \times \left(\frac{A_{\text{cloud}}}{\text{pc}^2} \right)^{-1} (M_{\odot} \text{ pc}^{-2}) \tag{2.6}$$

$$\Sigma_{\text{gas,cloud}} = 15 \left(\frac{A_V}{\text{mag}} \right) (M_{\odot} \text{ pc}^{-2}). \tag{2.7}$$

Measured cloud properties for c2d and GB clouds within a contour of $A_V > 2$ or A_V completeness limit are shown in Table 3.1.

Table 2.1. Measured Quantities for Clouds.

Cloud	$N_{\text{YSOs,tot}}$	$N_{\text{YSOs,I}}$	$N_{\text{YSOs,F}}$	Distance (pc)	Ω (deg ²)	A_{cloud} (pc ²)	$M_{\text{gas,cloud}}$ (M_{\odot})	$\Sigma_{\text{gas,cloud}}$ (M_{\odot} pc ⁻²)	SFR (M_{\odot} Myr ⁻¹)	Σ_{SFR} (M_{\odot} yr ⁻¹ kpc ⁻²)
(1)	(2)	(3)	(4)	(5)	(6)	(7)	(8)	(9)	(10)	(11)
Cha II	24	0	2	178±18	1.0	9.9±2.0	637.4±296.3	64.3±26	6.0±3.2	0.61±0.35
Lup I	13	2	1	150±20	1.3	8.9±2.4	512.5±308.2	57.9±31	3.2±1.8	0.37±0.22
Lup III	68	2	6	200±20	1.3	15.4±3.1	912.1±517.3	59.1±31	17.0±9.2	1.10±0.63
Lup IV	12	1	0	150±20	0.4	2.5±0.7	189.3±95.5	75.1±32	3.0±1.6	1.19±0.72
Oph	290	27	44	125±25	6.2	29.6±11.8	3115.3±1754.3	105.4±41	72.5±39.0	2.45±1.65
Per	385	76	35	250±50	3.8	73.2±29.3	6585.3±3557.1	90.0±32	96.2±51.8	1.32±0.88
Ser	224	31	21	260±10	0.8	17.0±1.3	2336.7±640.2	137.3±36	56.0±30.2	3.29±1.79
AurN	2	1	0	300±30	0.1	2.4±0.5	223.9±51.9	92.8±10	0.5±0.3	0.21±0.12
Aur	171	43	24	300±30	1.8	50.0±10.0	4617.5±1072.7	92.4±10	42.8±23.0	0.86±0.49
Cep	118	30	10	300±30	1.4	38.0±7.6	2610.3±168.5	68.7±17	29.5±15.9	0.78±0.45
Cha III	4	1	0	200±20	2.3	28.0±5.6	1326.0±386.2	47.4±10	1.0±0.5	0.04±0.02
Cha I	89	10	12	200±20	0.8	9.4±1.9	857.3±206.3	91.1±12	22.2±12.0	2.36±1.36
CrA	41	7	3	130±25	0.6	3.0±1.2	279.2±114.0	92.3±12	10.2±5.5	3.39±2.24
IC5146E	93	13	9	950±80	0.2	61.4±10.3	3365.2±872.9	54.8±10	23.2±12.5	0.38±0.21
IC5146NW	38	16	3	950±80	0.3	87.6±14.8	5178.1±1257.3	59.1±10	9.5±5.1	0.11±0.06
Lup VI	45	0	1	150±20	1.0	6.7±1.8	454.9±141.4	67.5±10	11.2±6.1	1.67±1.00
Lup V	43	0	0	150±20	1.7	11.7±3.1	704.7±223.5	60.5±10	10.8±5.8	0.92±0.55
Mus	12	1	0	160±20	0.9	6.8±1.7	335.1±109.1	49.1±10	3.0±1.6	0.44±0.26
Sco	10	2	1	130±15	1.4	7.3±1.7	620.6±17.4	85.2±22	2.5±1.3	0.34±0.20
Ser-Aqu	1440	146	96	260±10	8.7	179.5±13.8	24441.3±3025.2	136.2±13	360.0±193.9	2.01±1.09
Cloud Averages	156.1±71.5	20.5±7.9	13.4±5.2	274.6±53.3	1.8±0.5	32.4±9.6	2965.1±1204.9	79.3±5.8	39.0±17.9	1.2±0.2
Cloud Total	3122.0	409.0	268.0	-	36.0	648.3	59302.7	91.5	780.5	1.2
Data from Literature:										
Taurus ^I	148	-	-	137	44	252	27207	108	37	0.147

Note. — Columns are : (1) Cloud name.; (2) Total number of YSOs at all A_V .; (3) Number of Class I objects at all A_V .; (4) Number of Flat SED objects at all A_V .; (5) Distances to each cloud.; (6) Solid angle.; (7) Area (pc²).; (8) Mass (M_{\odot}).; (9) Surface gas density (M_{\odot} pc⁻²).; (10) Star formation rate (M_{\odot} Myr⁻¹).; (11) Star formation rate density (M_{\odot} yr⁻¹ kpc⁻²).; (I) Total A_V mass from Pineda et al. (2010) and YSO data from Rebull et al. (2010).

2.2.2 Estimating Star Formation Rates from YSO Counts

We estimate the SFR from the total number of YSOs ($N_{\text{YSO,tot}}$) contained in an area where $A_V > 2$, as described in § 2.2.1. We assume a mean YSO mass ($\langle M_{\text{YSO}} \rangle$) of $0.5 \pm 0.1 M_{\odot}$, where the mean estimated error in mass is derived from the mass distribution of YSOs in Cha II from Spezzi et al. (2008). The mean YSO mass is consistent with IMF studies by Chabrier (2003); Kroupa (2002); Ninkovic & Trajkovska (2006). We also assume a period for star formation ($t_{\text{Class II}}$) of 2 ± 1 Myr, based on the estimate of the elapsed time between formation and the end of the Class II phase (Evans et al. 2009). This SFR assumes that star formation has been continuous over a period greater than $t_{\text{Class II}}$. All clouds have Class III objects, indicating that star formation has continued for longer than $t_{\text{Class II}}$. The SFR measured in this way could be underestimated or overestimated in any particular cloud, but over an ensemble of 20 clouds, it should be the most reliable SFR indicator available because no extrapolation from the massive star tail of the IMF is needed. We base our error estimates by choosing the largest error from either the systematic error, combined in quadrature from mean YSO mass and period of star formation, or the Poisson error from YSO number counts.

$$\Sigma_{\text{SFR}} = N_{\text{YSO,tot}} \times \left(\frac{\langle M_{\text{YSO}} \rangle}{M_{\odot}} \right) \times \left(\frac{t_{\text{Class II}}}{\text{Myr}} \right)^{-1} \times \left(\frac{A_{\text{cloud}}}{\text{kpc}^2} \right)^{-1} (M_{\odot} \text{ yr}^{-1} \text{ kpc}^{-2}) \quad (2.8)$$

Table 3.1 lists values for clouds within a contour of $A_V > 2$ for all c2d

and GB clouds. We show our estimated $\Sigma_{\text{gas,cloud}}$ and Σ_{SFR} for the c2d and GB clouds in Figure 2.1. $\Sigma_{\text{gas,cloud}}$ ranges from $\sim 50\text{--}140 M_{\odot} \text{ pc}^{-2}$, and Σ_{SFR} ranges from $\sim 0.4\text{--}3.4 M_{\odot} \text{ kpc}^{-2} \text{ yr}^{-1}$. We use these units for convenience in comparing to the extragalactic relations.

We compare the observations to the predicted values for Σ_{SFR} using $\Sigma_{\text{gas,cloud}}$ that we calculate for the c2d and GB clouds. We plot these extragalactic relations in Figure 2.1 and will include them in all the following SFR–gas relation figures. The solid lines represent the regime where they were fitted to data and the dashed lines are extrapolated relations spanning the range of Σ_{gas} . The blue line is from disk-averaged or global SFR measurements based on $\text{H}\alpha$ emission and the total ($\text{H}\text{I}+\text{CO}$) gas surface densities in a sample of normal spirals and starburst galaxies from Kennicutt (1998b). The red line is from Bigiel et al. (2008), who made sub-kpc resolution measurements in a sample of spiral and dwarf galaxies using SFRs based on a combination of *Spitzer* $24\mu\text{m}$ and GALEX UV data and use CO measurements to obtain a relation for H_2 gas surface density. Both of these studies trace either obscured ($24\mu\text{m}$) or unobscured ($\text{H}\alpha$ and UV) massive star formation and are blind to regions of low-mass star formation that we are measuring in this work. We also compare to the theoretical total ($\text{H}\text{I}+\text{CO}$) gas and SFR relation of Krumholz et al. (2009) (orange solid line). This prediction takes into account three factors: the conversion of atomic to molecular gas, metallicity, and clumping of the gas. For our comparisons, we choose galactic solar metallicity and a clumping factor of 1, which corresponds to clumping on 100 pc scales. We include data

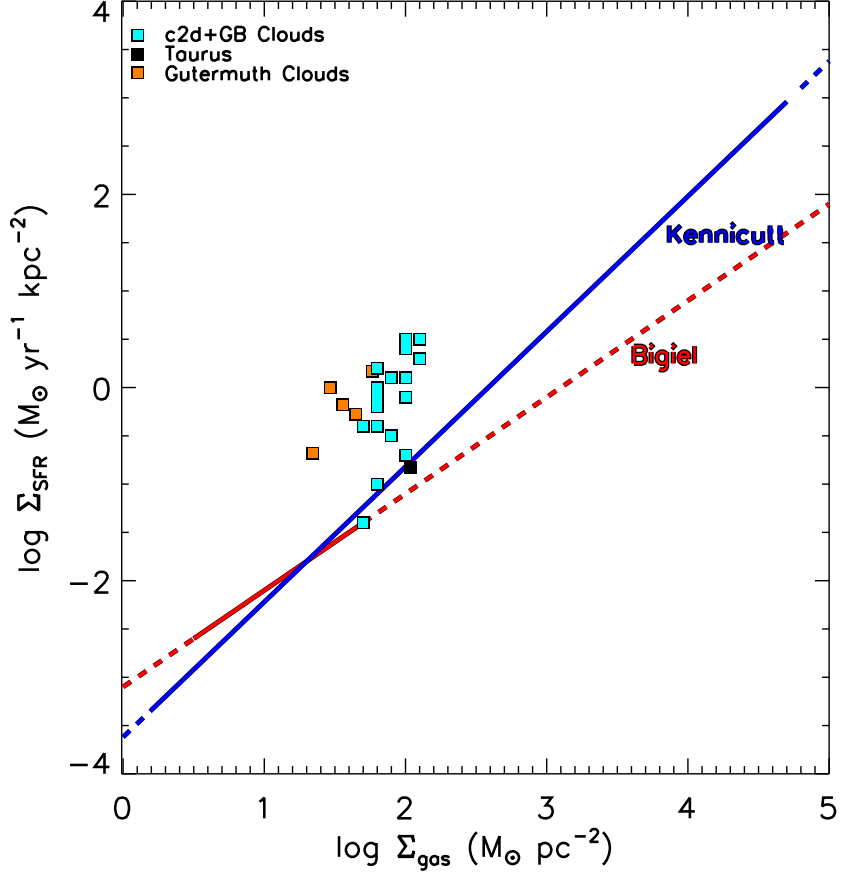


Figure 2.1 Σ_{SFR} is shown versus the Σ_{gas} for c2d and GB clouds (cyan squares) and the Gutermuth et al. (2011) cloud sample (orange squares). All cloud Σ_{gas} are measured above $A_V > 2$ (or the cloud completeness limit, see §Section 2.2.1). We also include an estimate for the Taurus molecular cloud (black square) which includes YSO counts from Rebull et al. (2010) and an $A_V > 2$ gas mass from Pineda et al. (2010). Extragalactic observed relations are shown for the sample of Kennicutt (1998b) and Bigiel et al. (2008) (blue solid and red lines, respectively).

points for the Taurus molecular cloud, including YSO counts from Rebull et al. (2010), Σ_{gas} from a 2MASS extinction map (Pineda et al. 2010), and the total ^{13}CO and ^{12}CO gas mass from Goldsmith et al. (2008).

If we take the average $\Sigma_{\text{gas,cloud}}$ defined as the total $M_{\text{gas,cloud}}$ divided by the total area (A_{cloud}) in pc^2 , we would find that the average molecular cloud in this study has a surface density of $91.5 M_{\odot} \text{pc}^{-2}$ and a Σ_{SFR} of $1.2 M_{\odot} \text{kpc}^{-2} \text{yr}^{-1}$. Taking this average $\Sigma_{\text{gas,cloud}}$ and calculating what the extragalactic relations would predict for the average cloud SFR surface density, we would get 0.13, 0.07, and $0.03 M_{\odot} \text{kpc}^{-2} \text{yr}^{-1}$ for Kennicutt (1998b), Bigiel et al. (2008), and Krumholz et al. (2009), respectively. The observed values exceed the observed extragalactic Σ_{SFR} predictions by factors of ~ 9 –17 and the theoretical prediction by a factor of ~ 40 . While the star formation surface density, Σ_{SFR} of $1.2 M_{\odot} \text{kpc}^{-2} \text{yr}^{-1}$, seem high, the clouds fill only a small fraction of the local square kpc. From Table 1, the total SFR is $780.5 M_{\odot} \text{Myr}^{-1}$. If we remove the IC5146 clouds, which are more distant than 0.5 kpc, the SFR within 0.5 kpc is $748 M_{\odot} \text{Myr}^{-1}$ or $7.5 \times 10^{-4} M_{\odot} \text{yr}^{-1}$. Extrapolated to the Galaxy with a star-forming radius of 10 kpc, this would amount to $0.3 M_{\odot} \text{yr}^{-1}$, less than the rate estimated for the entire galaxy of 0.68 to $1.45 M_{\odot} \text{yr}^{-1}$ (Robitaille & Whitney 2010). This local, low-mass star formation mode thus could account for a substantial, but not dominant, amount of star formation in our Galaxy.

2.2.3 Estimating Σ_{gas} and Σ_{SFR} for the Youngest YSOs as a Function of A_V

The last section gave us estimates over the whole molecular cloud including all YSOs in each cloud. Early work surveying large areas of clouds (e.g., Lada (1992)) suggested that star formation is concentrated in regions within molecular clouds in regions of high densities ($n \sim 10^4 \text{ cm}^{-3}$). The c2d and GB studies of many whole clouds have clearly established that star formation is not spread uniformly over clouds, but is concentrated in regions at high extinction. Furthermore, the youngest YSOs and dense cores (Enoch et al. 2007) are the most highly concentrated at high A_V (Evans et al. 2009, Bressert et al. 2010, submitted). Older YSOs can leave their original formation region or even disperse the gas and dust. Taking the average velocity dispersion of a core to be 1 km s^{-1} , a 2 Myr old YSO could travel $\sim 2 \text{ pc}$, roughly the average radius of a cloud in this study. We therefore apply a conservative approach and only estimate the SFRs using the youngest Class I or Flat SED YSOs (see Greene et al. (1994) for the definition of classes) that have not yet migrated from their birth place. To classify YSOs as Class I or Flat SED, we use the extinction corrected spectral index from Evans et al. (2009) for the c2d clouds and the uncorrected spectral index for the GB clouds (Table 3.1). These two classes of YSOs have timescales of 0.55 ± 0.28 and $0.36 \pm 0.18 \text{ Myr}$, respectively (Allen et al. 2010, in preparation).

In order to measure Σ_{SFR} and Σ_{gas} for the youngest YSOs, we divide the clouds into equally spaced contour levels of A_V or $\Sigma_{\text{gas,con}}$ and measure the

SFR, mass (M_{con}), and area (A_{con}) enclosed in that contour level. The contour intervals start from the extinction map completeness limits (§ 2.2.1) and are spaced such that they are wider than our map beam size of $270''$ as shown in Figure 2.2. We compute the gas surface density ($\Sigma_{\text{gas,con}}$) in the same way as in equation 2.6, but this time using only the mass ($M_{\text{gas,con}}$) and area (A_{con}) enclosed in the A_V contour region.

$$\Sigma_{\text{gas,con}} = \left(\frac{M_{\text{gas,con}}}{M_{\odot}} \right) \times \left(\frac{A_{\text{con}}}{\text{pc}^2} \right)^{-1} (M_{\odot} \text{ pc}^{-2}). \quad (2.9)$$

If there are no YSOs found in the contour region, we compute an upper limit to the SFR by assuming that there is one YSO in that region. The upper limits are denoted by the asterisks in Table 2.3. We estimate the uncertainties in the both the SFR and Σ_{SFR} by choosing the largest error: either the systematic or Poisson error from YSO counts.

2.2.3.1 MISidentified YSOs from SED FITS (MISFITS)

The c2d and GB surveys have classified YSOs based on the SED slope from a fit to photometry between $2\mu\text{m}$ and $24\mu\text{m}$ (Evans et al. 2009; Allen et al. 2010, in preparation). However, we find that some of the Class I and Flat SED YSOs are not clustered and lie farther from the extinction peaks than expected for their age. Most of these suspicious objects are found, on average, to lie at $A_V \sim 6$ magnitude. If these Class I and Flat SED objects are true young YSOs, they are more likely to be centrally concentrated toward the densest regions in a cloud (Lada 1992). Class I and Flat SED YSOs

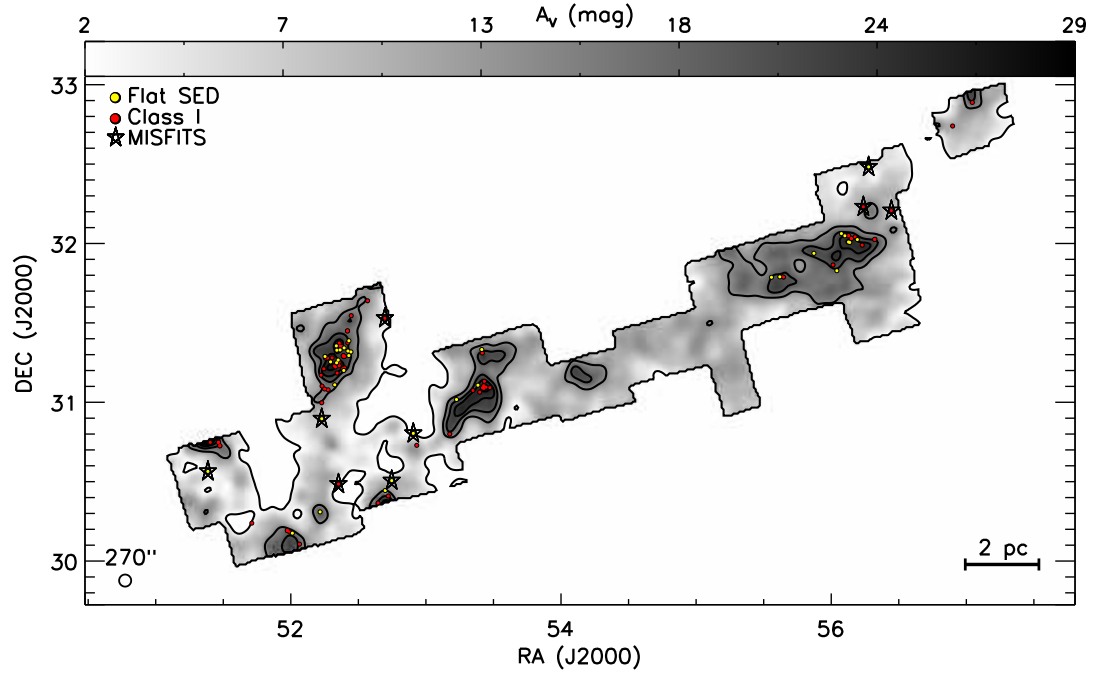


Figure 2.2 An example of the Σ_{gas} measurement method in the Perseus molecular cloud from the c2d survey. The grayscale image is the extinction map with black contours ranging from 2–29 in intervals of 4.5 mag. The yellow filled circles are Flat SED sources and the red filled circles are Class I sources. Sources that have an open star correspond to suspicious YSOs (MISFITS) that were observed in $\text{HCO}^+ J=3-2$ at the CSO and were not detected. We measure the Σ_{gas} from each map in each contour of extinction. Contours are spaced in intervals wider than the extinction map beam size of $270''$. To estimate SFR, we count the YSOs in corresponding contour levels (§Section 2.2.2).

should be associated with a dense, centrally concentrated, envelope of gas. We therefore performed a follow up survey of these suspicious objects for a subset of c2d and GB clouds using the Caltech Submillimeter Observatory (CSO). Our work was motivated by a study performed by van Kempen et al. (2009), who mapped $\text{HCO}^+ J=4-3$ using the James Clerk Maxwell Telescope and found that 6 previously classified Class I YSOs in Ophiuchus had no detections down to 0.1 K.

With high effective and critical densities, $n \sim 10^4$ and $\sim 10^6 \text{ cm}^{-3}$ (Evans 1999), the $\text{HCO}^+ J=3-2$ transition provides a good tracer of the dense gas contained in protostellar envelopes. We observed Class I and Flat SED YSOs at the CSO from the Aur, Cep, IC5146, Lup, Oph, Per, Sco, Ser, and Ser-Aqu molecular clouds using the $\text{HCO}^+ J=3-2$ (267.557620 GHz) line transition as a dense stage I gas tracer to test if they are truly embedded YSOs. A survey of all observable c2d and GB clouds with detailed results will be published in a later paper.

Observations were made during June and December of 2009 and July 2010 with an atmospheric optical depth (τ_{225}) ranging from 0.05–0.2. We observed each source using position switching for an average of 120 seconds on and off source. If a source was detected, we integrated until we reach a signal-to-noise of $\geq 2\sigma$ (most sources have $\geq 3\sigma$ detections). Using an average main beam efficiency (η) of 0.80 and 0.61 for December 2009 and July 2010 observing runs, respectively, we compute the main beam temperatures and integrated intensities of detected sources. The results are shown in Table 2.2.

Table 2.2. Properties of Suspicious YSOs and MISFITS

Cloud	RA J2000	DEC J2000	Classification	α	$\int T_{\text{MB}} dV$ (K km s ⁻¹)	T_{MB} (K)	SED class	A_V (mag)	comments
(1)	(2)	(3)	(4)	(5)	(6)	(7)	(8)	(9)	(10)
Aur	04:18:21.27	+38:01:35.88	YSOc	-0.09		<0.23	Flat	4	
Aur	04:19:44.67	+38:11:21.98	YSOc_star+dust(IR1)	-0.07		<0.23	Flat	7	
Aur	04:29:40.02	+35:21:08.95	YSOc_star+dust(IR1)	0.51		<0.31	I	8	
Aur	04:30:14.96	+36:00:08.53	YSOc_red	1.77	0.42±0.09	0.69±0.15	I	8	
Aur	04:30:23.83	+35:21:12.35	YSOc_red	0.61		<0.30	I	8	
Aur	04:30:41.17	+35:29:41.08	YSOc_red	1.49	0.76±0.07	1.49±0.14	I	7	self-reversed
Aur	04:30:44.23	+35:59:51.16	YSOc	1.08	0.76±0.15	0.78±0.15	I	8	
Aur	04:30:48.52	+35:37:53.76	YSOc_red	1.46	1.01±0.13	1.15±0.15	I	7	self-reversed
Aur	04:30:56.62	+35:30:04.55	YSOc_red	2.35	0.49±0.07	1.00±0.15	I	7	
Cep	22:29:33.35	+75:13:16.01	YSOc_red	0.20		<0.42	Flat	6	
Cep	22:35:00.82	+75:15:36.42	YSOc_star+dust(IR2)	-0.29		<0.46	Flat	6	
Cep	22:35:14.09	+75:15:02.61	YSOc_red	0.36		<0.42	I	6	
Cep	21:01:36.07	+68:08:22.54	YSOc	-0.21		<0.42	I	5	
Cep	21:01:43.89	+68:14:03.31	YSOc_red	0.14		<0.40	I	6	
Cep	21:02:14.06	+68:07:30.80	YSOc_red	0.49		<0.40	I	6	
Cep	21:02:21.22	+67:54:20.28	YSOc_red	0.68	0.89± 0.18	1.74± 0.34	I	9	double peak
Cep	21:02:21.22	+67:54:20.28	YSOc_red	0.68	0.72± 0.11	2.33± 0.34	I	9	double peak
Cep	21:02:21.36	+68:04:36.11	YSOc_PAH-em	0.52		<0.42	I	5	
Cep	21:02:59.46	+68:06:32.24	YSOc_red	0.65		<0.42	I	5	
IC5146E	21:52:46.58	+47:12:49.32	YSOc_star+dust(IR2)	-0.19		<0.34	Flat	5	
IC5146E	21:53:36.24	+47:10:27.84	YSOc_star+dust(IR1)	-0.12		<0.30	Flat	6	
IC5146E	21:54:18.76	+47:12:09.73	YSOc_star+dust(IR2)	-0.23		<0.26	Flat	4	
IC5146E	21:52:14.36	+47:14:54.60	YSOc_star+dust(IR2)	0.67		<0.28	I	4	
IC5146E	21:52:37.78	+47:14:38.40	YSOc_star+dust(IR1)	0.64	1.59± 0.25	1.80± 0.28	I	5	
IC5146E	21:53:06.94	+47:14:34.80	YSOc	0.34	0.71± 0.27	0.66± 0.25	I	5	
IC5146E	21:53:55.70	+47:20:30.13	YSOc_PAH-em	1.59		<0.34	I	4	
IC5146NW	21:45:31.22	+47:36:21.24	YSOc	0.13	0.44± 0.19	0.61± 0.26	Flat	5	
IC5146NW	21:44:43.08	+47:46:43.68	YSOc_red	0.63	1.92± 0.11	4.18± 0.23	I	4	
IC5146NW	21:44:48.31	+47:44:59.64	YSOc_red	1.83	0.65± 0.05	3.11± 0.23	I	5	
IC5146NW	21:44:53.98	+47:45:43.56	YSOc_star+dust(IR1)	0.76	0.70± 0.11	1.75± 0.28	I	4	
IC5146NW	21:45:02.64	+47:33:07.56	YSOc_red	1.18	0.77± 0.22	1.03± 0.30	I	4	

Table 2.2 (cont'd)

Cloud	RA J2000	DEC J2000	Classification	α	$\int T_{\text{MB}} dV$ (K km s ⁻¹)	T_{MB} (K)	SED class	A_V (mag)	comments
(1)	(2)	(3)	(4)	(5)	(6)	(7)	(8)	(9)	(10)
IC5146NW	21:45:08.31	+47:33:05.77	YSOc_red	0.74	3.72± 0.53	2.07± 0.30	I	4	
IC5146NW	21:45:27.86	+47:45:50.40	YSOc_star+dust(IR4)	0.42		<0.36	I	3	
IC5146NW	21:47:06.02	+47:39:39.24	YSOc_red	0.43	0.40± 0.14	0.70± 0.25	I	5	
Lup I	15:38:48.35	-34:40:38.24	YSOc_PAH-em	0.31		<0.42	I	3	
Lup I	15:43:02.29	-34:44:06.22	YSOc_star+dust(IR1)	0.14		<0.38	Flat	<2	
Lup III	16:07:03.85	-39:11:11.59	YSOc_star+dust(IR1)	-0.14		<0.30	Flat	<2	
Lup III	16:07:08.57	-39:14:07.75	YSOc	-0.01		<0.32	Flat	<2	
Lup III	16:07:54.73	-39:15:44.49	YSOc_red	-0.15		<0.28	Flat	2	
Lup IV	16:02:21.61	-41:40:53.70	YSOc_PAH-em	0.56		<0.36	I	4	
Lup VI	16:24:51.78	-39:56:32.66	YSOc	0.22		<0.48	Flat	8	
Oph	16:21:38.72	-22:53:28.26	YSOc_star+dust(IR1)	0.99		<0.35	I	<3	
Oph	16:23:40.00	-23:33:37.36	YSOc	0.01		<0.37	Flat	3	
Oph	16:44:24.27	-24:01:24.56	YSOc_PAH-em	0.27		<0.35	Flat	<3	
Oph	16:45:26.65	-24:03:05.41	YSOc_red	0.37		<0.36	I	<3	
Oph	16:21:45.13	-23:42:31.63	YSOc_star+dust(IR1)	0.30		<0.36	I	9	
Oph	16:31:31.24	-24:26:27.87	YSOc_star+dust(IR4)	-0.24		<0.38	Flat	<3	
Oph	16:25:27.56	-24:36:47.55	YSOc_star+dust(IR1)	0.06		<0.42	Flat	7	
Oph	16:23:32.22	-24:25:53.82	YSOc_star+dust(IR2)	-0.04	0.36± 0.17	0.66± 0.31	Flat	4	
Oph	16:22:20.99	-23:04:02.35	YSOc_PAH-em	0.17		<0.44	Flat	4	
Oph	16:23:05.43	-23:02:56.73	YSOc_star+dust(IR2)	-0.27		<0.46	Flat	4	
Oph	16:23:06.86	-22:57:36.61	YSOc	-0.19		<0.44	Flat	5	
Oph	16:23:40.00	-23:33:37.36	YSOc	0.01		<0.46	Flat	4	
Per	03:25:19.52	+30:34:24.16	YSOc	-0.11		<0.27	Flat	2	
Per	03:26:37.47	+30:15:28.08	YSOc_red	0.99	0.20±0.04	0.77±0.14	I	2	double peak
Per	03:26:37.47	+30:15:28.08	YSOc_red	0.99	0.11±0.03	0.49±0.14	I	2	double peak
Per	03:28:34.49	+31:00:51.10	YSOc_star+dust(IR1)	0.89	0.31±0.05	0.95±0.15	I	6	
Per	03:28:34.94	+30:54:54.55	YSOc	0.01		<0.32	Flat	3	
Per	03:29:06.05	+30:30:39.19	YSOc_red	0.72		<0.30	I	2	
Per	03:29:51.82	+31:39:06.03	red	3.34	3.22±0.20	2.41±0.15	I	6	
Per	03:30:22.45	+31:32:40.53	YSOc_star+dust(IR2)	0.35		<0.34	I	3	
Per	03:30:38.21	+30:32:11.93	YSOc_star+dust(IR2)	-0.10		<0.29	Flat	4	

Table 2.2 (cont'd)

Cloud	RA J2000	DEC J2000	Classification	α	$\int T_{\text{MB}} dV$ (K km s ⁻¹)	T_{MB} (K)	SED class	A_V (mag)	comments
(1)	(2)	(3)	(4)	(5)	(6)	(7)	(8)	(9)	(10)
Per	03:31:14.70	+30:49:55.40	YSOc_star+dust(IR1)	-0.09		<0.30	Flat	2	
Per	03:31:20.98	+30:45:30.06	YSOc_red	1.10	2.70±0.17	2.68±0.17	I	5	
Per	03:44:24.84	+32:13:48.36	YSOc_red	1.69		<0.31	I	6	
Per	03:44:35.34	+32:28:37.18	YSOc_red	-0.09		<0.32	Flat	3	
Per	03:45:13.82	+32:12:10.00	YSOc_red	0.43		<0.28	I	3	
Per	03:47:05.43	+32:43:08.53	YSOc_red	0.48	0.93±0.09	1.48±0.14	I	5	
Sco	16:46:58.27	-09:35:19.76	YSOc_red	0.66		<0.44	I	12	
Sco	16:48:28.85	-14:14:36.45	YSOc_PAH-em	0.48		<0.48	I	5	
Sco	16:22:04.35	-19:43:26.76	YSOc	0.02		<0.66	Flat	6	
Ser	18:28:41.87	-00:03:21.34	YSOc_star+dust(IR1)	0.14		<0.47	Flat	8	
Ser	18:28:44.78	+00:51:25.79	YSOc_red	1.05	0.86±0.23	0.83±0.22	I	8	
Ser	18:28:44.96	+00:52:03.54	YSOc_red	1.27	1.61±0.34	1.36±0.28	I	8	
Ser	18:29:16.18	+00:18:22.71	YSOc	-0.13	1.28±0.29	0.98±0.22	Flat	7	
Ser	18:29:40.20	+00:15:13.11	YSOc_star+dust(IR1)	0.68		<0.50	I	<6	
Ser	18:30:05.26	+00:41:04.58	red	1.24		<0.44	I	<6	
Ser	18:28:44.01	+00:53:37.93	YSOc_red	0.29		<0.42	Flat	7	
Ser	18:29:27.35	+00:38:49.75	YSOc	0.24		<0.38	Flat	13	
Ser	18:29:31.96	+01:18:42.91	YSOc_star+dust(IR1)	0.32	0.63± 0.27	0.69± 0.30	I	11	
Ser-Aqu	18:13:45.05	-03:26:02.67	YSOc_star+dust(IR1)	0.39		<0.58	I	6	
Ser-Aqu	18:27:03.33	-02:45:33.42	YSOc_red	0.44		<0.54	I	5	
Ser-Aqu	18:29:16.80	-01:17:30.68	YSOc	0.78		<0.54	I	10	
Ser-Aqu	18:30:32.48	-03:50:01.21	YSOc_star+dust(MP1)	0.37		<0.54	I	9	
Ser-Aqu	18:33:03.49	-02:08:42.53	YSOc_PAH-em	1.25		<0.56	I	8	
Ser-Aqu	18:37:39.24	-00:25:35.18	YSOc_star+dust(IR1)	0.72		<0.56	I	7	
Ser-Aqu	18:37:46.90	-00:01:55.83	YSOc_PAH-em	1.19		<0.52	I	8	
Ser-Aqu	18:37:52.77	-00:23:03.10	YSOc_star+dust(MP1)	0.59		<0.50	I	7	
Ser-Aqu	18:37:55.79	-00:23:31.59	YSOc	1.14		<0.58	I	8	
Ser-Aqu	18:05:31.11	-04:38:09.63	YSOc	0.23		<0.60	Flat	9	
Ser-Aqu	18:10:28.90	-02:37:42.79	YSOc	-0.18		<0.62	Flat	6	
Ser-Aqu	18:26:32.81	-03:46:27.26	YSOc_red	0.08		<0.60	Flat	10	
Ser-Aqu	18:27:24.87	-03:58:21.15	YSOc	-0.22		<0.60	Flat	10	

Table 2.2 (cont'd)

Cloud	RA J2000	DEC J2000	Classification	α	$\int T_{\text{MB}} dV$ (K km s ⁻¹)	T_{MB} (K)	SED class	A_V (mag)	comments
(1)	(2)	(3)	(4)	(5)	(6)	(7)	(8)	(9)	(10)
Ser-Aqu	18:28:09.49	-02:26:31.95	YSOc_star+dust(IR2)	-0.11		<0.58	Flat	5	
Ser-Aqu	18:29:16.72	-01:17:36.92	YSOc_star+dust(MP1)	-0.08		<0.62	Flat	10	
Ser-Aqu	18:30:06.06	-01:10:19.33	YSOc	-0.15		<0.56	Flat	6	
Ser-Aqu	18:30:13.01	-01:25:36.64	YSOc_star+dust(IR2)	-0.23		<0.60	Flat	8	
Ser-Aqu	18:36:02.64	-00:02:20.70	YSOc_star+dust(MP1)	-0.28		<0.58	Flat	8	
Ser-Aqu	18:38:55.77	-00:23:40.81	YSOc	-0.05		<0.64	Flat	7	
Ser-Aqu	18:40:12.06	+00:29:27.74	YSOc_red	-0.07		<0.50	Flat	8	

Note. — Columns are : (1) Cloud (2) Source Right Ascension in J2000 coordinates; (3) Source Declination in J2000 coordinates; (4) Source classification (see Evans et al. (2009)); (5) Spectral Index, extinction corrected values for c2d clouds only; (6) Integrated main beam HCO⁺line intensity.; (7) Main beam HCO⁺line temperature, upper limits are computed as $2\sigma_{\text{rms}}$; (8) SED class based on Greene et al. (1994); (9) A_V in source position. Values that are found outside the A_V map completeness limit are given as < limit; (10) Line profile comments.

For this paper, we observed a total of 98 suspicious sources, 45 Flat SED and 53 Class I sources. We find that 74% (73/98) of the observed sources are not detected in $\text{HCO}^+ J=3-2$. Out of the 42 Flat SED sources, we detect only 3, but we detect 42% (22/53) of the Class I sources. The YSO MISFITS are a small fraction of the total number (3146) of YSOs or Class I plus Flat sources (681) in the c2d and GB studies, but they could bias the statistics upward at low gas surface densities. The undetected MISFITS may be background galaxies or later stage YSOs, and we will explore this in more detail in a later paper. Figure 2.2 shows the distribution of Class I (red filled circles), Flat SED YSOs (yellow filled circles) and non-detected MISFITS, indicated by the open stars on the Per cloud A_V map. MISFITS that we do not detect in $\text{HCO}^+ J=3-2$ are removed from the sample when we measure $\Sigma_{\text{gas,con}}$ and Σ_{SFR} in A_V contours (§Section 2.2.4).

2.2.4 Results: The Youngest YSOs as a Function of Σ_{gas}

After removing the MISFITS from our Class I and Flat SED YSO sample, we show the number, $M_{\text{gas,con}}$, $\Sigma_{\text{gas,con}}$, SFRs, and Σ_{SFR} in Table 2.3 for all contour levels in each cloud or separate cloud component (see §Section 2.2). In Figure 2.3, we show the $\Sigma_{\text{gas,con}}$ and Σ_{SFR} densities for both Class I and Flat SED sources (green and magenta stars) and upper limits for each class (green and magenta inverted triangles) that we measured in contour regions described in § 2.2.3, with extragalactic observational relations over-plotted. A wider range in both Σ_{gas} ($\sim 45\text{--}560 M_{\odot} \text{ pc}^{-2}$), and Σ_{SFR} ($\sim 0.03\text{--}95 M_{\odot} \text{ kpc}^{-2} \text{ yr}^{-1}$)

are found for contour regions compared to the total cloud measurements. We note that the points for Sco and Cep (Kirk et al. 2009) clouds are obtained by co-adding the separate cloud regions using the same contour intervals. Since these points sample regions with non-uniform A_V , they only provide an estimate of Σ_{SFR} and Σ_{gas} . These points lie at $\Sigma_{\text{SFR}} < 6 M_{\odot} \text{ kpc}^{-2} \text{ yr}^{-1}$ and high $\Sigma_{\text{gas}} > 330 M_{\odot} \text{ pc}^{-2}$.

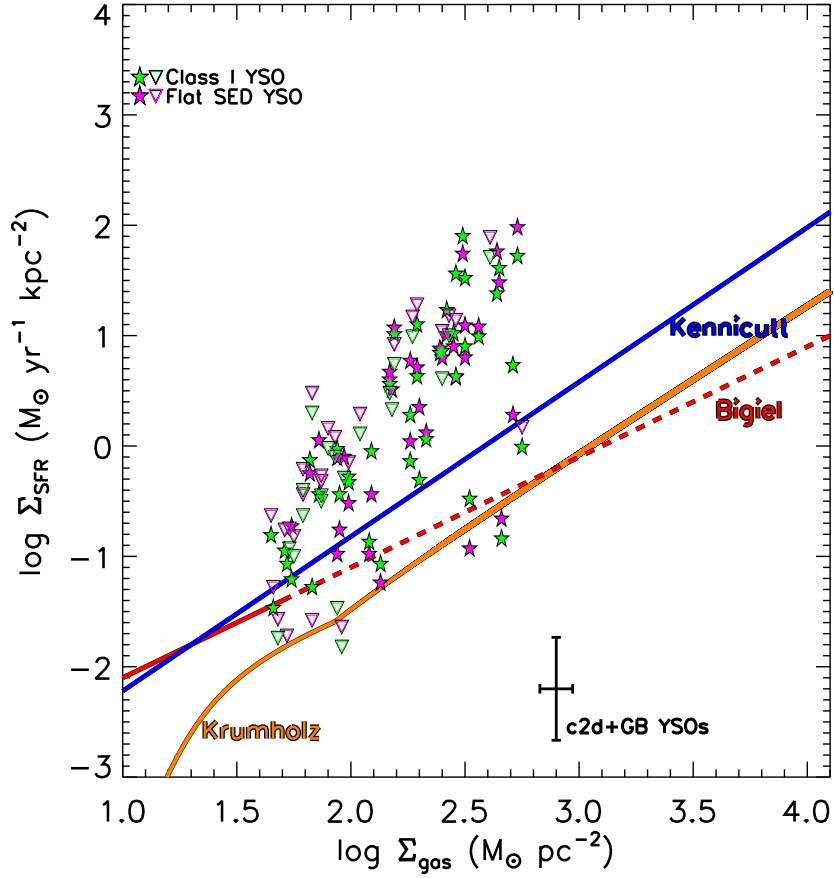


Figure 2.3 Gas surface densities measured from extinction maps and SFRs estimated from Class I (green stars) and Flat SED (magenta stars) YSO number counts in c2d and Gould’s belt clouds are shown. For contour levels that do not contain any YSOs, we calculate an upper limit for that region using one YSO (open inverted triangles). Extragalactic observed relations are shown for the sample of Kennicutt (1998b) and Bigiel et al. (2008) (blue solid and red lines, respectively).

Table 2.3. Measured Quantities for Clouds in A_V Contours

Cloud	$N_{\text{YSOs,I}}$	$N_{\text{YSOs,F}}$	Contour levels ^I (mag)	Ω (deg ²)	A_{con} (pc ²)	M_{con} (M_{\odot})	$\Sigma_{\text{gas,con}}$ (M_{\odot} pc ⁻²)	SFR, I (M_{\odot} Myr ⁻¹)	SFR, F (M_{\odot} Myr ⁻¹)	$\Sigma_{\text{SFR,I}}$ (M_{\odot} yr ⁻¹ kpc ⁻²)	$\Sigma_{\text{SFR,F}}$ (M_{\odot} yr ⁻¹ kpc ⁻²)
(1)	(2)	(3)	(4)	(5)	(6)	(7)	(8)	(9)	(10)	(11)	(12)
Cha II	0	0	5.2	0.8	7.78±1.57	416.9±223.1	53.6±26.6	0.9±1.0*	1.4±1.0*	0.1±0.1*	0.2±0.1*
Cha II	0	1	8.2	0.2	1.76±0.36	162.6±58.7	92.3±27.6	0.9±1.0*	1.4±1.0	0.5±0.6*	0.8±0.6
Cha II	0	1	11.8	0.03	0.30±0.06	43.9±12.7	147.0±30.4	0.9±1.0*	1.4±1.0	3.0±3.3*	4.7±3.3
Cha II	1	0	16.0	0.01	0.07±0.01	14.0±3.8	193.9±34.7	0.9±1.0	1.4±1.0*	12.6±13.8	19.2±13.8*
Lup I	1	0	6.0	1.2	8.05±2.15	417.5±273.2	51.9±31.0	0.9±1.0	1.4±1.0*	0.1±0.1	0.2±0.1*
Lup I	0	0	10.0	0.1	0.71±0.19	77.8±31.0	109.3±32.4	0.9±1.0*	1.4±1.0*	1.3±1.4*	2.0±1.4*
Lup I	0	0	16.0	0.01	0.09±0.02	17.2±5.8	184.1±39.0	0.9±1.0*	1.4±1.0*	9.8±10.7*	14.9±10.7*
Lup III	1	2	8.0	1.2	14.89±2.98	815.8±490.4	54.8±31.1	0.9±1.0	2.8±1.5	0.1±0.1	0.2±1.4
Lup III	0	1	14.0	0.03	0.42±0.08	65.0±20.3	153.1±36.6	0.9±1.0*	1.4±1.0	2.1±2.4*	3.3±2.4
Lup III	1	0	20.0	0.01	0.13±0.03	31.3±8.7	249.0±48.0	0.9±1.0	1.4±1.0*	7.2±8.0	11.1±8.0*
Lup IV	0	0	8.0	0.3	2.26±0.60	139.0±79.8	61.4±31.2	0.9±1.0*	1.4±1.0*	0.4±0.4*	0.6±0.4*
Lup IV	0	0	14.0	0.02	0.17±0.04	26.0±9.2	156.6±36.5	0.9±1.0*	1.4±1.0*	5.5±6.0*	8.4±6.0*
Lup IV	0	0	23.0	0.01	0.09±0.02	24.3±7.8	266.8±46.9	0.9±1.0*	1.4±1.0*	10.0±11.0*	15.3±11.0*
Oph	0	2	10.5	5.6	26.61±10.64	2323.2±1421.2	87.3±40.4	0.9±1.0*	2.8±1.5	0.03±0.04*	0.1±1.4
Oph	1	3	18.0	0.4	1.86±0.75	368.1±170.7	197.4±46.3	0.9±1.0	4.2±2.2	0.5±0.5	2.2±1.7
Oph	5	5	25.5	0.1	0.57±0.23	182.3±80.1	319.6±58.1	4.5±2.5	6.9±3.7	8.0±5.4	12.2±8.2
Oph	9	14	33.0	0.1	0.34±0.14	147.5±63.8	436.7±72.0	8.2±4.5	19.4±10.5	24.2±16.4	57.6±38.6
Oph	10	12	41.0	0.04	0.17±0.07	94.3±40.8	541.8±89.8	9.1±5.0	16.7±9.0	52.2±35.4	95.8±64.2
Per	3	0	6.5	2.7	52.28±20.91	3504.2±2158.9	67.0±31.4	2.7±1.5	1.4±1.0*	0.1±1.7	0.03±0.02*
Per	15	4	11.0	0.8	15.39±6.16	1880.9±910.5	122.2±33.3	13.6±7.5	5.6±3.0	0.9±3.9	0.4±2.0
Per	18	14	15.5	0.2	3.79±1.52	734.4±331.1	193.6±40.3	16.4±9.0	19.4±10.5	4.3±4.2	5.1±3.7
Per	28	11	20.0	0.1	1.49±0.60	388.8±170.4	260.3±46.7	25.5±13.9	15.3±8.2	17.0±11.6	10.2±6.9
Per	8	1	24.5	0.01	0.22±0.09	69.8±30.2	316.9±52.8	7.3±4.0	1.4±1.0	33.0±22.4	6.3±4.5
Per	0	0	30.0	0.001	0.02±0.01	7.2±3.2	403.0±81.0	0.9±1.0*	1.4±1.0*	50.9±56.0*	77.8±56.0*
Ser	2	1	10.2	0.6	13.34±1.03	1588.5±479.4	119.1±34.7	1.8±1.0	1.4±1.0	0.1±1.4	0.1±0.1
Ser	2	2	14.5	0.1	2.54±0.20	456.7±104.0	179.9±38.5	1.8±1.0	2.8±1.5	0.7±1.4	1.1±1.4
Ser	7	5	18.8	0.04	0.91±0.07	221.5±44.3	243.2±44.9	6.4±3.5	6.9±3.7	7.0±3.9	7.6±4.1
Ser	20	9	23.0	0.01	0.23±0.02	70.1±13.3	306.6±53.3	18.2±9.9	12.5±6.7	79.6±44.0	54.7±29.8
Aur	19	6	8.8	1.8	48.05±9.61	4293.9±1001.2	89.4±10.7	17.3±9.4	8.3±4.5	0.4±4.4	0.2±2.4
Aur	20	15	15.5	0.1	1.77±0.35	274.0±60.1	154.9±13.9	18.2±9.9	20.8±11.2	10.3±6.0	11.8±6.8

Table 2.3 (cont'd)

Cloud	$N_{\text{YSOs,I}}$	$N_{\text{YSOs,F}}$	Contour levels ^I (mag)	Ω (deg ²)	A_{con} (pc ²)	M_{con} (M_{\odot})	$\Sigma_{\text{gas,con}}$ (M_{\odot} pc ⁻²)	SFR, I (M_{\odot} Myr ⁻¹)	SFR, F (M_{\odot} Myr ⁻¹)	$\Sigma_{\text{SFR,I}}$ (M_{\odot} yr ⁻¹ kpc ⁻²)	$\Sigma_{\text{SFR,F}}$ (M_{\odot} yr ⁻¹ kpc ⁻²)
(1)	(2)	(3)	(4)	(5)	(6)	(7)	(8)	(9)	(10)	(11)	(12)
Aur	2	1	22.2	0.01	0.18±0.04	49.7±11.8	282.8±35.8	1.8±1.0	1.4±1.0	10.4±6.0	7.9±5.7
AurN	0	0	5.2	0.01	0.46±0.09	30.9±7.8	67.4±10.4	0.9±1.0*	1.4±1.0*	2.0±2.2*	3.0±2.2*
AurN	1	0	8.3	0.1	1.95±0.39	193.0±44.2	98.8±11.0	0.9±1.0	1.4±1.0*	0.5±0.5	0.7±0.5*
Cep	13	3	7.5	1.3	35.77±35.77	2327.7±597.5	331.9±52.1	11.8±7.5	4.2±3.0	0.3±0.2	0.1±0.1
Cep	13	3	13.0	0.1	2.21±2.21	282.6±63.3	507.2±51.3	11.8±7.0	4.2±3.0	5.4±3.3	1.9±1.4
Cha I	3	6	8.0	0.6	7.44±1.49	544.1±136.0	73.1±11.0	2.7±1.5	8.3±4.5	0.4±1.7	1.1±2.4
Cha I	7	5	14.0	0.1	1.75±0.35	256.0±57.5	146.6±15.0	6.4±3.5	6.9±3.7	3.6±2.6	4.0±2.3
Cha I	0	1	21.0	0.02	0.22±0.04	56.0±13.1	253.6±30.9	0.9±1.0*	1.4±1.0	4.1±4.5*	6.3±4.5
Cha III	1	0	5.0	2.2	26.85±5.37	1228.5±364.1	45.8±10.0	0.9±1.0	1.4±1.0*	0.03±0.04	0.05±0.04*
Cha III	0	0	8.0	0.1	1.14±0.23	97.5±23.0	85.2±10.6	0.9±1.0*	1.4±1.0*	0.8±0.9*	1.2±0.9*
CrA	2	1	9.3	0.5	2.45±0.94	162.8±68.1	66.5±11.0	1.8±1.0	1.4±1.0	0.7±1.4	0.6±0.4
CrA	1	2	16.7	0.09	0.47±0.18	87.2±34.7	183.5±18.2	0.9±1.0	2.8±1.5	1.9±2.1	5.8±3.9
CrA	4	0	24.0	0.02	0.10±0.04	29.1±11.6	289.8±28.4	3.6±2.0	1.4±1.0*	36.2±24.2	13.8±9.9*
IC5146E	0	0	4.7	0.2	50.60±8.52	2424.3±673.2	47.9±10.6	0.9±1.0*	1.4±1.0*	0.02±0.02*	0.03±0.02*
IC5146E	11	6	7.4	0.04	10.82±1.82	940.8±204.1	86.9±11.9	10.0±5.5	8.3±4.5	0.9±3.3	0.8±2.4
IC5146NW	7	0	5.5	0.3	73.75±12.42	3831.8±989.0	52.0±10.2	6.4±3.5	1.4±1.0*	0.1±2.6	0.02±0.01*
IC5146NW	8	3	9.0	0.05	13.83±2.33	1346.3±275.4	97.3±11.3	7.3±4.0	4.2±2.2	0.5±2.8	0.3±1.7
Lup V	0	0	4.5	1.3	9.08±2.42	514.5±166.2	56.7±10.3	0.9±1.0*	1.4±1.0*	0.1±0.1*	0.2±0.1*
Lup V	0	0	7.0	0.4	2.57±0.69	190.0±57.5	73.9±10.6	0.9±1.0*	1.4±1.0*	0.4±0.4*	0.5±0.4*
Lup VI	0	0	4.5	0.6	3.83±1.02	237.4±75.4	62.0±10.7	0.9±1.0*	1.4±1.0*	0.2±0.3*	0.4±0.3*
Lup VI	0	0	9.0	0.4	2.90±0.77	216.4±65.8	74.6±10.9	0.9±1.0*	1.4±1.0*	0.3±0.3*	0.5±0.3*
Mus	1	0	4.5	0.8	5.86±1.47	259.2±88.0	44.2±10.2	0.9±1.0	1.4±1.0*	0.2±0.2	0.2±0.2*
Mus	0	0	7.0	0.1	0.95±0.24	75.4±21.4	79.1±10.7	0.9±1.0*	1.4±1.0*	1.0±1.0*	1.5±1.0*
Sco	1	1	7.5	1.2	6.35±6.35	484.7±130.6	456.4±63.9	0.9±1.0	1.4±1.0	0.1±0.2	0.2±0.2
Sco	1	0	17.0	0.2	0.94±0.94	135.8±34.3	567.1±57.6	0.9±1.0	1.4±1.0*	1.0±1.1	1.5±1.1*
Ser-Aqu	0	0	7.0	3.0	61.01±4.69	5509.9±782.3	90.3±10.8	0.9±1.0*	1.4±1.0*	0.02±0.02*	0.02±0.02*
Ser-Aqu	9	4	12.0	4.6	95.23±7.33	12818.2±1540.2	134.6±12.4	8.2±4.5	5.6±3.0	0.1±3.0	0.1±2.0
Ser-Aqu	16	12	17.0	0.6	12.57±0.97	2658.5±298.5	211.4±17.3	14.5±8.0	16.7±9.0	1.2±4.0	1.3±3.5
Ser-Aqu	31	20	22.0	0.3	6.66±0.51	1929.6±219.8	289.6±24.3	28.2±15.4	27.8±15.0	4.2±5.6	4.2±4.5
Ser-Aqu	31	25	27.0	0.1	2.88±0.22	1036.8±125.3	359.6±33.5	28.2±15.4	34.7±18.7	9.8±5.6	12.0±6.6

Table 2.3 (cont'd)

Cloud	$N_{\text{YSOs,I}}$	$N_{\text{YSOs,F}}$	Contour levels ^I (mag)	Ω (deg ²)	A_{con} (pc ²)	M_{con} (M_{\odot})	$\Sigma_{\text{gas,con}}$ (M_{\odot} pc ⁻²)	SFR, I (M_{\odot} Myr ⁻¹)	SFR, F (M_{\odot} Myr ⁻¹)	$\Sigma_{\text{SFR,I}}$ (M_{\odot} yr ⁻¹ kpc ⁻²)	$\Sigma_{\text{SFR,F}}$ (M_{\odot} yr ⁻¹ kpc ⁻²)
(1)	(2)	(3)	(4)	(5)	(6)	(7)	(8)	(9)	(10)	(11)	(12)
Ser-Aqu	50	24	33.0	0.1	1.10±0.08	488.4±65.1	442.5±48.2	45.5±24.9	33.3±18.0	41.2±22.8	30.2±16.4
Contour Averages	6.6±1.2	4.1±0.7	-999.0±-999.0	0.6±0.1	10.6±2.5	972.1±248.0	188.1±17.7	6.0±1.1	5.7±1.0	7.7±2.0	8.6±2.3

Note. — Columns are : (1) Cloud name.; (2) Number of Class I YSOs in contour level.; (3) Number of Flat SED YSOs in contour level.; (4) A_V contour level in mag at which mass measurement was made. The contour levels start at $A_V=2$ or the cloud completeness limit and increase in even intervals to the listed contour level.; (5) Solid angle.; (6) Area in contour level (pc⁻²).; (7) Mass in contour level (M_{\odot}).; (8) Surface gas density in contour level (M_{\odot} pc⁻²).; (9) Star formation rate in contour level (M_{\odot} Myr⁻¹) for Class I YSOs. Asterisks denote that measurement is an upper limit.; (10) Star formation rate in contour level (M_{\odot} Myr⁻¹) for Flat SED YSOs. Asterisks denote that measurement is an upper limit.; (11) Star formation rate density in contour level (M_{\odot} yr⁻¹ kpc⁻²) for Class I YSOs. Asterisks denote that measurement is an upper limit.; (12) Star formation rate density in contour level (M_{\odot} (yr⁻¹ kpc⁻²) for Flat SED YSOs. Asterisks denote that measurement is an upper limit.; (I) Contour levels start at $A_V = 2$ for all clouds except for Serpens and Ophiuchus which are covered by the c2d survey completely down to $A_V = 6$ and 3 as discussed in §Section 2.2.1.

We compare our YSO contour results to extragalactic relations and find that most points lie well above the extragalactic relations. Excluding upper limits, the mean values of Σ_{SFR} and $\Sigma_{\text{gas,con}}$ are of $9.7 M_{\odot} \text{ kpc}^{-2} \text{ yr}^{-1}$ and $225 M_{\odot} \text{ pc}^{-2}$, respectively. Evaluated at this mean gas surface density, the extragalactic relations under-predict Σ_{SFR} by factors of ~ 21 – 54 . The mean YSO contour lies above the Krumholz et al. (2009) extragalactic SFR–gas relation prediction by ~ 2 orders of magnitude. We explore the differences between the Galactic and extragalactic SFR–gas relations in §Section 2.3.

2.3 Why are Galactic SFR–gas Relations different from Extragalactic Relations?

The differences between our findings on Galactic scales and the extragalactic relations, both on global or disk-averaged scales (Kennicutt 1998b) and scales of hundreds of pc (Kennicutt et al. 2007; Thilker et al. 2007; Bigiel et al. 2008; Blanc et al. 2009; Braun et al. 2009; Verley et al. 2010), might be explained in the following ways. Firstly, using ^{12}CO to measure the H_2 in galaxies might give systematically different Σ_{gas} than do A_V measurements (§Section 2.3.1). Secondly, the local c2d and GB clouds are forming low-mass stars; since extragalactic SFR tracers respond only to massive stars, the two star forming regimes might behave differently. In §Section 2.3.2, we will investigate whether massive star forming regions agree with the extragalactic SFR–gas relations and if they vary from low-mass star forming regions. Finally, averaging over whole galaxies on scales of hundreds of pc includes both

gas contained in the parts of molecular clouds that are forming stars and diffuse molecular gas that is not forming stars (§Section 2.3.3). A local example of this is a study of the Taurus molecular cloud; Goldsmith et al. (2008), found a large amount of diffuse ^{12}CO at lower gas densities where no young stars are forming. Extragalactic studies averaging over hundreds of pc scales would include this gas, causing an increase in the amount of CO flux that is being counted as star forming gas.

2.3.1 The use of CO versus A_V to determine Σ_{gas}

Since extinction maps are direct probes of Σ_{gas} , they provide the best measure of the total gas and are optimal for use in determining the Σ_{gas} of molecular clouds. However, A_V maps are not easily obtainable in extragalactic studies, which instead employ CO maps, particularly $^{12}\text{CO } J=1-0$, to determine Σ_{gas} of molecular hydrogen. Since the molecular hydrogen (H_2) rotational transitions require high temperatures not found in the bulk of molecular clouds, other tracers of dense gas are used to estimate the amount of H_2 . The next most abundant molecule with easily observable excitation properties in a molecular cloud is $^{12}\text{CO } J=1-0$. In this study, we want to explore how well CO traces A_V as a function of M_{gas} or Σ_{gas} . We can directly test this in two galactic clouds, Perseus and Ophiuchus, which both have $^{12}\text{CO } J=1-0$ and $^{13}\text{CO } J=1-0$ maps from the Five College Radio Astronomy Observatory (FCRAO) COordinated Molecular Probe Line Extinction Thermal Emission (COMPLETE) Survey of Star Forming Regions (Ridge et al. 2006).

In order to directly compare the CO maps from the COMPLETE survey to the A_V maps in this study, we interpolate the CO data onto the A_V map grid with a pixel size of $45''$. We integrate the publicly available CO data cubes over the velocity range from $0\text{--}15\text{ km s}^{-1}$ to create moment zero maps of integrated intensity defined as: $I_{\text{CO}}(x, y) \equiv \int T_{\text{mb}}(x, y, z) dV\text{ K km s}^{-1}$, where $T_{\text{mb}} \equiv T_{\text{A}}^*/\eta_{\text{mb}}$ is the main beam brightness temperature defined as the antenna temperature (T_{A}^*) divided by the main beam efficiency (η_{mb}) of 0.45 and 0.49 for $^{12}\text{CO } J=1\text{--}0$ and $^{13}\text{CO } J=1\text{--}0$, respectively, from Pineda et al. (2008). Corresponding rms noise maps ($\sigma_{\text{T}(x,y)}$) were constructed by calculating the standard deviation of intensity values within each spectroscopic channel where no signal is detected. In order to determine the gas surface density of H_2 (Σ_{H_2}), we must first compute the column density of H_2 . The column density of H_2 is estimated from the ^{12}CO map by using a CO-to- H_2 conversion factor (X_{CO}), which is defined as the ratio of H_2 column density to the integrated intensity ($X_{\text{CO}} \equiv N_{\text{H}_2}/I_{\text{CO}}$). Similarly for the ^{13}CO map, the column density is derived from the ^{12}CO and ^{13}CO maps, assuming LTE and an abundance ratio of H_2 -to- ^{13}CO . To compare Σ_{H_2} from ^{12}CO and ^{13}CO to the Σ_{gas} from A_V , we use only regions in the CO maps that have emission lines with positive integrated intensities and line peaks that are greater than 5 times the rms noise. Our masses from extinction measurements used for this comparison are therefore slightly lower than those in Tables 3.1 and 2.3 by $\sim 5\%$ (See Tables 2.4 and 2.5).

The X_{CO} factor for ^{12}CO has been derived using a variety of methods such as gamma ray emission caused by the collision of cosmic rays with hydro-

Table 2.4. A_V , ^{12}CO , and ^{13}CO Masses and Σ_{gas} for Per and Oph Clouds

Cloud	$M_{\text{cloud,gas}}$ (M_{\odot})	$M_{\text{cloud},^{12}\text{CO}}$ (M_{\odot})	$M_{\text{cloud},^{13}\text{CO}}$ (M_{\odot})	$\Sigma_{\text{cloud,gas}}$ ($M_{\odot} \text{ pc}^{-2}$)	$\Sigma_{\text{cloud},^{12}\text{CO}}$ ($M_{\odot} \text{ pc}^{-2}$)	$\Sigma_{\text{cloud},^{13}\text{CO}}$ ($M_{\odot} \text{ pc}^{-2}$)
(1)	(2)	(3)	(4)	(5)	(6)	(7)
Per	5997±3387	9657±2416	1073±110	82±33	132±33	15±2
Oph	2270±1533	2596±659	348±39	77±42	88±22	12±1
Data from Literature:						
Taurus ^I	27207	16052		108	64	

Note. — (1) Cloud name.; (2) Mass from A_V map (M_{\odot}) where there is positive ^{12}CO and ^{13}CO emission.; (3) ^{12}CO Mass (M_{\odot}); (4) ^{13}CO Mass (M_{\odot}); (5) Surface gas density from A_V map ($M_{\odot} \text{ pc}^{-2}$); (6) ^{12}CO Surface gas density ($M_{\odot} \text{ pc}^{-2}$); (7) ^{13}CO Surface gas density ($M_{\odot} \text{ pc}^{-2}$); (I) Combined ^{12}CO and ^{13}CO mass from Goldsmith et al. (2008) and A_V mass from (Pineda et al. 2010).

gen (Bloemen et al. 1986), virial mass methods (Solomon et al. 1987; Blitz et al. 2007), maps of dust emission from *IRAS* and assuming a constant dust-to-gas ratio (Frerking et al. 1982), extinction maps from optical star counts (Duvert et al. 1986; Bachiller & Cernicharo 1986; Langer et al. 1989) and 2MASS data (Lombardi et al. 2006; Pineda et al. 2008), and theoretically by the assumption that giant molecular clouds are in gravitational equilibrium (Dickman et al. 1986; Heyer et al. 2001). All these studies find a range of X_{CO} of $0.9\text{--}4.8 \times 10^{20} \text{ cm}^{-2} \text{ K}^{-1} \text{ km}^{-1} \text{ s}$, but they were almost all restricted to regions with $A_V < 6$ mag. Studies of extragalactic SFR-gas relations chose values close to the average galactic X_{CO} measurements in the literature: $2.0 \times 10^{20} \text{ cm}^{-2} \text{ K}^{-1} \text{ km}^{-1}$ (Bigiel et al. 2008)) or $2.8 \times 10^{20} \text{ cm}^{-2} \text{ K}^{-1} \text{ km}^{-1} \text{ s}$ from Bloemen et al. (1986) (Kennicutt 1998b; Kennicutt et al. 2007; Blanc et al. 2009). Since the goal of this study is to compare to extragalactic measurements, we choose a X_{CO} of

$2.8 \pm 0.7 \times 10^{20} \text{ cm}^{-2} \text{ K}^{-1} \text{ km}^{-1} \text{ s}$ from Bloemen et al. (1986) to be consistent with the study of Kennicutt (1998b).

We compute the column density of H_2 from ^{12}CO measurements using the equation:

$$N_{\text{H}_2(^{12}\text{CO})} = X_{^{12}\text{CO}} \times I_{^{12}\text{CO}} \text{ (cm}^{-2}\text{)}. \quad (2.10)$$

This can be rewritten in terms of gas surface density:

$$\begin{aligned} \Sigma_{\text{H}_2(^{12}\text{CO})} &= (2m_{\text{H}} \times N_{\text{H}_2(^{12}\text{CO})} \times A_{\text{pixel}}) / A_{\text{cloud}} \\ &\approx 10^{-33} \times m_{\text{H}} \times \left(\frac{N_{\text{H}_2(^{12}\text{CO})}}{\text{cm}^{-2}} \right) \times \left(\frac{A_{\text{pixel}}}{\text{cm}^2} \right) \times \\ &\quad \left(\frac{A_{\text{cloud}}}{\text{pc}^2} \right)^{-1} (M_{\odot} \text{ pc}^{-2}), \end{aligned}$$

where we take the total number of hydrogen atoms is $N(\text{H}) \equiv 2N(\text{H}_2)$. We use this factor of two instead of the mean molecular weight of H_2 ($\mu_{\text{H}_2} = 2.8$, derived from cosmic abundances of 71% hydrogen, 27% helium, and 2% metals, e.g., Kauffmann et al. (2008)) to be consistent with the extragalactic studies of Kennicutt (1998b) and Bigiel et al. (2008). This factor of 2 does not account for helium, which is an additional factor of ~ 1.36 (Hildebrand 1983). The errors in our gas surface density measurements include both the error from the rms intensity maps and the error in the CO-to- H_2 conversion factor from Bloemen et al. (1986).

Table 2.5. A_V , ^{12}CO , and ^{13}CO Masses and Σ_{gas} for Per and Oph Clouds in A_V Contours

Cloud	Contour levels (mag)	$M_{\text{con,gas}}$ (M_{\odot})	$M_{\text{con},^{12}\text{CO}}$ (M_{\odot})	$M_{\text{con},^{13}\text{CO}}$ (M_{\odot})	$\Sigma_{\text{con,gas}}$ (M_{\odot} pc^{-2})	$\Sigma_{\text{con},^{12}\text{CO}}$ (M_{\odot} pc^{-2})	$\Sigma_{\text{con},^{13}\text{CO}}$ (M_{\odot} pc^{-2})
(1)	(2)	(3)	(4)	(5)	(6)	(7)	(8)
Per	6.5	3144.7±2068.5	6050.8±1514.5	518.0±54.0	60.2±31	115.7±28	9.9±1
	11.0	1774.0±875.5	2555.9±639.3	349.1±35.3	115.3±33	166.1±41	22.7±2
	15.5	652.9±302.6	654.0±163.6	120.3±12.1	172.1±40	172.4±43	31.7±3
	20.0	369.7±163.5	343.7±86.0	76.2±7.6	247.6±46	230.2±57	51.0±5
	24.5	49.5±23.0	49.4±12.4	8.9±0.9	224.9±52	224.5±56	40.5±4
	30.0	6.1±2.8	3.3±0.8	0.7±0.1	339.3±80	187.7±46	37.6±3
Oph	10.5	1577.2±1246.7	1982.0±505	183.3±23	76.8±40	74.5±19	6.9±0
	18.0	349.4±164.3	328.4±82	71.1±7	187.4±46	176.1±44	38.1±3
	25.5	161.3±72.5	135.9±34	42.6±4	282.8±58	238.3±59	74.7±7
	33.0	111.5±50.8	97.1±24	32.2±3	330.3±72	287.5±71	95.3±9
	41.0	70.6±32.3	52.9±13	18.6±1	405.9±89	304.0±76	106.6±10

Note. — (1) Cloud name.; (2) A_V contour level in mag at which mass measurement was made. The contour levels start at $A_V=2$ or the cloud completeness limit and increase in even intervals to the listed contour level.; (3) A_V Mass (M_{\odot}) where there is positive ^{12}CO and ^{13}CO emission.; (4) ^{12}CO Mass (M_{\odot}).; (5) ^{13}CO Mass (M_{\odot}).; (6) A_V Surface gas density ($M_{\odot} \text{ pc}^{-2}$).; (7) ^{12}CO Surface gas density ($M_{\odot} \text{ pc}^{-2}$).; (8) ^{13}CO Surface gas density ($M_{\odot} \text{ pc}^{-2}$).

The top two panels of Figure 2.4 show the ^{12}CO integrated intensity versus the visual extinction derived from the 2MASS and *Spitzer* data for both Per (left) and Oph (right). We over-plot the conversion factor derived from the gamma ray study of Bloemen et al. (1986) (dashed line). ^{12}CO is seen to correlate with A_V out to $A_V \sim 7\text{--}10$, where ^{12}CO starts to saturate and the distribution flattens out to higher A_V . A large difference in the amount of ^{12}CO integrated intensity produced relative to that predicted by $X_{^{12}\text{CO}}$ between the Per and Oph molecular clouds is seen. This may be due to higher opacity at higher A_V in Oph relative to Per. Extinction values around 10–20 mag are found to be essentially invisible to ^{12}CO . This figure demonstrates the non-linear, non-monotonic behavior of CO emission with A_V .

^{12}CO , however, is not the most reliable tracer of star forming gas because of high opacity and varying ^{12}CO -to- H_2 abundance due to photodissociation or depletion on to dust grains. Studies of molecular clouds (Carpenter et al. 1995; Heyer et al. 1996; Goldsmith et al. 2008) show that ^{12}CO contains a significant diffuse component in the low column density regime $A_V < 4$. ^{13}CO emission is a more reliable tracer of dense gas ranging from $1000\text{--}7000\text{ cm}^{-3}$ than ^{12}CO because it is optically thin for most conditions within a cloud and ^{13}CO abundance variations are small for densities $< 5000\text{ cm}^{-3}$ and temperatures of $> 15\text{ K}$ (Bachiller & Cernicharo 1986; Duvert et al. 1986; Heyer & Ladd 1995; Caselli et al. 1999).

To estimate the column densities from the $^{13}\text{CO } J=1\text{--}0$ integrated intensity maps we assume local thermodynamic equilibrium (LTE), optically

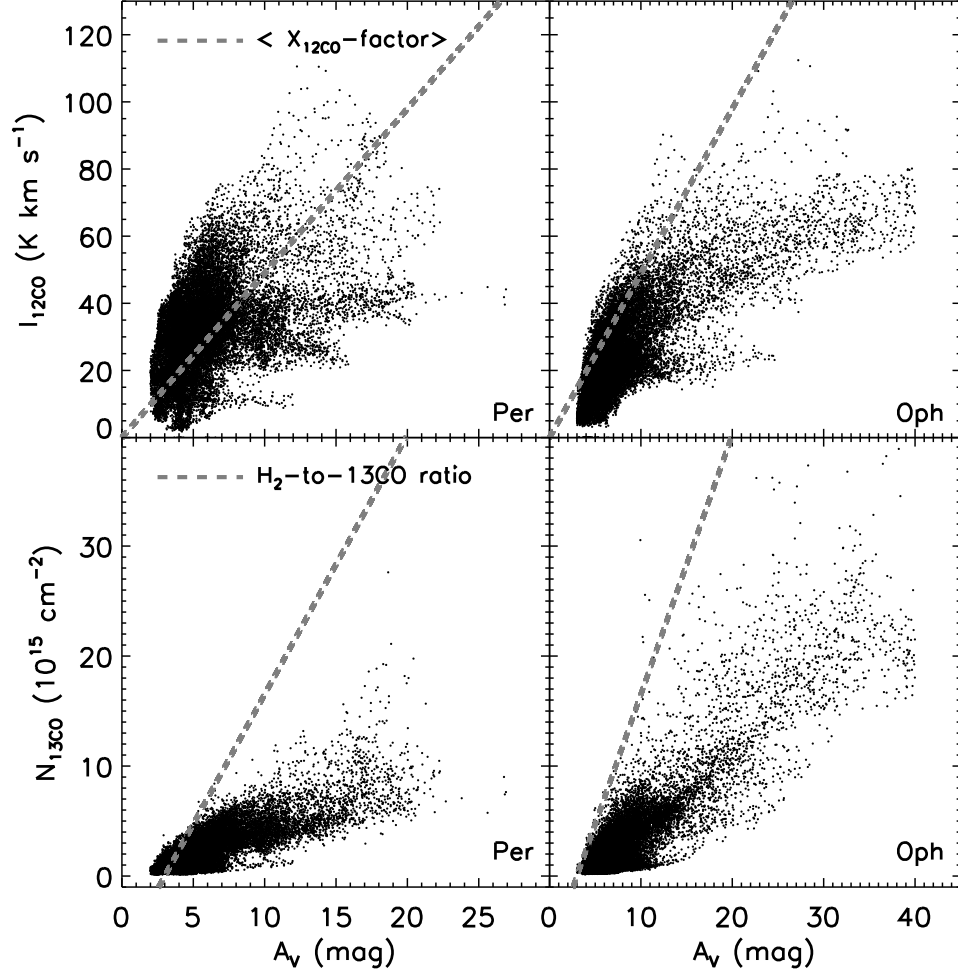


Figure 2.4 **top panels:** ^{12}CO integrated intensity versus visual extinction (A_V) for Per (left) and Oph (right). The standard X_{CO} -factor fit from Bloemen et al. (1986) is shown by the dashed grey lines (§Section 2.3.1). **bottom panels:** ^{13}CO column densities versus visual extinction (A_V) for Per (left) and Oph (right). The average H_2 -to- ^{13}CO abundance ratio from the literature is shown by the grey dashed lines (§Section 2.3.1).

thin $^{13}\text{CO } J=1-0$, and that $^{12}\text{CO } J=1-0$ and $^{13}\text{CO } J=1-0$ have equivalent excitation temperatures. In order to derive column densities, we also determine an optical depth ($\tau_{^{13}\text{CO}}$) and excitation temperature (T_{ex}) from comparison to the $^{12}\text{CO } J=1-0$ line. We can derive this by assuming the $^{12}\text{CO } J=1-0$ is optically thick; as $\tau \rightarrow \infty$,

$$T_{\text{ex}} = \frac{5.5}{\ln \left(1 + \frac{5.5}{T_{\text{peak},^{12}\text{CO}} + 0.82} \right)} \text{ (K)}, \quad (2.11)$$

where $T_{\text{peak},^{12}\text{CO}}$ is the $^{12}\text{CO } J=1-0$ peak main beam brightness temperature which we measure on a pixel-by-pixel basis.

The $^{13}\text{CO } J=1-0$ optical depth is then

$$\tau_{^{13}\text{CO}} = -\ln \left(1 - \frac{T_{\text{peak},^{13}\text{CO}}}{5.3} \left[\frac{1}{\exp(5.3/T_{\text{ex}}) - 1} - 0.16 \right]^{-1} \right), \quad (2.12)$$

where $T_{\text{peak},^{13}\text{CO}}$ is the $^{13}\text{CO } J=1-0$ peak main beam brightness temperature measured in each pixel. We can then use the definition of ^{13}CO optical depth and column density from Rohlfs & Wilson (1996) to estimate the column density of ^{13}CO :

$$N_{^{13}\text{CO}} = 2.6 \times 10^{14} \left(\frac{\tau_{^{13}\text{CO}}}{1 - \exp^{-\tau_{^{13}\text{CO}}}} \right) \times \left(\frac{I_{^{13}\text{CO}}}{1 - \exp(-5.3/T_{\text{ex}})} \right) \text{ (cm}^{-2}\text{)}. \quad (2.13)$$

Certain regions near A_V peaks in the clouds are optically thick and are affected by ^{12}CO self absorption. In these regions, we cannot accurately determine T_{ex} and therefore $\tau_{^{13}\text{CO}}$. This problem affects $\sim 10\%$ of the pixels in Oph ($A_V > 30$ mag) and $\sim 5\%$ of the pixels in Per ($A_V > 20$ mag). Since most of the mass lies at low A_V , we mask out the pixels that have ^{13}CO self absorption and do not include them in determining the ^{13}CO column density and mass estimate discussed below.

For comparison with extragalactic work, where clouds are not resolved, we derive ^{13}CO column densities by using average spectra to determine T_{ex} and $\tau_{^{13}\text{CO}}$ using a $T_{\text{peak},^{12}\text{CO}}$ of 3 and 5.3 K and a $T_{\text{peak},^{13}\text{CO}}$ of 0.7 and 1.5 K for Per and Oph, respectively. Comparing the two methods, we find that using peak temperatures from average spectra or a constant T_{ex} and $\tau_{^{13}\text{CO}}$ will result in higher $N_{^{13}\text{CO}}$ by a factor of ~ 2 at $A_V < 10$ over the pixel-by-pixel measurements.

In order to convert the $N_{^{13}\text{CO}}$ column density into H_2 column density, we use a H_2 -to- ^{13}CO abundance ratio. The $\text{H}_2/^{13}\text{CO}$ abundance ratio for the Per cloud was determined by Pineda et al. (2008), who found a value of $3.98 \pm 0.07 \times 10^5$ for $A_V < 5$ mag. Dividing the cloud into separate regions, they found an average abundance ratio of 3.8×10^5 . Other values found in the literature range from 3.5 – 6.7×10^5 , with an average value of $\sim 4 \times 10^5$ using both extinction maps (Pineda et al. 2008) and star counts (Bachiller & Cernicharo 1986; Duvert et al. 1986; Langer et al. 1989). We adopt the average $\text{H}_2/^{13}\text{CO}$ ratio from the literature of $(4 \pm 0.4) \times 10^5$ to convert ^{13}CO to H_2 .

column densities using the relation:

$$N_{\text{H}_2(^{13}\text{CO})} = (4 \pm 0.4) \times 10^5 N_{^{13}\text{CO}} \text{ (cm}^{-2}\text{)} \quad (2.14)$$

or in terms of surface densities:

$$\begin{aligned} \Sigma_{\text{H}_2(^{13}\text{CO})} &= (2m_{\text{H}} \times N_{\text{H}_2(^{13}\text{CO})} \times A_{\text{pixel}}) / A_{\text{cloud}} \\ &\approx 10^{-33} \times m_{\text{H}} \times \left(\frac{N_{\text{H}_2(^{13}\text{CO})}}{\text{cm}^{-2}} \right) \times \left(\frac{A_{\text{pixel}}}{\text{cm}^2} \right) \times \\ &\quad \left(\frac{A_{\text{cloud}}}{\text{pc}^2} \right)^{-1} (\text{M}_{\odot} \text{ pc}^{-2}), \end{aligned}$$

where we choose a factor of two instead of the mean molecular weight in order to consistently compare to ^{12}CO . We show the ^{13}CO integrated intensity versus the visual extinction derived from the 2MASS and *Spitzer* data for both Per (left) and Oph (right) in the bottom two panels of Figure 2.4. The average $\text{H}_2/^{13}\text{CO}$ ratio is shown by the dashed line. A turnover in ^{13}CO is seen at $A_V \sim 7$ (Per) and ~ 10 (Oph) that is likely due to an increase in optical depth. The amount of ^{13}CO in Per follows the average abundance ratio out to $A_V \sim 5$, but in Oph, the ^{13}CO integrated intensity is underproduced.

To test how well CO traces A_V as a function of M_{gas} or Σ_{gas} , we measure Σ_{gas} densities in our A_V maps and Σ_{H_2} in the CO maps in the overlapping area where there is a positive CO integrated intensity over 5 times the rms noise. In Figure 2.5, we plot the ratio of Σ_{H_2} and Σ_{gas} from A_V , which are effectively mass ratios, since the area measured is the same. The cyan squares and circles

are points for the c2d and GB clouds ($\Sigma_{\text{H}_2(^{12}\text{CO,cloud})}, \Sigma_{\text{H}_2(^{13}\text{CO,cloud})}$) and the filled green and yellow squares and circles are measurements in contours of A_V using the same method as in §Section 2.2.3 ($\Sigma_{\text{H}_2(^{12}\text{CO,con})}, \Sigma_{\text{H}_2(^{13}\text{CO,con})}$) for Oph and Per, respectively (Tables 2.4 and 2.5). A measurement for the Taurus cloud using both ^{12}CO and ^{13}CO above $A_V = 2$ from (Goldsmith et al. 2008) is also shown (cyan triangle). If CO traces the mass we find using extinction maps, we would expect the ratio of CO/ A_V mass to be of order unity as shown by the solid black line in Figure 2.5. For ^{12}CO , we find the total cloud measurement for Per to have Σ_{H_2} of $\sim 1.6\Sigma_{\text{gas}}$ at $\Sigma_{\text{gas}} \lesssim 100 M_\odot \text{ pc}^{-2}$, but the ratio is close to unity within the errors. We find that ^{12}CO traces A_V relatively well in the Oph cloud out to $\sim 200 M_\odot \text{ pc}^{-2}$. At $\Sigma_{\text{gas}} \gtrsim 200 M_\odot \text{ pc}^{-2}$, ^{12}CO underestimates the A_V mass in both Per and Oph by $\sim 30\%$, on average.

Since ^{13}CO should trace denser gas (Duvert et al. 1986; Bachiller & Cernicharo 1986), we also explore how it traces A_V as a function of Σ_{gas} . We plot this on Figure 2.5 for the total clouds (cyan points) and contour measurements (green points). We find a constant value of ^{13}CO versus the surface density of extinction, but find that it underestimates Σ_{gas} by a factor of $\sim 4\text{--}5$ and lies below measurements of ^{12}CO by a factor of ~ 5 , on average. The difference we find between ^{13}CO and H_2 measured by A_V , could be due to the LTE method we used to compute ^{13}CO masses or the assumption that there is a constant abundance of CO relative to H_2 . Heyer et al. (2009) explored the properties of galactic molecular clouds using ^{13}CO emission and found that the assumption of equivalent excitation temperatures for both ^{12}CO and

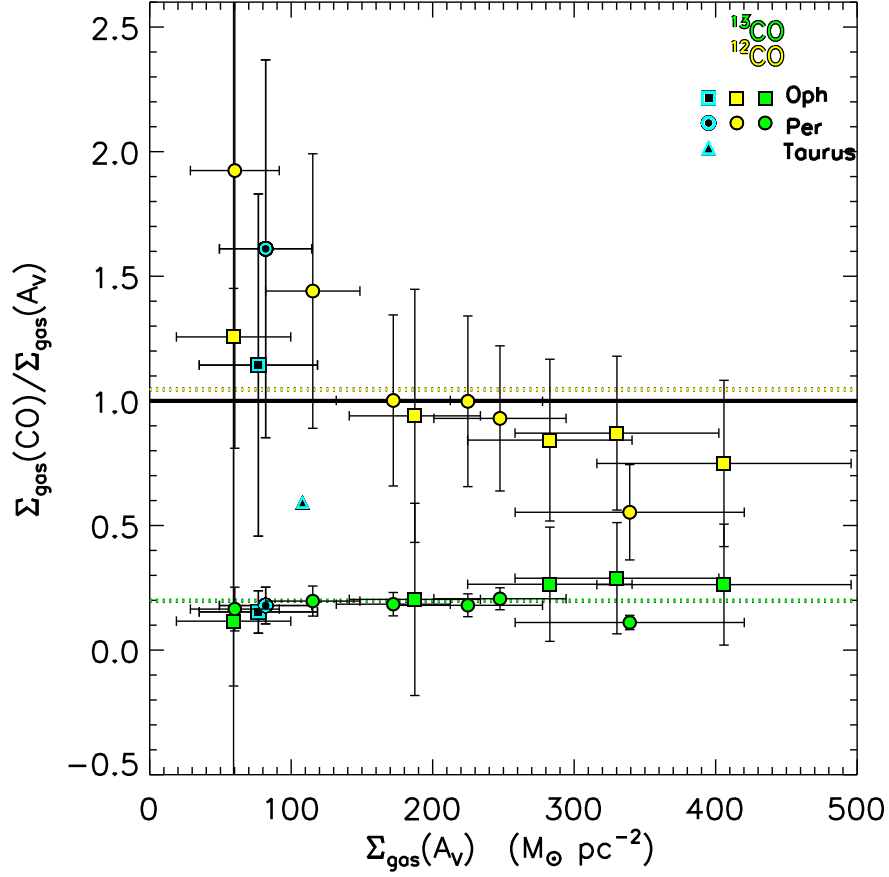


Figure 2.5 The ratio of H_2 gas surface densities from CO compare to that estimated from A_V maps (Σ_{gas}). The cyan squares and circles are points for the Oph and Per clouds, respectively. The filled green (^{13}CO) and yellow (^{12}CO) squares (Oph) and circles (Per) are measurements in evenly spaced contour intervals of A_V . The dashed horizontal green and yellow lines are the average of ^{13}CO and ^{12}CO contour points. If CO traces the mass we find using extinction maps, we would expect the ratio of CO/ A_V to be of order unity as shown by the solid black line.

^{13}CO in the LTE method may underestimate the true column density of ^{13}CO in subthermally excited regions. As the ^{13}CO density increases, the $J=1-0$ transition becomes thermalized, and the column density estimates are more accurate. Also, both Heyer et al. (2009) and Goldsmith et al. (2008) found that if ^{13}CO -to- H_2 abundance variations in LTE-derived cloud masses are not considered, they would underestimate the true column densities by factors of 2–3. Since we only include ^{13}CO emission greater than 5 times the rms noise, we are likely measuring gas that is thermalized with little abundance variation. Assuming a constant abundance ratio will therefore not account for the difference between A_V and ^{13}CO masses. ^{13}CO , might therefore be a more consistent tracer of Σ_{gas} , but it may underestimate the mass by factors of ~ 4 –5, which can be corrected for.

Variations in the CO-to- H_2 conversion factor may impact the slope of the SFR–gas relations as measured by extragalactic studies. Since we are resolving molecular clouds, we cannot place constraints on gas densities lower than $\sim 50 M_{\odot} \text{ pc}^{-2}$, typical of spiral galaxies (Bigiel et al. 2008). However if we consider the effects of using CO as a tracer of the total gas density, it underestimates the mass measured from A_V by $\gtrsim 30\%$ for $\Sigma_{\text{gas}} \gtrsim 200 M_{\odot} \text{ pc}^{-2}$. This would effectively shift the extragalactic observed points to the right above $200 M_{\odot} \text{ pc}^{-2}$. This shift would flatten the slope slightly in the fitted Kennicutt (1998b) relation. These small factors, however do not explain the large discrepancy between the extragalactic relations and the much higher SFR in the local clouds, seen both in the whole molecular clouds and looking at the

youngest YSOs as a function of Σ_{gas} .

2.3.2 Do High-mass and Low-mass Star Forming Regions Behave Differently?

By studying nearby molecular clouds, we can obtain the most accurate measurement of Σ_{gas} and Σ_{SFR} , but it is regions of *massive* star formation that form the basis for extragalactic studies. Massive star forming regions are the only readily visible regions forming stars at large distances and thus are the only probes of star formation in distant regions in the Milky Way and external galaxies. We can measure Σ_{SFR} and Σ_{gas} in individual massive star forming regions to see if there is better agreement with extragalactic SFR–gas relations.

To investigate where individual regions of massive star formation fall on the SFR–gas relation, we use data from the molecular line survey of dense gas tracers in > 50 massive dense ($\langle n \rangle \sim 10^6 \text{ cm}^{-3}$, e.g. Plume et al. (1997)) clumps from Wu et al. (2010). The Wu et al. (2010) survey measured clump sizes, virial masses, and dense gas surface densities using HCN $J=1-0$ as a tracer (Σ_{HCN}) at FWHM of the peak intensity. These are the sites of formation of clusters and massive stars. The most popular tracers of massive star formation include the ultraviolet, $\text{H}\alpha$, FIR, and singly ionized oxygen; however, due to high extinction toward and in these regions, we can use only the total IR luminosity to measure the SFR in these massive clumps.

Since HCN $J=1-0$ gas has been shown to be tightly correlated with the

total IR luminosity in clumps as long as $L_{IR} > 10^{4.5} L_{\odot}$ (Wu et al. 2005), as well as in both normal spiral and starburst galaxies (Gao & Solomon 2004a,b), we can use it to compare gas and star formation from the total IR luminosity in both the Milky Way and external galaxies.

Σ_{HCN} is calculated using the mass contained within the FWHM size (R_{HCN}) of the HCN gas, following the methods used in Shirley et al. (2003):

$$\Sigma_{\text{HCN}} = \pi^{-1} \times \left(\frac{M_{\text{vir}}}{M_{\odot}} \right) \left(\frac{R_{\text{HCN}}}{\text{pc}} \right)^{-2} (M_{\odot} \text{ pc}^{-2}), \quad (2.15)$$

where M_{vir} is the virial mass enclosed in the source size at FWHM intensity. Uncertainties in the Σ_{HCN} are computed by adding in quadrature the errors in the FWHM size and the mass as discussed in Wu et al. (2010).

We compute the SFR for massive dense clumps following extragalactic methods using the total infrared (IR) luminosity (L_{IR} ; 8–1000 μm) derived from the 4 IRAS bands. We assume the conversion $\text{SFR}_{\text{IR}} (M_{\odot} \text{ yr}^{-1}) \approx 2 \times 10^{-10} L_{\text{IR}} (L_{\odot})$ from Kennicutt (1998a). $\Sigma_{\text{SFR}_{\text{IR}}}$ are computed using the FWHM source sizes:

$$\Sigma_{\text{SFR}_{\text{IR}}} = \pi^{-1} \times \left(\frac{\text{SFR}_{\text{IR}}}{M_{\odot} \text{ yr}^{-1}} \right) \left(\frac{R_{\text{HCN}}}{\text{kpc}} \right)^{-2} (M_{\odot} \text{ yr}^{-1} \text{ kpc}^{-2}). \quad (2.16)$$

The uncertainties in the $\Sigma_{\text{SFR}_{\text{IR}}}$ density only include the error in FWHM size and a 30% error in SFR calibrations using the IR. In fact, the uncertainties are larger. The SFR calibration assumes that the observed far-IR emission is

re-radiated by dust heated by O, B, and A stars (Kennicutt 1998a). For low SFR, heating by older stars of dust unrelated to star formation can contaminate the SFR signal, causing an overestimate of the SFR. This is not a problem for the regions of massive star formation in our Galaxy, where the heating is certainly due to the recent star formation. A bigger issue for the Galactic regions is that the full L_{IR} seen in the extragalactic studies is not reached unless the individual region forms enough stars to fully sample the IMF and is old enough that the stars have reached their full luminosity. These conditions may not be met during the time span of an individual massive clump (Krumholz & Thompson 2007; Urban et al. 2010). In particular, Urban et al. (2010) have calculated the ratio of luminosity to SFR in a simulation of a cluster forming clump. They find that L/SFR increases rapidly with time, but lies a factor of 3-10 below the relation in Kennicutt (1998a) when their simulations end at times of 0.7 to 1.4 Myr. Therefore, we may expect both large variations and a tendency to underestimate the SFR in individual regions. Unfortunately, despite these issues, L_{IR} remains the best measure of SFR available to us at present in these regions. While it would be suspect to apply a correction factor based on the Urban et al. simulation, increasing the SFR of the regions of massive star formation by 0.5-1 order of magnitude would bring them into better agreement with the highest surface density points from the nearby clouds.

For the sample of ~ 50 massive dense clumps, 42 sources have corresponding IR measurements. The resulting gas surface densities and Σ_{SFR} for the sample of massive dense clumps are shown in Figure 2.6 and Table 2.6.

The relation between SFR and dense gas mass, $M_{\text{dense}}(\text{H}_2)$, for galactic clumps can be derived from $\langle L_{\text{IR}}/L_{\text{HCN}(1-0)} \rangle = 911 \pm 227 (\text{K km s}^{-1} \text{ pc}^2)^{-1}$, and $\langle M_{\text{dense}}(\text{H}_2)/L_{\text{HCN}(1-0)} \rangle = 11 \pm 2 M_{\odot} (\text{K km s}^{-1} \text{ pc}^2)^{-1}$ from Wu et al. (2005). These relations can be combined with the IR SFR conversion from above to obtain a relation for $\Sigma_{\text{SFR}_{\text{IR}}}$ and Σ_{HCN} :

$$\Sigma_{\text{SFR}_{\text{IR}}} \sim 1.66 \times 10^{-2} \left(\frac{\Sigma_{\text{HCN}(1-0)}}{1 M_{\odot} \text{ pc}^{-2}} \right) (M_{\odot} \text{ yr}^{-1} \text{ kpc}^{-2}). \quad (2.17)$$

This equation is equivalent to that shown in Wu et al. (2005), which is the fit to both massive clumps and galaxies.

Wu et al. (2005) found a decline in the linear $L - L'_{\text{HCN}(1-0)}$ correlation at $L_{\text{IR}} < 10^{4.5} L_{\odot}$, where the clump is not massive or old enough to sample the IMF. Since the majority of the points with $L_{\text{IR}} < 10^{4.5} L_{\odot}$ in Figure 2.6 lie off this relation, we include only massive dense clumps with $L_{\text{IR}} > 10^{4.5} L_{\odot}$. The resulting number of $\text{HCN } J=1-0$ sources is 25 (Table 2.6). The $\text{HCN } J=1-0$ clumps are found to range from $\sim 10^2 - 4.5 \times 10^3 M_{\odot} \text{ pc}^{-2}$ in Σ_{HCN} and from $2 - 130 M_{\odot} \text{ kpc}^{-2} \text{ yr}^{-1}$ in $\Sigma_{\text{SFR}_{\text{IR}}}$. These Σ_{gas} and $\Sigma_{\text{SFR}_{\text{IR}}}$ values are similar to those of circumnuclear starburst galaxies from Kennicutt (1998b), which range from $\sim 10^2 - 6 \times 10^4 M_{\odot} \text{ pc}^{-2}$ and $0.1 - 9.5 \times 10^2 M_{\odot} \text{ kpc}^{-2} \text{ yr}^{-1}$ (see Figure 2.7). The average $\text{HCN } J=1-0$ clump has $\Sigma_{\text{HCN}(1-0)}$ of $(1.3 \pm 0.2) \times 10^3 M_{\odot} \text{ pc}^{-2}$ and $\Sigma_{\text{SFR}_{\text{IR}}}$ of $28 \pm 6 M_{\odot} \text{ kpc}^{-2} \text{ yr}^{-1}$.

We also compare the relation we find for the massive dense clumps to known extragalactic relations in Figure 2.8. In this figure we compare to the

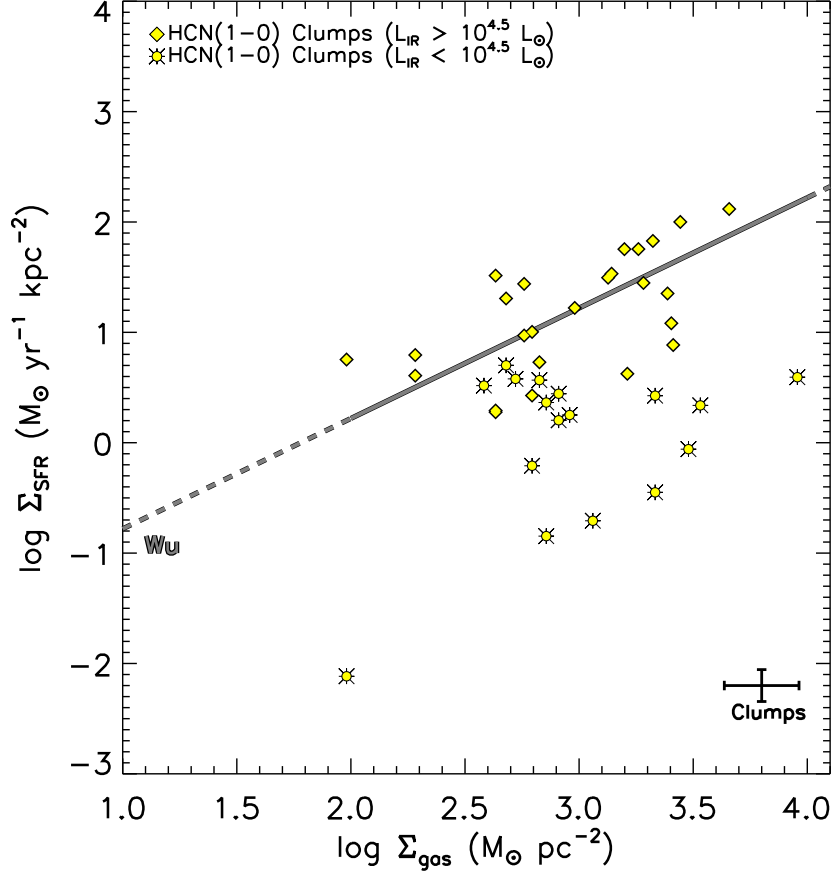


Figure 2.6 Σ_{gas} and Σ_{SFR} are shown for the sample of massive dense clumps from the survey of Wu et al. (2010). Gas surface densities are measured from the HCN $J=1-0$ maps and SFRs are estimated from the total IR luminosity, using the extragalactic prescription from Kennicutt (1998b). The relation between SFR and dense gas from Wu et al. (2005) is shown (grey solid line) and is extrapolated to lower Σ_{gas} . We make a cut at $L_{\text{IR}} > 10^{4.5} L_{\odot}$, below which the clumps are not massive enough to sample the IMF and lie off the linear relation (§Section 2.3.2).

Table 2.6. Massive Clumps HCN $J=(1-0)$

Source	$\log \Sigma_{\text{HCN}}$ ($M_{\odot} \text{ pc}^{-2}$)	$\log \Sigma_{\text{SFR}_{\text{IR}}}$ ($M_{\odot} \text{ yr}^{-1} \text{ kpc}^{-2}$)
(1)	(2)	(3)
W3(OH)	3.39 \pm 0.13	1.35 \pm 0.12
RCW142	3.40 \pm 0.14	1.08 \pm 0.13
W28A2(1)	3.66 \pm 0.14	2.12 \pm 0.13
G9.62+0.10	3.28 \pm 0.13	1.45 \pm 0.14
G10.60-0.40	3.32 \pm 0.12	1.83 \pm 0.12
G12.21-0.10	2.63 \pm 0.24	0.28 \pm 0.23
G13.87+0.28	2.28 \pm 0.15	0.61 \pm 0.13
G23.95+0.16	2.28 \pm 0.25	0.79 \pm 0.21
W43S	2.63 \pm 0.14	1.51 \pm 0.14
W44	2.79 \pm 0.18	1.00 \pm 0.16
G35.58-0.03	3.41 \pm 0.24	0.89 \pm 0.22
G48.61+0.02	1.98 \pm 0.14	0.75 \pm 0.13
W51M	3.14 \pm 0.17	1.53 \pm 0.17
S87	2.76 \pm 0.16	0.97 \pm 0.12
S88B	2.68 \pm 0.19	1.31 \pm 0.15
K3-50	3.26 \pm 0.12	1.75 \pm 0.13
ON1	2.83 \pm 0.14	0.73 \pm 0.13
ON2S	2.76 \pm 0.16	1.44 \pm 0.14
W75N	3.13 \pm 0.13	1.50 \pm 0.12
DR21S	3.20 \pm 0.13	1.75 \pm 0.12
W75(OH)	3.21 \pm 0.13	0.62 \pm 0.13
CEPA	3.44 \pm 0.17	2.00 \pm 0.13
IRAS20126	2.98 \pm 0.18	1.22 \pm 0.13
IRAS20220	2.63 \pm 0.21	0.29 \pm 0.18
IRAS23385	2.79 \pm 0.19	0.43 \pm 0.15
Clump Average	3.12 \pm 0.16	1.44 \pm 0.15

Note. — Columns are : (1) Source name (2) Surface gas density; (3) SFR surface gas density.

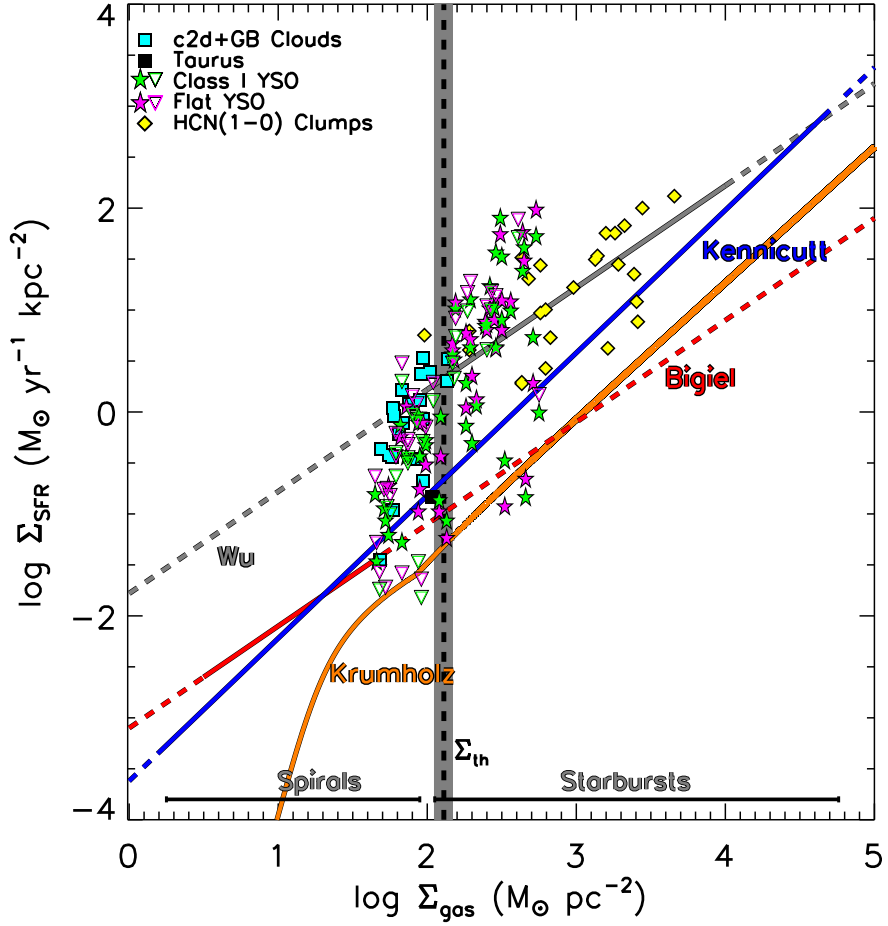


Figure 2.7 Comparison of Galactic total c2d and GB clouds, YSOs, and massive clumps to extragalactic relations. SFR and gas surfaces densities for the total c2d and GB clouds (cyan squares), c2d Class I and Flat SED YSOs (green and magenta stars), and $L_{\text{IR}} > 10^{4.5} L_{\odot}$ massive clumps (yellow diamonds) are shown. The range of gas surface densities for the spirals and circumnuclear starburst galaxies in the Kennicutt (1998b) sample are denoted by the grey horizontal lines. The grey shaded region denotes the range for Σ_{th} of $129 \pm 14 M_{\odot} \text{ pc}^{-2}$.

H₂ gas surface density relation from Bigiel et al. (2008) and the total (HI+H₂) gas surface density relation from Kennicutt (1998b). We find that most of the points for the HCN $J=1-0$ line lie above both the Bigiel et al. (2008) and Kennicutt (1998b) extragalactic relations with the average clump lying a factor of $\sim 5-20$ above the Kennicutt (1998b) and Bigiel et al. (2008) relations, respectively.

In Figure 2.9 we plot the ratio of $\Sigma_{\text{SFR}}/\Sigma_{\text{gas}}$ versus Σ_{gas} for c2d and GB clouds, YSOs, and massive clumps. We find a steep decline in Σ_{SFR} and $\Sigma_{\text{SFR}}/\Sigma_{\text{gas}}$ at around $\sim 100-200 M_{\odot} \text{ pc}^{-2}$. We identify this steep change in Σ_{SFR} over $\sim 100-200 M_{\odot} \text{ pc}^{-2}$ as a star forming threshold (Σ_{th}) between regions actively forming stars and those that are forming few or no low-mass stars.

In Figure 2.7 we show points for the massive dense clumps, c2d and GB clouds, the youngest YSOs, and both the Wu et al. (2005) and extragalactic relations. We also show the range of gas surface densities for spiral and circumnuclear starburst galaxies from the sample of Kennicutt (1998b). $\Sigma_{\text{gas,con}}$ for Class I and Flat SED YSOs lie intermediate between the regions where spiral galaxies and starburst galaxies are found on the Kennicutt (1998b) relation. At $\Sigma_{\text{gas}} > \Sigma_{\text{th}}$, the youngest Class I and Flat SED YSOs overlap with the massive clumps (Figure 2.7). Therefore, high-mass and low-mass star forming regions behave similarly in the $\Sigma_{\text{SFR}}-\Sigma_{\text{gas}}$ plane. The difference between extragalactic relations and c2d and GB clouds is not caused by the lack of massive stars in the local clouds. Also, the overlap with the massive

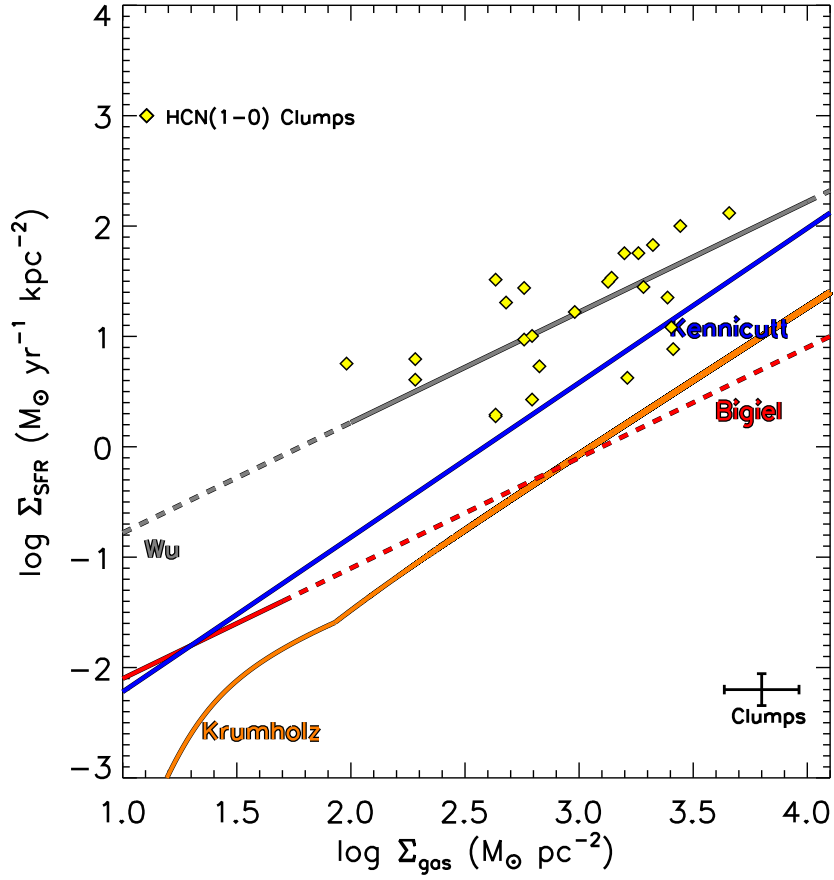


Figure 2.8 Comparison of massive, dense clumps with $L_{\text{IR}} > 10^{4.5} L_\odot$ to extragalactic relations (Kennicutt (1998b), Bigiel et al. (2008), and Krumholz et al. (2009), blue, red, and orange lines, respectively). The relation between SFR and dense gas from Wu et al. (2005) is also shown (grey solid line).

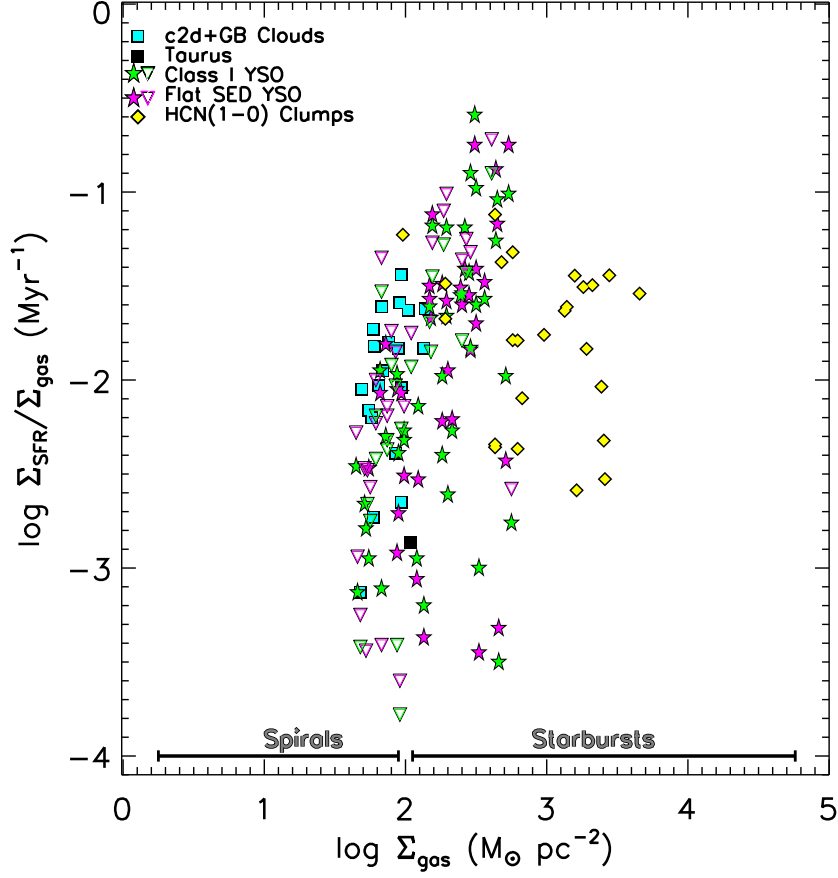


Figure 2.9 The ratio of Σ_{SFR} and Σ_{gas} compared to Σ_{gas} for low and high-mass star forming regions. We find a steep fall off in $\Sigma_{\text{SFR}}/\Sigma_{\text{gas}}$ in the range of $\Sigma_{\text{gas}} \sim 100\text{--}200 M_{\odot} \text{ pc}^{-2}$. We denote this steep fall off as a star forming threshold, Σ_{th} , between active star forming regions and inactive regions.

clumps in Figure 2.7 suggests that L_{IR} provides a reasonable SFR indicator, as long as it exceeds $10^{4.5} L_{\odot}$, though an upward correction would produce better agreement.

A steep increase and possible leveling off in Σ_{SFR} at a threshold $\Sigma_{\text{th}} \sim 100\text{--}200 M_{\odot} \text{ pc}^{-2}$ is seen in both Figures 2.9 and 2.7. We further constrain this steep increase and the possibility of Σ_{SFR} flattening at $\Sigma_{\text{gas}} > \Sigma_{\text{th}}$, by approximating it as broken power law with a steep rise that levels off in §Section 2.3.2.1.

2.3.2.1 Star Formation Threshold

In order to determine a robust estimate of Σ_{th} , we fit the data using two models: a single power law ($y = Nx + A$, where $y = \log_{10} \Sigma_{\text{SFR}}$; $x = \log_{10} \Sigma_{\text{gas}}$) and a broken power law ($y_1 = N_1x + A_1$; $y_2 = N_2x + A_2$). We first fit Class I and Flat SED YSO points ($\Sigma_{\text{SFR,con}}, \Sigma_{\text{gas,con}}$) and massive clumps ($\Sigma_{\text{SFR}_{\text{IR}}}, \Sigma_{\text{HCN}(1-0)}$) to a single power law. We do not include upper limits for YSOs or points for Sco and Cep clouds, which are co-added separate cloud regions and only provide a rough estimate of Σ_{SFR} and Σ_{gas} . The single power law fit yields $N = 1.57 \pm 0.09$ and $A = -3.0 \pm 0.2$, and a reduced chi-square (χ_r^2) of 3.7 (84 dof). We fit the data for both YSOs and massive clumps to a broken power law for the range of $\Sigma_{\text{gas}} = 50\text{--}250 M_{\odot} \text{ pc}^2$. We minimize the total χ^2 for the two segments of the broken power law using a simplex routine, which yields best fit parameters: $N_1 = 4.58 \pm 0.5$, $A_1 = -9.18 \pm 0.9$, $N_2 = 1.12 \pm 0.07$, $A_2 = -1.89 \pm 0.2$ with a χ_r^2 of 3.04 (82 dof). We attribute the large χ_r^2 to

the scatter and large errors in the data, but since the χ_r^2 is $\sim 18\%$ lower for the broken power law compared to the single power law, we take it to be the best fit model. Equating the broken power law fits ($y_1 = y_2$), we obtain a power law break at $\Sigma_{\text{th}} = 129.2 M_{\odot} \text{ pc}^2$ ($A_V = 8.6$) with a statistical 1-sigma deviation in χ^2 of $\pm 14 M_{\odot} \text{ pc}^2$ giving a range in Σ_{th} of $\sim 115\text{--}143 M_{\odot} \text{ pc}^2$. Figure 2.10 shows the broken power law fit (cyan and magenta lines), Σ_{th} , and the 1-sigma statistical range of Σ_{th} (dashed black vertical line and grey shaded region, respectively). The slope of the broken power law changes from a steep relation at $\Sigma_{\text{gas}} < \Sigma_{\text{th}}$ (slope of ~ 4.6) to linear relation (slope of ~ 1.1) at $\Sigma_{\text{gas}} > \Sigma_{\text{th}}$. We note however, that variations in cloud distances will change this threshold slightly. One example is for Ser, which has a recent distance estimate by Dzib et al. (2010) of 415 pc and another estimate by Straizys et al. (1996) of 260 pc (used in this paper). If we use the larger distance of 415 pc, this would change our star formation threshold slightly to $126 \pm 12 M_{\odot} \text{ pc}^2$ ($A_V = 8.4$).

This star forming threshold we find is in agreement with the threshold found in a study of local molecular clouds by Lada, Lombardi, & Alves (2010, submitted) at $A_V \sim 7$ or $116 M_{\odot} \text{ pc}^2$. Enoch et al. (2007) also found extinction thresholds for dense cores found in Bolocam 1.1mm maps in the Perseus, Serpens, and Ophiuchus clouds of $A_V \sim 8, 15$, and 23 , respectively ($\sim 120, 225$, and $350 M_{\odot} \text{ pc}^2$), with a low probability of finding cores below these thresholds. Onishi et al. (1998) surveyed Taurus in C^{18}O and found a star forming column density threshold of $8 \times 10^{21} \text{ cm}^{-2}$, which corresponds to

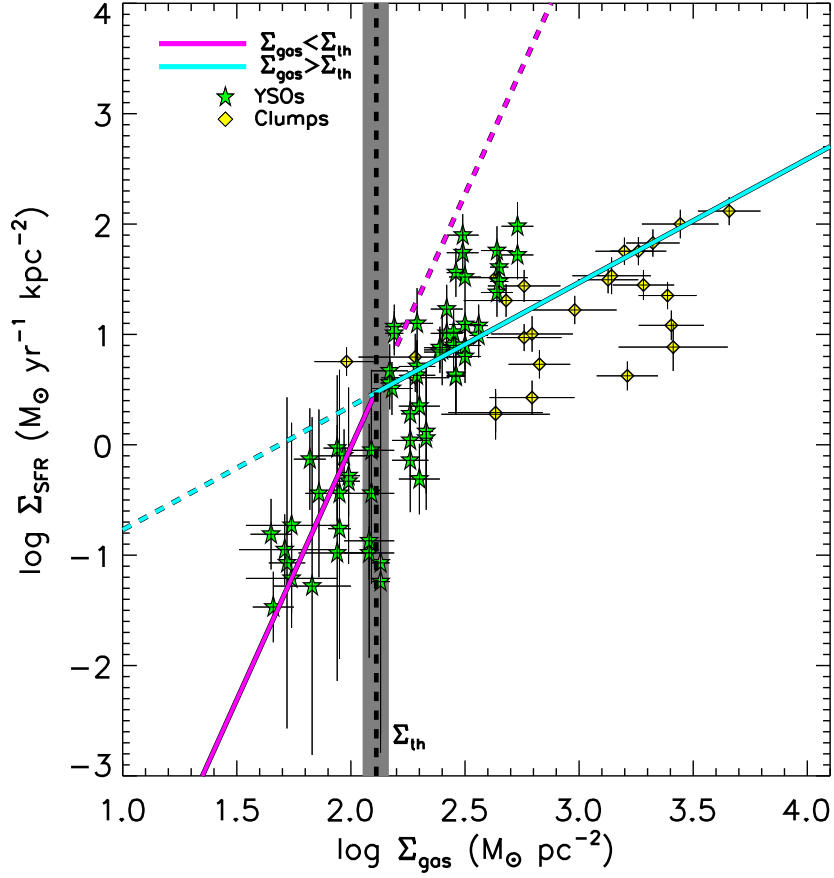


Figure 2.10 We fit Class I and Flat SED YSOs (green stars) and massive clumps (yellow diamonds) to a broken power law (§Section 2.3.2) and obtain an estimate for the star forming threshold, Σ_{th} , of $129 \pm 14 M_{\odot} \text{ pc}^{-2}$ (grey shaded region). The slope changes from 4.6 below Σ_{th} to 1.1 above Σ_{th} .

a gas surface density of $128.1 M_{\odot} \text{ pc}^2$ ($A_V=8.5$). Similarly, both Johnstone et al. (2004) and André et al. (2010) find thresholds of $A_V \sim 10$ ($150 M_{\odot} \text{ pc}^2$).

Mouschovias & Spitzer (1976) proposed the idea of a physical column density threshold corresponding to the central surface density above which the interstellar magnetic field cannot support the gas from self gravitational collapse. This was later modified by McKee (1989) who considered the local ionization states owing to UV radiation. Mouschovias & Spitzer (1976) predicted that when clumps combine to form a large cloud complex, there exists a natural surface density threshold (Σ_{crit}) for a given magnetic field:

$$\Sigma_{\text{crit}} > \left(\frac{80}{M_{\odot} \text{ pc}^2} \right) \times \left(\frac{B}{30 \mu\text{G}} \right). \quad (2.18)$$

The total mean strength of the line-of-sight magnetic field (B_{los}) measured in molecular clouds ($n \sim 10^3\text{--}10^4 \text{ cm}^3$) is $\sim 10\text{--}20 \mu\text{G}$ (Crutcher 1999; Troland & Crutcher 2008). Since statistically $B_{\text{los}} \approx \frac{1}{2} B_{\text{tot}}$ (Heiles & Crutcher 2005), the corresponding total magnetic field, B_{tot} , is $\sim 20\text{--}40 \mu\text{G}$. Using equation 2.18, the corresponding $\Sigma_{\text{crit}} > 50\text{--}110 M_{\odot} \text{ pc}^2$. A similar idea of a threshold at a particular extinction was predicted by McKee (1989) for photoionization-regulated star formation. This model predicts that the rate of star formation is controlled by ambipolar diffusion and therefore depends on the ionization levels in the cloud. Star formation in a “standard” ionization case will occur at $A_V \gtrsim 4\text{--}8$ mag, which translates into a $\Sigma_{\text{crit}} \gtrsim 60\text{--}120 M_{\odot} \text{ pc}^2$. Both of these predictions for a critical density of star formation are

similar to $\Sigma_{\text{th}} = 129 \pm 14 M_{\odot} \text{ pc}^2$. We note, however, that both these models are for parts of clouds that are in a “quasi-static” or turbulence-supported state. Alternatively, these parts of clouds may never become bound and are transient (Vázquez-Semadeni et al. 2009). In this picture, the threshold would correspond to parts of molecular clouds that become gravitationally bound and form stars.

2.3.3 Does the Lack of Resolution in Extragalactic Studies Explain the Discrepancy in Σ_{SFR} ?

The third possibility is based on the fact that the extragalactic relations are averaging over large scales which do not resolve the regions where stars are forming. Current “spatially resolved” extragalactic measurements are still limited to scales of ~ 0.2 -2 kpc (Kennicutt et al. 2007; Bigiel et al. 2008; Blanc et al. 2009); therefore, we cannot directly measure extragalactic SFRs on scales of galactic star forming regions. In any given spatially resolved extragalactic measurement of Σ_{SFR} and Σ_{gas} , the beam will contain a fraction of diffuse gas that does not trace star formation and a fraction of dense, star forming gas (f_{dense}). As discussed in §Section 2.3.1, the dense gas that is forming stars is not well traced by CO so there will be an excess of non-star forming gas in each beam measurement. A local example of this is a study of the Taurus molecular cloud; Goldsmith et al. (2008) found that 33% of diffuse ^{12}CO is contained in regions not associated with ^{13}CO , which is a more reliable tracer of dense, star forming gas (§Section 2.3.1). Even in the regions with $A_V > 2$ studied by the c2d and GB projects, star formation is highly concentrated to

regions of high extinction (e.g., Figure 2.2). Extragalactic studies averaging over hundreds of pc scales would include this diffuse gas, causing an increase in the amount of CO flux that is being counted as star forming gas. In order to better understand approximately how much gas is forming stars at present, a measurement of the fraction of gas that contains YSOs over a larger area on kpc scales in the Galaxy is needed.

Lada & Lada (2003) proposed the idea that clusters of stars which form in clumps located in giant molecular clouds are the fundamental building blocks of galaxies. The rate at which these stellar clusters form is set by the mechanisms that enable these clumps to condense out of their low density parent cloud. A similar idea was explored by Wu et al. (2005), who proposed that there is a basic unit of clustered star formation with the following typical properties: $L_{\text{IR}} > 10^5 L_{\odot}$, $R_{\text{dense}} \sim 0.5$ pc, and $M_{\text{vir}} \sim 300\text{--}1000 M_{\odot}$. As more of these basic units are contained in a galaxy, the SFR increases linearly. This linear correlation between SFR_{IR} and the mass of dense gas (M_{dense}) from HCN $J=1\text{--}0$ was seen in a sample of both spiral and luminous or ultra-luminous IR galaxies (LIRGS and ULIRGS) (Gao & Solomon 2004b), and Wu et al. (2005) showed that the same relation fit the Galactic massive dense clumps. It is therefore the dense gas tracers, such as HCN, that directly probe the volume of gas from which stars form in dense clumps and produce the star formation in external galaxies.

If a linear relation between dense gas and the SFR is assumed at all Σ_{gas} and Σ_{SFR} densities, how can we explain the non-linear behavior of the

Kennicutt–Schmidt SFR–gas relation? Let us suppose that the underlying star formation relation is what we actually observe in regions forming massive stars: a threshold around $129 \text{ M}_\odot \text{ pc}^{-2}$ and a roughly linear relation between dense gas and star formation above that threshold:

$$\Sigma_{\text{SFR}} \propto \Sigma_{\text{dense}}. \quad (2.19)$$

Let us also assume, the Kennicutt–Schmidt relation for the gas surface density averaged over large scales ($\langle \Sigma_{\text{gas}} \rangle$):

$$\Sigma_{\text{SFR}} \propto \langle \Sigma_{\text{gas}} \rangle^{1.4}. \quad (2.20)$$

Then, the fraction of gas above the threshold (f_{dense}) would have to scale with mean surface density of all gas:

$$\begin{aligned} f_{\text{dense}} &= \Sigma_{\text{dense}} / \langle \Sigma_{\text{gas}} \rangle \\ &\propto \Sigma_{\text{SFR}} / \langle \Sigma_{\text{gas}} \rangle \\ &\propto \langle \Sigma_{\text{gas}} \rangle^{0.4}. \end{aligned} \quad (2.21)$$

Near the Σ_{th} of $\sim 129 \text{ M}_\odot \text{ pc}^{-2}$, the average Σ_{SFR} measured on small scales is about $\sim 3 \text{ M}_\odot \text{ yr}^{-1} \text{ kpc}^{-2}$ (taking the average between Class I and Flat SED sources) and f_{dense} is about $1/40$. When $\langle \Sigma_{\text{gas}} \rangle \sim 300 \Sigma_{\text{th}}$, $f_{\text{dense}} \sim 1$. At this point, all the gas is dense enough to form stars and star formation is most efficient, creating a maximal starburst. This is also where the dense gas (Wu et al. 2005) and CO (Kennicutt 1998a) relations cross (see Figure 2.9).

Above $\sim 300\Sigma_{\text{th}}$, the only way to increase star formation efficiency is to make it more efficient even in the dense gas. This is possible because even in dense gas, the star formation rate per free-fall time is less than unity (Zuckerman & Evans 1974; Krumholz & Tan 2007).

Is there local evidence for a preponderance of gas below the threshold? Complete maps of CO for the local 0.5 kpc are not readily available, but we can measure the mass below and the mass above the threshold of $A_V = 8$ for the 16 clouds with Spitzer coverage down to $A_V = 2$. The ratio of total mass lying below the threshold to the total mass above the threshold is 4.6. The massive star forming region, Orion, also has a similar ratio of 5.1 for the mass below over the mass above $A_V = 8$ (M. Heyer, unpublished data). A few clouds have been mapped to still lower levels and a factor of two more mass is found in Taurus, for example Goldsmith et al. (2008). Alternatively, if we assume Orion to contain the largest reservoir of molecular material within 0.5 kpc, we can derive the ratio of mass from ^{12}CO and A_V maps to get 6.4 (M. Heyer, unpublished data). Taken together, these factors make it plausible that there is 10 times more molecular mass than mass above the threshold. Furthermore, most of the gas within 0.5 kpc is atomic. If that is included, the predictions of the extragalactic Kennicutt–Schmidt relation for total gas agree reasonably with the local star formation rate surface density (see Evans (2008) and references therein).

Finally, if the underlying star formation law in the dense gas is linear, then the arguments invoking the density dependence of the free-fall time to

get a power of 1.5 (see §Section 4.1) are specious. In fact, the idea of a single free-fall time for a molecular cloud with an enormous range of densities is highly dubious in the first place.

2.4 Comparison to High Redshift Mergers

We compare the relation we find for Galactic YSOs, clouds, and massive dense clumps and find that the Galactic YSOs and clumps above a threshold for efficient star formation (Heiderman et al. 2010) lie on a similar relation to high redshift mergers (Daddi et al. 2010) indicating that the bulk of gas in these systems trace star forming clouds (Figure 2.11).

2.5 Summary and Conclusions

We investigate the relation between star formation rate (SFR) and gas surface densities in a sample of young stellar objects (YSOs) and massive dense clumps. Our YSO sample consists of objects located in 20 large molecular clouds from the *Spitzer* cores to disks (c2d) and Gould’s Belt (GB) surveys. We estimate the Σ_{gas} in the c2d and GB clouds from A_V maps and Σ_{SFR} from the number of YSOs, assuming a mean mass and star formation timescale for each source. We also divide the clouds into evenly spaced contour levels of A_V . In each contour interval, we measure the $\Sigma_{\text{gas,con}}$ and estimate the Σ_{SFR} by counting only Class I and Flat SED YSOs which have not yet migrated from their birthplace. We use ^{12}CO and ^{13}CO gas maps of the Perseus and Ophiuchus clouds from the COMPLETE survey to estimate Σ_{H_2} densities and

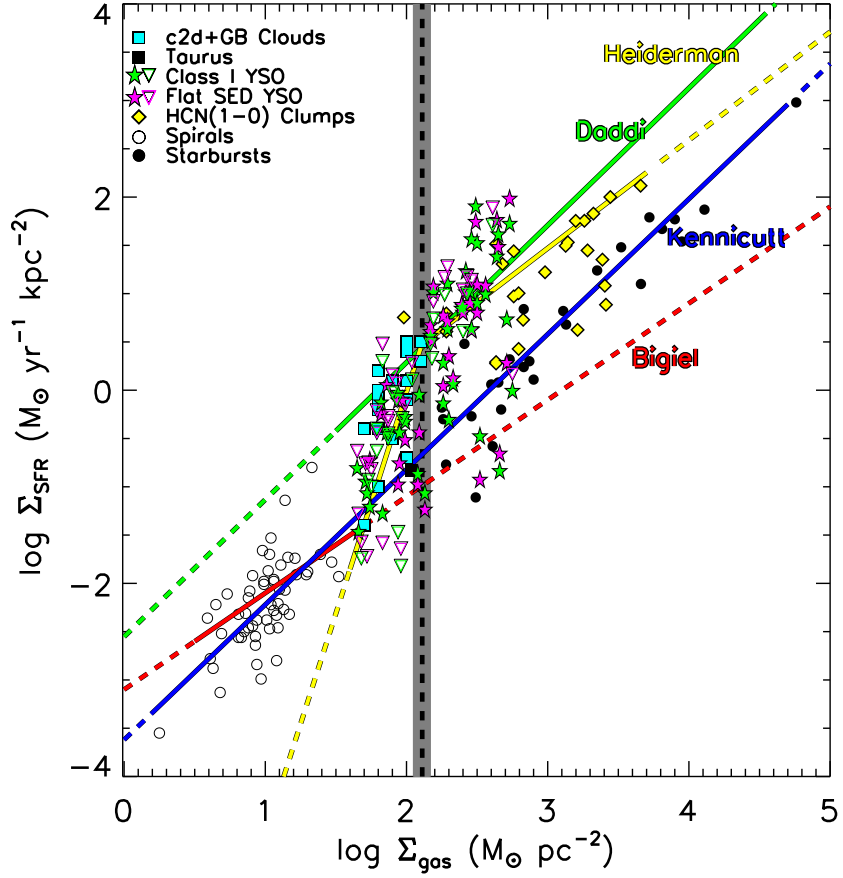


Figure 2.11 I compare clumps, clouds, and YSOs to the relation found for high redshift mergers by Daddi et al. (2010) (see also Genzel et al. (2010)). I find Galactic clumps and YSOs above the star forming threshold (Σ_{th} ; grey line) to lie around the relation for high redshift mergers which suggests the bulk of gas in mergers traces star forming clouds.

compare to measurements from A_V maps. We also compare the c2d and GB low-mass star forming regions to a sample of massive star forming clumps from Wu et al. (2010). We derive SFRs from the total IR luminosity and use HCN gas maps to estimate SFR surface densities ($\Sigma_{\text{SFR}_{\text{IR}}}$) and gas surface densities (Σ_{HCN}) for the massive clumps. Our results are as follows:

- The c2d and GB clouds lie above the extragalactic SFR-gas relations (e.g., Kennicutt–Schmidt Law) by factors of 9–17. We compare the total cloud points to the theoretical prediction of Krumholz et al. (2009) for galactic metallicity and a clumping factor of 1, corresponding to scales of 100 pc, and find the clouds to lie above this prediction by a factor of ~ 40 .
- We perform a follow up survey of suspicious YSOs (MISFITS) at the CSO using the $\text{HCO}^+ J=3-2$ line transition as a dense gas tracer. We choose the youngest YSOs (Class I and Flat SED) that have not yet had time to migrate from their birthplace. These sources are spatially positioned at low extinction levels, most are not clustered, and most lie outside the A_V peaks. In this paper, we present results for a total of 98 sources, including 45 Flat SED and 53 Class I YSOs (detailed results from the full survey will be published in a later paper). We find that 74% or 73 out of the 98 MISFITS observed to date are not detected in HCO^+ which indicates that they do not have a dense envelope of gas, and could be either later class YSOs or background galaxies. These are

a small fraction of the total number of YSOs in the sample, but they could bias the statistics upward at low Σ_{gas} .

- We divide the c2d and GB clouds into contours using evenly spaced intervals of A_V (§Section 2.2.2). We count only the youngest YSOs, removing any Class I or Flat SED YSOs (MISFITS) that are not detected in HCO^+ (§Sections 2.2.3.1 and 2.2.4). We find that the observed extragalactic relations (Kennicutt 1998b; Bigiel et al. 2008) under-predict the average Σ_{SFR} of $\sim 9.7 M_{\odot} \text{ yr}^{-1} \text{ kpc}^{-2}$ by factors of ~ 21 –54 and that our data lie above the theoretical relation (Krumholz et al. 2009) by ~ 2 orders of magnitude.
- We compare Σ_{gas} calculated from A_V maps to Σ_{H_2} estimated from ^{12}CO in §Section 2.3.1. We find that the mass estimated from ^{12}CO may underestimate the Σ_{gas} at $\Sigma_{\text{gas}} \gtrsim 200 M_{\odot} \text{ pc}^{-2}$ by $>30\%$ (Figure 2.9). If the Σ_{H_2} from ^{12}CO underestimates the H_2 mass at $\Sigma_{\text{gas}} \gtrsim 200 M_{\odot} \text{ pc}^{-2}$, then this would effectively shift the extragalactic observed data to the right above this threshold, flattening the slope in the Kennicutt (1998b) relation. However, this small change is not enough to account for the discrepancy between Galactic and extragalactic measurements.
- We also compare Σ_{H_2} from ^{13}CO maps to Σ_{gas} from A_V maps. If ^{13}CO traces the mass we find using extinction maps, we would expect the ratio of $^{13}\text{CO}/A_V$ mass to be of order unity. However, we find the mass estimated from ^{13}CO to be lower than the A_V mass by factors of ~ 4 –5

(§Section 2.3.1).

- We find a steep decrease in $\Sigma_{\text{SFR}}/\Sigma_{\text{gas}}$ (Figure 2.9) and denote this as a star formation threshold (Σ_{th}). In order to determine Σ_{th} , we fit a single power law and broken power law models to data for Class I and Flat SED YSOs and massive clumps. We find the best fit to the SFR–gas relation between YSOs and clumps to be a broken power law (§Section 2.3.2.1) with a break $\Sigma_{\text{th}} = 129 \pm 14 M_{\odot} \text{ pc}^{-2}$. We find a steep relation at $\Sigma_{\text{gas}} < \Sigma_{\text{th}}$ (slope of ~ 4.6) and a linear relation at $\Sigma_{\text{gas}} > \Sigma_{\text{th}}$ with a slope of ~ 1.1 (§Section 2.3.2.1).
- Since the c2d and GB clouds are forming low–mass stars, and extragalactic studies are only able to use tracers that measure the light coming from massive stars, the two star forming regimes might behave differently, accounting for the large difference we measure. However, we find that both high and low–mass star forming regions in the Galaxy follow roughly the same linear relation above Σ_{th} (§Section 2.3.2).
- A contributing factor to the difference seen between Milky Way clouds and extragalactic measurements both on disk–averaged and spatially resolved scales is that extragalactic measurements average over large scales. These measurements include both star forming gas and gas that is not dense enough to form stars.
- Assuming the Kennicutt-Schmidt relation and that the fundamental correlation between Σ_{SFR} and the dense gas (Σ_{dense}) is linear, then the frac-

tion of dense star-forming gas is proportional to $\langle \Sigma_{\text{gas}} \rangle^{0.4}$. When $\langle \Sigma_{\text{gas}} \rangle$ reaches $\sim 300 \Sigma_{\text{th}}$, the fraction of dense gas is ~ 1 , creating a maximal starburst.

The authors thank Mark Krumholz, Charles Lada, Guillermo Blanc, Miranda Dunham, Amanda Bayless, and Jaime Pineda for informative discussions. A.H. and N.J.E. acknowledge support for this work, part of the Spitzer Legacy Science Program, provided by NASA through contract 1288664 issued by the Jet Propulsion Laboratory, California Institute of Technology, under NASA contract 1407 and from NSF Grant AST-0607793 to the University of Texas at Austin, and the State of Texas. L.A. and T.H. are supported by the Gould's Belt Spitzer Legacy grant 1298236. M.H is supported by NSF grant AST-0832222.

Chapter 3

The VIRUS-P Investigation of the eXtreme Environments of Starbursts VIXENS) Survey

3.1 VIXENS Project Motivation

A detailed understanding of the rate at which molecular gas is converted into stars is an essential prerequisite for models of galaxy formation and evolution. In fact, this rate, and the parameters that cause it to vary, are currently ill constrained, leading to large uncertainties in theoretical models of galaxy formation. This presents an observational need for a robust determination of the relation between star formation rate (SFR) and the amount of available dense molecular gas. Our focus is to explore the evolution of the rate at which molecular gas is converted into stars through detailed IFU spatially resolved observations of gas-rich nearby interacting galaxies.

Measuring the spatially resolved star formation efficiency in nearby starburst/ interacting galaxies has direct implication at high- z , where such galaxies play an increasing role in the total SFR density e.g., Le Floc'h et al. (2005). Recent work by Genzel et al. (2010) and Daddi et al. (2010) found a bi-modal relationship between the SFR and gas surface densities for high- z merging galaxies and normal disk galaxies (Figure 3). The high- z mergers

Genzel et al. (2010) lie along the same relation as Galactic low- and high-mass star-forming regions (Heiderman et al. 2010), suggesting that the bulk of gas in merging systems traces star forming gas. While starburst and interacting galaxies are relatively rare in the low- z universe, they are the dominant mode of star formation in the distant universe. Understanding the physics of star formation in nearby interacting/starburst systems is therefore paramount and will provide key insight to the physical processes of star formation in high- z interacting galaxies.

Recent studies suggest that the star formation histories of galaxies are more closely related to the physical processes in a galaxy’s environment than their structural properties (Blanton et al. 2005; Diaferio et al. 2001; Koopmann & Kenney 2004). Do the SFR–gas relations we find vary with galaxy environment or whether it is an isolated field galaxy or in a clusters/group? Our sample contains galaxies in each environment to test this (see Table 3.1, Figure 1.1).

Observations of many galaxies on global or disk-averaged scales have been fit to a power law of $N = 1.4$ (Kennicutt 1998b). Recently, this proposed SFR–gas relation has been studied on \sim kpc scales in nearby spiral galaxies where a deviation from the $N = 1.4$ Kennicutt power law is found e.g., Bigiel et al. (2008). While some work has been done on the integrated emission SFR–gas relation in extreme star-forming environments (Gao & Solomon 2004b), such as those in local (ultra)luminous infrared (IR) galaxies, ((U)LIRGs) (Sanders & Mirabel 1996), there has been little work done studying the spatially-

resolved relation between the SFR and gas surface densities in extreme environments such as the triggered starbursts in interacting galaxies. The VIXENS observational program will provide the required constraints on theoretical models for galaxy evolution as well as a comparison sample for multi-wavelength observational studies of high- z interacting galaxies.

3.2 VIXENS Survey Description

Galaxy interactions of mass ratio $M_1/M_2 > 1/10$ are found to have a significant impact on galaxy evolution, according to simulations. They include major interactions, which are defined to be those with a mass ratio of $1/4 < M_1/M_2 \leq 1/1$, as well as minor interactions with $1/10 < M_1/M_2 \leq 1/4$. Simulations show that major mergers of stellar systems typically destroy the outer disks, transforming them via violent relaxation, into systems with an $r^{1/4}$ de Vaucouleurs-type stellar profile, such as ellipticals (e.g., Negroponte & White 1983; Barnes & Hernquist 1991; Mihos & Hernquist 1996; Struck 1997; Naab & Burkert 2001). The different simulations suggest that ongoing/recent major mergers are associated with arcs, shells, ripples, tidal tails, large tidal debris, extremely asymmetric light distributions, double nuclei inside a common body, galaxies linked via tidal bridges of light, and galaxies enclosed within the same distorted envelope of light.

Conversely, minor interactions ($1/10 < M_1/M_2 \leq 1/4$) involving a spiral and a smaller satellite will not destroy the outer disk of the spiral (e.g., Hernquist & Mihos 1995; Smith & Madden 1997; Jogee et al. 1999). Typ-

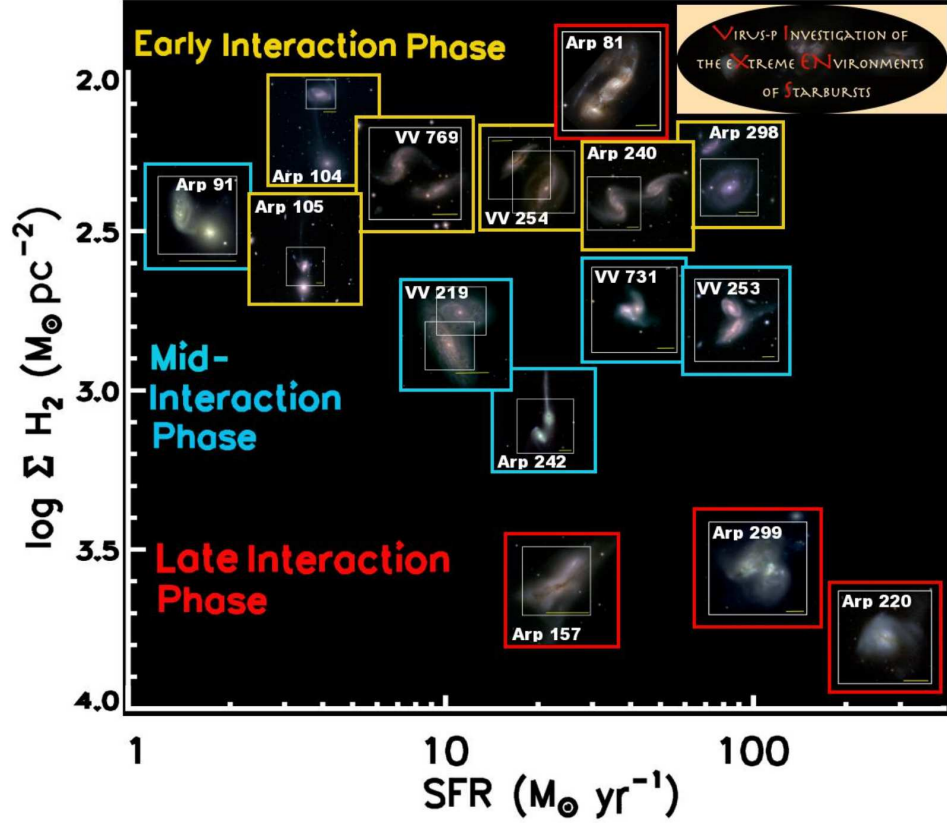


Figure 3.1 SDSS RGB (i,r,g) images of the VIXENS interacting galaxy sample. The white boxes show the VIRUS-P IFU field of view ($1.7' \times 1.7'$) and the yellow lines indicate a scale of 10 kpc. The range of total molecular hydrogen gas surface densities estimated from CO maps and SFRs from IRAS are shown.

ically, the smaller companion sinks via dynamical friction, may excite warps, bars, spirals, and other non-axisymmetric perturbations, and leads to vertical heating, arcs, shells, ripples, tidal tails, tidal debris, warps, offset rings, and highly asymmetric light distributions (e.g., Quinn et al. 1993; Hernquist & Mihos 1995; Mihos 1995; Smith & Madden 1997; Jogee et al. 1999; Jogee 2006).

The VIRUS-P¹ Investigation of the eXtreme Environments of Starbursts (VIXENS)² project is a large IFU survey of 15 nearby IR bright ($L_{IR} > 3 \times 10^{10} L_{\odot}$) interacting/starburst galaxies. The main goal of VIXENS is to investigate the relation between star formation and gas content on spatially resolved scales of 0.1-1 kpc in the extreme star forming environments of interacting/starburst galaxies. The interacting galaxies in this sample were chosen based on three carefully chosen criteria: (1) IRAS IR derived SFRs $\sim 5 - 280 M_{\odot} \text{ yr}^{-1}$, and molecular hydrogen gas surface densities, $\Sigma_{\text{H}_2} \sim 200 - 10^4 M_{\odot} \text{ pc}^{-2}$ from ^{12}CO maps, (2) Because star formation is crucially affected by the state of galaxy interactions (Nikolic et al. 2004), the sample is selected to include the full range of interaction stages (see below for definition) with morphological signatures that range from early stage (close pairs) to late stage mergers (single system with multiple nuclei) and implied mass ratios $1/3 < M_1/M_2 \leq 1/1$ estimated from optical luminosity ratios. The latter requirement is justified because simulations suggest that the interaction stage

¹VIRUS-P construction was possible thanks to support from the Cynthia & George Mitchell Foundation.

²<http://www.as.utexas.edu/alh/vixens.html><http://www.as.utexas.edu/alh/vixens.html>

significantly impacts the galaxies' evolution as seen in optical and HI imaging (Negroponte & White 1983; Barnes & Hernquist 1991; Mihos & Hernquist 1996; Struck 1997), and (3) the availability of ancillary data sets, (Table 3.1) which include archival *Spitzer* 24 μ m, GALEX far-UV, and existing $^{12}\text{CO}(1-0)$ and HI maps. In addition we have single dish line survey of dense gas as traced by molecules such as HCN(1-0), $\text{HCO}^+(1-0)$, and HNC(1-0) from Nobeyama 45m and IRAM 30m telescopes for the sample (Davis et al. , in prep.) , as well as HCN(1-0) maps for a subset of our sample from CARMA (Heiderman, Davis et al. , in prep.). Figure 1 shows SDSS RGB (i,r,g) images of the VIXENS sample with the exception of Arp 81, which instead shows an *HST* color image, as this galaxy is not covered by the SDSS.

Here we define interaction stages to be: (1) *early-interaction* phase or galaxies in a close pair that have clear tidal tails or bridges either optically or in HI, (2) *mid-interaction* phase in which galaxies share a common envelope, double nuclei, and may have faint tidal debris, and (3) *late-interaction* phase systems that are a clear result of two stellar systems coalescing with double nuclei or transformed via violent relaxation, into systems with an $r^{1/4}$ de Vaucouleurs-type stellar profile, such as ellipticals (e.g., Negroponte & White 1983; Barnes & Hernquist 1991; Mihos & Hernquist 1996; Struck 1997; Naab & Burkert 2001).

VIXENS uses the VIRUS-P spectrograph (now Mitchell Spectrograph) (currently the largest field of view, $1.7' \times 1.7'$, IFU in the world) on the 2.7-m Harlan J. Smith telescope at McDonald Observatory. VIRUS-P has a field

of view of $1.7' \times 1.7'$, and has 246 $4.3''$ optical fibers and a 1/3 filling factor for which three dithers provide contiguous coverage. One VIRUS-P pointing covers each system with the exception of VV 219 and VV 254 in which two pointings were necessary (Figure 1, Table 3.2). The spectra cover each object in the wavelength range 4560 Å-6850 Å and have a spectral resolution of 5 Å FWHM ($\sigma_{\text{inst}} \sim 120 \text{ km s}^{-1}$). The VIXENS IFU data will provide 2-D maps of ionized gas, SFRs, stellar and gas kinematics, and metallicities for a total of 735³ individual regions per pointing in 15 nearby interacting galaxies. Table 3.2 VIXENS observing run details for the sample.

VIRUS-P data reduction (Chapter 4) is done using VACCINE (Adams et al. 2011). Spectral analysis, including measurement of gas and stellar kinematics as well as emission line fitting, is performed using PARADA, a modified version of the GANDALF software [19], which includes an implementation of the Penalized Pixel-Fitting method (pPXF) (Cappellari & Emsellem 2004). Figure 2 shows VIXENS data products linearly interpolated based on the discrete values at each fiber position, including integrated 4555 Å-6830 Å stellar flux, stellar velocity field, H α flux, and H α velocity field, for the late interaction phase galaxy merger Arp 299.

³One fiber falls off the CCD due to an alignment issue.

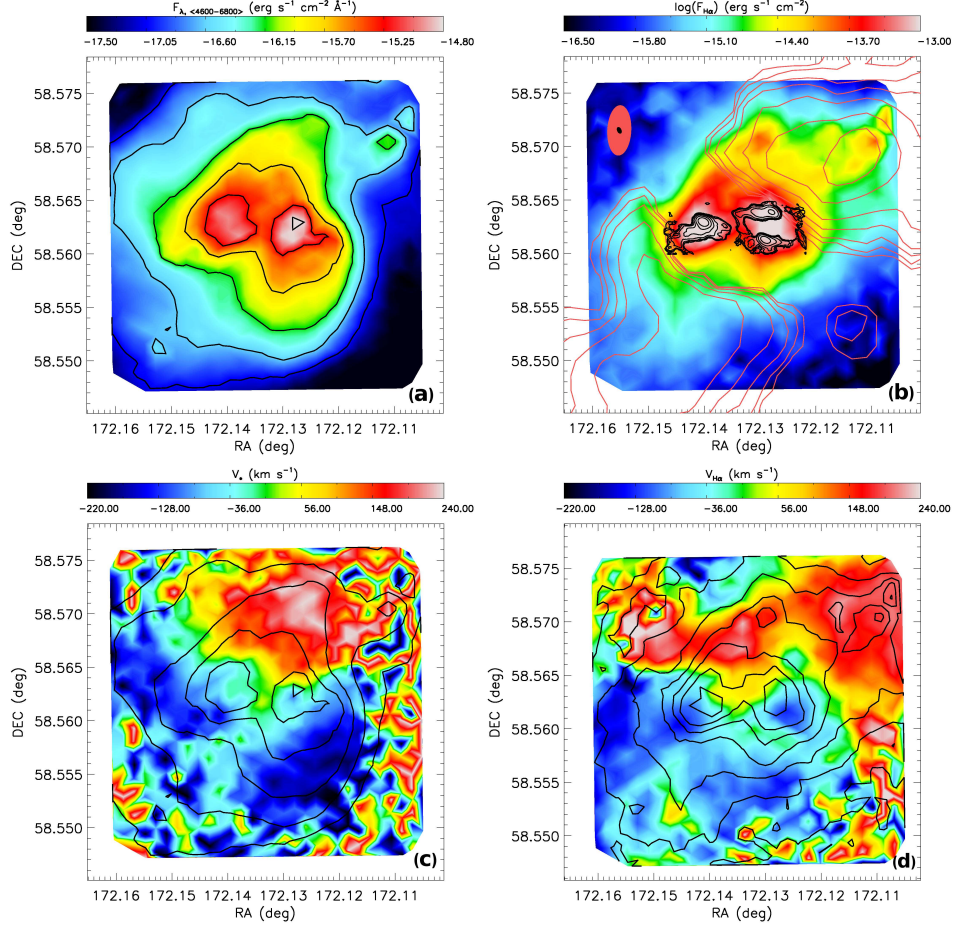


Figure 3.2 Late interaction phase galaxy merger Arp 299 VIRUS-P linearly interpolated IFU maps based on the discrete values at each fiber position of (a) 4600Å-6800Å integrated stellar flux, (b) H α flux overlaid with CO(2-1) and H I integrated intensity map contours in intervals of $1-\sigma_{\text{rms}}$ and beam sizes from the CO(2-1) (black) and H I (red) maps, (c) stellar velocity field, and (d) H α velocity field.

Table 3.1 **Interacting Galaxy Sample.** Columns are: (1) ARP or VV Peculiar Galaxy identifier. (2) Right Ascension (J2000). (3) Declination (J2000). (4) Interaction state: 1= early-interaction (close pairs, tidal tails or bridges), 2= mid-interaction (galaxies share common body or envelope, faint tidal debris, double nuclei), 3= late-interaction (spheroidal or unknown morphology, arcs, shells, ripples). (5) IR SFR derived from IRAS fluxes following the method used in Kewley (2002). (6) Estimated H_2 gas surface densities. (7) Comments and availability of archival data: S= Spitzer $24\mu\text{m}$, G= GALEX FUV, CO= CO map, HI= HI map, and environment of interacting systems: **P**= isolated pair, **Gr**= group, **Trp**= triplet, **Cl**= cluster.

ARP/ VV (1)	RA (J2000) (2)	DEC (J2000) (3)	Interaction State (4)	SFR_{IR} ($M_{\odot} \text{ yr}^{-1}$) (5)	$\log \Sigma_{\text{H}_2}$ ($M_{\odot} \text{ pc}^{-2}$) (6)	Comments (7)
ARP 157	1:24:35.1	+3:47:33	3	16.3	3.4	S,G,HI CO, P
ARP 105	11:11:13.1	+28:41:57	1	5.2	3.6	G,HI CO, Cl
ARP 242	12:46:10.5	+30:43:40	2	12.2	3	S,G,HI,CO, P
VV 219	12:36:33.5	+11:14:53	2	12.5	2.8	S,G,HI, CO, Cl
ARP 104	13:32:08.9	+62:44:02	1	8.5	3.4	S,G,HI, CO,E-Sp, P
ARP 240	13:39:55.2	+0:50:13	1	52.5	2.4	S,G,HI, CO, Gr
VV 253	13:52:16.2	+02:06:16	1	64	2.6	S,G,HI,CO, Gr
ARP 91	15:34:33.7	+15:11:49	2	4.84	2.4	S,G,HI,CO, Gr
ARP 81	18:12:57.6	+68:21:32	3	29.3	2.2	S,G,HI,CO, P/Trp
ARP 298	23:03:16.9	+08:53:01	1	39.2	2.2	S,G,HI,CO, P
VV 731	23:18:22.2	-04:25:01	2	41	2.4	S,G,HI,CO, P
VV 769	1:16:18.5	+46:44:38	1	8.9	2.2	S,G,HI,CO, P
VV 254	00:01:40.2	+23:29:23	1	14	2.2	S,G,HI,CO, Gr
ARP 220	15:34:57.1	+23:30:11	3	274	4.0	S,G,HI,CO, P
ARP 299	11:28:30.4	+58:34:10	3	88.2	5.6	S,G,HI,CO, P

Table 3.2. VIXENS Observing Runs

Date (1)	Number of Nights Total (2)	Grating Setting (3)	Target Name (4)	Interaction Phase (5)	Comments (6)
05/15–05/19/09	4	VENGA red	VV 219 P1&P2 VV 253 Arp 81 Arp 91 Arp 220 Arp 240 P2 Arp 299	mid mid late mid late early late	[SII]/ H α redshifted off chip [SII]/ H α redshifted off chip D2&D3 pointing offset, data bad missing D3 (D1& D2 only)
08/14–08/17/09	3	VIXENS red	Arp 81 Arp 157 Arp 298 P1 VV 254 P1&P2	late late mid early	
12/15–12/21/09*	7	VIXENS red	Arp 298 P2 VV 731 VV 769	early mid early	*Data taken during a VENGARun
01/18–01/22/10	4	VIXENS red	Arp 105 Arp 240 P1 Arp 242	early early mid	missing D2&D3, D1 only guider shutter failed, data bad?
04/15–04/18/10	2	VIXENS red	Arp 104 Arp 242 VV 253	early mid mid	

Note. — P= pointing; D= dither; (1) Dates of observations.; (2) Total number of nights objects were observed.; (3) VIRUS-P grating setup used. VENGARed set up: $\mu=8.88$ mm; $\gamma=62.52$ deg (4592-5710 Å). VIXENS red setup: $\mu=6.28$ mm; $\gamma=62.25$ deg (4630-6850 Å). (4) Galaxies observed.; (5) Interaction phase early stage (separated pairs), mid-interaction phase (close pairs), and late stage mergers (single system with multiple nuclei).; (6) Comments/ data issues.

Chapter 4

Extreme Star Formation in Arp 299 from VIXENS: Constraints on the Spatially Resolved SFR–Gas Relations in a Nearby Merger

I investigate the relationship between star formation and gas content in late interaction phase galaxy merger Arp 299 from the VIRUS-P Investigation of the eXtreme Environments of Starbursts (VIXENS) integral field unit (IFU) survey. By comparing IFU $H\alpha$ and $Pa\alpha$ hydrogen recombination line and $24\mu\text{m}$ data to $COJ = 2 \rightarrow 1$, $COJ = 3 \rightarrow 2$, $HCNJ = 1 \rightarrow 0$, $HCO^+J = 1 \rightarrow 0$, and HI maps, I explore the relation between the star formation rate (SFR) and gas surface densities on spatially resolved kpc scales. Extinction laws for a diffuse interstellar medium ($R_V = 3.1$) and in molecular clouds ($R_V = 5.5$) are compared and I find the latter to recover the intrinsic $H\alpha/Pa\alpha$ ratio within a factor of ~ 2 , indicating $H\alpha$ and $Pa\alpha$ are heavily extinguished and do not reliably trace star formation. Visual extinctions (A_V) from $H\alpha/H\beta$ and $H\alpha/Pa\alpha$ line ratios are a factor of ~ 10 below A_V from CO maps. No evidence is found in our IFU data for an AGN in the nuclear regions of IC 694 or near the X-ray confirmed AGN in the nucleus of NGC 3690, however I find high $[O\text{I}]/H\alpha$ and $[S\text{II}]/H\alpha$ extranuclear line ratios which could be attributed to either a Seyfert-

like ionization cone or shocked outflow from a superwind. The system average $\text{SFR}_{[\text{H}\alpha+24\mu\text{m}]}$ ($90\pm10 \text{ M}_{\odot} \text{ yr}^{-1}$) agrees well with the total infrared (IR) SFR from IRAS ($77\pm5 \text{ M}_{\odot} \text{ yr}^{-1}$), while $\text{SFR}_{[\text{H}\alpha]}$ and $\text{SFR}_{[24\mu\text{m}]}$ underestimate the total SFR by factors of ~ 4 and 2, respectively. SFRs derived from $\text{Pa}\alpha$ centered on the nuclear 1.3 kpc regions are found to be a factor of ~ 2 below that derived from $\text{SFR}_{[\text{H}\alpha+24\mu\text{m}]}$. Comparing $\text{SFR}_{[\text{H}\alpha]}$ to $\text{SFR}_{[\text{H}\alpha+24\mu\text{m}]}$ I find $\text{H}\alpha$ reliably traces star formation in the C-C' star forming complex and in regions north of the nuclei in the disk of IC 694. An $\text{H}\alpha$ peak to the northwest is associated with the HI peak and a stellar cluster seen in the *HST* optical image suggestive of a tidal dwarf galaxy or possibly a large star cluster in the disk of IC 694 or externally triggered from tidally stripped material. I explore relations between the $\text{SFR}_{[\text{H}\alpha+24\mu\text{m}]}$ and molecular (SFR–Mol) gas surface density using $\text{CO}J = 2 \rightarrow 1$ and $\text{CO}J = 3 \rightarrow 2$ and find nuclear regions and integrated values to lie on the SFR–Mol gas surface density seen in high- z mergers (Daddi et al. 2010), while regions throughout the merger lie above the high- z relation which is likely due to the choice of CO–to- H_2 conversion factor. The SFR–Dense gas surface density relation in nuclear regions agrees well with the Gao & Solomon (2004b) relation for normal spirals and (U)LIRGs, however integrated and spatially resolved points lie above this relation with the differences being the choice of $\text{HCN}J = 1 \rightarrow 0$ and $\text{HCO}^+J = 1 \rightarrow 0$ to dense gas conversion factor. I compare $\Sigma_{\text{SFR} [\text{H}\alpha]}$ and Σ_{HI} in extranuclear regions and find the SFR–HI surface density relation on 4.7 kpc scales in Arp 299 follows similar trends seen in the outer disks of normal spirals and dwarf galaxies. The

average star formation efficiency in extranuclear regions is a factor of ~ 6 compared to spirals and dwarfs, which may indicate star formation is being driven by turbulent motions compressing the gas to dense clumps. Using $[\text{NII}]/\text{H}\alpha$ strong line ratio, I find a mean metallicity for Arp 299 to be $12 + \log(\text{O}/\text{H})$ of 8.57 and see lower or diluted metallicities in the nuclear region compared to outer regions in agreement with the merger scenario in which galaxy interactions drive gas from outer regions inward. Using the relation between metallicity and CO integrated intensity, I find the median CO-to- H_2 conversion factor for Arp 299 to be $\sim 3.2\text{--}3.6 \text{ M}_\odot \text{ pc}^{-2} (\text{K km s}^{-1})^{-1}$ which lowers the dispersion in the SFR–Mol relation and moves 1.3 kpc regions in Arp 299 to lie in between the Kennicutt (1998b) normal spiral and starburst and Daddi et al. (2010) high- z SFR–gas relations. A relation between IRAS F_{60}/F_{100} – α_{CO} and $T_{\text{dust}}\text{--}\alpha_{\text{CO}}$ gives a range in α_{CO} of 0.67–0.99 $\text{M}_\odot \text{ pc}^{-2} (\text{K km s}^{-1})^{-1}$. This indicates a Galactic α_{CO} may be more suitable, however α_{CO} likely varies as a function of interaction phase based on whether the system is in starburst mode and region by region in galaxy mergers.

4.1 Introduction and Motivation

A detailed understanding of the rate at which molecular gas is converted into stars is an essential prerequisite for models of galaxy formation and evolution. In fact this rate, and the parameters that cause it to vary are currently ill constrained, leading to large uncertainties in theoretical models of galaxy formation. This presents an observational need for a robust deter-

mination of the relation between star formation rate (SFR) and the amount of available dense molecular gas. Our focus is to explore the evolution of the rate at which molecular gas is converted into stars through spatially resolved observations of gas-rich nearby interacting galaxies with an IFU.

Measuring the spatially resolved star formation efficiency in nearby starburst/ interacting galaxies has direct implication at high redshifts, where such galaxies play an increasing role in the total SFR density (Le Floc'h et al. 2005). Recent work by Genzel et al. (2010) and Daddi et al. (2010) found a bi-modal relationship between the SFR and gas surface densities for high redshift merging galaxies and normal disk galaxies (Figure 3). The high redshift mergers from Genzel et al. (2010) lie along the same relation as Galactic low and high mass star forming regions from Heiderman et al. (2010), suggestive that the bulk of gas in merging systems traces star forming gas. While infrared bright starburst and interacting galaxies are a relatively rarity in the low- z universe, they are the dominant mode of star formation in the distant universe. Understanding the physics of star formation in these systems is therefore paramount. This motivates the observational requirement to study the star formation efficiency in starburst/interacting galaxies.

The idea that there should be a relation between the density of star formation and gas density was first proposed by Schmidt (1959). Schmidt investigated this relation, now known as the “Schmidt law”, assuming that it should be in the form of a power law and suggested that the density of star formation was proportional to gas density squared. Observations of many

galaxies on global or disk-averaged scales have been fit to a power law of the form $\Sigma_{\text{SFR}} \propto \Sigma_{\text{gas}}^N$, where $N=1.4$ (Kennicutt 1998b). While this relation has previously been called the “Kennicutt–Schmidt law”, we refrain from calling this a “law” and instead refer to it as a SFR–gas relation since it is only an assumption that there is *only one relation* that regulates how gas forms stars. Recently, this proposed SFR–gas relation has been studied on $\sim\text{kpc}$ scales in nearby spiral galaxies where a deviation from the Kennicutt–Schmidt power law index is found (e.g., Bigiel et al. 2008; Rahman et al. 2012). While some work on the integrated emission SFR–gas relation in extreme star forming environments has been done (Gao & Solomon 2004a,b), such as those in local (ultra)luminous infrared (IR) galaxies, (U)LIRGs, (Sanders & Mirabel 1996) there has been little work done studying the spatially resolved relation between the SFR and gas surface densities in extreme environments such as the triggered starbursts in interacting galaxies. The VIXENS observational program (Section 4.2) will provide the required constraints on theoretical models for galaxy evolution as well as provide a comparison sample to multiwavelength observational studies of high- z interacting galaxies.

On global scales, the total IR SFR correlates with gas content measured from CO luminosities (e.g., Sanders & Mirabel 1996). However, extreme star forming environments like those in local (U)LIRGs, lie above the classical Kennicutt–Schmidt relation when a starburst CO–to–H₂ conversion factor is used (Genzel et al. 2010; Daddi et al. 2010). With critical densities $\sim 100\text{--}300$ times larger than CO, the HCN $J = 1 \rightarrow 0$ line traces dense gas better than

CO and is found to have a tighter, linear correlation between the IR SFR over two orders of magnitude in luminosity from normal spirals to (U)LIRGs (Gao & Solomon 2004b), as well as on smaller scales in massive star forming regions (Wu et al. 2005). Furthermore, it has been shown that starbursting IR luminous systems exhibit enhanced dense $\text{HCN } J = 1 \rightarrow 0$ gas luminosity compared to CO gas at moderate density (Juneau et al. 2009). This may be due to the gas inflow produced by the gravitational tidal torques into the nuclear region. Alternatively it may be due to an increase in gas velocity dispersion during the interaction, triggering the formation of star forming clouds with densities $\gtrsim 10^4 \text{ cm}^{-3}$ (Gao & Solomon 2004a) far outside the nuclei as predicted in recent theoretical simulations (Bournaud et al. 2010).

Arp 299 is a nearby ($z^1 = 0.010$) infrared luminous ($L_{\text{IR}} \sim 5.1 \times 10^{11} L_{\odot}$; Table 4.1) late interaction phase merger. This system is composed of two main separate galaxies IC 694 (Arp 299 A) and NGC 3690 with two components Arp 299 B and C (Gehrz et al. 1983). Since Arp 299 is a LIRG, we can assume most of the total bolometric luminosity is emitted in the infrared with luminosity ratios ($\sim L_{\text{IR,NGC 3690}}:L_{\text{IR,IC 694}} = 1.4 \times 10^{11} L_{\odot}:2.6 \times 10^{11} L_{\odot} = 1:2$, estimated from total IR luminosity fractions from Alonso-Herrero et al. (2000)) and a separation of $\sim 4.3 \text{ kpc}$, indicative of late interaction stage 2:1 mass ratio major merger. The Arp 299 C-C' component is considered a non-nuclear component as it has a dense molecular gas concentration (Aalto et al. 1997; Casoli et al.

¹In this paper, we assume a flat cosmology with $\Omega_m = 1 - \Omega_{\lambda} = 0.3$ and $H_0 = 70 \text{ km s}^{-1} \text{ Mpc}^{-1}$ and the distance to Arp 299 is 44.1 Mpc and $1'' = 214 \text{ pc}$.

1999; Imanishi & Nakanishi 2006), but lacks evidence for a significant potential well for it to be considered an individual galaxy as this region does not contain a concentration of old redder stars (Alonso-Herrero et al. 2000). Optical and HI observations (Hibbard & Yun 1999) show that Arp 299 likely results from a prograde- retrograde encounter as the system contains one tidal tail in both the optical and HI stripped from the disk of NGC 3690, while the HI disk of IC 694 remains relatively intact and displays one prominent spiral arm with a dust lane in the optical (Figure 4.1, Mihos & Hernquist 1996). The merger is estimated to have occurred ~ 750 Myr ago between a gas- rich Sab-Sb galaxy (IC 694) and an SBc-Sc galaxy (NGC 3690). Based on this and the rotational speed of 240 km s^{-1} Hibbard & Yun (1999) predict the system will merge in $\sim 20\text{-}60$ Myr. The age of star formation bursts in each component ranges from $\sim 4\text{-}5$ Myr (C-C'), ~ 7.5 My (B), and ~ 11 Myr (A) based on evolutionary synthesis model fits (Alonso-Herrero et al. 2000).

4.2 The VIRUS-P Investigation of the eXtreme ENvironments of Starbursts (VIXENS) Survey

VIXENS² is a large integral field unit (IFU) survey of 15 nearby IR bright ($L_{IR} > 3 \times 10^{10} L_{\odot}$) interacting/starburst galaxies (see Heiderman et al. (2011) for full survey description). Our sample is selected to include a full range of interaction stages (from early stage close pairs to late stage systems with multiple nuclei) and interacting galaxies with implied mass ratios of $1/3$

²<http://www.as.utexas.edu/~alh/vixens.html>

Table 4.1. Global Star Formation Rates

Band (1)	Luminosity $10^{42} \text{ erg s}^{-1}$ (2)	SFR $M_{\odot} \text{ yr}^{-1}$ (3)
IR (1-1000 μm) ^a	1973 \pm 118	76.6 \pm 4.6
H α , cor	$\geq 3.52 \pm 0.12$	$\geq 18.9 \pm 0.7$
24 μm	$\geq 461 \pm 1.9$	$\geq 43.6 \pm 6.3$
H α +24 μm ^b	$L_{\text{H}\alpha, \text{obs}} + 0.031 L_{24\mu\text{m}} \geq 16.6 \pm 1.9$	$\geq 89.8 \pm 9.9$
	$L_{\text{H}\alpha, \text{obs}} = 2.34 \pm 0.01$	-

Note. — Total IR luminosity calculated from $F_{\text{FIR}} = 1.26 \times 10^{-14} (2.58 F_{60} + F_{100})$ (W m^{-2}) (Helou 1986) ($F_{60} = 105.82 \text{ Jy}$, $F_{100} = 111.16 \text{ Jy}$ from the IRAS galaxies and quasars catalog) and the ratio of total IR (1-1000 μm) to FIR luminosity: $L_{\text{IR}}/L_{\text{FIR}} \sim 1.75$, assuming a few percent contribution to the total IR luminosity from 1-8 μm (Calzetti et al. 2000).

(b) Mixed H α +24 μm luminosity and SFR using the 24 μm extinction corrected observed H α luminosity using equation 6 from Murphy et al. (2011).

(1) Wavelength band; (2) Total luminosity in wavelength band above an observed H α flux S/N of 5; (3) Star formation rate using same Kroupa (2001) IMF and SFR calibrations taken from Murphy et al. (2011).

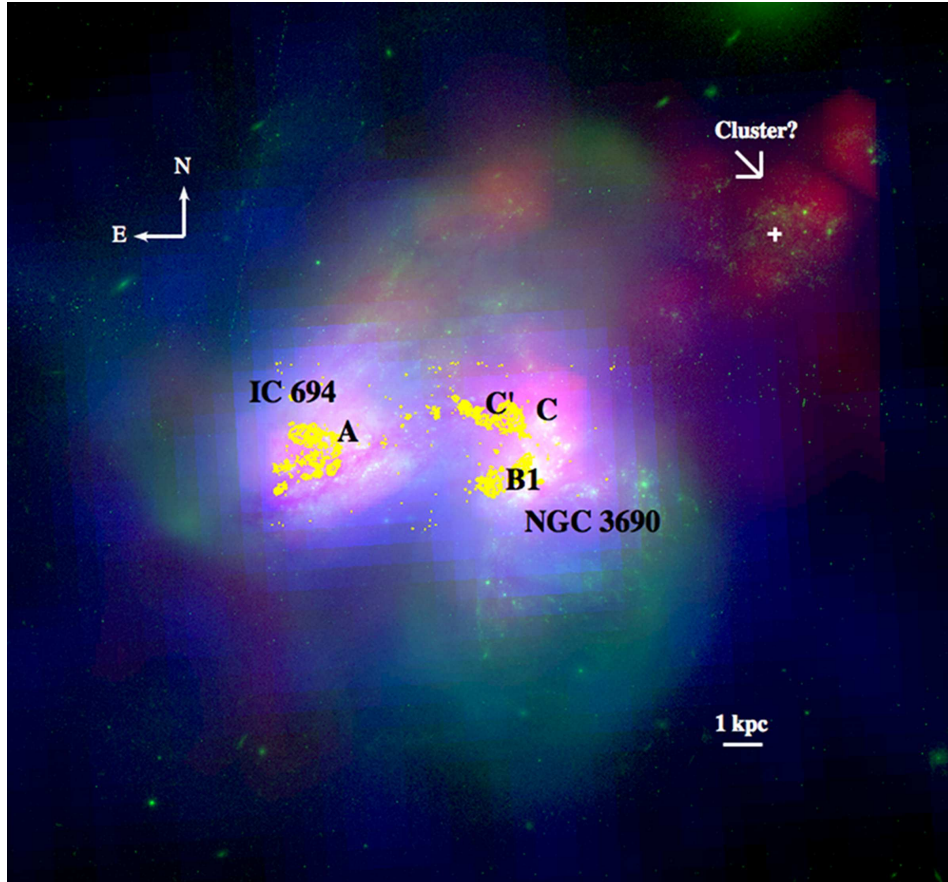


Figure 4.1 RGB image of interpolated $H\alpha$ flux map based on discrete values at each IFU fiber position (red), archival *HST* 814W image (green), *Spitzer* $24\mu\text{m}$ image (blue), and contours of *HST* $\text{Pa}\alpha$ emission (yellow; note coordinates are offset see Alonso-Herrero et al. (2000)). The two main separate components of the Arp 299 merger IC 694 and NGC 3690 and individual nuclei (A and B1) and star forming complexes (C, and C' are indicated. Also shown is a possible stellar cluster associated with a peak in both $H\alpha$ and HI .

$< M_1/M_2 \leq 1/1$ estimated from optical luminosity ratios. Systems in our sample have existing ancillary data sets including *Spitzer* 24 μ m, and CO and HI maps. In addition we have single dish line survey of dense gas as traced by molecules such as $\text{HCO}J = 1 \rightarrow 0$, $\text{HCO}^+J = 1 \rightarrow 0$, and $\text{HNC}J = 1 \rightarrow 0$ from Nobeyama 45m and IRAM 30m telescopes for the sample (Davis et al. , in prep.), as well as $\text{HCN}(1-0)$ maps for a subset of our sample from CARMA (Heiderman, Davis et al. , in prep.).

4.3 Observations

We use the VIRUS-P (now Mitchell Spectrograph) on the 2.7-m Harlan J. Smith telescope at McDonald Observatory. The IFU has a field of view (FOV) of $1.7' \times 1.7'$, and has 246 4.3'' optical fibers with a 1/3 filling factor for which three dithers provide contiguous coverage. The spectra covers the wavelength range 4555–6830Å and has a mean instrumental spectral resolution of $\simeq 5.4\text{Å}$ FWHM or $\sigma_{\text{inst}} \simeq 120.5 \text{ km s}^{-1}$ (Section 4.4.1). The observations of Arp 299 were taken on May 16, 2009 with an average seeing of 1.''2. The central coordinates of Arp 299 are J2000 $(\alpha, \delta) = (11:28:28.33, +58:33:38.6)$ and we obtain three dithers from the central position at $(\Delta\alpha, \Delta\delta) = (0''.0, 0''.0), (-3''.6, -2''.0)$, and $(0''.0, -4''.0)$ for full coverage of our FOV. We obtained three 10 minute exposures on each dither position bracketed by a 5 minute sky exposure each with a 30' off position. The spectrophotometric standard star PG1708+602 was observed using a 6-point dither pattern with and exposure time of 200 seconds each to ensure sampling of the PSF for

flux calibration. Taking into account one fiber which falls off the CCD due to alignment, this gives a total of 735 individual spectra with a spatial resolution of $4.''235$ or ~ 900 pc at the distance of Arp 299.

4.3.1 IFU Data Reduction and Emission Line Flux Measurements

4.3.1.1 Data Reduction, Flux Calibration, Astrometry, and Final Data Products

We provide an overview of the VIXENS IFU data reduction, astrometric calibration, and flux calibration below. A detailed description of data reduction and flux calibration will be included in a forthcoming paper (or rather just in dissertation). The reduction of VIXENS IFU data is performed using the VACCINE reduction pipeline (Adams et al. 2011). Due to the unique gimbal mount design of VIRUS-P, the instrument is kept at constant gravity, providing negligible flexure effects on the light path to the CCD. Bias frames spanning the entire observing run are combined and all data (arc lamp, twilight flat field, sky, and science frames) are first overscan then bias subtracted using the combined bias frame. Cosmic ray rejection is performed on the overscan and bias subtracted science frames using the LA-Cosmic (van Dokkum 2001), an algorithm based on a variation of laplacian edge detection with an additional two pixel buffer applied. Residual cosmic rays such as those that hit the CCD at an oblique angle will be removed when the three frames for each dither position are combined (Section 4.4.1). A combined twilight flat field frame is made and then used to trace the position of each fiber spectrum on the CCD. The solar spectrum is removed from the master flat field by using

a B-spline fit to combined neighboring fibers with similar spectral resolution. Each fiber is then normalized by the combined spectrum and the frame is median smoothed. The Ne+Cd arc frames are combined and the wavelength solution is initially computed using a 4th order polynomial to 10 matched emission lines. Then, all frames are flat fielded using the median smoothed solar spectrum subtracted master flat. The final wavelength solution is determined by using the initial parameters determined before on the flat fielded master arc frame, varying parameters until reaching a solution. Sky subtraction is done in two steps: 1) since the sky brightness varies non-linearly throughout the observations, we determine a variable fit during the time frame for our science observations as a function of wavelength and 2) the before and after sky frames corrected for this variate for each science exposure are averaged before background subtracting science frames. To perform the first step, we rebin spectra over our science frames (both of Arp 299 and our spectrophotometric standard PG1708+602) into 500 Å bins and measure the median value per bin. A cubic-spline fit to the median rebinned spectra over the time span of our observations were performed to obtain a correction factor to the sky frames. A 5th order polynomial fit to these correction factors as a function of wavelength is determined and sky frames are multiplied by this smooth function to obtain final sky frames. We then perform the second step, averaging the before and after corrected sky frames and use these to background subtract our science frames. The initial astrometric calibration is performed using guide camera pointing that is offset by $\sim 9'$ North of the IFU field which images a $4'.5 \times 4'.5$

FOV positioned on the corresponding pixel coordinates of a guide star. We determine our final astrometry as discussed below.

Observations of spectrophotometric standard PG1708+602 (Massey et al. 1988) are used to perform relative flux calibration as a function of wavelength for the Arp 299 IFU data. Since the IFU only samples a portion of the standard star’s PSF, we observe in an overlapping 6–point dither pattern to fully sample the PSF and recover the star’s total flux. The centroid position is calculated by taking the first order moment or the weighted average of the fiber fluxes as a function of position, which is used to reconstruct the shape of the PSF. The reconstructed PSF is fit to a Moffat profile which gives the total flux measured in each of the fibers. Each spectrum was normalized by the fraction of total flux sampled and an average value above 5σ was used to determine the total instrumental spectrum. The total spectrum was corrected for atmospheric extinction measured at McDonald Observatory as a function of wavelength and the spectrum of PG1708+602 from Massey et al. (1988) was used to determine our relative flux calibration. We estimate the systematic uncertainty in our relative flux calibration during these observations to be 3.6% by normalizing and averaging derived flux calibration curves as a function of wavelength for the four standard stars obtained during the same VIXENS May 2009 observing run. We use this average flux calibration curves over the entire observing run for our relative flux calibration for Arp 299.

We perform absolute flux calibration and final astrometry using a cross-correlation between a reconstructed broad-band image of Arp 299 from our IFU

data with an SDSS-III DR8 r -band image mosaic³. We measure the monochromatic flux at the effective wavelength of the r -band filter by integrate each fiber's spectrum over the corresponding SDSS transmission curve. The r -band image is simultaneously convolved with a Gaussian kernel to match the PSF plus seeing of our observations and fiber size aperture photometry is performed at each fiber position as determined in our initial astrometric calibration. We then fit a linear relation ($F_{r\text{-band}} = N \times F_{\text{fiber}} + B$) to the atmospheric extinction corrected IFU fluxes (F_{fiber}) at the airmass of our observations with fluxes from our photometry ($F_{r\text{-band}}$) to recover a normalization factor (N) and residual background (B) for our absolute flux calibration. The mean fit parameters for our three dithers on Arp 299 are $\langle N \rangle = 1.1 \pm 0.001$ and $\langle B \rangle = 5.9 \pm 2 \times 10^{-19}$ erg s⁻¹ cm⁻² Å⁻¹ which is a factor of 50 smaller than the continuum level of the average spectrum ($\sim 3 \times 10^{-17}$ erg s⁻¹ cm⁻² Å⁻¹), so sky subtraction residuals are minimal.

Since systematic offsets were found in astrometry between identical pointings over different observations with the largest variations found over different observing runs (Adams et al. 2011), we determine our final astrometry calibration using the SDSS r -band image. To determine and correct for astrometric offsets, we vary the initial astrometry in both RA and DEC by small amounts (ΔRA and ΔDEC) simultaneously during our fit for the absolute flux calibration until a minimum χ^2 is reached for the fit. The average astrometric offsets for the three dither positions for our observations are

³<http://data.sdss3.org/mosaics>

$\langle \Delta \text{RA} \rangle = 3''.3 \pm 0.03$ and $\langle \Delta \text{DEC} \rangle = 1''.6 \pm 0.03$, which is within the IFU fiber size. We use the corrected registered coordinates from this procedure as the final astrometry for the Arp 299 data.

4.3.2 Ancillary Data

4.3.2.1 Molecular Gas Maps

We use $^{12}\text{CO}J = 2 \rightarrow 1$ and $^{12}\text{CO}J = 3 \rightarrow 2$ maps from the Luminous IR Galaxies Submillimeter Array (SMA) Survey (Wilson et al. 2008) which were corrected for short spacings using the James Clerk Maxwell Telescope (JCMT) (Sliwa et al. 2012) and $\text{HCN}J = 1 \rightarrow 0$ and $\text{HCO}^+J = 1 \rightarrow 0$ maps from Imanishi & Nakanishi (2006) to derive molecular gas masses. The beam sizes for $\text{CO}J = 2 \rightarrow 1$ and $\text{CO}J = 3 \rightarrow 2$ are $3''.0 \times 1''.8$ and $2''.2 \times 1''.9$, respectively and $4''.2 \times 3''.8$ for the $\text{HCN}(1-0)$ and $\text{HCO}^+(1-0)$ maps. The $1-\sigma_{\text{rms}}$ noise in each map are 1.7 and $3.5 \text{ Jy beam}^{-1} \text{ km s}^{-1}$ for $\text{CO}J = 2 \rightarrow 1$ and $\text{CO}J = 3 \rightarrow 2$ corresponding to a molecular gas surface density (Σ_{Mol}) of 4.1 and $4.8 \text{ M}_{\odot} \text{ pc}^{-2}$ accounting for the contribution from Helium using a CO-to- H_2 conversion factor of $0.4 \text{ M}_{\odot} \text{ pc}^{-2} (\text{k km s}^{-1})^{-1}$ (see Section 4.4.2). The $\text{HCN}J = 1 \rightarrow 0$ and $\text{HCO}^+J = 1 \rightarrow 0$ maps have a $1-\sigma_{\text{rms}}$ noise level of $545 \text{ mJy beam}^{-1} \text{ km s}^{-1}$ corresponding to a Σ_{Dense} of $\sim 36 \text{ M}_{\odot} \text{ pc}^{-2}$ using dense gas conversion factor of $5 \text{ M}_{\odot} \text{ pc}^{-2} (\text{k km s}^{-1})^{-1}$ (Section 4.4.2).

4.3.3 Neutral Hydrogen Map

We use the Very Large Array (VLA) neutral hydrogen (HI) combined C+D array configuration map from Hibbard & Yun (1999) with a robust weighting of 1 and a beam size of $22'' \times 20''$ (4.7×4.3 kpc). The $1-\sigma_{\text{rms}}$ noise per 10.5 km s^{-1} channel in the HI map is $0.30 \text{ mJy beam}^{-1}$ which corresponds to a HI gas surface density (Σ_{HI}) of $0.09 \text{ M}_{\odot} \text{ pc}^{-2}$ (Section 4.4.2).

4.3.3.1 *Spitzer* 24 μm Data

We obtain the *Spitzer* MIPS 24 μm image of Arp 299 directly from the *Spitzer* Heritage Archive (P.I. Giovanni Fazio, unpublished). The FWHM of the MIPS PSF at 24 μm is $6''$. Flux outside of this beam is non-Gaussian, however we only consider flux measurements that lay inner to the first Airy ring so this is a minor concern. To obtain our science image, we set the edges of the Post-Basic Calibrated Data map to zero and fit a plane to subtract the background under the assumption that this will subtract both the contribution from zodiacal light and diffuse emission from the Milky Way. The 24 μm image is saturated in nuclear regions (Figure 4.1) and thus we will treat the saturated flux measurements as a lower limit (Section 4.6). For spatially resolved measurements of the SFR and gas surface densities, we convolve all other data to the 24 μm data $6''$ (1.3 kpc) resolution.

4.3.3.2 *HST* NICMOS Pa α Data

The nuclear regions of Arp 299 were imaged by *HST* NICMOS 2 by Alonso-Herrero et al. (2000). F190N continuum subtracted F187N Pa α images of IC 694 and NGC 3690 were kindly provided by those authors. These images have a FOV of $19''.5 \times 19''.5$ each and a plate scale of $0''.076 \text{ pixel}^{-1}$ (Figure 4.1). The data reduction, calibration, and continuum subtraction are described in Alonso-Herrero et al. (2000) and references therein.

4.4 Data Analysis

4.4.1 Emission Line Flux Measurements

Before we measure emission lines from our calibrated data we first extract the fiber fluxes and combine the three data frames for each dither into a multidimensional row stacked spectrum (RSS) Flexible Image Transportation System (FITS) files. Our final RSS FITS file includes: 1) flux ($F_\lambda(\lambda)$) in units of $\text{erg s}^{-1} \text{ cm}^{-2} \text{ \AA}^{-1}$ and corresponding error in flux as a function of wavelength, 2) the wavelength at each pixel center, 3) the J2000 Right Ascension and Declination in units of degrees, and 4) the instrumental FWHM as a function of wavelength. To calculate $F_\lambda(\lambda)$, the data is regridded into 1.1 \AA bins and flux in each fiber as a function of wavelength is computed from the weighted average of the calibrated data in an aperture of five pixels is given by the relation:

$$F_\lambda(\lambda) = \frac{\sum_{i=1}^5 w_i F_{\lambda,i}(\lambda)}{\sum_{i=1}^5 w_i}, \quad (4.1)$$

where w_i are the weights and are the inverse of the errors from VACCINE squared ($w_i = 1/\sigma_i^2$). We make a 3σ cut to remove any residual cosmic rays and mask fluxes and the coordinates are from the final astrometry calibration discussed in Section 4.3.1. The instrumental spectral resolution as a function of wavelength for each fiber is determined from performing a Gaussian fit to the unblended emission lines in the combined arc lamp frame and then fitting a second order polynomial fit to the FWHM from the Gaussian fits as a function of wavelength. The final instrumental spectral resolution has a range of 4.4–6.1Å with a mean of $\simeq 5.4$ Å FWHM ($\sigma_{\text{inst}} \simeq 120.5 \text{ km s}^{-1}$).

Emission line fluxes are measured using GANDALF software developed by Sarzi et al. (2006). Empirical stellar templates from version 9.1 of the MILES stellar library (Sánchez-Blázquez et al. 2006; Falcón-Barroso et al. 2011) are used. We use a subset of the MILES library containing 72 stars that span a range in luminosity classes (I–V), spectral types (O–M), metallicities ($-2 < [\text{Fe}/\text{H}] < 1.5$), and include horizontal giant branch and asymptotic giant branch stars. The templates and data are convolved using a changing Gaussian kernel with a FWHM equal to the highest instrumental resolution of the data, $\sigma_{\text{inst}} = 149 \text{ km s}^{-1}$. We first mask regions around bright night sky lines that have high residuals from our sky subtraction and use GANDALF to fit the full spectrum of each fiber including the emission lines. In order to more accurately measure emission lines at low S/N , we tie the kinematics of all emission lines to a common gas velocity and dispersion of the $\text{H}\alpha$ the brightest emission line in the spectrum and perform a simultaneous kinematic fit to all lines. The stellar

kinematics are measured using the Penalized Pixel-Fitting method, pPXF, (Cappellari & Emsellem 2004) and the details of the kinematic measurements are beyond the scope of this paper and are discussed in detail in (Heiderman et al. , in prep.). A secondary fit is then performed by GANDALF in which it recomputes weights given to stellar templates from the pPXF kinematics solution while modeling emission lines using Gaussian profiles. Figures 4.2 and 4.3 show an example of the observed and fit spectrum for both a fiber with a low S/N as determined using the A/N criteria (Sarzi et al. 2006, Section 4.7) of 7 and a high A/N of 100. The observed spectrum and 1σ uncertainties are shown in black and the green envelope, respectively. The best fit stellar plus emission line spectrum is shown by the red solid line and the dotted blue line shows the stellar component of the fit without the emission lines. The vertical green bands are masked regions around sky line residuals.

We derived errors in emission line fluxes by running a Monte Carlo emission line flux simulation assuming errors in line amplitude, velocity, and velocity dispersion are uncorrelated. Since the measurement of the other emission lines are tied to the $H\alpha$ kinematics, GANDALF provides errors in only the $H\alpha$ emission line flux, velocity, and velocity dispersion. For all other emission lines, GANDALF only outputs emission line amplitudes and associated errors as well as the velocity and velocity dispersion. For each emission line, we use these line amplitudes, errors in line amplitudes and the $H\alpha$ line velocity and dispersion errors combined with the instrumental spectral resolution ($\sigma_{\text{inst}}=149 \text{ km s}^{-1}$) to compute simulated emission line fluxes in a Gaussian

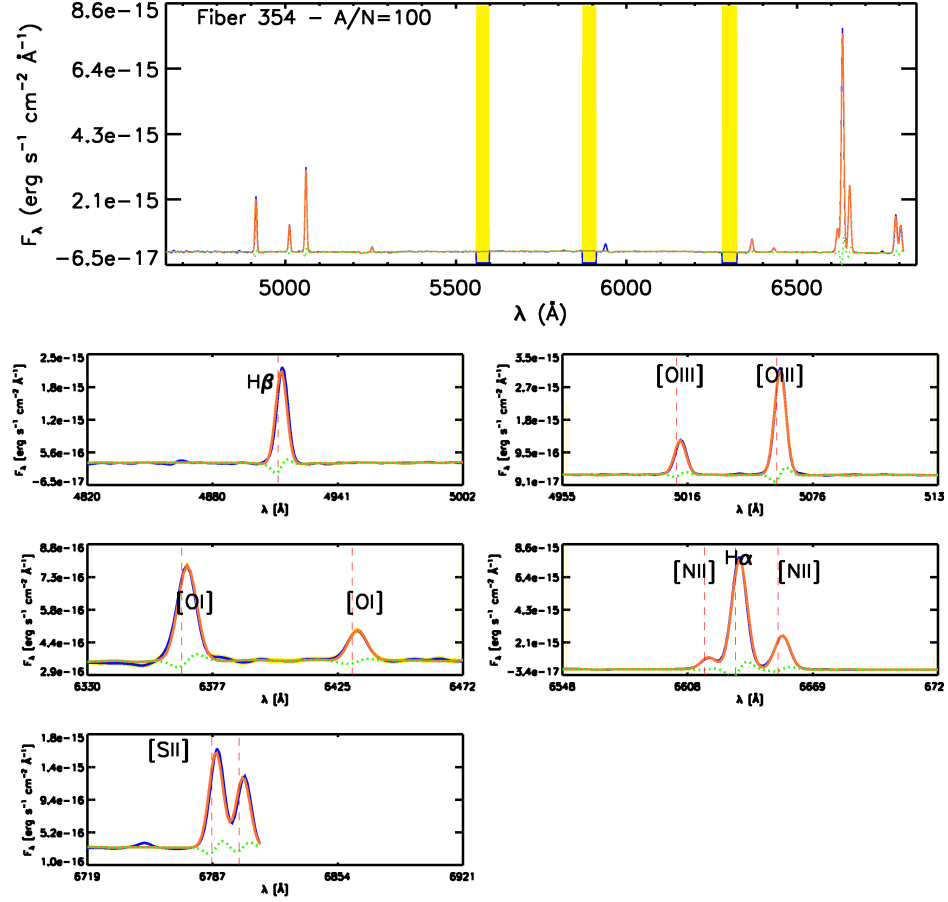


Figure 4.2 Spectrum of fiber 354 with a high $A/N = 100$ in the Arp 299 data cube. The observed spectrum and 1σ uncertainties are shown in blue and the yellow envelope, respectively. The best fit stellar plus emission line spectrum is shown by the orange solid line and the dotted green line shows the stellar component of the fit without the emission lines. The vertical yellow bands are masked regions around sky line residuals.

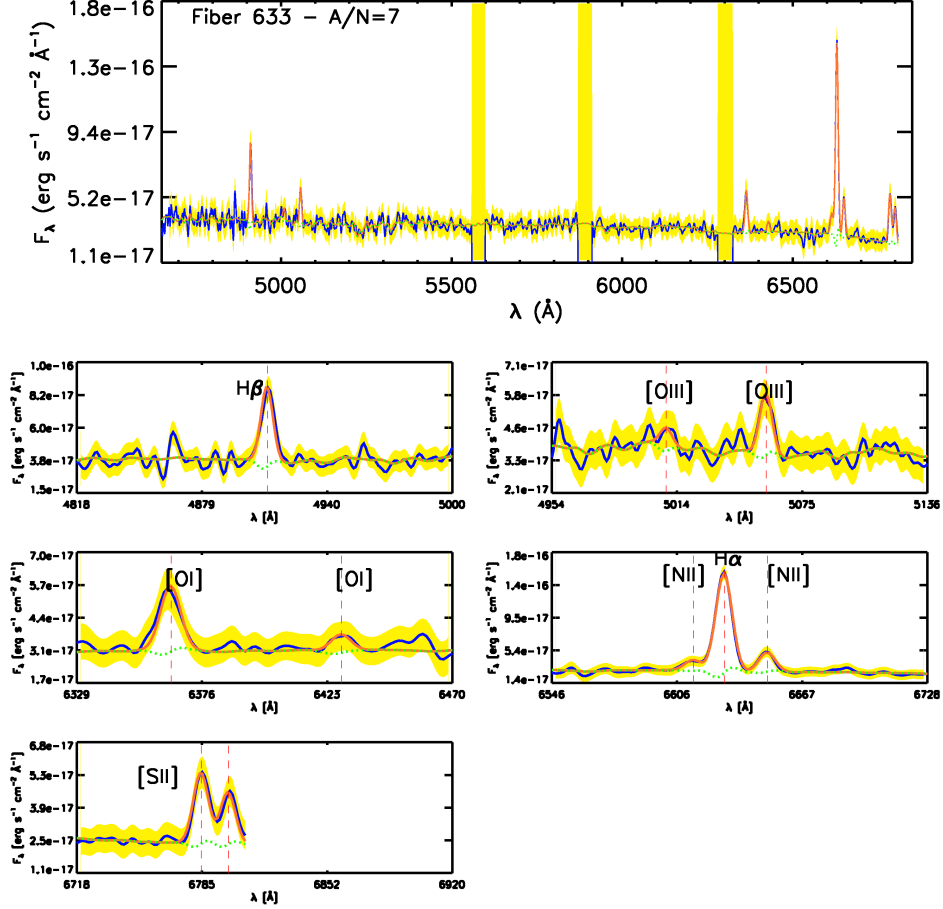


Figure 4.3 Spectrum of fiber 633 with a low $A/N = 7$ in the Arp 299 RSS file. The observed spectrum and 1σ uncertainties are shown in blue and the yellow envelope, respectively. The best fit stellar plus emission line spectrum is shown by the orange solid line and the dotted green line shows the stellar component of the fit without the emission lines. The vertical yellow bands are masked regions around sky line residuals.

profile for 100 realizations. To obtain our emission line flux errors, we compute the standard deviation of Gaussian distribution for the 100 simulated emission line fluxes.

4.4.2 Molecular Gas Surface Density Measurements

We derive molecular hydrogen (H_2) gas surface densities from the maps of CO $J = 2 \rightarrow 1$ and $J = 3 \rightarrow 2$, made with the SMA and corrected for short spacings with data from the JCMT (Sliwa et al. 2012) (Section 4.3.2.1).

These integrated intensities are first put on the scale of the integrated intensity of the $J = 1 \rightarrow 0$ line ($I(\text{CO})$) in K km s^{-1} . by assuming a constant ratio $R_{ij} = \text{CO}(J = i \rightarrow i - 1) / \text{CO}(J = j \rightarrow j - 1)$. Sliwa et al. (2012) find the following average values over their maps: $R_{21} = 1.4 \pm 0.08$, and $R_{31} = 0.95 \pm 0.09$.

The mass surface density is then

$$\Sigma_{\text{H}_2} = \alpha_{\text{CO}} \times R_{ij} \times \left(\frac{I(\text{CO})}{\text{K km s}^{-1}} \right) (M_{\odot} \text{ pc}^{-2}) \quad (4.2)$$

where α_{CO} is a conversion factor to surface density from the integrated intensity of CO $J = 1 \rightarrow 0$. For local clouds in the Milky Way, $\alpha_{\text{CO}} = 3.6 M_{\odot} \text{ pc}^{-2} (\text{K km s}^{-1})^{-1}$, but centers of galaxies, including the Milky Way, have evidence for values lower by factors of 3 to 10. Based on LVG models of their CO and ^{13}CO data, Sliwa et al. (2012) find a best match for $\alpha_{\text{CO}} = 0.4 \pm 0.3 M_{\odot} \text{ pc}^{-2} (\text{K km s}^{-1})^{-1}$. This value is consistent with the values of

$\alpha_{\text{CO}} = 0.35 - 0.42 \text{ M}_{\odot} \text{ pc}^{-2} (\text{K km s}^{-1})^{-1}$ found by Papadopoulos et al. (2012) for Arp 299, using LVG models of single-dish data including higher J lines of CO and lines of HCN. Since the resulting molecular mass ($1-1.2 \times 10^9 \text{ M}_{\odot}$) using this range of α_{CO} values would imply a star formation rate per unit gas mass above the usual maximum value, Papadopoulos et al. (2012) suggest that higher values of α_{CO} remain possible if most of the gas is in dense gas structures that are forming stars with maximum efficiency.

We will adopt the value of $\alpha_{\text{CO}} = 0.40 \pm 0.3 \text{ M}_{\odot} \text{ pc}^{-2} (\text{K km s}^{-1})^{-1}$. However we consider the possibility of higher values in Section 4.8.6.1. An additional factor of 1.37 to include helium was applied to our gas surface density measurements resulting in $\Sigma_{\text{Mol}} = 1.37 \Sigma_{\text{H}_2}$. As discussed by Kennicutt & Evans (2012) these simple conversion factors can hide a great deal of uncertainty and variability from place to place in a galaxy.

We also consider dense gas tracers, in particular, the $J = 1 \rightarrow 0$ transitions of $\text{HCO}^+(1-0)$ and $\text{HCN}(1-0)$. These transitions have critical densities that are roughly 100-300 times larger than those of CO for $T_K = 100 \text{ K}$. The critical density (e.g., $2.7 \times 10^6 \text{ cm}^{-3}$ for HCN $J = 1 \rightarrow 0$ at $T_K = 100 \text{ K}$) will greatly overestimate the actual density. For example, to produce a radiation temperature for HCN $J = 1 \rightarrow 0$ of 1 K at $T_K = 100 \text{ K}$ in a resolved region with typical column density, an effective density (for definition and examples, see Evans 1999; Reiter et al. 2011) of $6.0 \times 10^3 \text{ cm}^{-3}$ will suffice. However, the same argument applies to CO, with the result that the ratio of effective densities is also 300 to 1000.

Dense molecular gas surface densities were calculated using the relation:

$$\Sigma_{\text{Dense}} = \alpha_{\text{Dense}} \left(\frac{I(\text{Dense})}{\text{K km s}^{-1}} \right) (M_{\odot} \text{ pc}^{-2}) \quad (4.3)$$

where $I(\text{Dense})$ is the integrated intensity of a tracer of denser gas and α_{Dense} is a conversion factor parallel to α_{CO} . From a study of dense clumps in the Milky Way, Wu et al. (2010) found

$$\log(L_{\text{HCN}(1-0)}) = 1.04 \times \log(M_{\text{Vir}}(R_{\text{HCN}(1-0)})) - 1.35, \quad (4.4)$$

where $L_{\text{HCN}(1-0)}$ is the HCN(1–0) line luminosity and M_{Vir} is the virial mass inside the radial distribution. This relation would suggest a value of $\alpha_{\text{Dense}} \sim 20 M_{\odot} \text{ pc}^{-2} (\text{K km s}^{-1})^{-1}$. A commonly used value for extragalactic studies is $\alpha_{\text{Dense}} = 10 M_{\odot} \text{ pc}^{-2} (\text{K km s}^{-1})^{-1}$ (Gao & Solomon 2004b; García-Burillo et al. 2012). These simple conversions are subject to the same caveats that apply to α_{CO} , as discussed in detail by Papadopoulos et al. (2012) and García-Burillo et al. (2012).

Observations by Imanishi & Nakanishi (2006) with a $4''.2$ by $3''.8$ beam, using the Nobeyama Millimeter Array show strong HCN and HCO^+ emission toward component A, and weaker emission by both toward component C, but only rather weak HCO^+ emission toward component B1. While Graciá-Carpio et al. (2006) have argued that X-rays from AGN enhance the HCN emission, Imanishi & Nakanishi (2006) show that all the HCN/ HCO^+ ratios in Arp 299, even those toward the AGN in component B, are consistent with

starburst ratios, suggesting that the large quantity of dense gas may mitigate any effects from X-rays.

From the maps in Sliwa et al. (2012) and Imanishi & Nakanishi (2006), kindly supplied by those authors, we computed line luminosities and mean line intensities in circular apertures of $4''.235$ diameter (corresponding to 0.9 kpc) around components A, B1, C and C'. If we use $\alpha_{\text{Dense}} = 10 \text{ M}_{\odot} \text{ pc}^{-2}/(\text{K km s}^{-1})$ for both HCN and HCO^+ emission, the resulting values, $M_{\text{Dense}} = 3.7 \times 10^8 \text{ M}_{\odot}$ for HCN and $4.6 \times 10^8 \text{ M}_{\odot}$ for HCO^+ in component A, exceed the total molecular mass from CO of $3 - 3.6 \times 10^8 \text{ M}_{\odot}$, indicating that α_{Dense} is lower for the same kind of reasons that α_{CO} appears to be lower. Alternatively, α_{CO} may be higher than we assumed, which would allow a higher value of α_{Dense} .

We adopt values of $\alpha_{\text{CO}} = 0.4 \pm 0.3$, with a correction of 1.37 for He, and $\alpha_{\text{Dense}} = 5 \pm 2.5$ (assuming a 50% error in α_{Dense}) for further analysis. As a result, the mean mass surface densities in a $4''.235$ diameter aperture centered on region A are Σ_{Mol} of 460 and 560 $\text{M}_{\odot} \text{ pc}^{-2}$ for CO $J = 2 \rightarrow 1$ and $J = 3 \rightarrow 2$, respectively, and Σ_{Dense} of 289 and 358 $\text{M}_{\odot} \text{ pc}^{-2}$ for HCN $J = 1 \rightarrow 0$ and HCO^+ , respectively (Table 4.2). Masses and surface densities for the other regions are lower, with Σ_{Mol} lower by factors of 3-4. HCN is only clearly detected for region A; however all three components show clear detections in maps with higher sensitivity (Casoli et al. 1999).

Table 4.2. Star formation and Gas Surface Densities in Regions A, B1, C, and C'

Region Name (1)	Σ [H α] (2)	Σ [24 μ m] (3)	Σ [H α +24 μ m] (4)	Σ [Pa α] (5)	Σ_{Mol} [CO(2-1)] (6)	Σ_{Mol} [CO(3-2)] (7)	Σ_{Dense} [HCN(1-0)] (8)	Σ_{Dense} [HCO $^+$ (1-0)] (9)
4''.235 apertures^a								
A	1.66 \pm 0.003	-	-	3.79 \pm 3.6	460.8 \pm 346	560.7 \pm 423	289.0 \pm 147	357.9 \pm 183
B1	1.56 \pm 0.003	-	-	2.16 \pm 2.6	170.8 \pm 128	209.7 \pm 158	<11.2 \pm 5	122.9 \pm 62
C	2.65 \pm 0.003	-	-	3.90 ^b \pm 3.5	126.0 \pm 94	100.0 \pm 75	<21.0 \pm 10	107.6 \pm 54
C'	1.34 \pm 0.002	-	-	-	110.3 \pm 82	118.6 \pm 89	<32.5 \pm 16	83.6 \pm 42
6'' apertures								
A	0.68 \pm 0.001	2.6 \pm 0.10	3.0 \pm 0.06	2.42 \pm 2.0	303.6 \pm 228	347.3 \pm 262	213.5 \pm 109	275.6 \pm 143
B1	0.60 \pm 0.001	4.2 \pm 0.12	5.0 \pm 0.07	1.56 \pm 1.5	113.0 \pm 84	132.7 \pm 100	<9.1 \pm 4	93.6 \pm 47
C	1.00 \pm 0.001	2.9 \pm 0.10	3.6 \pm 0.06	2.95 \pm 2.3	92.4 \pm 69	66.9 \pm 50	<18.1 \pm 9	94.9 \pm 48
C'	0.62 \pm 0.001	2.3 \pm 0.09	2.7 \pm 0.06	-	86.3 \pm 64	93.8 \pm 70	<28.6 \pm 14	83.1 \pm 42

Note. — (a) Measurements on fiber size scales are restricted to only the H α and Pa α map due to the limitation placed by the 24 μ m PSF; (b) Pa α SFR measured for the C-C' complex at the Pa α peak; (1) Region name using source coordinates from Neff et al. (2004) their Table 3; (2)–(5): SFR surface densities in units of $M_{\odot} \text{ yr}^{-1} \text{ kpc}^{-2}$; (3)–(8): Σ_{Mol} or Σ_{Dense} gas surface densities in units of $M_{\odot} \text{ pc}^{-2}$ using values of $\alpha_{\text{CO}}=0.4$ and $\alpha_{\text{Dense}}=5 M_{\odot} \text{ pc}^{-2} (\text{K km s}^{-1})^{-1}$, respectively. The 4''.235 apertures can only be used to measure Pa α SFRs reliably as the 6'' apertures lie outside of the FoV of the Pa α images. See Sections 4.4.2 and 4.6.

Since the molecular gas maps only reliably cover the central regions of Arp 299 with significant $\gtrsim 3\sigma$ detections, we use the neutral hydrogen (HI) map of Arp 299 from Hibbard & Yun (1999) (Section 4.3.3) to measure atomic hydrogen gas surface densities outside the nuclear regions. Σ_{HI} is calculated from the integrated HI brightness temperature including a factor of 1.37 for helium using the relation:

$$\Sigma_{\text{HI}} = 1.99 \times 10^{-2} \left(\frac{I(\text{HI})}{\text{K km s}^{-1}} \right) (M_{\odot} \text{ pc}^{-2}) \quad (4.5)$$

The HI distribution is likely associated with the disk of IC 694 as the HI (Hibbard & Yun (1999), their Figure 3) and $\text{H}\alpha$ kinematics from our IFU data (Figures 4.4 and 4.5) are consistent. However, there is a disassociated peak in $\text{H}\alpha$ velocity near the HI peak in the southeast. The central region of Arp 299 is seen in HI absorption against all the nuclear continuum sources, A, B1, C, and C' (Baan & Haschick 1990) with an estimated integrated $\Sigma_{\text{HI}} \sim 8\text{--}16 M_{\odot} \text{ pc}^{-2}$ (Hibbard & Yun 1999). The HI absorption is found to have both a broad and narrow component at the systemic velocities of IC 694 and NGC 3690, respectively and Baan & Haschick (1990) conclude that the absorbed HI originates from the outer disks of IC 694 and NGC 3690. Since this material is not associated with the nuclear regions where we have CO, HCN, and HCO^+ coverage, we do not include it in our analysis.

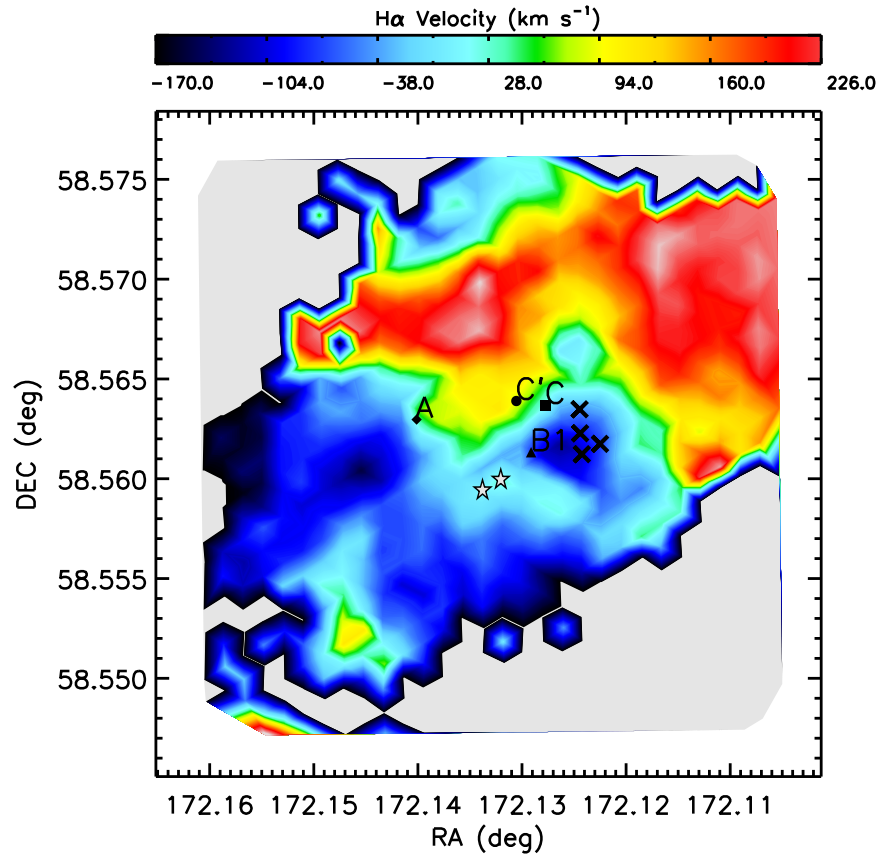


Figure 4.4 H α ionized gas velocity field. AGN contaminated regions are marked with black cross (X-ray) and stars (IFU).

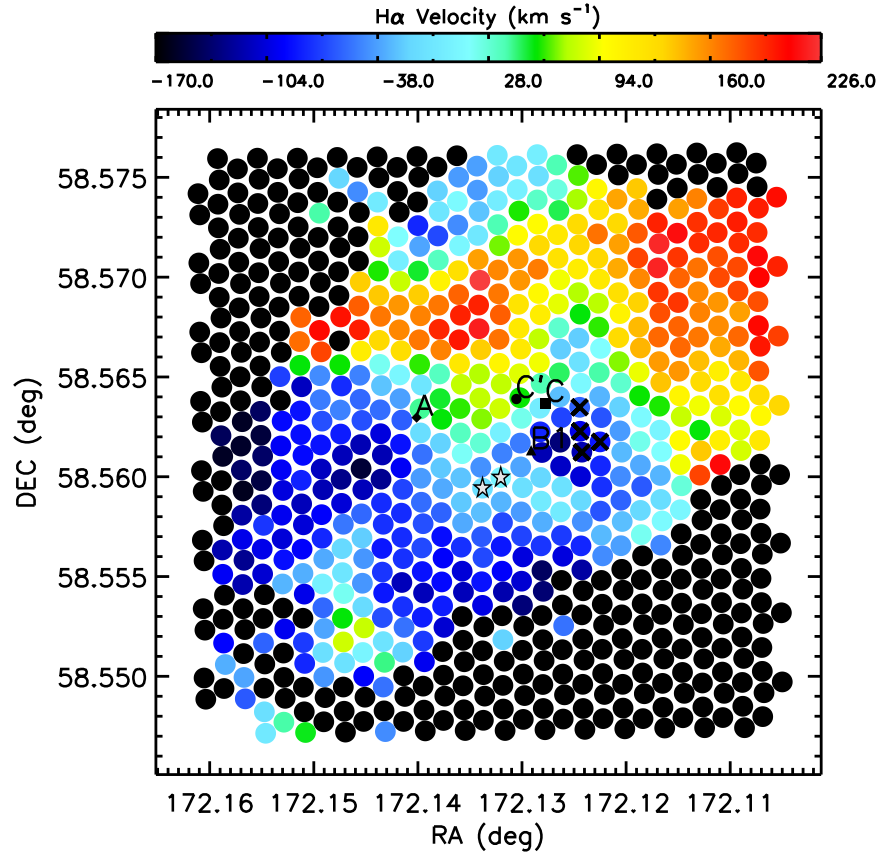


Figure 4.5 H α ionized gas velocity field. AGN contaminated regions are marked with black cross (X-ray) and stars (IFU) .

4.5 Extinction

The observed line flux ratio of two lines (e.g., H α and H β) can be used to determine the foreground extinction that the lines suffer if we know the intrinsic ratio of those lines $(F_{\text{H}\alpha}/F_{\text{H}\beta})_{\text{int}}$ and the ratio of total to selective extinction for those lines, $R_{\text{H}\alpha} = A_{\text{H}\alpha}/E(\beta - \alpha) = \kappa(\text{H}\alpha)/[\kappa(\text{H}\alpha) - \kappa(\text{H}\beta)]$, where $\kappa(\text{H}\alpha)$ is the opacity at the wavelength of H α .

$$\begin{aligned}
 A_{\text{H}\alpha} &= E(\beta - \alpha) R_{\text{H}\alpha} \\
 &= -2.5 \log \left[\left(\frac{F_{\text{H}\alpha}}{F_{\text{H}\beta}} \right)_{\text{obs}} \times \left(\frac{F_{\text{H}\alpha}}{F_{\text{H}\beta}} \right)_{\text{int}}^{-1} \right] \times \\
 &\quad \left(\frac{\kappa(\text{H}\alpha)}{\kappa(\text{H}\alpha) - \kappa(\text{H}\beta)} \right) \tag{4.6}
 \end{aligned}$$

A similar equation applies for the ratio of Pa α to H α , with $R_{\text{Pa}\alpha} = \kappa(\text{Pa}\alpha)/[\kappa(\text{Pa}\alpha) - \kappa(\text{H}\alpha)]$.

Since the nebular conditions in starburst galaxies are well constrained to have electron densities of $n_e \sim 5 \times 10^2 - 5 \times 10^4 \text{ cm}^{-3}$ and low temperatures, $T_e \sim 5 \times 10^3 \text{ K}$ (Roy et al. 2008 and references therein), the range of case B recombination line intensities is small. We adopt intrinsic H α /H β and H α /Pa α flux ratios of 3.00 and 7.58, respectively for a temperature of $5 \times 10^3 \text{ K}$ and a density of 10^4 cm^{-3} from Osterbrock & Ferland (2006).

Galactic extinction laws (Draine 2003) vary with density, and R_V increases from 3.1 in the diffuse interstellar medium to something similar to $R_V = 5.5$ in molecular clouds. Because the overall extinction is high in Arp

299, we apply both extinction laws to see how much difference they make. Using values of κ from the online tables⁴, we find $R_{\text{H}\alpha} = 1.997$ for $R_V = 3.1$ and $R_{\text{H}\alpha} = 2.841$ for $R_V = 5.5$. For $\text{Pa}\alpha$, $R_{\text{Pa}\alpha} = 0.236$ for $R_V = 3.1$ and $R_{\text{Pa}\alpha} = 0.212$ for $R_V = 5.5$.

Over the smaller ($19''.5$ by $19''.5$) region with $\text{Pa}\alpha$ data, we can compute extinctions from comparing $\text{Pa}\alpha$ to $\text{H}\alpha$, using the data from Alonso-Herrero et al. (2000) described in Section 4.3.3.2. We linearly interpolate the $\text{H}\alpha$ IFU data on to a grid with a pixel scale of $0.5''$ and we convolve the higher resolution NICMOS image to match the fiber sized Gaussian FWHM and use fiber sized apertures diameter of $4''.235$ (0.9 kpc) to measure the line fluxes from our $\text{H}\alpha$ map and the $\text{Pa}\alpha$ image.

In Figures 4.6 and 4.7, we show the $\text{H}\alpha$ flux after extinction correction using the Balmer decrement versus extinction-corrected $\text{Pa}\alpha$ flux, using the $\text{H}\alpha/\text{Pa}\alpha$ line ratio, and a histogram of the ratios of the extinction-corrected $\text{H}\alpha$ fluxes and $\text{Pa}\alpha$ fluxes. We also show $\text{Pa}\alpha$ contours (yellow) overlaid on our $\text{H}\alpha$ IFU map (red) in Figure 4.1. The black dashed line indicates the intrinsic $\text{H}\alpha/\text{Pa}\alpha$ line ratio of 7.58 from case B recombination theory for a typical starburst galaxy as discussed above. Values for the four densest concentrations of star formation, A, B1, C, and C' are used as test cases. Since the $\text{Pa}\alpha$ image could not be registered properly (Alonso-Herrero et al. 2000), we choose apertures centered on the $\text{Pa}\alpha$ peaks of A, B1, and C (Figure 4.1). We could

⁴Available at <http://www.astro.princeton.edu/~draine/dust/dust.html>

not determine the Pa α peak reliably to C', so we do not include a measurement of that region. Correcting for extinction using $R_V = 5.5$ works substantially better, yielding a mean ratio of 3.8 for extinction corrected H α to extinction corrected Pa α , while $R_V = 3.1$ gives a mean ratio of 2.7. These values are factors of ~ 2 and 3 below the intrinsic H α /Pa α line ratio for R_V of 5.5 and 3.1, respectively. However, even with $R_V = 5.5$, in three dense regions of star formation lie well below the expected ratio, indicating that neither the H α or Pa α line reliably trace all of the star formation.

We can compare the extinctions from the recombination lines to other estimates. For convenience, we refer extinctions in the V-band. For $R_V = 3.1$, $A_V/A_{H\alpha} = 1.552$ versus 1.94 for $R_V = 5.5$. For the nuclear regions A, B1, C, and C' using the Balmer decrement and $R_V = 5.5$, A_V is 1.3, 1.2, 0.78, 0.66 mag and using the H α to Pa α line ratio for A, B1, and C, A_V is 2.3, 1.6, and 1.4 mag. Using the gas surface densities from Section 4.4.2, and the Draine (2003) $R_V = 5.5$ extinction law, we would predict a total extinction in the visible for the four regions of $A_V = 29, 11, 7.9$, and 6.9 mag for A, B1, C, and C', respectively. Figures 4.8 and 4.9 show the spatial distribution and histogram of A_V from the Balmer decrement fiber measurements. Figure 4.10 shows the fiber to fiber extinction corrected H α map using the Draine (2003) $R_V = 5.5$ extinction law. We correct all of our lines for extinction using the Balmer decrement and an $R_V = 5.5$ extinction law.

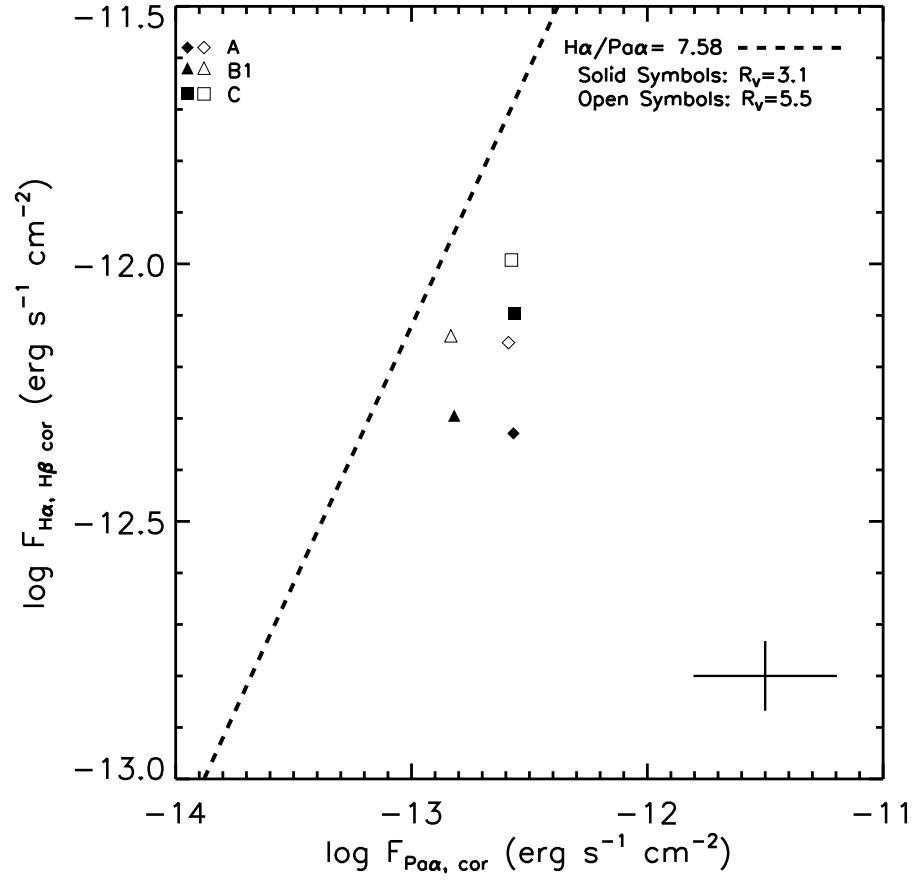


Figure 4.6 Extinction corrected H α versus P $\alpha\alpha$ fluxes measured in 6'' size apertures in the nuclear regions in Arp 299.

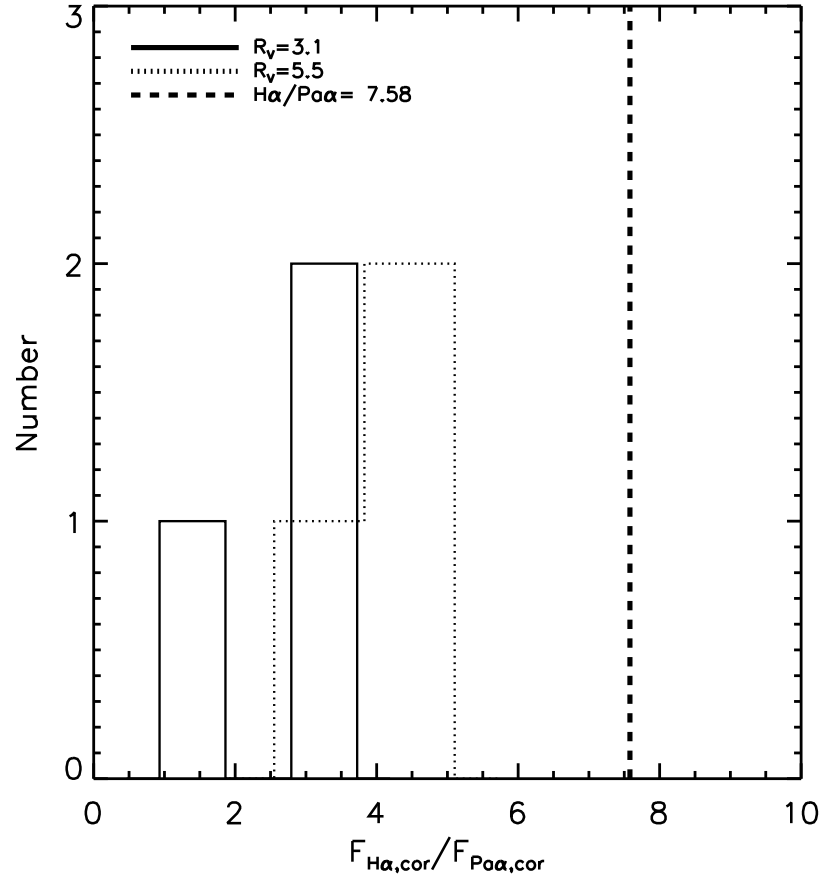


Figure 4.7 Histogram of the extinction corrected H α / Pa α flux ratio. The dashed line indicates the intrinsic H α /Pa α line ratio of 7.58 from case B recombination line theory.

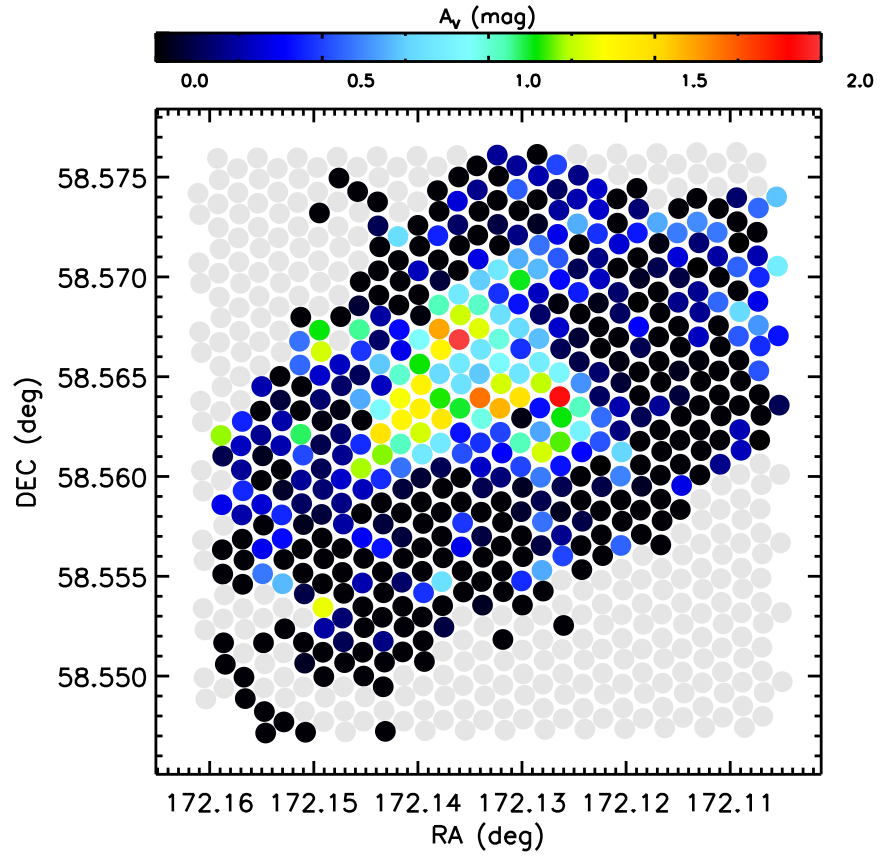


Figure 4.8 Visual extinction map (A_V) from the Balmer decrement ($H\beta/H\alpha$) line ratio in IFU fiber sized regions assuming a foreground dust screen model, and a mean interstellar extinction law from Draine (2003).

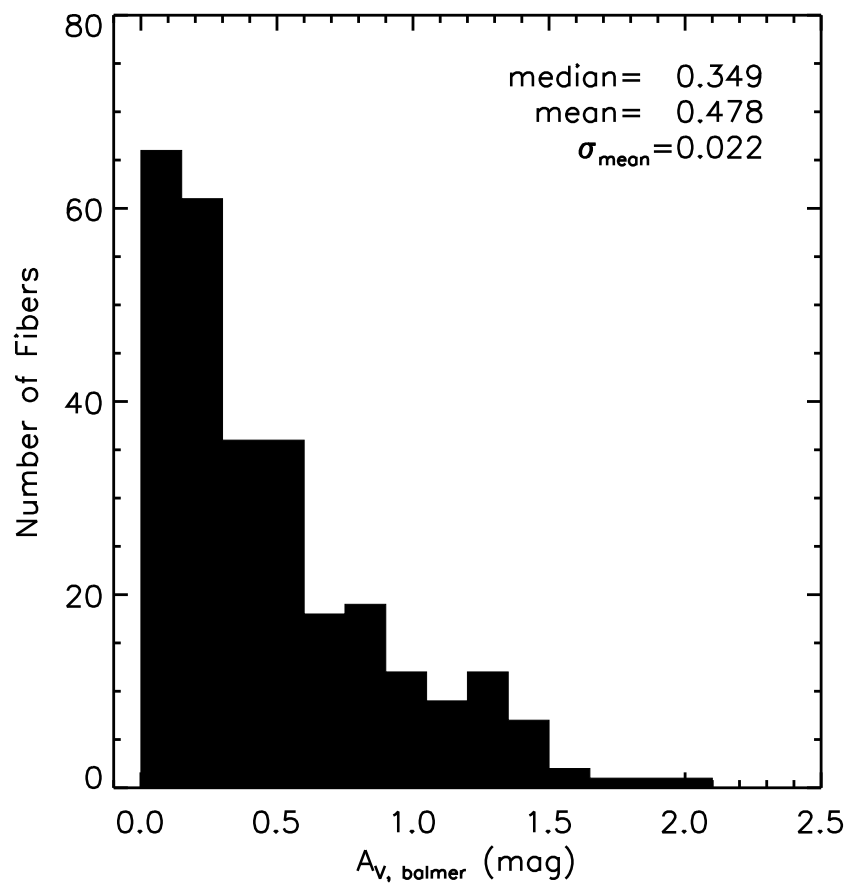


Figure 4.9 Visual extinctions for IFU fiber sized regions with a $S/N > 5$ from the Balmer decrement ($H\beta/H\alpha$) line ratio, a foreground dust screen model, and a Galactic extinction law from Draine (2003).

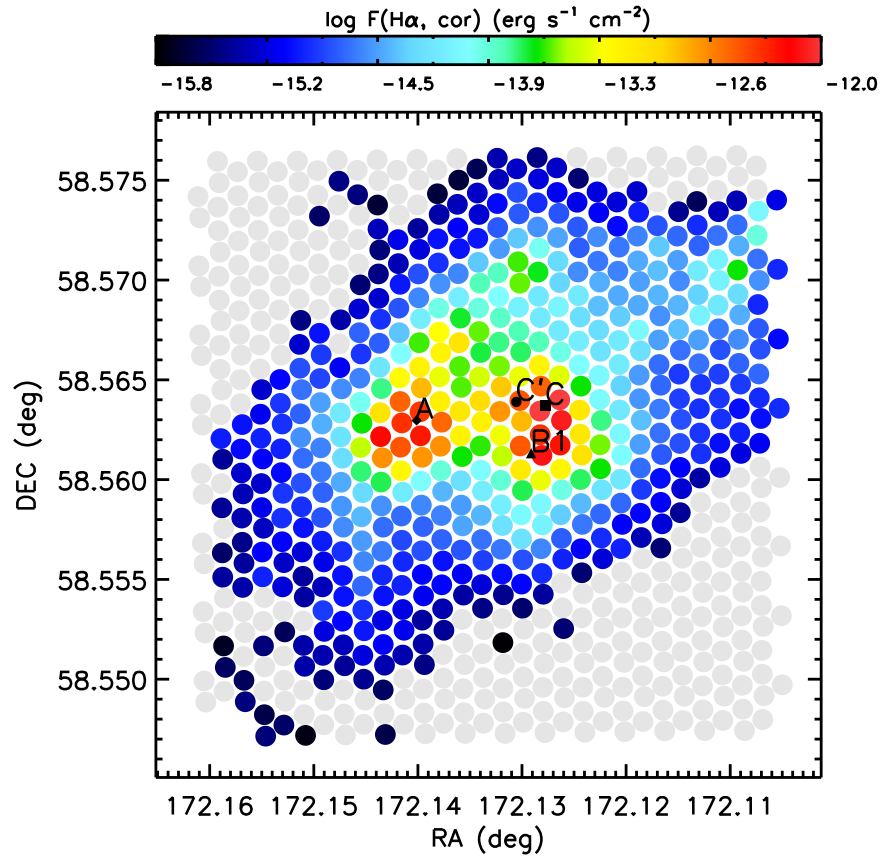


Figure 4.10 Extinction corrected fiber to fiber $\text{H}\alpha$ map of Arp 299 with the locations of nuclear regions A, B1, C, and C' indicated.

4.6 Star Formation Rates and Surface Density Measurements

We use star formation calibrations from Murphy et al. (2011) to derive SFRs with a consistent Kroupa (Kroupa 2001) IMF. The $H\alpha$ based SFR ($SFR_{[H\alpha]}$) is calculated using the extinction corrected $H\alpha$ line flux from Section 4.5 by the following equation:

$$SFR [H\alpha] (M_{\odot} \text{ yr}^{-1}) = 5.37 \times 10^{-42} L_{H\alpha, \text{cor}} (\text{erg s}^{-1}). \quad (4.7)$$

Assuming an intrinsic $H\alpha/Pa\alpha$ line ratio of 7.58, we convert the $SFR_{[H\alpha]}$ from Murphy et al. (2011) into a $Pa\alpha$ SFR ($SFR_{[Pa\alpha]}$) by the following relation:

$$SFR [Pa\alpha] (M_{\odot} \text{ yr}^{-1}) = 4.07 \times 10^{-41} L_{Pa\alpha, \text{cor}} (\text{erg s}^{-1}). \quad (4.8)$$

We compute the $24\mu\text{m}$ based SFR using the formula:

$$SFR [24\mu\text{m}] (M_{\odot} \text{ yr}^{-1}) = 5.58 \times 10^{-36} [\nu L_{\nu}, 24\mu\text{m}]^{0.826} (\text{erg s}^{-1}). \quad (4.9)$$

Since we find $H\alpha$ and $Pa\alpha$ do not reliably trace all the star formation (Section 4.5), we also use the observed $H\alpha$ luminosity extinction corrected by the $24\mu\text{m}$ luminosity to derive the $SFR_{[H\alpha+24\mu\text{m}]}$, accounting for the obscured and unobscured star formation using the equation:

$$\text{SFR} [\text{H}\alpha + 24\mu\text{m}] (M_{\odot} \text{ yr}^{-1}) = 5.37 \times 10^{-42} [\text{L}_{\text{H}\alpha, \text{obs}} + 0.031 \text{L}_{24\mu\text{m}}] (\text{ergs}^{-1}). \quad (4.10)$$

We calculate the SFR surface density of each SFR tracer using the relation:

$$\Sigma_{\text{SFR}} [\text{tracer}] = \frac{\text{SFR} [\text{tracer}]}{A_{\text{kpc}}} (M_{\odot} \text{ kpc}^{-2}), \quad (4.11)$$

where tracer is either $\text{H}\alpha$, $\text{Pa}\alpha$, or $\text{H}\alpha + 24\mu\text{m}$ and A_{kpc} is the area of the measurement aperture in kpc. We measure the SFR surface densities using $\text{SFR}_{[\text{H}\alpha]}$ and $\text{SFR}_{[\text{Pa}\alpha]}$ using apertures on fiber sized scales of $4''.235$ (0.9 kpc). For the $24\mu\text{m}$ SFR prescriptions we are limited to the FWHM of the $24\mu\text{m}$ PSF which is $6''$ (1.3 kpc) and thus we derive $\text{SFR}_{[24\mu\text{m}]}$ and $\text{SFR}_{[\text{H}\alpha + 24\mu\text{m}]}$ surface densities on this scale. We show measurements for the nuclear star forming regions of Arp 299 in Table 4.2 and discuss the results in Section 4.8.

4.7 Active Galactic Nuclei Activity in Arp 299

Since our goal is to investigate the star formation activity in Arp 299, we must first disentangle any contribution from an AGN component in the nuclear regions. The difficult aspect of separating a starburst region from an AGN in a LIRG is that the concentration of gas and dust fueling the central energy source typically obscure the AGN. Methods to investigate the presence of a

buried AGN typically require 1) hard X-ray band ($E > 2$ keV) measurements where the AGN spectral signature of Fe-K α lines appear and the AGN emits stronger at this wavelength than a starburst, 2) millimeter interferometric observations that look for chemical signatures, and 3) infrared spectroscopy. We can however use our extinction corrected IFU optical emission line fluxes to explore Baldwin-Phillips-Terlevich (BPT) diagrams (Baldwin et al. 1981) and classify the dominant energy sources in IC 694 and NGC 3690 on a fiber-by-fiber basis and compare that to previous studies. The BPT diagnostic criteria are based on a theoretical maximum line ratio value for a starburst from a combination of stellar population synthesis and stellar photoionization models. AGN dominated regions that lie above the maximal starburst line are likely to be dominated by an AGN (Kewley et al. 2006).

Using the [OIII] /H β and [NII]/H α emission line fluxes, Coziol et al. (1998) showed that IC 694 can be classified as a pure starburst, while NGC 3690 showed properties that border starburst and liner classification. García-Marín et al. (2006) used integral field spectroscopy and separated IC 694 and NGC 3690 into nuclear components A and B, respectively, as well as an interface region C between the nuclei. They found that the nucleus B of NGC 3690 showed clear signs of an AGN with a mix of starburst and liner-like ionization surrounding the nucleus. Nucleus A in IC 694, however, was found to be starburst dominated and surrounded by liner-like ionization.

X-ray observations from the *BeppoSAX* satellite (Della Ceca et al. 2002) showed the presence of a highly obscured ($N_{\text{H}} \simeq 2.5 \times 10^{24} \text{cm}^{-2}$) AGN

in Arp 299, however the spatial location remained unresolved. Later *XMM-Newton* (Ballo et al. 2004) and high resolution *Chandra* (Zezas et al. 2003) observations showed the clear presence AGN in the nuclear region B1 of NGC 3690 and recovered positional coordinates. Evidence remains ambiguous, however, that the central power source in nuclear region of IC 694 is an AGN. Observations indicate the possibility of an obscured ($N_{\text{H}} \leq 10^{22} \text{cm}^{-2}$) low luminosity ($L_X \sim 10^{41} \text{ergs}^{-1}$) AGN surrounded by a strong nuclear starburst in IC 694, however the emission may be due to integrated emission from X-ray binaries combined with a thermal component.

Infrared imaging (Gallais et al. 2004 and references therein) and spectroscopy (Gallais et al. 2004; Imanishi & Nakanishi 2006), as well as interferometric observations (Imanishi & Nakanishi 2006) have been used to investigate the presence of a buried AGN in Arp 299. These studies find NGC 3690 nuclear region clearly harbor a dust enshrouded AGN, however no clear AGN signatures from the nuclear region of IC 694 was seen and evidence points to a pure nuclear starburst as the dominant energy source.

BPT diagnostic diagrams for extinction corrected line ratios in Arp 299 are shown in Figures 4.11-4.13. These diagrams show the relative strengths of emission lines to determine the nebular conditions, either photoionization dominated by star formation or photoionization dominated by a hard radiation field from an accretion disk of a central AGN. We select fibers based on the Kewley et al. (2001) extreme starburst criteria (red solid line and hashed diagonal line region) where AGN dominated fibers lie above that criteria and

starburst/HII region dominated fibers lie below. To make a S/N cut, we use the line amplitude-to-noise ratio ($A/N \geq 4$) as defined in Sarzi et al. (2006). We checked individual spectra by eye for the [OI] (6300Å) line which is red shifted near a bright sky line at 6363.78Å and for [SII]($\lambda 6717\text{Å} + \lambda 6731\text{Å}$), which lies near the edge of the VIRUS-P chip and in some fibers falls completely outside the chip. For the 121 fibers that contained both [SII] lines, we found a mean ratio of $[\text{SII}]\lambda 6731\text{Å} / [\text{SII}]\lambda 6717\text{Å}$ of 0.74 ± 0.09 and applied it to the 332 fibers that contained only the strongest [SII] (6717Å) line. The top panels in Figures 4.11-4.13 show the points selected from our criteria and the bottom panels show the position of fibers on flux map. The Kewley et al. (2006) Seyfert-LINER line is shown by the blue solid and dashed lines on the $[\text{OIII}] / \text{H}\beta$ versus $[\text{SII}] / \text{H}\alpha$ and $[\text{OIII}] / \text{H}\beta$ versus $[\text{OI}] / \text{H}\alpha$ BPT diagrams. The integrated line ratios for the whole system are shown as yellow stars. Points that lie above the Kewley et al. (2001) starburst criteria are shown as solid stars. The hard ($E > 2$ keV) *Chandra* X-ray centroid position for the confirmed AGN in NGC 3690 is marked by a thick cross in the right panels in Figures 4.11-4.13. Four fiber regions around this centroid that might be contaminated that lie within the hard X-ray region, a $6''$ radius of the X-ray centroid, are also indicated by crosses.

We find 164 extra nuclear regions that lie above the Kewley et al. (2001) starburst criteria in at least two of the the $[\text{OIII}] / \text{H}\beta$ versus $[\text{SII}] / \text{H}\alpha$ and $[\text{OIII}] / \text{H}\beta$ versus $[\text{OI}] / \text{H}\alpha$ BPT diagrams and those points are outlined with boxes in Figures 4.11-4.13. Four fibers that show clear Seyfert-like ionization in three

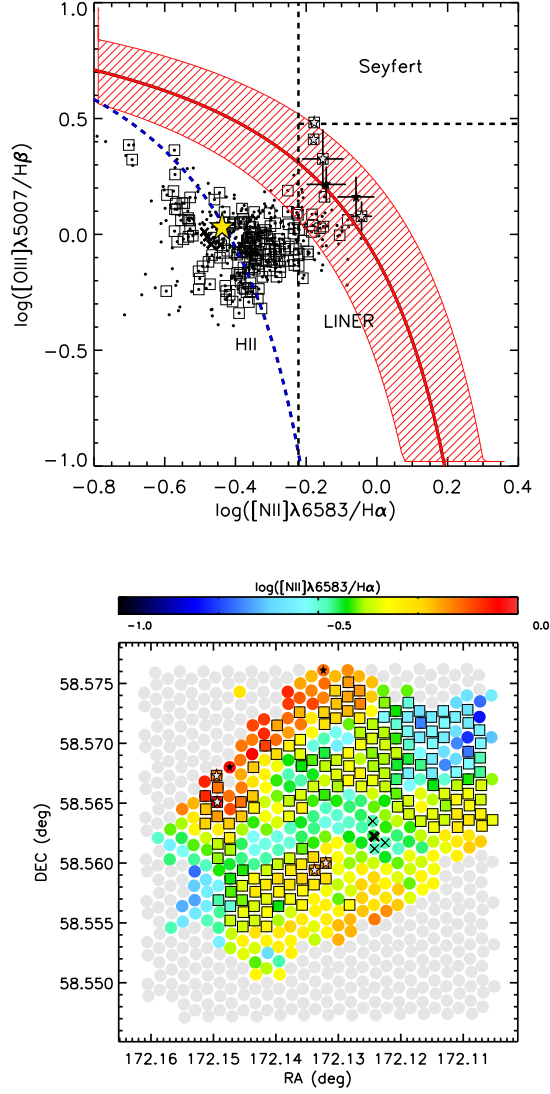


Figure 4.11 **Top:** BPT diagram showing Kewley et al. (2001) extreme starburst classification line (red solid line) and errors (red diagonal line region), the pure star formation classification line from Kauffmann et al. (2003) (blue solid line), and the Ho et al. (1997) classification schemes (black dashed lines). White star points indicated regions that were selected by all three BPT diagrams, boxed points indicate regions selected by two or more BPT diagrams, and crosses mark regions within a $6''$ radius of the X-ray selected AGN from (Ballo et al. 2004). The solid yellow star shows the integrated ratio for the system. **Bottom:** The AGN selected regions (star and boxed points) are overlaid on an fiber-by-fiber $[\text{NII}]/\text{H}\alpha$ flux map.

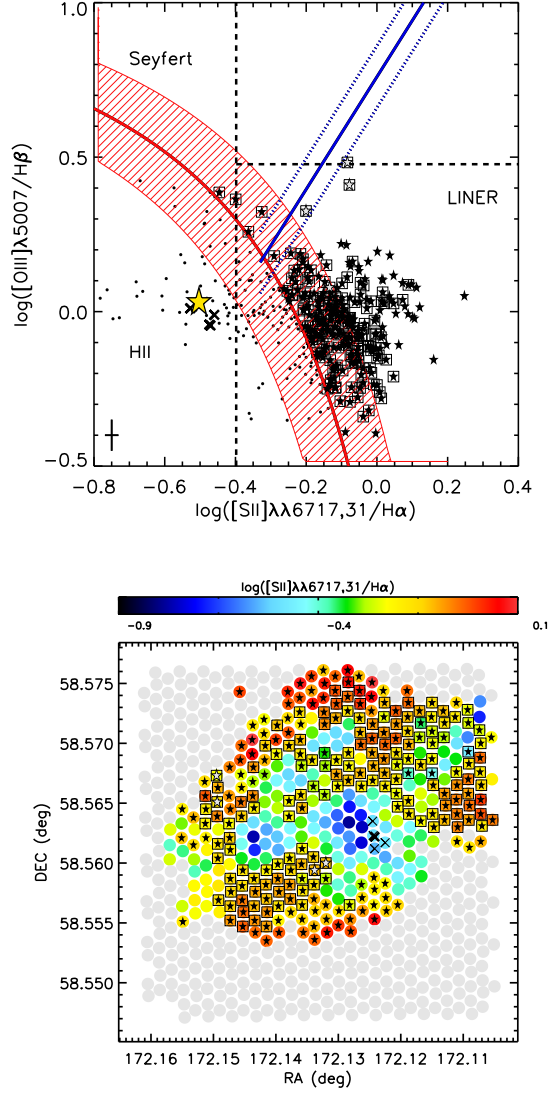


Figure 4.12 **Top:** BPT diagram showing Kewley et al. (2001) extreme starburst classification line (red solid line) and errors (red diagonal line region), the Kewley et al. (2006) Seyfert-LINER line (blue and solid diagonal lines), and the Ho et al. (1997) classification schemes (black dashed lines). White star points indicated regions that were selected by all three BPT diagrams, boxed points indicate regions selected by two or more BPT diagrams, and crosses mark regions within a $6''$ radius of the X-ray selected AGN from (Ballo et al. 2004). The solid yellow star shows the integrated ratio for the system. **Bottom:** The AGN selected regions (star and boxed points) are overlaid on an fiber-by-fiber $[\text{SII}]/\text{H}\alpha$ flux map.

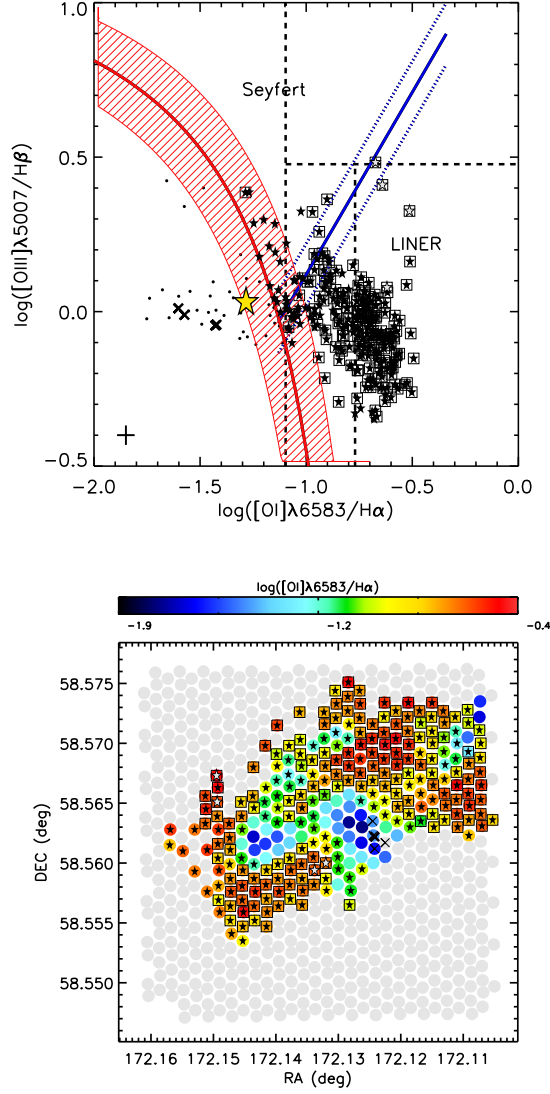


Figure 4.13 **Top:** BPT diagram showing Kewley et al. (2001) extreme starburst classification line (red solid line) and errors (red diagonal line region), the Kewley et al. (2006) Seyfert-LINER line (blue and solid diagonal lines), and the Ho et al. (1997) classification schemes (black dashed lines). White star points indicated regions that were selected by all three BPT diagrams, boxed points indicate regions selected by two or more BPT diagrams, and crosses mark regions within a $6''$ radius of the X-ray selected AGN from (Ballo et al. 2004). The solid yellow star shows the integrated ratio for the system. **Bottom:** The AGN selected regions (star and boxed points) are overlaid on an fiber-by-fiber $[\text{O I}]/\text{H}\alpha$ flux map.

BPT diagrams are shown as white stars. Two of these regions lie far from the nuclear regions have low $A/N \sim 4-10$ and low $S/N \sim 3-7$ as defined by the line flux over the error in line flux so low we discount these regions as AGN contaminated. The AGN selected fibers are denoted by stars in all three BPT diagrams and lie near, but on opposite sides of the X-ray centroid in NGC 3690 and are likely a signature of photoionization of the extranuclear interstellar gas by the central AGN or a shocked outflow from a starburst superwind (Heckman et al. 1999). A Seyfert-like ionization cone located below the nuclear region of NGC 3690 was first reported by García-Marín et al. (2006) using integral field spectroscopy, however their data did not cover the region of high ionization above the nucleus so they only saw high line fluxes below the nuclear region in NGC 3690. The other possibility is that the interstellar gas, especially the regions that aren't Seyfert-like, are being heated by photoionization by massive stars. Many regions that lie outside $>3\text{kpc}$ from the nuclear regions show a high $[\text{OI}]/\text{H}\alpha$ and $[\text{SII}]/\text{H}\alpha$ ratios which could also be explained by a large population of Wolf-Rayet (W-R) stars that are a signature of recent star formation. W-R stars have higher effective temperatures than OB stars and provide more hard energy photons for excitation of the interstellar gas. Another possibility are cooling shocks (Dopita & Sutherland 1995). These shocks would naturally form outside of the starburst nucleus due to supernova explosions that followed shortly after the starburst leading to a superwind blow out or shocked outflow of interstellar gas from the nuclear region. There is also an area of dense gas as traced by $\text{CO} J = 3 \rightarrow 2$ (Figure 4.14) as well as a region

of higher metallicities (Section 4.8.6.1) that trace a potential outflow from a starburst superwind. Heckman et al. (1999) used a combination of X-ray data and long slit spectra that intercepted the nuclear regions B1 and C concluded that Arp 299 had enough internal energy to heat up the ISM to significant temperature and outflow velocity such that gas may be able to escape from the system, making a superwind dominated system is highly plausible. We mark both regions within a $6''$ radius of the X-ray centroid (Zezas et al. 2003) as well as the 164 extranuclear regions that were selected by the AGN criteria in the BPT diagrams throughout the paper.

4.8 Results

4.8.1 Comparison of Global SFRs

We measure the system wide average or global SFRs for the Arp 299 merger in a contour aperture region that has a $A/N \geq 4$ in $H\alpha$ line flux as determined from our interpolated $H\alpha$ map. For the SFR comparisons, we use Murphy et al. (2011) calibrations that have a common (Kroupa (2001) IMF). These measurements are shown in Table 4.1 and an image showing all star formation tracers is shown in Figure 4.1. Comparing to the total SFR_{IR} of $76.6 \pm 4.6 M_{\odot} \text{ yr}^{-1}$ from IRAS, we are only recovering $\lesssim 1/4$ of the global SFR from the $H\alpha$ flux from our IFU data ($SFR_{[H\alpha]} = 18.9 \pm 0.7 M_{\odot} \text{ yr}^{-1}$), and $\lesssim 1/2$ of the total IR SFR from the saturated $24 \mu\text{m}$ image ($SFR_{[24\mu\text{m}]} = 43.6 \pm 6.3 M_{\odot} \text{ yr}^{-1}$). However, when we correct the observed $H\alpha$ luminosity for extinction using $24\mu\text{m}$ luminosity, we obtain a total $SFR_{[H\alpha+24\mu\text{m}]}$ of 89.8 ± 9.9

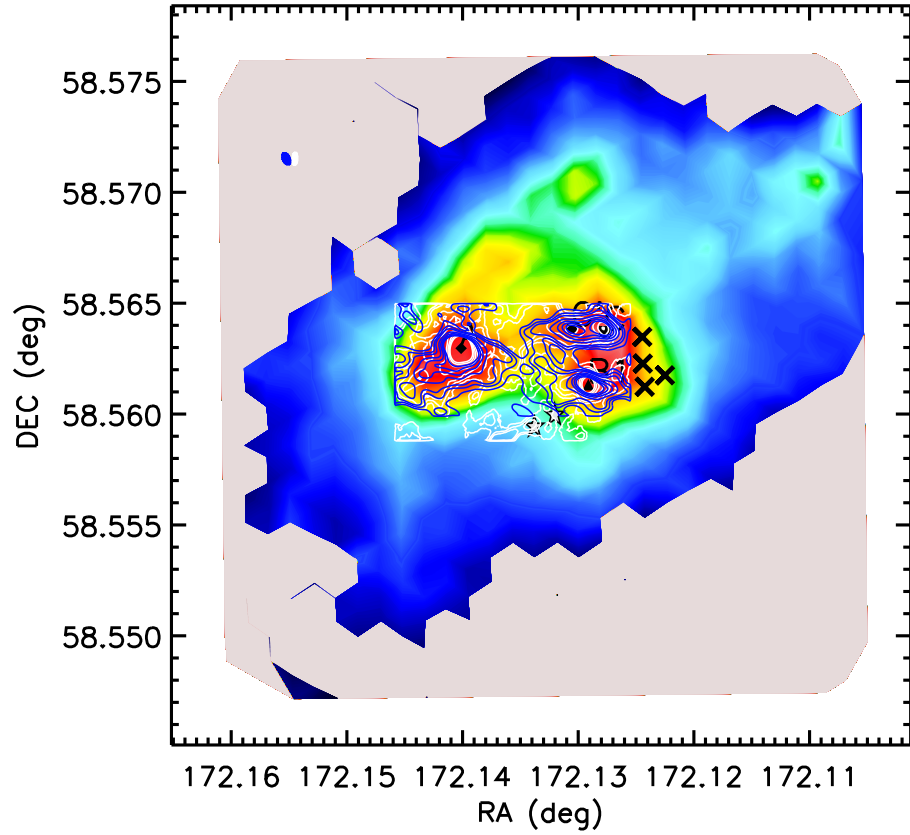


Figure 4.14 Interpolated H α flux map based on discrete values at each IFU fiber position overlaid with HI (red) contours and contours starting at 2σ above the noise level and increase intervals of 2σ ... H α flux map overlaid with COJ = $2 \rightarrow 1$ (blue) COJ = $3 \rightarrow 2$ (white) contours starting at 2σ above the noise level and increase... Map beam sizes are shown in the top left corner. AGN contaminated regions are marked with black cross (X-ray) and stars (IFU).

$M_{\odot} \text{ yr}^{-1}$ in agreement with the SFR from IRAS within the errors. Since the beam sizes of the IRAS 60 and $100\mu\text{m}$ (see Table 4.1) bands are $1.5' \times 4.75'$ and $3' \times 5'$, respectively, it fully covers the Arp 299 merger so there is little missing IR flux. The $\text{Pa}\alpha$ image only covers the nuclear regions so we can only estimate the $\text{SFR}_{[\text{Pa}\alpha]}$ to be $\gtrsim 13 \pm 3 M_{\odot} \text{ yr}^{-1}$, similar to the *total* $\text{H}\alpha$ flux over the whole system. A comparison of the $\text{SFR}_{[\text{Pa}\alpha]}$ to $\text{SFR}_{[\text{H}\alpha+24\mu\text{m}]}$ show the $\text{SFR}_{[\text{H}\alpha+24\mu\text{m}]}$ are a factor of $\gtrsim 2$ higher on average in $6''$ regions centered at the peak $\text{Pa}\alpha$ emission. This is due to the high extinction in both the $\text{Pa}\alpha$ and $\text{H}\alpha$ line fluxes. Since the total SFR_{IR} from IRAS is in agreement with the total $\text{SFR}_{[\text{H}\alpha+24\mu\text{m}]}$ within the errors, we use this SFR indicator for the rest of our analysis with the exception of the comparison to HI (Section 4.8.6).

4.8.2 Region-by-Region Comparison of SFRs

In order to directly compare our IFU data to the *Spitzer* $24 \mu\text{m}$ map, we convolve our interpolated $\text{H}\alpha$ map using a Gaussian kernel with a FWHM of the *Spitzer* $24\mu\text{m}$ $6''$ PSF then regrid onto the $2.45''$ plate scale of the $24 \mu\text{m}$ image. We measure our $\text{H}\alpha$ map and $24 \mu\text{m}$ image in only regions where the $\text{H}\alpha$ fiber flux has a $A/N \geq 4$ using apertures matched to the $6''$ (~ 1.3 kpc) $24\mu\text{m}$ image PSF. In Figure 4.15, we compare the SFR derived from the observed $\text{H}\alpha$ luminosity extinction corrected by the $24\mu\text{m}$ luminosity versus the Balmer decrement extinction corrected $\text{H}\alpha$ SFR. Regions determined to be contaminated by an AGN in NGC 3690 by either the X-ray or optical spectroscopy from our IFU fiber analysis are marked by open squares. We find

a linear relation that is offset by a factor of ~ 10 from a 1:1 correspondence between the two SFR tracers. This offset indicates that our extinction corrected $H\alpha$ flux is underestimating the total SFR in each region by at least a factor of ~ 10 on average compared to the observed $H\alpha$ flux corrected by the saturated $24\mu\text{m}$ SFR. While the average ratio of these two SFR tracers is very high, there are regions that are not as heavily extinguished where the Balmer decrement extinction corrections show an $H\alpha$ flux great enough to match the $24\mu\text{m}$ extinction corrected $H\alpha$ flux when both are converted to SFRs.

In order to understand where SFRs derived using $H\alpha$ might be reliable in a nearby merger, we show the distribution of the ratio of $\text{SFR}_{[H\alpha+24\mu\text{m}]} / \text{SFR}_{[H\alpha]}$ across the Arp 299 system in Figure 4.15 (bottom panel). We find a range of values for the ratio of $\text{SFR}_{[H\alpha+24\mu\text{m}]}$ to $\text{SFR}_{[H\alpha]}$ from 1 (linear, see Figure 4.15 top panel) to 60. This figure shows that dark blue regions near the C-C' complex, above both nuclei, and a region to the northwest (top right) where the $H\alpha$ flux is high enough to match the $24\mu\text{m}$ extinction corrected $H\alpha$ flux converted to a SFR. Most of these regions lie at low extinction (Figure 4.8), except for the region above both nuclei where there is a peak in the extinction map from the Balmer decrement. From this figure we show that $H\alpha$ flux likely traces the younger stellar population in regions that lie outside the nuclei in the north outer region of the Arp 299 merger.

We have measured $\Sigma_{\text{SFR } [H\alpha]}$, $\Sigma_{\text{SFR } [Pa\alpha]}$, $\Sigma_{\text{SFR } [24\mu\text{m}]}$, and $\Sigma_{\text{SFR } [H\alpha+24\mu\text{m}]}$ in both fiber ($4''.235$) and $6''$ scale regions of 0.9 and 1.3 kpc, respectively in nuclear regions A, B1, C and C' with the exception that we only measure at

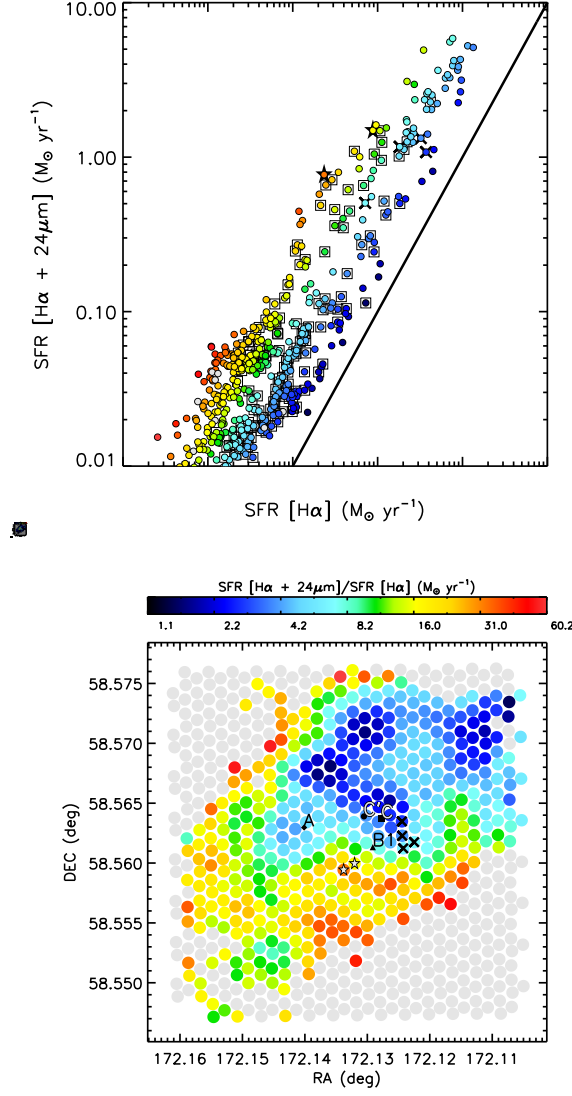


Figure 4.15 **Top:** Comparison of extinction corrected $H\alpha$ and $24\mu\text{m}$ SFRs measured on scales of $24\mu\text{m}$ resolution ($6''$). Potential AGN contaminated points are denoted by stars and open squares. The colors represent the ratio of $\text{SFR} [H\alpha + 24\mu\text{m}] / \text{SFR}[H\alpha]$ shown in the bottom panel. The dark blue points represent where there is a roughly linear relation between the $H\alpha + 24\mu\text{m}$ and $H\alpha$ based SFRs. The solid black line is a linear relation at a SFR of 0.01. **Bottom:** The ratio of $H\alpha + 24\mu\text{m}$ to extinction corrected $H\alpha$ SFRs measured on scales of $24\mu\text{m}$ resolution ($6''$). AGN contaminated regions are marked with black cross (X-ray) and stars (IFU).

the peak $\text{Pa}\alpha$ emission at the location of the C-C' region. Figure 4.16 shows the distribution of $\Sigma_{\text{SFR}} [\text{H}\alpha+24\mu\text{m}]$ on 1.3 kpc scales and Table 4.2 shows the measurements each tracer and region size. The nucleus of NGC 3690, B1, has the highest SFR surface density in all tracers using $24\mu\text{m}$ fluxes, which could mean there is contamination from the AGN in the region measured or the other regions have lower fluxes due to image saturation (Section 4.3.3.1). However, AGN contamination should not be the case since a measurement on either size scale lies outside of the X-ray emission peak (Section 4.7) and the potential IFU AGN contaminated regions. Measurements using $24\mu\text{m}$ fluxes ($\Sigma_{\text{SFR}} [\text{H}\alpha+24\mu\text{m}]$, $\Sigma_{\text{SFR}} [24\mu\text{m}]$) show that after region B1, the star forming complex region C has the highest SFR surface density followed by nucleus A and region C'. Region C has the highest $\Sigma_{\text{SFR}} [\text{H}\alpha]$, which is likely due to low extinction (Figure 4.8), in that region making $\text{H}\alpha$ a more reliable SFR tracer. The next highest $\Sigma_{\text{SFR}} [\text{H}\alpha]$ is seen in IC 694 nucleus (region A), followed by regions B1 and C'. Since nuclear region A is classified as pure starburst (Section 4.7), a low SFR surface density using recombination lines is likely due to a high level of extinction in $\text{H}\alpha$ and $\text{Pa}\alpha$ as discussed in Section 4.5.

The northwest region of this system shows evidence for star forming complex associated with and $\text{H}\alpha$ peak and the peak in the HI gas distribution in both the map from Hibbard & Yun (1999) and a higher resolution ($10''$) map from Stanford & Wood (1989). This region lies at low extinction (Figure 4.8) and contains a close association of stars visible in the *HST* F814W optical image (Figure 4.1). This association or cluster of stars could either be a tidal

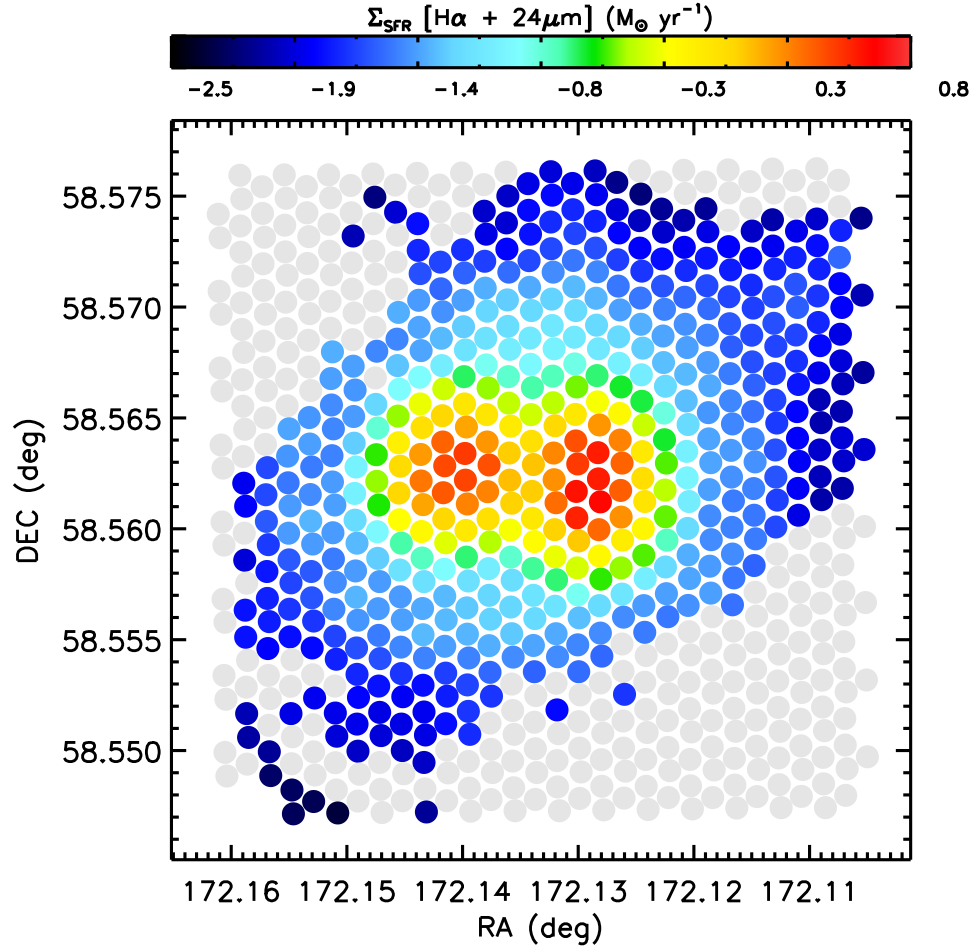


Figure 4.16 $\Sigma_{\text{SFR}} [\text{H}\alpha + 24\mu\text{m}]$ map where circles indicated 1.3 kpc scales and $\text{H}\alpha$ line fluxes have $A/N \geq 4$.

dwarf galaxy (if it is a bound structure) that is unresolved in the HI kinematics from Hibbard & Yun (1999) or is possibly a large (super?) star cluster in the disk of IC 694 or externally formed out of tidally stripped material. This feature has a higher redshifted H α velocity (Figure 4.4) which is slightly higher than the velocity seen in the HI tidal tail that extends linearly outward from this region. The H α derived SFR of this stellar cluster in an 11'' aperture is $0.029 \pm 0.001 \text{ M}_{\odot} \text{ yr}^{-1}$ and it has an HI gas surface density of $40.2 \pm 9 \text{ M}_{\odot} \text{ pc}^{-2}$.

4.8.3 SFR–Gas Surface Density Relation in Nuclear Regions

Measurements of the relations between SFRs and gas surface densities in starburst galaxies have been measured globally, most notably by Kennicutt (1998b), however little work has been done to explore this relation on smaller spatial scales comparable to the extensive work done by Bigiel et al. (2008) and others on non-interacting normal spiral and dwarf galaxies. In order to investigate this relation in the nuclear regions of the nearby Arp 299 merger, we use the SFR and gas surface densities from Sections 4.6 and 4.4.2 to look at the SFR–Gas surface density relation in the nuclear regions on 1.3 kpc (6'') size apertures. Figures 4.14 and 4.17 show the interpolated H α flux map with the CO $J = 2 \rightarrow 1$ (blue) and CO $J = 3 \rightarrow 2$ (white) and HCN $J = 1 \rightarrow 0$ (cyan) and HCO $^{+} J = 1 \rightarrow 0$ (white) contours overlaid, respectively. In Figure 4.18 shows the SFR–Mol gas relations for each nuclear region using molecular gas traced by CO $J = 2 \rightarrow 1$ (yellow points) and CO $J = 3 \rightarrow 2$ (orange points). We compare to SFR–gas relations on disk-averaged scales for spirals and star-

bursts using a combination of HI+CO gas (Kennicutt 1998b), using molecular gas as traced by CO only in high- z mergers (Daddi et al. 2010) and in 1 kpc regions in spirals and dwarf galaxies (Bigiel et al. 2011). The solid lines indicate the parameter space of the SFR-gas relation fit of Kennicutt (1998b) and the dashed lines are extrapolations. Another caveat is that each of these relations uses a different SFR tracer: $H\alpha$ (normal spirals) and IR (IR bright starbursts) (Kennicutt 1998b), $H\alpha$ and FUV+24 μ m (spirals), IR (starbursts/SMGs), and UV (BZKs/normal disks) (Daddi et al. 2010), and a combined *GALEX* far-UV (FUV) +24 μ m (Bigiel et al. 2011)). The nuclear regions lie on the relation for high- z mergers within the errors in Σ_{Mol} which is mainly due to the α_{CO} chosen for Arp 299. In Figure 4.19 we show the SFR-Dense gas relation as traced by $\text{HCN } J = 1 \rightarrow 0$ (cyan points) and $\text{HCO}^+ J = 1 \rightarrow 0$ (purple points). The $\text{HCN } J = 1 \rightarrow 0$ measurements for regions B1, C, and C' are upper limits denoted by arrows. The yellow line indicates the SFR-Dense gas relation from Gao & Solomon (2004b) where they converted to $\text{HCN } J = 1 \rightarrow 0$ integrated line intensities to dense gas masses using $\alpha_{\text{Dense}} = 10$ for a sample of spirals and (U)LIRGs. The black horizontal lines indicate the region of parameter space for spirals and (U)LIRGs from Gao & Solomon (2004b). Other than the upper limits, the nuclear regions lie close to the Gao & Solomon (2004b) SFR-Dense gas relation within the errors despite changing α_{Dense} to 5 for Arp 299. Changing the α_{Dense} to 5 in the Gao & Solomon (2004b) relation would shift the relation to the left in alignment with regions B1, C and C', but farther away from the starburst nucleus A.

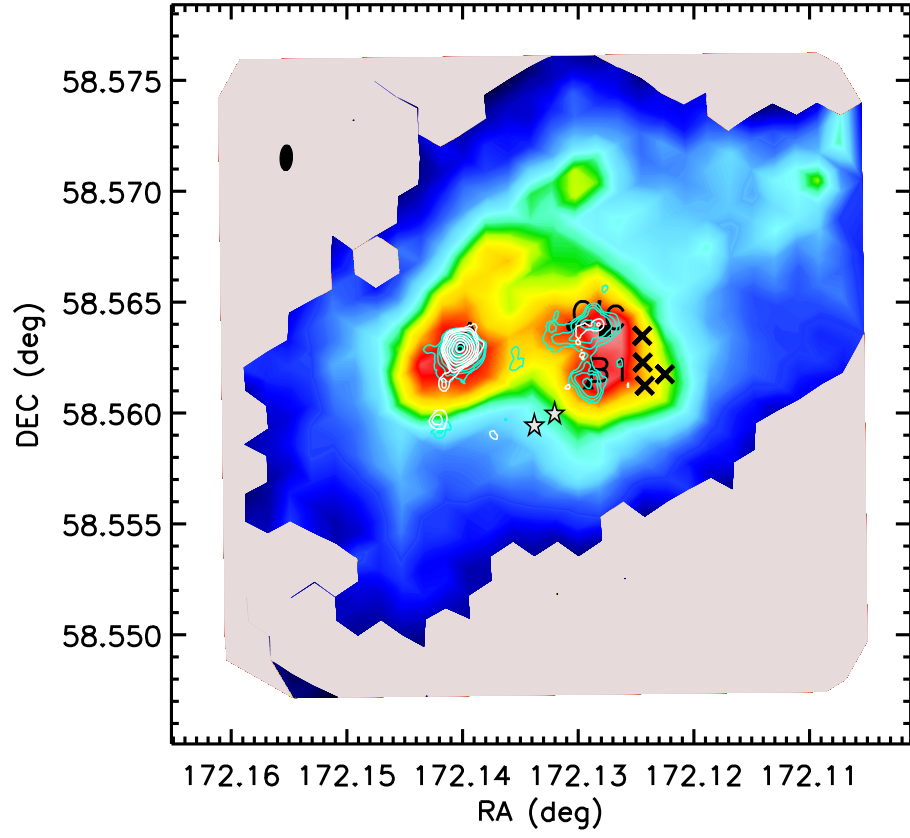


Figure 4.17 Interpolated H α flux map based on discrete values at each IFU fiber position overlaid with HCN(1–0) (cyan) contours and HCO⁺(1–0) contours (white) starting at 2σ above the noise level and increase intervals of 2σ . Map beam sizes are shown in the top left corner. AGN contaminated regions are marked with black cross (X-ray) and stars (IFU).

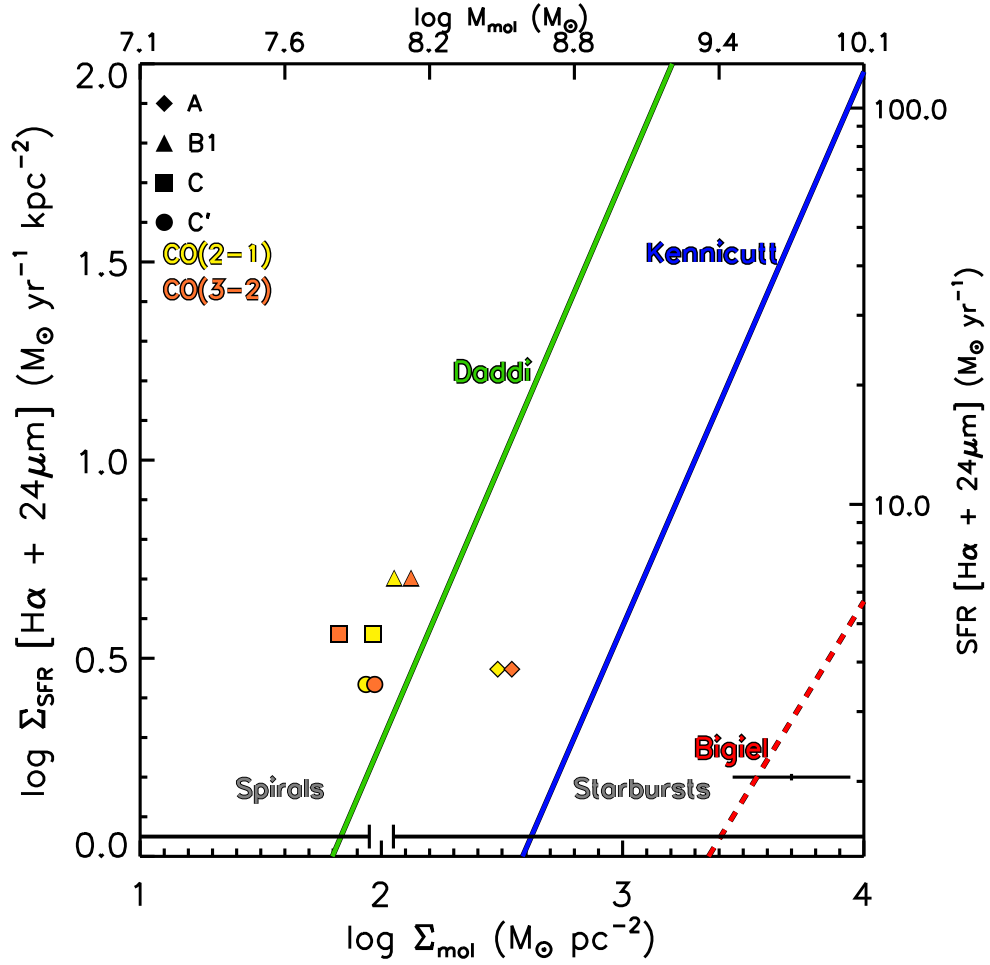


Figure 4.18 SFR–Mol gas surface density measurements of the nuclear regions of Arp 299 using $\text{CO}J = 2 \rightarrow 1$ and $\text{CO}J = 3 \rightarrow 2$ on scales of 1.3 kpc. The mass (M_{Mol}) is calculated using the same aperture area ($3''$ in radius). Lines indicate extragalactic relations on disk-averaged scales for spirals and starbursts (blue line; Kennicutt 1998b) and high- z mergers (green line; Daddi et al. 2010), as well as in 1 kpc regions in spirals and dwarf galaxies (red line; Bigiel et al. 2011).

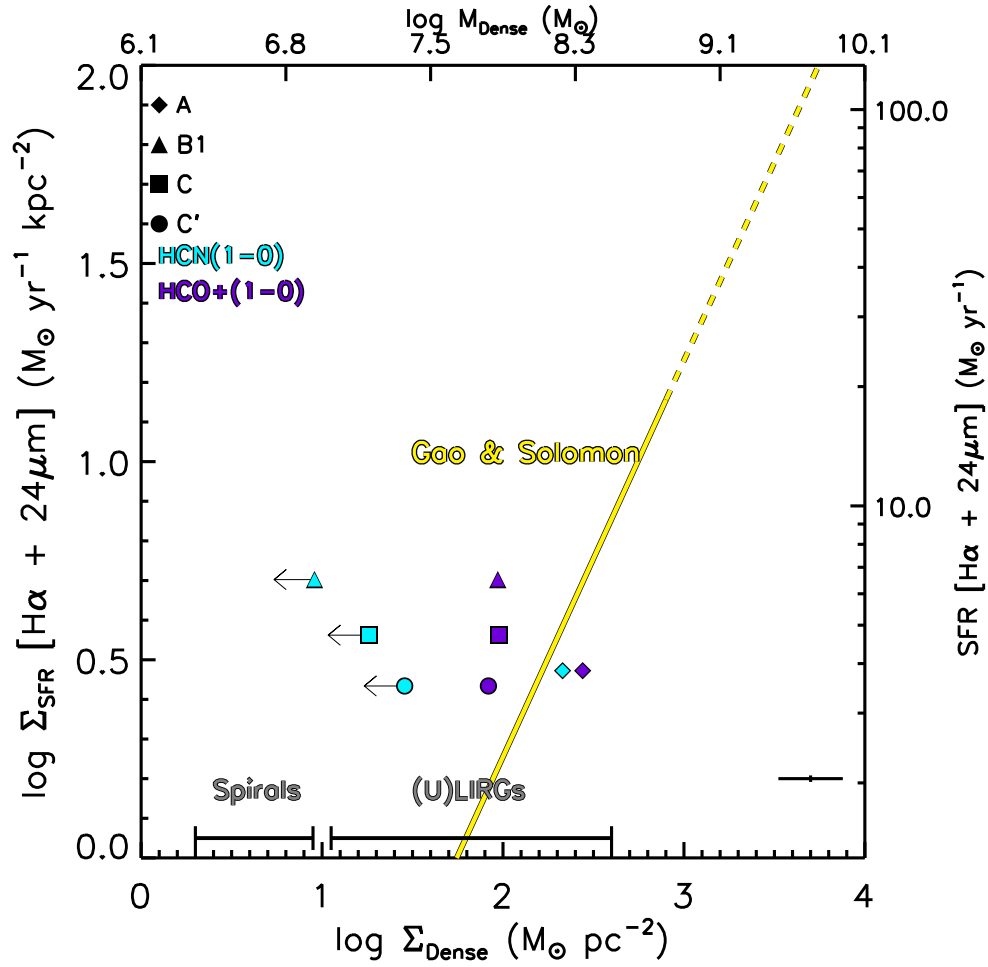


Figure 4.19 SFR–Dense gas surface density measurements of the nuclear regions of Arp 299 using HCN(1–0) and HCO⁺(1–0) on scales of 1.3 kpc. The mass (M_{Dense}) is calculated using the same aperture area (3'' in radius). The yellow line indicates the SFR–Dense gas relation on disk-averaged scales for spirals and (U)LIRGs (Gao & Solomon 2004b).

4.8.4 Spatially Resolved SFR–Gas Surface Density Relation

We show the spatially resolved SFR–gas surface density on 1.3 kpc scales in regions covered by the $\text{CO}J = 2 \rightarrow 1$ (blue) and $\text{CO}J = 3 \rightarrow 2$ maps in Figure 4.20 and 4.21 (yellow stars). Also shown are regions that may be affected by the AGN in NGC 3690 or by a starburst superwind (Section 4.7) as seen in line ratios from our IFU fiber measurements (stars, squares) as well as regions near the X-ray centroid (crosses). The depletion timescale (τ_{dep}) which is the inverse of the star formation efficiency (SFE) as defined by the SFR per unit gas mass or the $\Sigma_{\text{SFR}}/\Sigma_{\text{Mol}}$ (yr^{-1}) is indicated by the dotted diagonal lines. These regions lie mainly outside of the nuclear regions at low Σ_{Mol} or areas not covered by the CO maps, but there are a few regions with CO measurements that lie near the other points within the scatter. The SFR–Mol gas relations for disk–average measurement of non-interacting galaxies are also shown (Kennicutt 1998b; Daddi et al. 2010; Bigiel et al. 2011). We find that regions in both $\text{CO}J = 2 \rightarrow 1$ and $\text{CO}J = 3 \rightarrow 2$ transitions lie above the high- z merger relation from Daddi et al. (2010), which is likely due to the low value of α_{CO} used (Section 4.4.2), but was calculated directly for Arp 299 (Papadopoulos et al. 2012; Sliwa et al. 2012), however see Section 4.8.6.1. The Spearman rank correlation coefficient is 0.88 and 0.71 for $\text{CO}J = 2 \rightarrow 1$ and $\text{CO}J = 3 \rightarrow 2$, respectively, indicating a strong correlation between Σ_{Mol} and $\Sigma_{\text{SFR}} [\text{H}\alpha + 24\mu\text{m}]$ in both transitions. The integrated Σ_{Mol} and $\Sigma_{\text{SFR}} [\text{H}\alpha + 24\mu\text{m}]$ is also shown in both figures and are seen to lie on or near the Daddi et al. (2010) SFR–Mol relation.

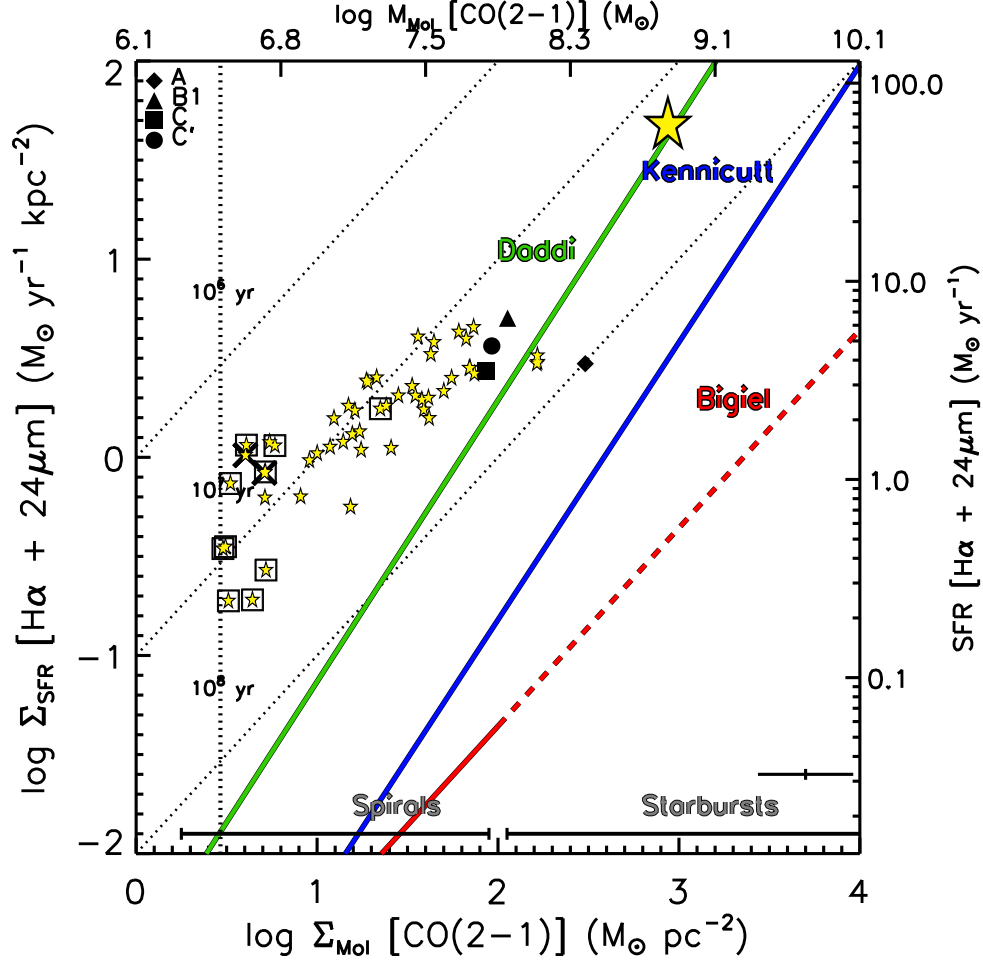


Figure 4.20 Spatially resolved SFR–Mol gas surface density relations from measurements at each IFU fiber position with CO $J=2-1$ coverage with data convolved to the $6''$ $24\mu\text{m}$ resolution (scales of 1.3 kpc). The mass (M_{Mol}) is calculated using the same aperture area ($3''$ in radius). The dotted vertical line is the sensitivity limit of the CO $J=2 \rightarrow 1$ map. Large yellow star is the integrated value for Arp 299. Lines indicate extragalactic relations on disk-averaged scales for spirals and starbursts (blue line; Kennicutt (1998b)) and high- z mergers (green line; Daddi et al. (2010)), as well as in 1 kpc regions in spirals and dwarf galaxies (red line; Bigiel et al. (2011)). AGN contaminated regions are marked with boxes from IFU line fluxes and black crosses (X-ray).

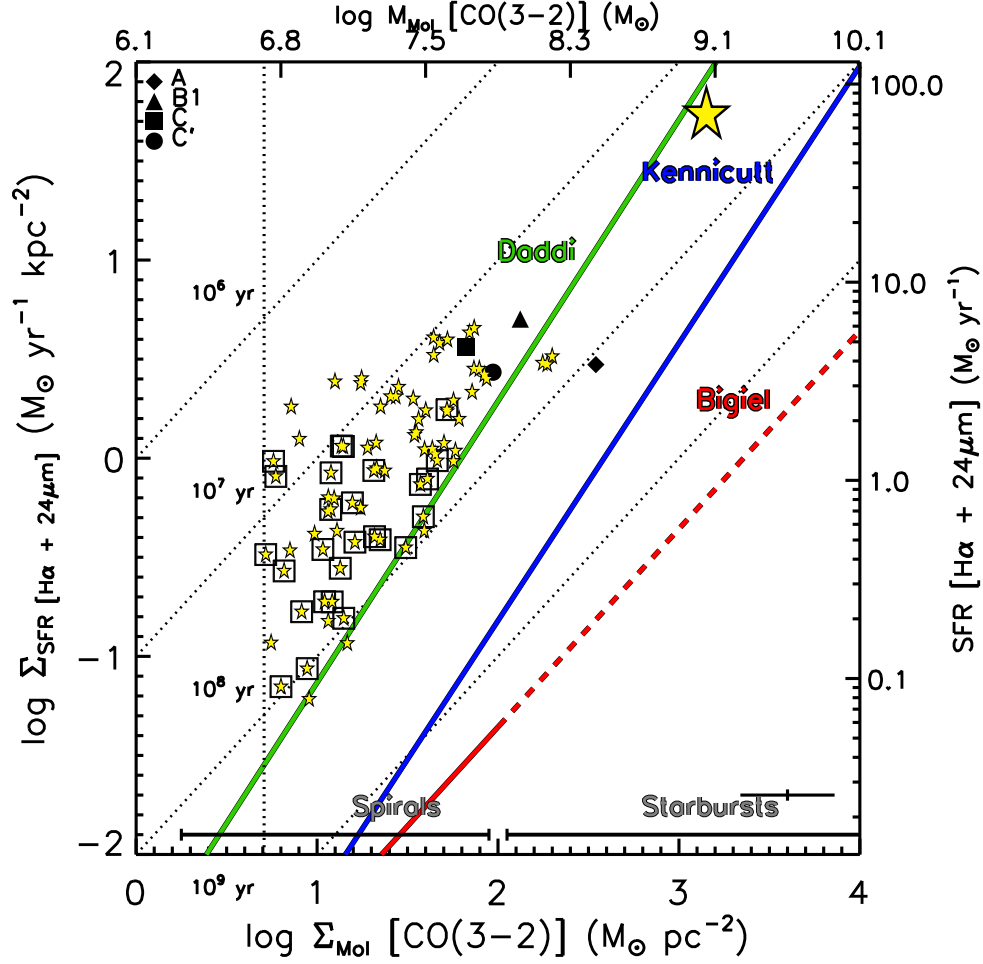


Figure 4.21 Spatially resolved SFR–Mol gas surface density relations from measurements at each IFU fiber position with CO $J=3-2$ coverage with data convolved to the $6''$ $24\mu\text{m}$ resolution (scales of 1.3 kpc). The mass (M_{Mol}) is calculated using the same aperture area ($3''$ in radius). The dotted vertical line is the sensitivity limit of the CO $J=2 \rightarrow 1$ map. Large yellow star is the integrated value for Arp 299. Lines indicate extragalactic relations on disk-averaged scales for spirals and starbursts (blue line; Kennicutt (1998b)) and high- z mergers (green line; Daddi et al. (2010)), as well as in 1 kpc regions in spirals and dwarf galaxies (red line; Bigiel et al. (2011)). AGN contaminated regions are marked with boxes from IFU line fluxes.

4.8.5 Spatially Resolved SFR–Dense Gas Surface Density Relation

Gao & Solomon (2004b) found the SFR–Dense gas relation to be a tighter linear relation in both non-interacting normal spiral galaxies and (U)LIRGs using the IRAS IR SFRs and the $\text{HCN } J = 1 \rightarrow 0$ line than the relation found using CO on *global* or disk-average scales. Since Arp 299 is a nearby IR bright merger, does this tight linear relation still hold on scales of 1.3 kpc? In Figure 4.22, we show the SFR–Dense gas relation for $\Sigma_{\text{SFR}} [\text{H}\alpha + 24\mu\text{m}]$ and Σ_{Dense} as traced by $\text{HCN } J = 1 \rightarrow 0$ and $\text{HCO}^+ J = 1 \rightarrow 0$. Also shown is the relation from Gao & Solomon (2004b) converted to Σ_{Dense} using an α_{Dense} of 10 (yellow solid line) and the dashed line is an extrapolation and τ_{dep} are the dotted diagonal lines. We also show the integrated values for $\text{HCN } J = 1 \rightarrow 0$ (cyan) and $\text{HCO}^+ J = 1 \rightarrow 0$ (purple) as large stars. The integrated values for both dense gas tracers line up remarkably well with the Gao & Solomon (2004b) SFR–Dense gas relation with the only offset being the choice of α_{Dense} where we used α_{Dense} of 5 for Arp 299. If we use an α_{Dense} of 10, this would shift the integrated points to lie on the Gao & Solomon (2004b) relation. The spatially resolved points (small cyan and purple stars) lie along the same line as the integrated values and have Spearman correlation coefficients of 0.68 and 0.83 for $\text{HCN } J = 1 \rightarrow 0$ and $\text{HCO}^+ J = 1 \rightarrow 0$, respectively, indicating there is a strong relation between $\Sigma_{\text{SFR}} [\text{H}\alpha + 24\mu\text{m}]$ and Σ_{Dense} for both dense gas tracers. Although the displacement between our points and the Gao & Solomon (2004b) relation is likely due to the choice of α_{Dense} , the difference in the SFR tracer ($\text{SFR}_{[\text{H}\alpha + 24\mu\text{m}]}$ versus SFR from IRAS) or the spatial scales measured

(global scales compared to 1.3 kpc scales) might also contribute to the offset.

4.8.6 Spatially Resolved SFR–HI Gas Surface Density Relation

Since we find that the $\text{SFR}_{[\text{H}\alpha]}$ recovers the $\text{SFR}_{[\text{H}\alpha+24\mu\text{m}]}$ within a factor of $\sim 2\text{--}3$ (Section 4.8.2) in the outer regions of the Arp 299 merger, we can use it to reliably estimate the SFR–gas relation using HI as a gas tracer. We are limited to the resolution of the HI map $\sim 22''$ and we make measurements in 11 apertures on scales of the HI resolution of 4.7 kpc. In Figure 4.23 we show the interpolated $\text{H}\alpha$ flux map with the HI contours overlaid in red as well as X-ray AGN contaminated regions (crosses) and IFU AGN regions (white stars). As discussed in Section 4.8.2, the HI peak emission is associated with a region that has bright $\text{H}\alpha$ flux and a stellar cluster as seen in the *HST* optical image. We convolve our IFU $\text{H}\alpha$ map with a Gaussian beam of $22''$ FWHM to match the HI map resolution. We compare our measurements to the data points from the outer disks of normal spiral and dwarf galaxies from Bigiel et al. (2010) on spatial scales of $15''$ or $\sim 0.6\text{--}1$ kpc at the distance of their sample galaxies. One caveat is that Bigiel et al. (2010) estimate the SFR using the *GALEX* FUV as a tracer which uses a slightly different normalization than the SFRs we derive using relations from Murphy et al. (2011). Their measurements are normalized to the same Kroupa (2001) IMF, however the normalization they use from Salim et al. (2007) is a factor of 1.3 lower than that derived in Murphy et al. (2011). We therefore multiply their SFRs by this factor in order to directly compare to our measurements and this distribution for

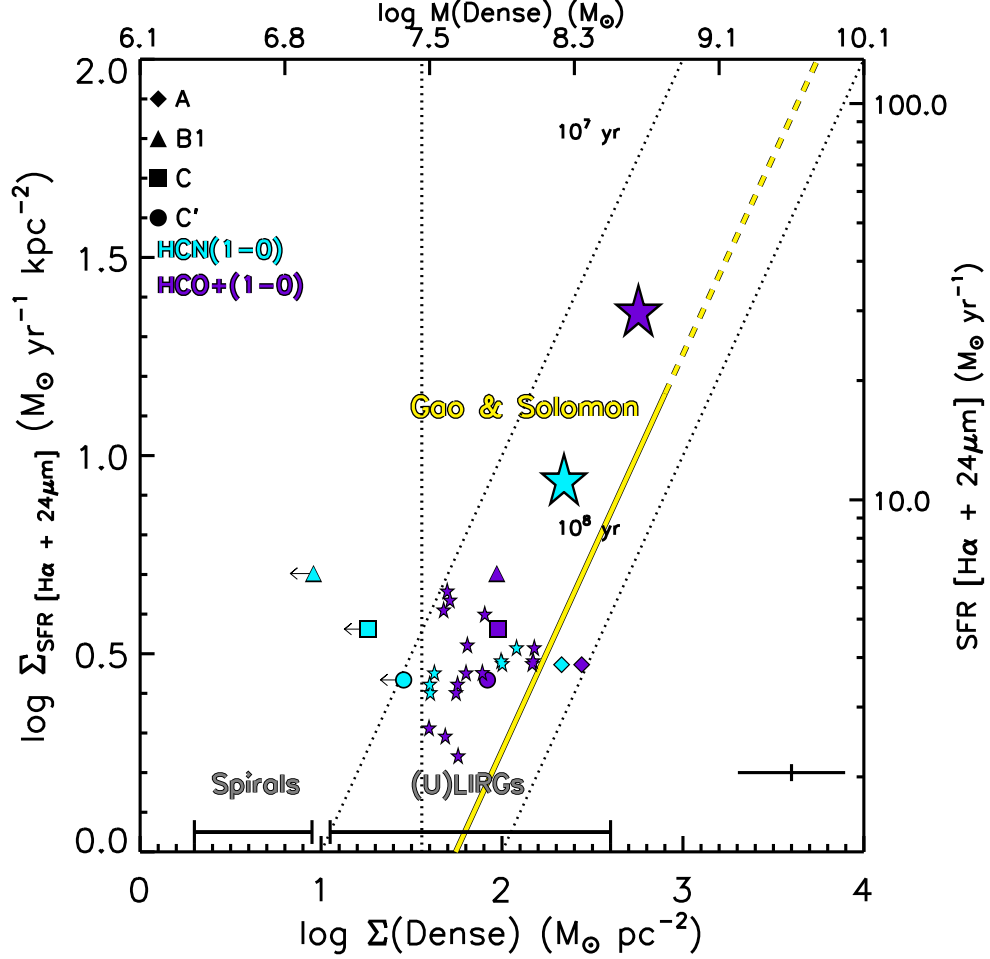


Figure 4.22 Spatially resolved SFR–Dense gas surface density relations from measurements at using HCN(1–0) and HCO⁺(1–0) each IFU fiber position with data convolved to the 6'' 24μm resolution (scales of 1.3 kpc). The mass (M_{Dense}) is calculated using the same aperture area (3'' in radius). The dotted vertical line is the sensitivity limit of the HCN $J = 1 \rightarrow 0$ and HCO⁺ $J = 1 \rightarrow 0$ maps. The large cyan and purple stars are the integrated value of HCN $J = 1 \rightarrow 0$ and HCO⁺ $J = 1 \rightarrow 0$ for Arp 299. The yellow line indicates the SFR–Dense gas relation on disk-averaged scales for spirals and (U)LIRGs (Gao & Solomon 2004b).

normal spirals (orange points) and dwarf galaxies (purple points) is shown in Figure 4.24. We also include a factor of 1.37 to account for helium in their measurements of Σ_{HI} . Another caveat is that their spatial scales are a factor of ~ 5 -8 lower than the regions we measure in Arp 299.

Figure 4.24 shows the SFR–HI extranuclear relation (yellow stars) as well as the range of normal spiral and starburst galaxies from Kennicutt (1998b) and τ_{dep} (where $\tau_{\text{dep}}=1/\text{SFE}$) are the dotted diagonal lines. The Spearman's correlation coefficient for the 11 regions in Arp 299 is 0.15 which indicates a weak correlation that can be attributed to the wide scatter in data points. However, we do find points that are likely associated with the disk of IC 694 to lie along the same relation as the outer disks of normal spiral and dwarf galaxies. We also find there to be points that lie above the distribution of spirals and dwarfs. Since we are measuring points in the outer region of the Arp 299 merger, the star formation could be coming from a different physical process than that seen in the nuclear regions (i.e., gas driven inflow of dense material collapsing to form stars). Extranuclear star formation in galaxy mergers could be driven by turbulence due to the high velocity dispersion in the gas which can either support clouds against gravitational collapse or turbulent flows can compress the gas to form dense clumps and drive star formation (Elmegreen 2002). These processes may explain the difference in SFR–gas relations at high- z (Genzel et al. 2010; Daddi et al. 2010) and in nearby spirals and starbursts on global scales (Kennicutt 1998b) as seen in numerical simulations (Teyssier et al. 2010). The SFR–HI relation seen in 4.7

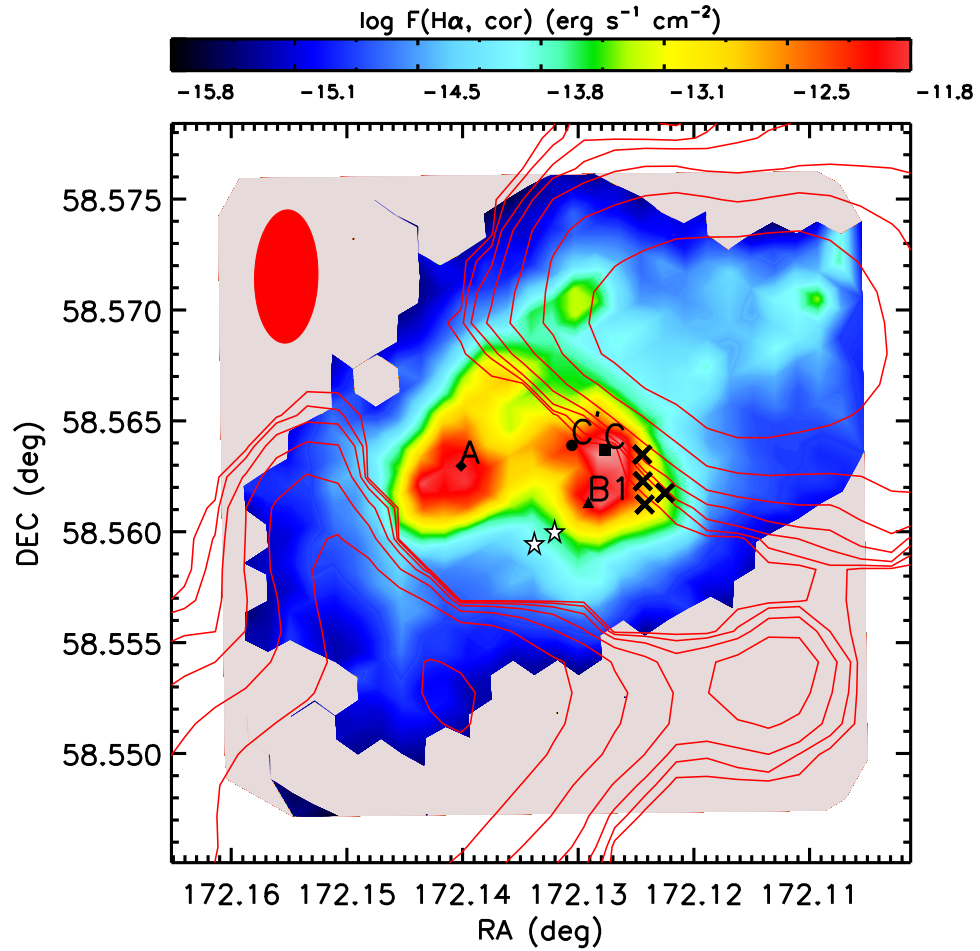


Figure 4.23 Interpolated $\text{H}\alpha$ flux map based on discrete values at each IFU fiber position overlaid with HI (red) contours and contours starting at 2σ above the noise level and increase intervals of 2σ . The two main separate components of the Arp 299 merger IC 694 and NGC 3690 and individual nuclei (A, B1, and B2) and star forming complexes (C, and C') are indicated. AGN contaminated regions are marked with black cross (X-ray) and stars (IFU).

kpc regions in the Arp 299 merger follow the same trends with the exception of a few points. On average, the SFE as defined by the SFR per unit gas mass or the $\Sigma_{\text{SFR}}/\Sigma_{\text{H I}}$ (yr^{-1}) is found to be higher by a factor of ~ 6 than the sample of normal spiral galaxies. The increase in SFE may be due to turbulent motions, but the increase is not extreme as it is likely the extranuclear star formation in Arp 299 is being driven by molecular cloud collapse at a lower rate than the nuclear regions. There could be significant deviation from this relation, for example, in interacting galaxies at different interaction phases which is something that we will test with the VIXENS sample of interacting galaxies (Heiderman et al. 2011).

4.8.6.1 Variation of CO-to-H₂ Conversion Factor with Metallicity, IRAS F_{60}/F_{100} Flux Ratio, and Dust Temperature

Since it is unlikely that there is only a single CO-to-H₂ conversion factor in any given galaxy, we investigate the variation of the CO-to-H₂ conversion factor (α_{CO}) on small scales in the Arp 299 system as a function of metallicity and compare to the commonly assumed starburst (Downes & Solomon 1998) and Galactic (Bloemen et al. 1986) conversion factors. We use the model proposed by Narayanan et al. (2012) for the conversion factor ($\alpha_{\text{CO}}(Z')$) as a function of metallicity normalized by the solar value (Z') described by the equation:

$$\alpha_{\text{CO}}(Z') = 10.7 \times \left(\frac{\langle I(\text{CO}) \rangle^{-0.32}}{\text{K km s}^{-1}} \right) \times \left(\frac{1}{Z'^{0.65}} \right) (M_{\odot} \text{ pc}^{-2} (\text{K km s}^{-1})^{-1}). \quad (4.12)$$

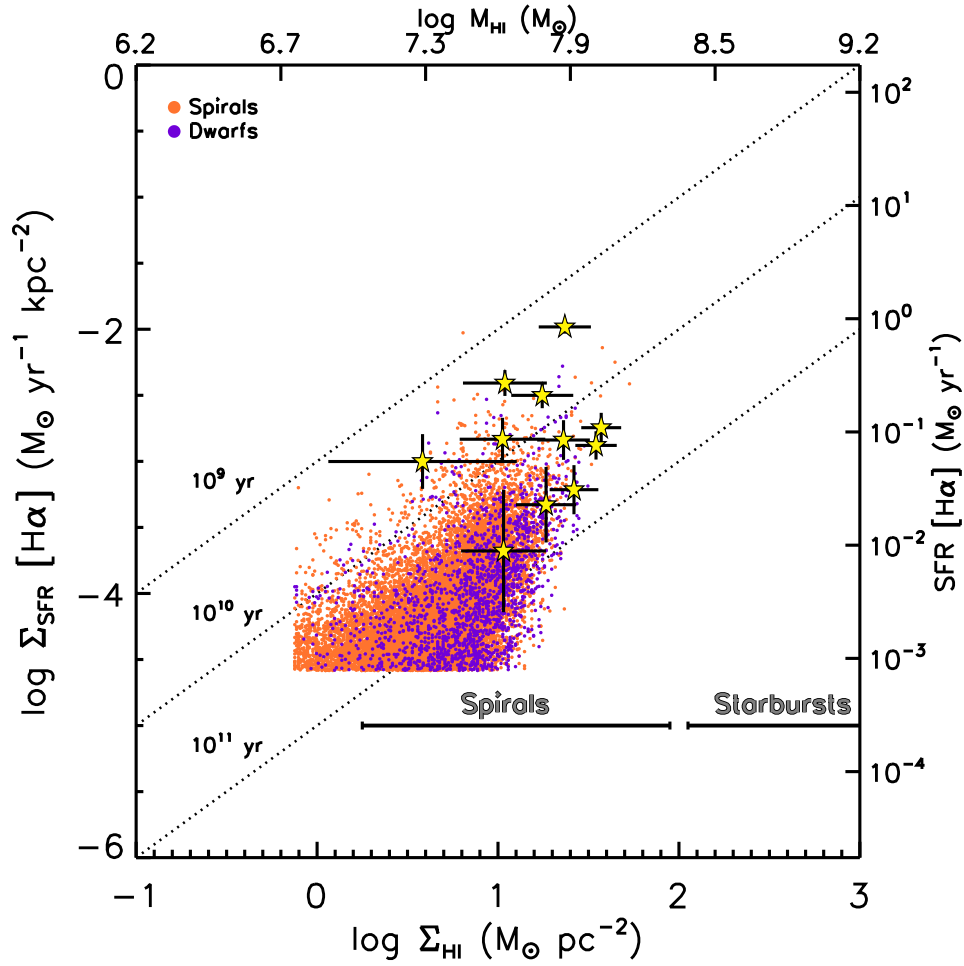


Figure 4.24 Spatially resolved SFR–HI gas surface density relation from measurements with data convolved to the HI map resolution on scales of 4.7 kpc in the outer regions of Arp 299. The mass (M_{HI}) is calculated using the same aperture area (11'' in radius). Regions for the outer disks in normal spiral and dwarf galaxies on scales of 0.6–1 kpc are shown as orange and purple circles, respectively from Bigiel et al. (2010).

The N2 metallicity calibration from Pettini & Pagel (2004) which uses the $[\text{NII}]/\text{H}\alpha$ strong line ratio was used to determine metallicities assuming a solar metallicity of $12 + \log(\text{O}/\text{H}) = 8.69 \pm 0.05$ (Asplund et al. 2009). Figure 4.25 shows the fiber-to-fiber distribution of metallicities across the merger. The mean metallicity of Arp 299 is 8.57 ± 0.01 . We find higher metallicities in the outer regions of the merger and lower or diluted metallicities in the nuclear regions in agreement with merger scenario in which galaxy interactions drive lower metallicity gas from the outer regions of the system into the central regions (Kewley et al. 2010 and references therein).

Using the relationship between metallicity and integrated CO line intensity from Narayanan et al. (2012), we explore the variation in $\alpha_{\text{CO}}(Z')$ on a $6''$ or 1.3 kpc spatial scale to compare later with our $\text{H}\alpha + 24\mu\text{m}$ based SFRs. To measure over 1.3 kpc apertures, we use our fiber-to-fiber metallicity measurements and make an interpolated 2-D metallicity map and convolve this with a Gaussian kernel with a $6''$ FWHM. Figure 4.26 shows the distribution of $\alpha_{\text{CO}}(Z')$ for both $\text{CO}J = 1 \rightarrow 0$ and $\text{CO}J = 3 \rightarrow 2$ integrated line intensities converted to $\text{CO}J = 1 \rightarrow 0$ using the line ratios in Section 4.4.2 on $6''$ scales. We find that $\alpha_{\text{CO}}(Z')$ varies slightly based on which CO line transition is used to make the measurement. The median $\alpha_{\text{CO}}(Z')$ using $\text{CO}J = 2 \rightarrow 1$ integrated intensities is $3.6 \pm 0.2 \text{ M}_{\odot} \text{ pc}^{-2} (\text{K km s}^{-1})^{-1}$ and using the $\text{CO}J = 3 \rightarrow 2$ line intensity it is $3.2 \pm 0.1 \text{ M}_{\odot} \text{ pc}^{-2} (\text{K km s}^{-1})^{-1}$ on 1.3 kpc scales. We find lower values of $\alpha_{\text{CO}}(Z')$ in the nuclear regions ranging from $1.6\text{--}2.5 \text{ M}_{\odot} \text{ pc}^{-2} (\text{K km s}^{-1})^{-1}$ (Figures 4.27 and 4.28). The difference be-

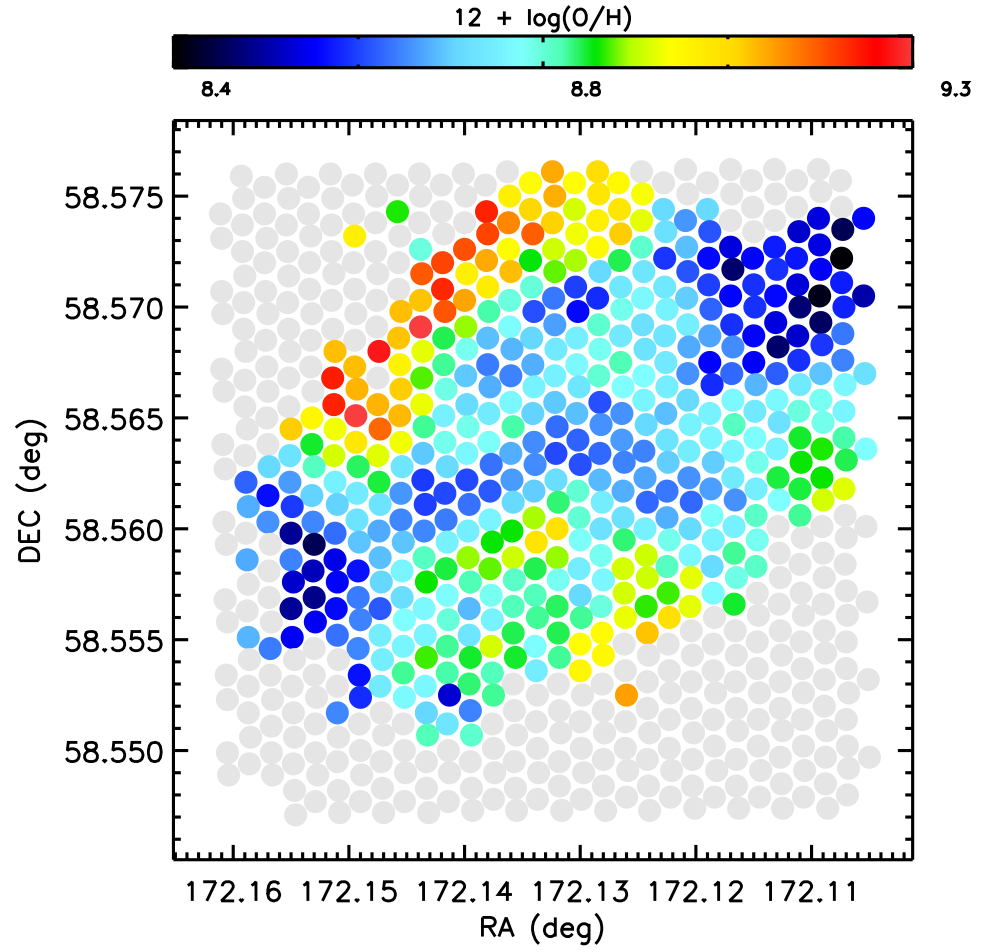


Figure 4.25 Metallicity map of Arp 299 using the N2 calibration from Pettini & Pagel (2004) and fiber $[\text{NII}]/\text{H}\alpha$ line ratios.

tween $\text{CO}J = 2 \rightarrow 1$ and $\text{CO}J = 3 \rightarrow 2$ is likely due to the cloud filling factor with $\text{CO}J = 2 \rightarrow 1$ emission being more extended and $\text{CO}J = 3 \rightarrow 2$ emission being more compact (see Figure 4.14). Overall on average, the $\alpha_{\text{CO}}(Z')$ factors agree well with the commonly used Galactic conversion factor of $4.5 \text{ M}_{\odot} \text{ pc}^{-2} (\text{K km s}^{-1})^{-1}$ (Bloemen et al. 1986) rather than the commonly used starburst factor (Downes & Solomon 1998) and α_{CO} calculated using this relation. We find little variation in metallicity across Arp 299 so the values obtained for α_{CO} are dominated by the variation in integrated line intensity for both CO transitions in these regions.

We explore the SFR–gas surface density relations using the varying $\alpha_{\text{CO}}(Z')$ factor in Figures 4.29 and 4.30 which show the SFR–Mol surface density relations on 1.3 kpc using $\alpha_{\text{CO}}(Z')$ and a factor of 1.37 for helium to convert from H_2 to total molecular gas surface densities. We find using $\alpha_{\text{CO}}(Z')$ does lower the dispersion in the SFR–Mol relations compared to what we found using just a single conversion factor (Figures 4.20 and 4.21) and since higher α_{CO} values were found using the metallicity–CO line intensity relation, the points move to the right in gas surface density.

An alternative method to determine α_{CO} is to use a measurement of the dust content. Assuming a dust emissivity spectral index $\beta = 1.5$ and the ratio of F_{60}/F_{100} IRAS fluxes from Table 4.1, we calculate a dust temperature (T_{dust}) of 42.5 K. Using the linear relations between the IRAS flux ratio and CO–to– H_2 conversion factor ($F_{60}/F_{100} - \alpha_{\text{CO}}$) and our derived dust temperature and conversion factor ($T_{\text{dust}} - \alpha_{\text{CO}}$) from Magnelli et al. (2012) (their Table 4),

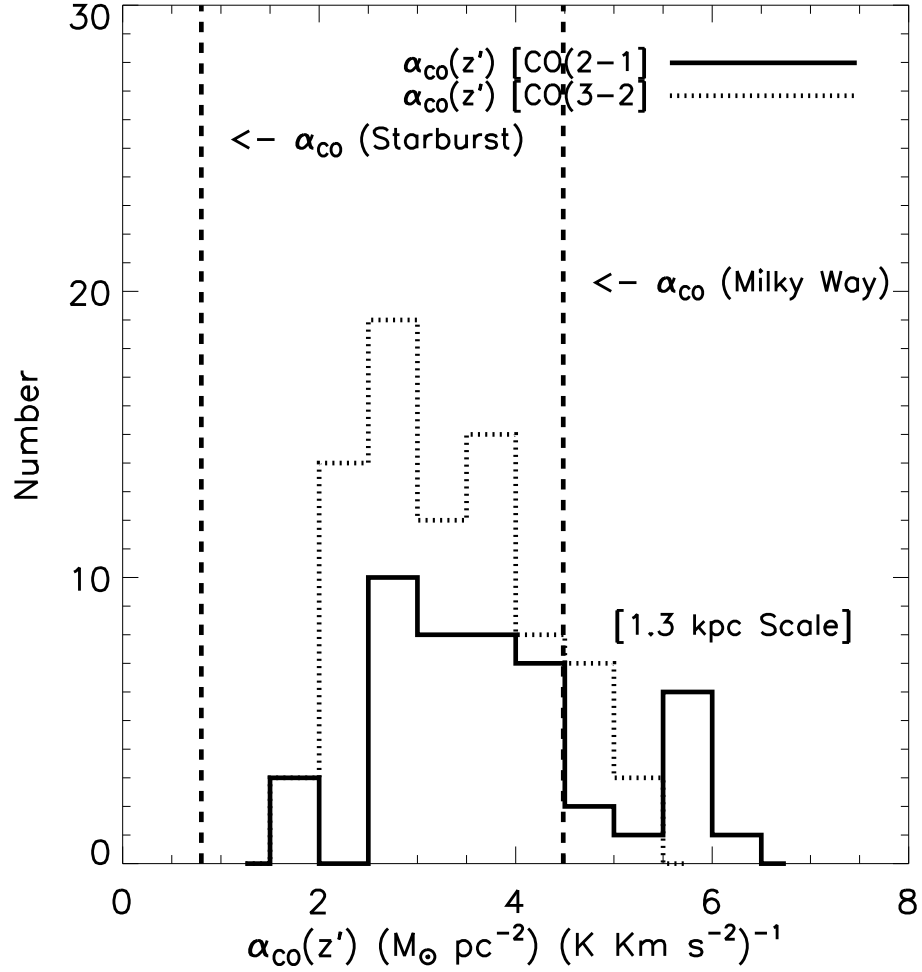


Figure 4.26 Metallicity dependent CO-to-H₂ conversion factor, $\alpha_{\text{CO}}(Z')$, from Narayanan et al. (2012) on scales of 1.3 kpc corresponding to the resolution of $24\mu\text{m}$ PSF for CO $J = 2 \rightarrow 1$ (solid black line) and CO $J = 3 \rightarrow 2$ (dotted black line). The commonly use single value starburst conversion factor (Downes & Solomon 1998) and Galactic conversion factor from (Bloemen et al. 1986) are shown by the dashed black lines.

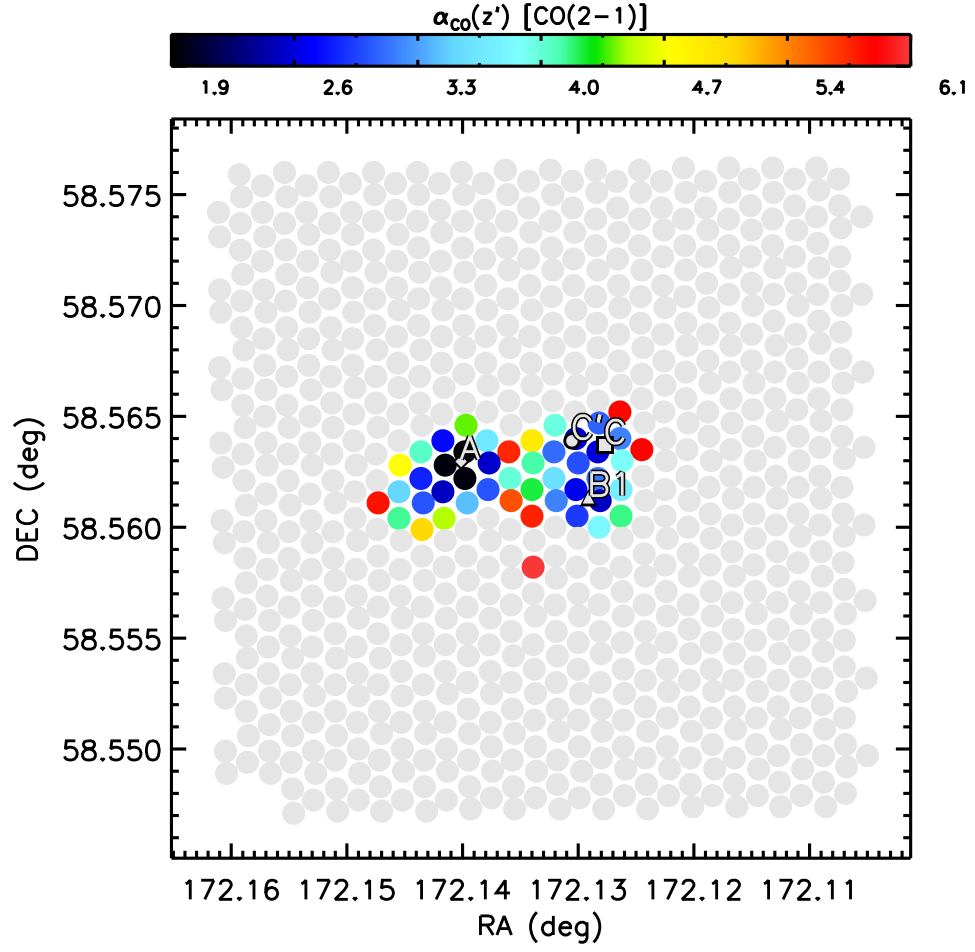


Figure 4.27 Spatial distribution of the metallicity dependent CO-to-H₂ conversion factor, $\alpha_{\text{CO}}(Z')$, from Narayanan et al. (2012) on scales of 1.3 kpc corresponding to the resolution of $24\mu\text{m}$ PSF derived using CO $J = 2 \rightarrow 1$ line intensities.

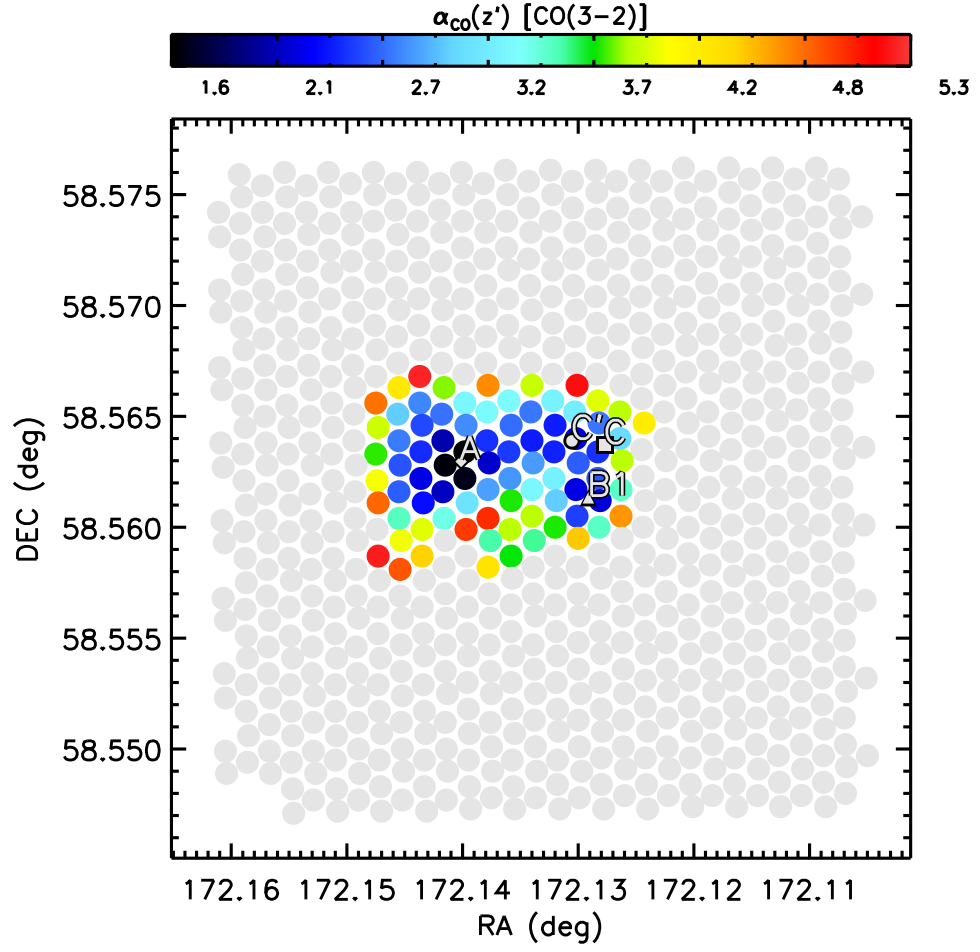


Figure 4.28 Spatial distribution of the metallicity dependent CO-to-H₂ conversion factor, $\alpha_{\text{CO}}(Z')$, from Narayanan et al. (2012) on scales of 1.3 kpc corresponding to the resolution of $24\mu\text{m}$ PSF derived using CO $J = 3 \rightarrow 2$ line intensities.

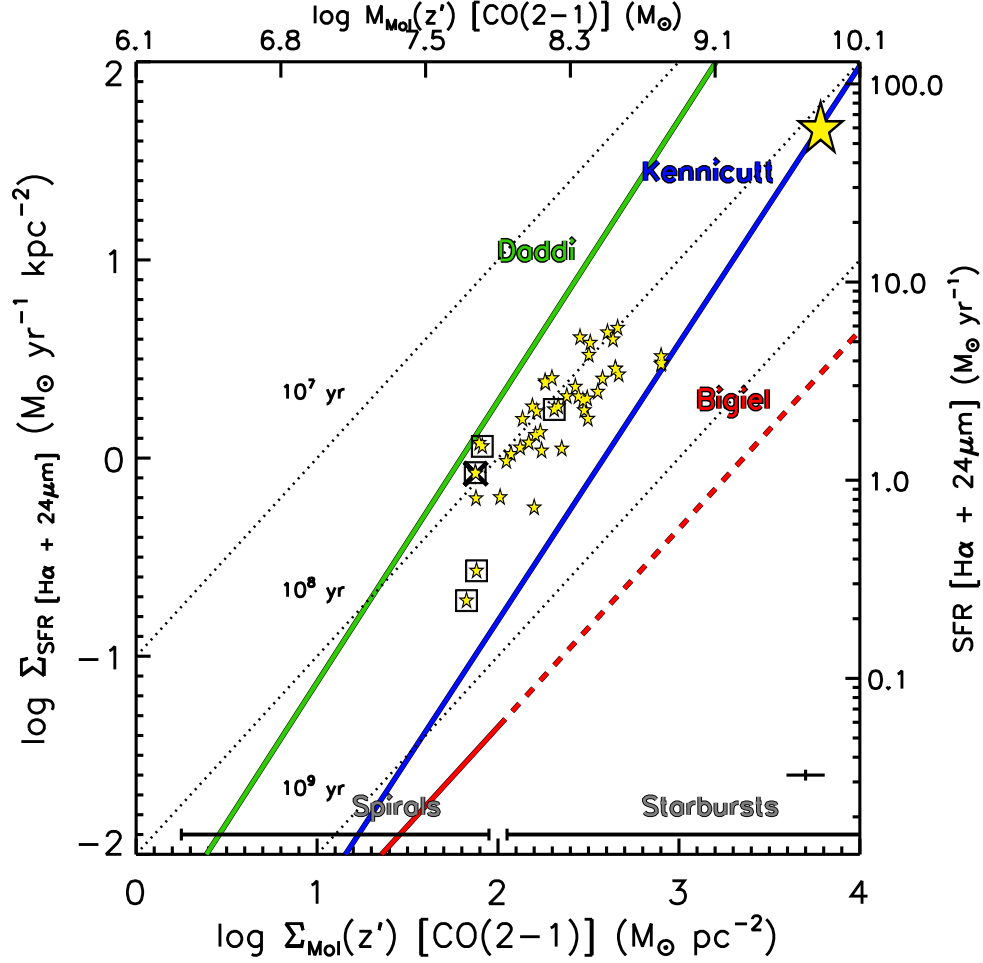


Figure 4.29 Spatially resolved SFR–Mol gas surface density relations from measurements at each IFU fiber position with $\text{CO} J = 2 \rightarrow 1$ coverage using a metallicity dependent conversion factor ($\alpha_{\text{CO}}(Z')$) from Narayanan et al. (2012) on scales of 1.3 kpc. The mass (M_{Mol}) is calculated using the same aperture area ($3''$ in radius). The dotted vertical line is the sensitivity limit of the $\text{CO} J = 2 \rightarrow 1$ map. Large yellow star is the integrated value for Arp 299. Lines indicate extragalactic relations on disk-averaged scales for spirals and starbursts (blue line; Kennicutt (1998b)) and high- z mergers (green line; Daddi et al. (2010)), as well as in 1 kpc regions in spirals and dwarf galaxies (red line; Bigiel et al. (2011)) AGN contaminated regions are marked with boxes from IFU line fluxes and black crosses (X-ray).

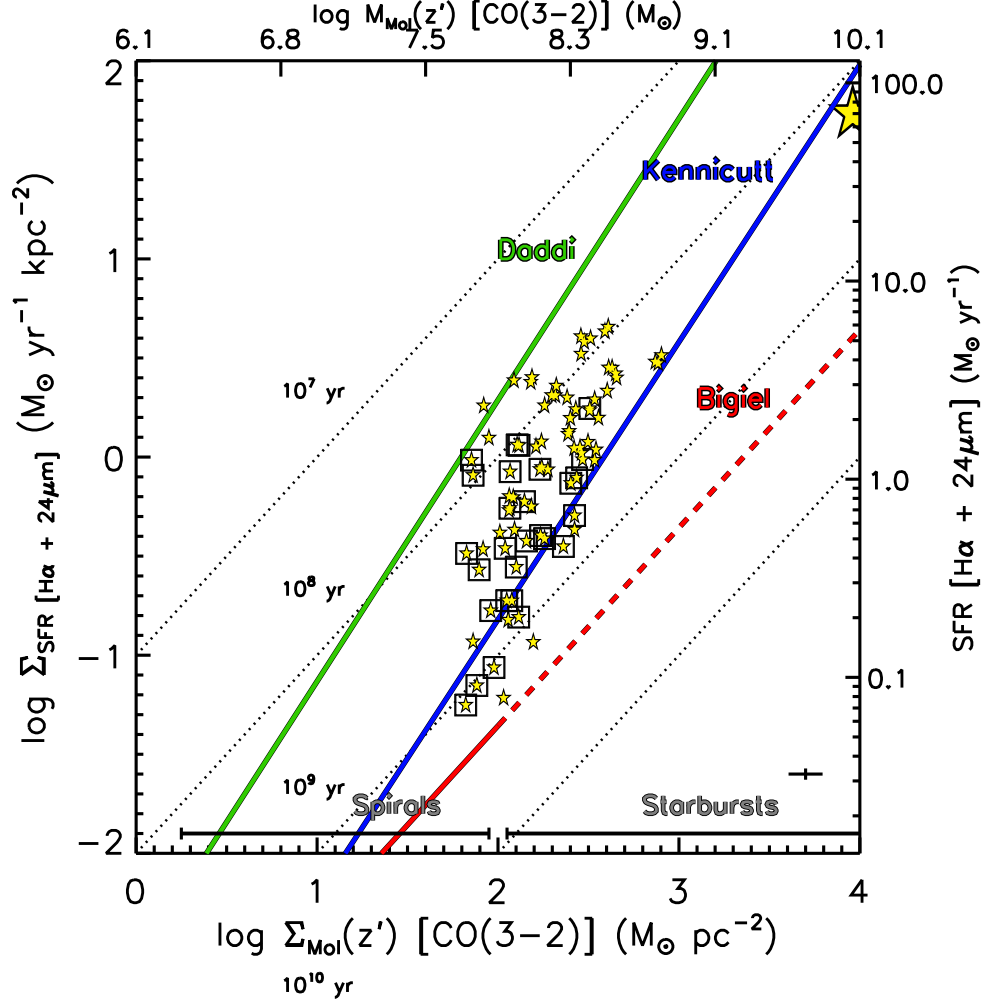


Figure 4.30 Spatially resolved SFR–Mol surface density relations from measurements at each IFU fiber position with $\text{CO} J = 3 \rightarrow 2$ coverage using a metallicity dependent conversion factor ($\alpha_{\text{CO}}(Z')$) from Narayanan et al. (2012) on scales of 1.3 kpc. The mass (M_{Mol}) is calculated using the same aperture area ($3''$ in radius). The dotted vertical line is the sensitivity limit of the $\text{CO} J = 2 \rightarrow 1$ map. Large yellow star is the integrated value for Arp 299. Lines indicate extragalactic relations on disk-averaged scales for spirals and starbursts (blue line; Kennicutt (1998b)) and high- z mergers (green line; Daddi et al. (2010)), as well as in 1 kpc regions in spirals and dwarf galaxies (red line; Bigiel et al. (2011)). AGN contaminated regions are marked with boxes from IFU line fluxes.

we obtain a value of 0.67 and 0.99 $M_{\odot} \text{ pc}^{-2} (\text{ km s}^{-1})^{-1}$. These values lie in between the α_{CO} from Sliwa et al. (2012) and Papadopoulos et al. (2012) for Arp 299 and our results using the metallicity–CO line intensity relation from Narayanan et al. (2012). This indicates that a higher Milky Way like value for α_{CO} may be more suitable for Arp 299 than the two lower values previously found. Another possibility is that α_{CO} likely varies as a function of interaction phase based on if the system is in starburst mode and therefore a bimodal α_{CO} (eg., starburst or Galactic) is highly unlikely (Tacconi et al. 2008). In order to better understand these relations and conversion factors α_{CO} and α_{Dense} in more detail as a function of interacting phase in nearby galaxy mergers, obtaining molecular gas maps with more coverage and higher sensitivity and resolution from facilities such as IRAM, CARMA, and ALMA would be highly beneficial.

4.9 Comparison to Galactic Star Forming Regions

In Chapter 2 (Figure 2.11) we compared the relation we find for Galactic YSOs (Heiderman et al. 2010) and clouds, as well as massive dense clumps (Heiderman et al. 2010; Wu et al. 2010) and found that the Galactic YSOs and clumps above a threshold for efficient star formation (Heiderman et al. 2010) lie on a similar relation to high redshift mergers (Genzel et al. 2010) indicating that the bulk of gas in these systems trace star forming clouds. Comparing the Galactic points in this figure to SFR-Mol gas relation for Arp 299 on 1.3 kpc scales, we find regions in Arp 299 to lie still above most of the

Galactic star forming regions, however there is some overlap at the high gas surface density end of the relation for Arp 299.

4.10 Summary

We investigate relations between the SFR and gas surface densities using a variety of star formation and gas tracers in the nearby IR bright galaxy merger Arp 299. We use an IFU $H\alpha$ map from the VIXENS survey of interacting galaxies, archival $24\mu\text{m}$ and *HST* $\text{Pa}\alpha$, to derive SFR surface densities and use maps of molecular gas from $\text{CO}J = 2 \rightarrow 1$ and $\text{CO}J = 3 \rightarrow 2$, dense gas from $\text{HCN}J = 1 \rightarrow 0$ and $\text{HCO}^+J = 1 \rightarrow 0$, and atomic gas from HI to compute gas surface densities.

Our results are as follows:

1. We compare two Galactic extinction laws from Draine (2003) using $R_V = 3.1$ (diffuse ISM) and $R_V = 5.5$ (molecular clouds), using the Balmer decrement $H\alpha/H\beta$ flux ratio from our IFU data and from the $H\alpha/\text{Pa}\alpha$ flux ratio from the IFU $H\alpha$ map and an *HST* NICMOS $\text{Pa}\alpha$ map. We find that the $R_V = 5.5$ extinction law yields a higher $H\alpha/\text{Pa}\alpha$ ratio than using $R_V = 3.1$ in the nuclear regions of Arp 299, however the ratio is still a factor of ~ 2 below the intrinsic $\text{Pa}\alpha/\text{Ha}$ ratio from recombination line theory indicating that neither the $H\alpha$ or $\text{Pa}\alpha$ line reliably trace all of the star formation (Section 4.5). Comparing the A_V from the $H\alpha/H\beta$ ($\sim 0.7\text{--}1.3$ mag) and $H\alpha/\text{Pa}\alpha$ ($\sim 1.4\text{--}2.3$) we find A_V both flux ratios are

much lower by a factor of ~ 10 than those found using CO maps ($\sim 7\text{--}29$ mag).

2. Using BPT line diagnostic diagrams, we find no evidence for an AGN in either of the two nuclear regions A and B1 (Section 4.7). Two regions are selected as AGN by all three BPT diagrams that lie near the nuclear region of B1 similar to that reported in García-Marín et al. (2006) which could be a Seyfert-like ionization cone, however it could also be a interstellar gas heated by photoionization by massive stars. We also find high $[\text{OI}]/\text{H}\alpha$ and $[\text{SiII}]/\text{H}\alpha$ line ratios covering a large area outside the nuclear regions which can be attributed to either a large population of Wolf-Rayet stars or supernova driving a starburst superwind shocked outflow of gas.
3. SFR tracers are calibrated using a common IMF (Murphy et al. 2011) are used to compare the global or system-averaged SFR for different tracers. We find the $\text{SFR}_{[\text{H}\alpha+24\mu\text{m}]}$ ($90\pm 10 \text{ M}_{\odot} \text{ yr}^{-1}$) is in agreement with the total IR SFR from IRAS ($77\pm 5 \text{ M}_{\odot} \text{ yr}^{-1}$), while the $\text{SFR}_{[\text{H}\alpha]}$ (19 ± 1) and $\text{SFR}_{[24\mu\text{m}]}$ (44 ± 6) underestimate the total SFR by factors of ~ 4 and 2, respectively (Section 4.8.1). The total nuclear $\text{SFR}_{[\text{Pa}\alpha]}$ is $\gtrsim 13\pm 3$ is similar to the *total* $\text{SFR}_{[\text{H}\alpha]}$, which is due to the high extinction in both the $\text{Pa}\alpha$ and $\text{H}\alpha$ line fluxes. The $\text{SFR}_{[\text{Pa}\alpha]}$ in $6''$ apertures centered on the peak $\text{Pa}\alpha$ emission are a factor of ~ 2 lower on average than the $\text{SFR}_{[\text{H}\alpha+24\mu\text{m}]}$.

4. We compare $\text{SFR}_{[\text{H}\alpha]}$ to $\text{SFR}_{[\text{H}\alpha+24\mu\text{m}]}$ on a region-by-region basis to see the extent to which using $\text{H}\alpha$ to trace star formation in a nearby galaxy merger is limited. We find a linear relation with a large scatter between $\text{SFR}_{[\text{H}\alpha]}$ and $\text{SFR}_{[\text{H}\alpha+24\mu\text{m}]}$ which demonstrates that the $\text{SFR}_{[\text{H}\alpha]}$ underestimates the true SFR by at least a factor of ~ 10 on average but ranges from 1-60 (Section 4.8.2). The reliability of $\text{H}\alpha$ as a tracer of star formation in Arp 299 is tested and we find that regions near the C-C' complex, as well as regions to the north and northwest of the nuclei have a similar $\text{SFR}_{[\text{H}\alpha]}$ and $\text{SFR}_{[\text{H}\alpha+24\mu\text{m}]}$ within factor of ~ 1 -3. $\text{H}\alpha$ recovers the true SFR outside the nuclei and in the interface region of Arp 299.
5. The nucleus of NGC 3690, region B1, has the highest SFR surface density when a $24\mu\text{m}$ SFR tracer is used and star forming complex region C has the highest $\Sigma_{\text{SFR} [\text{H}\alpha]}$ followed by IC 694 nucleus (region A), B1 and C' (Section 4.8.2). The low hydrogen recombination line SFR surface density in region A is likely due to the high level of extinction in $\text{H}\alpha$ and $\text{Pa}\alpha$ (Section 4.5).
6. The northwest region of Arp 299 has an $\text{H}\alpha$ peak associated the HI peak and a stellar cluster seen in the *HST* F814W optical image, which could either be a tidal dwarf galaxy or possible a large cluster in the disk of IC 694 or external cluster formed out of tidally stripped material (Section 4.8.2).
7. We explore the SFR-Mol relation between the SFR using $\text{SFR}_{[\text{H}\alpha+24\mu\text{m}]}$

and molecular gas surface densities in the nuclear regions of Arp 299 using $\text{CO}J = 2 \rightarrow 1$ and $\text{CO}J = 3 \rightarrow 2$ converted to $\text{CO}J = 1 \rightarrow 0$ using a line ratio. We also look at the SFR-dense gas surface density relation using $\text{HCN}J = 1 \rightarrow 0$ and $\text{HCO}^+J = 1 \rightarrow 0$ lines as dense gas tracers. We find the nuclear regions to lie on the SFR-Mol surface density relation found in high- z mergers (Daddi et al. 2010) and on the SFR-dense gas relation of Gao & Solomon (2004b) within the errors (Section 4.8.3).

8. Spatially resolved regions of size 1.3 kpc throughout the Arp 299 merger using $\text{CO}J = 2 \rightarrow 1$ and $\text{CO}J = 3 \rightarrow 2$ are strongly correlated in $\Sigma_{\text{SFR}} [\text{H}\alpha+24\mu\text{m}]$ and Σ_{Mol} and are found to lie above the Daddi et al. (2010) high- z merger relation in the SFR-Mol gas surface density plane while the integrated SFR-Mol surface densities lie on the (Daddi et al. 2010) relation (Section 4.8.4). The discrepancy is likely due to the lower α_{CO} chosen for Arp 299 or a combination of that and the choice in SFR tracer and spatial scale measured.
9. The SFR–Dense gas relations on 1.3 kpc scales in Arp 299 using $\Sigma_{\text{SFR}} [\text{H}\alpha+24\mu\text{m}]$ and $\text{HCN}J = 1 \rightarrow 0$ and $\text{HCO}^+J = 1 \rightarrow 0$ to trace Σ_{Dense} are strongly correlated and lie along the same line as the integrated values for Arp 299 (Section 4.8.5). Both the integrated and spatially resolved points lie above the Gao & Solomon (2004b) relation with the differences being the choice of α_{Dense} for Arp 299 of 5 and α_{Dense} of 10 used in that study, the SFR tracer ($\text{SFR}_{[\text{H}\alpha+24\mu\text{m}]}$ versus SFR from IRAS), or comparing different spatial scales.

10. Since $\text{SFR}_{[\text{H}\alpha]}$ recovers $\text{SFR}_{[\text{H}\alpha+24\mu\text{m}]}$ within a factor of $\sim 2\text{--}3$ (Section 4.8.2), we use it to investigate the SFR–HI gas surface density relation in the extranuclear regions of Arp 299 on 4.7 kpc scales. We compare SFR–HI surface density relation in Arp 299 to a sample of spiral and dwarf galaxies from Bigiel et al. (2010) and find that regions in Arp 299 seem to follow the same general trend as in the outer disks of normal spirals and dwarfs with the exception of a few points that have higher SFR surface densities (Section ??). The SFE of regions in Arp 299 are higher by a factor of ~ 6 compared to spirals and dwarfs and this could be due to the effects of a high velocity dispersion in interacting galaxies driving star formation, however the increase in SFE is not extreme and star formation is likely driven by molecular cloud collapse at a lower rate than in the nuclear regions.
11. We use the $[\text{NII}]/\text{H}\alpha$ strong line ratio was used to determine metallicities and find the mean metallicity of Arp 299 to be $12 + \log(\text{O}/\text{H})$ of 8.57 ± 0.01 (Section 4.8.6.1). Higher metallicities are found in the outer regions of Arp 299 and lower or diluted metallicities in the nuclear regions in agreement with merger scenario in which galaxy interactions drive lower metallicity gas from the outer regions of the system into the central regions (Kewley et al. 2010 and references therein).
12. A large uncertainty in calculating Σ_{Mol} is the CO–to– H_2 conversion factor, α_{CO} . We explore the variation of α_{CO} as a function of metallicity

IRAS 60 to 100 μ m flux ratio, and dust temperature. We use the relation from Narayanan et al. (2012) to compute $\alpha_{\text{CO}}(Z')$ as well as the F_{60}/F_{100} – α_{CO} and T_{dust} – α_{CO} from Magnelli et al. (2012) (Section 4.8.6.1). We find α_{CO} varies based on CO line transition used with a median value for $\text{CO}J = 2 \rightarrow 1$ of $3.2 \text{ M}_{\odot} \text{ pc}^{-2}(\text{K km s}^{-1})^{-1}$ to 3.6 using $\text{CO}J = 3 \rightarrow 2$ $\text{M}_{\odot} \text{ pc}^{-2}(\text{K km s}^{-1})^{-1}$ and the variation in α_{CO} is dominated by the lower $I(\text{CO})$ line intensities (Section 4.8.6.1). Both values are closer to the commonly used Galactic value of $4.5 \text{ M}_{\odot} \text{ pc}^{-2}(\text{K km s}^{-1})^{-1}$ (Bloemen et al. 1986) as opposed to the common starburst conversion factor of $0.8 \text{ M}_{\odot} \text{ pc}^{-2}(\text{K km s}^{-1})^{-1}$ (Downes & Solomon 1998) and the value previously found for Arp 299 of $\sim 0.4 \text{ M}_{\odot} \text{ pc}^{-2}(\text{K km s}^{-1})^{-1}$. The SFR–Mol relation using $\alpha_{\text{CO}}(Z')$ lowers the dispersion in the relations compared to a single conversion factor and moves the points to the right in Σ_{Mol} in between the Daddi et al. (2010) and Kennicutt (1998b) relations. The conversion factor using F_{60}/F_{100} and T_{dust} for Arp 299 are 0.67 and 0.99 $\text{M}_{\odot} \text{ pc}^{-2}(\text{K km s}^{-1})^{-1}$, respectively. A higher Milky Way value of α_{CO} for late interaction phase merger, Arp 299, may be more suitable than the lower values previously found. The other possibility is that α_{CO} likely varies as a function of interaction phase based on whether the system is in starburst mode and region by region in interacting galaxies.

The authors thank Daniela Calzetti and Brent Groves for informative discussions. A.H., N.J.E., and K.G. acknowledge support for this work from NSF Grant AST–0607793 to the University of Texas at Austin, and the State

of Texas. T. A. D. acknowledges funding from the European Community's Seventh Framework Programme (/FP7/2007-2013/) under grant agreement No 229517.

SDSS-III is managed by the Astrophysical Research Consortium for the Participating Institutions of the SDSS-III Collaboration including the University of Arizona, the Brazilian Participation Group, Brookhaven National Laboratory, University of Cambridge, Carnegie Mellon University, University of Florida, the French Participation Group, the German Participation Group, Harvard University, the Instituto de Astrofisica de Canarias, the Michigan State/Notre Dame/JINA Participation Group, Johns Hopkins University, Lawrence Berkeley National Laboratory, Max Planck Institute for Astrophysics, Max Planck Institute for Extraterrestrial Physics, New Mexico State University, New York University, Ohio State University, Pennsylvania State University, University of Portsmouth, Princeton University, the Spanish Participation Group, University of Tokyo, University of Utah, Vanderbilt University, University of Virginia, University of Washington, and Yale University.

Chapter 5

Interacting Galaxies in the A901/902 Supercluster with STAGES

I present a study of galaxy mergers and the influence of environment in the Abell 901/902 supercluster at $z \sim 0.165$, based on 893 bright ($R_{\text{Vega}} \leq 24$) intermediate mass ($M_* \geq 10^9 M_\odot$) galaxies. I use *HST* ACS F606W data from the Space Telescope A901/902 Galaxy Evolution Survey (STAGES), COMBO-17, *Spitzer* 24 μm and *XMM-Newton* X-ray data. My analysis utilizes both a physically driven visual classification system, and quantitative CAS parameters to identify systems which show evidence of a recent or ongoing merger of mass ratio $> 1/10$ (i.e., major and minor mergers). My results are: (1) After visual classification and minimizing the contamination from false projection pairs, I find that the merger fraction f_{merge} is 0.023 ± 0.007 . The estimated fractions of likely major mergers, likely minor mergers, and ambiguous cases are 0.01 ± 0.004 , 0.006 ± 0.003 , and 0.007 ± 0.003 , respectively. (2) All the mergers lie outside the cluster core of radius $R < 0.25$ Mpc: the lack of mergers in the core is likely due to the large galaxy velocity dispersion in the core. The mergers, instead, populate the region ($0.25 \text{ Mpc} < R \leq 2 \text{ Mpc}$) between the core and the cluster outskirts. In this region, the estimated frequency of mergers is similar to those seen at typical group overdensities in N-body simulations

of accreting groups in the A901/902 clusters. This suggests ongoing growth of the clusters via accretion of group and field galaxies. (3) I compare our observed merger fraction with those reported in other clusters and groups out to $z \sim 0.4$. Existing data points on the merger fraction for $L \leq L^*$ galaxies in clusters allow for a wide spectrum of scenarios, ranging from no evolution to evolution by a factor of ~ 5 over $z \sim 0.17$ to 0.4 . (4) In A901/902, the fraction of mergers, which lie on the blue cloud is $80\% \pm 18\%$ (16/20) versus $34\% \pm 7\%$ or (294/866) for non-interacting galaxies, implying that interacting galaxies are preferentially blue. (5) The average SFR, based on UV or a combination of UV+IR data, is enhanced by a factor of ~ 1.5 to 2 in mergers compared to non-interacting galaxies. However, mergers in the A901/902 clusters contribute only a small fraction (between 10% and 15%) of the total SFR density, while the rest of the SFR density comes from non-interacting galaxies.

5.1 Introduction and Motivation

Understanding how galaxies evolve in various environments (field, groups, and clusters), and as a function of redshift is a key step toward developing a coherent picture of galaxy evolution. Present-day cluster and field galaxies differ due to several factors, which are often grouped under the umbrella of ‘nature’ versus ‘nurture’. First, in cold dark matter (CDM) cosmogonies, the first galaxies formed and evolved early in cluster cores, as the higher initial overdensities led to faster gravitational collapse and more rapid mergers of proto-galaxies (e.g., Cole et al. (2000); Steinmetz & Navarro (2002)). Second,

in the context of the bottom-up CDM assembly paradigm, the outer parts of clusters and superclusters, grow at late times via mergers, smooth accretion, and discrete accretion of groups and field galaxies. This idea is supported by observational studies (e.g., Zabludoff & Franx (1993); Abraham et al. (1996); Balogh & Morris (2000)), which suggest that clusters continuously grew by the accretion of groups. Third, the dominant physical processes affecting galaxies differ in cluster and field environments due to the different galaxy number density, galaxy velocity dispersion, and intracluster medium (ICM). Among these processes are close galaxy-galaxy interactions, such as strong tidal interactions and mergers (e.g., Barnes (1992); Moore et al. (1998)) and galaxy harassment (e.g., Moore et al. (1996)), which stems from the cumulative effect of weak interactions. Furthermore, in clusters where the hot ICM makes up as much as 15% of the total mass, galaxy-ICM interactions, such as ram pressure stripping (Gunn & Gott 1972; Larson et al. 1980; Quilis et al. 2000; Balogh & Morris 2000), can play an important role in removing the diffuse gas from galaxies. The tidal field of the cluster potential may also play a relevant role in the dynamical evolution of cluster galaxies (Gnedin 2003).

Systematic studies of the differences between cluster, group, and field galaxies at different redshifts are needed to shed light on the relative importance of these various processes in their respective environments. Several differences have been observed between galaxies in the field and those in the rich cluster environment, but the physical drivers behind these variations are still under investigation. At $z \sim 0$, the relative percent of massive

early type (E+S0) galaxies to spirals rises from (10%+10%:80%) in the field to (40%+50%:10%) in the cores of very rich clusters, leading to the so-called morphology density relation (Dressler 1980; Dressler et al. 1997). However, recent Sloan Digital Sky Survey (SDSS) studies suggest that masses and star formation (SF) histories of galaxies are more closely related to environmental physical processes rather than their structural properties (Blanton et al. 2005). The SF histories of galaxies depend on both luminosity (Cole et al. 2001) and environment (Diaferio et al. 2001; Koopmann & Kenney 2004). The fraction of blue galaxies in clusters appears to rise with redshift, an effect known as the Butcher Oemler effect (Butcher & Oemler 1978; Margoniner et al. 2001; De Propris et al. 2003). There is also evidence that SF in bright ($M_v < -18$) cluster galaxies is suppressed compared to field galaxies (e.g., Balogh et al. (1998, 1999)), for reasons that are not well understood.

Galaxy interactions and mergers have been proposed as a mechanism for the change in galaxy populations in clusters from that of the field (e.g., Toomre & Toomre (1972); Lavery & Henry (1988); Lavery et al. (1992). There have been various studies on the properties of galaxies (e.g., Dressler (1980); Postman & Geller (1984); Giovanelli et al. (1986); Gavazzi & Jaffe (1985); Kennicutt & Kent (1983); Whitmore et al. (1993)) and of galaxy interactions and mergers (e.g., Lavery & Henry (1988); Lavery et al. (1992); Zepf (1993); Dressler et al. (1994); Couch et al. (1998); van Dokkum et al. (1998, 1999); Tran et al. (2005, 2008)) in different environments. Some of these studies suggest that galaxy interactions and mergers may play a role in morphological

transformations of galaxies in clusters, but there have been few systematic studies of galaxy mergers and interactions in clusters, based on high resolution *HST* images as well as *Spitzer* 24 μ m, and X-ray images.

In this work we present a study of the frequency, distribution, color, and star formation properties of galaxy mergers in the A901/902 supercluster at $z \sim 0.165$. We use *HST* ACS F606W data taken as part of the Space Telescope A901/902 Galaxy Evolution Survey (STAGES; Gray et al. (2009)), along with ground-based COMBO-17 imaging data (Wolf et al. 2004), *Spitzer* 24 μ m data (Bell et al. 2005, 2007), *XMM-Newton* X-ray data (Gilmour et al. 2007), and dark matter (DM) mass measurements from weak lensing (Heymans et al. 2008). With a resolution of 0.1'' or ~ 280 pc at $z = 0.165$, the *HST* images allow for the identification of merger signatures such as double nuclei, arcs, shells, tails, tidal debris, and accreting satellites. The COMBO-17 survey (Wolf et al. 2004) provides accurate spectrophotometric redshifts down to R_{Vega} of 24 and stellar masses (Borch et al. 2006). The *Spitzer* 24 μ m data (Bell et al. 2005, 2007) probe the obscured SF, while X-ray maps (Gilmour et al. 2007) provide information of how the ICM density changes throughout the cluster.

We present the data and sample selection in §5.2. In §5.3.2 and §5.3.4, we describe the two different methods that we use to identify galaxy mergers: a physically motivated classification system that uses visual morphologies, stellar masses, and spectrophotometric redshifts, and a method based on CAS asymmetry A and clumpiness S parameters (Conselice

et al. 2000). In §Section 5.4.1 and 5.4.2, we explore the frequency of galaxy mergers in A901/902 based on these two methods and present one of the first systematic comparisons to date between CAS-based and visual classification results in clusters. We set a lower limit on the fraction of major mergers (those with mass ratio $M_1/M_2 \geq 1/4$). In §Section 5.4.3, we examine the distribution of mergers in the A901/902 supercluster as a function of clustocentric radius, galaxy number density, local galaxy surface density, relative ICM density, and local DM mass surface density. In §Section 5.4.4, we compare our results on the fraction and distribution of mergers to expectations based on analytical estimates and simulations of mergers in different environments. In §Section 5.4.5, we compare our results on galaxy mergers in the A901/902 supercluster to groups and clusters at different redshifts out to $z \sim 0.8$. We investigate the fraction of mergers and non-interacting galaxies on the blue cloud and red sample as a function of clustocentric radius in §Section 5.4.6. Finally in §Section 5.4.7, we compare the star formation rate (SFR) of mergers and non-interacting galaxies in the A901/902 clusters. The results of this work are summarized in §Section 5.7. In this paper, we assume a flat cosmology with $\Omega_m = 1 - \Omega_\lambda = 0.3$ and $H_0 = 70 \text{ km s}^{-1} \text{ Mpc}^{-1}$ throughout this paper.

5.2 The A901/902 Supercluster: Dataset and Sample Selection

The A901/902 supercluster is composed of three clusters: A901a, A901b, and A902, and related groups (Gray et al. 2002; Heymans et al. 2008). This

study utilizes data from the STAGES survey Gray et al. (2009), which provides high resolution F606W *Hubble Space Telescope* (*HST*) Advanced Camera for Surveys (ACS) images over a $0.5^\circ \times 0.5^\circ$ field. Additional multi-wavelength data include *XMM-Newton* (Gilmour et al. 2007), *Spitzer* 24 μ m data (Bell et al. 2005, 2007), and ground based COMBO-17 imaging data (Wolf et al. 2004).

Stellar masses are taken from Borch et al. (2006). They were derived by fitting the 17-band COMBO spectral energy distributions (SEDs) with a library of template SEDs, which were constructed using the PEGASE stellar population synthesis model, assuming different star formation histories and a Kroupa (Kroupa et al. 1993) initial mass function (IMF) in the mass regime 0.1–120 M_\odot . Such stellar masses are consistent within 10% with masses estimated using a Kroupa (2001) or Chabrier (2003) IMF¹.

Accurate spectrophotometric redshifts down to $R_{\text{Vega}} \sim 24$ and spectral energy distributions, based on 5 broad bands (*UBVRI*) and 12 medium band filters, are available from the COMBO-17 project (Wolf et al. 2004). The 1-sigma redshift error ($\sigma_{z(R)}$) modeled from spectroscopic redshifts that are available for a subset of 420 galaxies, scales as:

$$\frac{\sigma_{z(R)}}{(1+z)} = 0.005 \times \sqrt{1 + 10^{0.6(R-20.5)}} \quad (5.1)$$

¹We adopt a Chabrier (2003) IMF when exploring the contribution of mergers to the SFR in §Section 5.4.7

where R is the apparent R -band magnitude of the galaxy measured in a $1.5''$ aperture.

The reduction of the ACS images and the selection of the A901/902 supercluster sample are described in detail in Gray et al. (2009), and we only provide a summary here. STAGES A901/902 object detection was automated using source extractor (SExtractor; Bertin & Arnouts 1996) on the ACS F606W images, yielding $\sim 12,500$ galaxies with matching COMBO-17 counterparts down to $R_{\text{Vega}} \sim 24$. A subset of these galaxies were considered to be supercluster members based on their spectrophotometric redshifts. The spectrophotometric redshifts of cluster members were assumed to follow a Gaussian distribution with a half-width (Δz) related to $\sigma_{z(R)}$. A galaxy is considered to be a cluster member if its spectrophotometric redshift z lies in the range $[0.17 - \Delta z, 0.17 + \Delta z]$, where

$$\Delta z(R) = \sqrt{0.015^2 + (1.65\sigma_{z(R)})^2} \quad (5.2)$$

The resulting dependence of the half-width Δz on R ensures a completeness level of $> 90\%$ at all magnitudes for $R_{\text{Vega}} \leq 24$. The field contamination (i.e., the fraction of galaxies that are field members) for this sample is estimated by assuming that the average number count of field galaxies as a function of magnitude and redshift is consistent with the trends determined from regions lying outside of the cluster. The amount of field contamination rises strongly at fainter magnitude due to the increase of $\sigma_{z(R)}$ at fainter R ,

and typical values are 20% at $R_{\text{Vega}} = 21.65$ and $\sim 70\%$ at $R_{\text{Vega}} = 24$ (see Figures 13 and 14 of Gray et al. (2009)).

The top panel of Figure 5.1 shows the distribution of apparent R -band magnitude, absolute magnitude M_V , and stellar mass for the sample of 1990 galaxies with $R_{\text{Vega}} \leq 24$. We obtain our working sample of 893 galaxies by applying a further cut of $M_* \geq 10^9 M_\odot$ for the following reasons. First, for $M_* \geq 10^9 M_\odot$, the sample is complete in stellar mass on the red cloud and blue sequence (Borch et al. 2006), while at lower masses incompleteness sets in. Second, as shown in the middle panel of Figure 5.1, most galaxies with $R_{\text{Vega}} \leq 24$ and $M_* \geq 10^9 M_\odot$ actually have apparent magnitudes of $R_{\text{Vega}} \leq 21.7$, where the field contamination is $\leq 20\%$ (see Figures 13 and 14 of Gray et al. (2009)). Third, most galaxies with $M_* \geq 10^9 M_\odot$ have a luminosity $M_V \leq -18$ (Figure 5.1), where the cluster luminosity function (Binggeli et al. 1988) is typically dominated by E to Sd galaxies, rather than small dwarf galaxies. The former galaxies are large and many of their morphological features (e.g., disks, bars, bulges, spiral arms, double nuclei, arcs, shells, tails, tidal debris, and accreting satellites) can be resolved by the STAGES ACS F606W images whose effective point spread function (PSF) of $\sim 0.1''$ correspond to ~ 280 pc at $z = 0.165$.

5.3 Methodology and Analysis

5.3.1 Galaxy Mergers in this study

Before outlining the methods (§Section 5.3.2 and §Section 5.3.4) that we use to identify mergers, we briefly discuss the types of mergers that are of

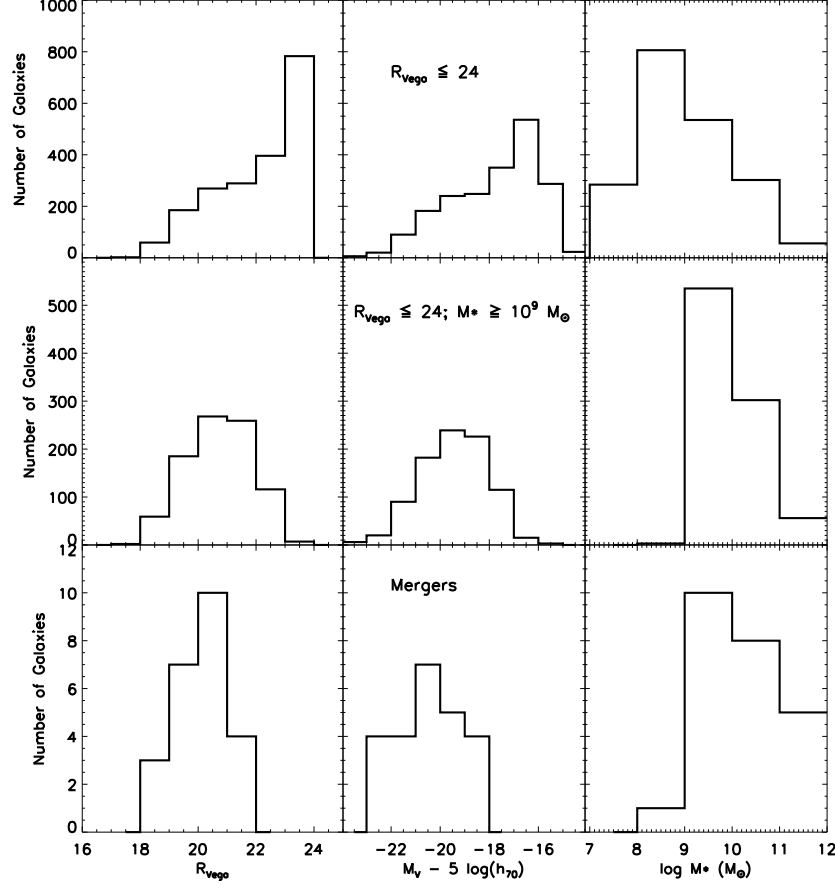


Figure 5.1 **Top panel:** Apparent R -band magnitude (R_{Vega}), absolute visual magnitude (M_V), and stellar mass (M_*) distributions of the full A901/902 supercluster sample ($R_{\text{Vega}} \leq 24$; 1983 galaxies). **Middle panel:** Same as the top panel, but showing the properties of the sample of 893 intermediate mass galaxies ($M_* \geq 10^9 M_\odot$). **Bottom panel:** Same as the middle panel, but only showing the properties of the 24 galaxies, which are part of the 20 morphologically distorted mergers identified among the sample (see §Section 5.3.2 and Table 5.2 for details). These 20 mergers are labeled with a starred identification number in Table 5.2 and are Cases 1–13, 16–18, 20, 24, 34, 35 in Table 5.2. For the four mergers of type 2b (which are close pairs resolved by COMBO-17) we plot the properties of the eight individual galaxies making up the pair, thus resulting in a total of 24 galaxies. Each pair has a galaxy of mass $M_* \geq 10^9 M_\odot$ and a second galaxy that may be of any mass.

interest to our study, their morphological signatures, and their typical post-merger products.

According to simulations, galaxy mergers of mass ratio $M_1/M_2 > 1/10$ tend to have a significant impact on galaxy evolution. They include major mergers, which are defined to be those with a mass ratio of $1/4 < M_1/M_2 \leq 1/1$, as well as minor mergers with $1/10 < M_1/M_2 \leq 1/4$. Simulations show that major mergers of stellar systems typically destroy the outer disks, transforming them via violent relaxation into systems with a steep central surface brightness profile, associated with a high Sérsic index n (typically $n > 2.5$; Hopkins et al. (2009)). These remnants include ellipticals and spheroids with a de Vaucouleurs-type stellar profile ($n = 4$) (e.g., Negroponte & White (1983); Barnes & Hernquist (1991); Mihos & Hernquist (1996); Struck (1997); Naab & Burkert (2001)). In gas-rich major mergers, a disk component can form or survive inside the resulting spheroidal component (Hopkins et al. 2009), producing a remnant whose overall profile is less steep than a de Vaucouleurs one, with $n < 4$. Irrespective of the details of the remnants, the above simulations suggest that ongoing/recent major mergers are associated with arcs, shells, ripples, tidal tails, large tidal debris, extremely asymmetric light distributions, double nuclei inside a common body, and tidal bridges/envelopes of light linking systems of similar mass.

Conversely, minor mergers involving a spiral galaxy and a smaller satellite of mass ratio $1/10 < M_1/M_2 \leq 1/4$, will not destroy the outer disk of the larger companion (e.g., Hernquist & Mihos 1995; Smith & Madden 1997; Jogee

et al. 1999). Typically, the smaller companion sinks via dynamical friction, may excite bars, spirals, and other non-axisymmetric perturbations in the disk of the larger galaxy, and leads to tidal heating, arcs, shells, ripples, tidal tails, tidal debris, warps, offset rings, and highly asymmetric light distributions (e.g., Quinn et al. 1993; Hernquist & Mihos 1995; Mihos 1995; Smith & Madden 1997; Jogee et al. 1999; Jogee 2006 and references therein).

In this work, we identify merging systems using two independent methods, which make use in different ways of the aforementioned morphological signatures seen in simulations. The first is a physically motivated classification system (§Section 5.3.2), which is similar to that defined in Jogee et al. (2008, 2009), and is based on visual morphologies, stellar masses, and spectrophotometric redshifts. The second method (§Section 5.4.2) uses the CAS merger criterion ($A > 0.35$ and $A > S$), which is based on quantitative asymmetry (A), and clumpiness (S) parameters derived using the CAS code (Conselice et al. 2000).

5.3.2 Visual classification of mergers and non-interacting galaxies

We visually classify the ACS F606W images of galaxies in the sample of 893 bright ($R_{\text{Vega}} \leq 24$) intermediate mass ($M_* \geq 10^9$) galaxies. This sample is complete for $M_* \geq 10^9 M_\odot$ (see §Section 5.2). In §Section 5.4.1, we will discuss whether further mass cuts should be applied in order to ensure the completeness of major and minor mergers, but for now we consider all the systems in the sample of 893 galaxies. A small fraction (below 1%) of

the sample could not be classified due to image defects, low signal to noise, and a highly compact appearance. As illustrated in Figure 5.2, the remaining galaxies are classified into 5 main visual classes: Mergers of types 1, 2a, and 2b, and Non-interacting systems of type Symmetric and Irr-1.

The visual class ‘Mergers’ is assigned to systems with evidence of a recent or ongoing merger of mass ratio $> 1/10$. The mergers are subdivided into 3 groups called Type 1, Type 2a, and Type 2b, because different criteria are used to identify these three types of mergers and different techniques are used to separate them into major and minor mergers. Non-interacting systems are subdivided into the visual classes of Symmetric and Irr-1. The results of the visual classification are illustrated in Tables 5.1- 5.2, and Figures 5.3- 5.5. Below are details of the 5 main visual classes.

(A) Mergers of type 1: Mergers of type 1 are systems, which appear as a single distorted remnant in the ACS F606W image (with effective PSF $\sim 0''.1$ or ~ 280 pc at $z = 0.165$), and which host morphological distortions similar to those produced in the afore-mentioned simulations of mergers of mass ratio $> 1/10$. Thus, mergers of type 1 likely represent the very advanced phases of such a merger, at a point where the 2 progenitor galaxies have coalesced into a single merger remnant. Among the sample of $M_* \geq 10^9 M_\odot$ systems, we find 13 mergers of type 1. Their properties are shown in Table 5.2 and Figure 5.3. They show morphological distortions such as tidal tails (Figure 5.3, Cases 10, 11), shells, ripples, warps, asymmetric tidal debris and distortions (e.g., Cases

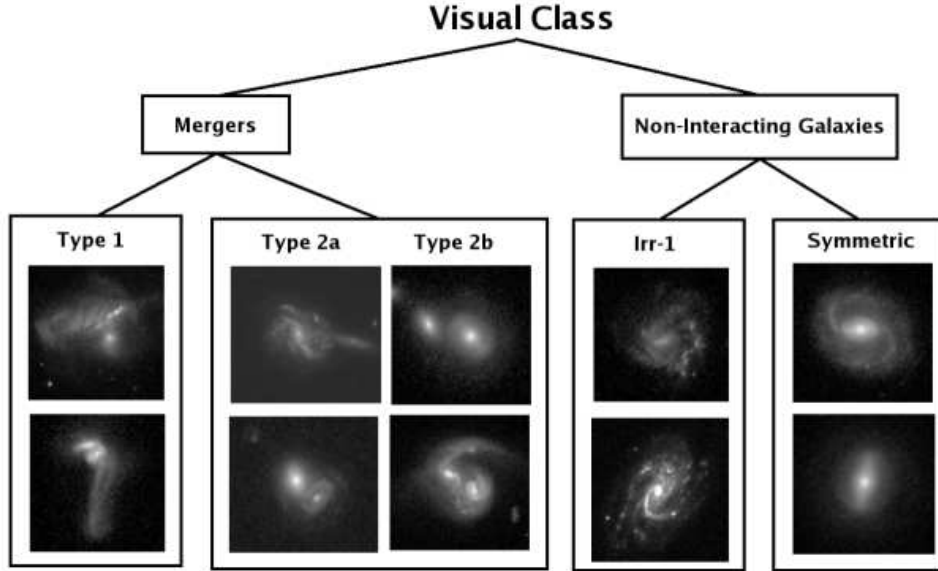


Figure 5.2 In our visual classification scheme (§Section 5.3.2), systems are classified as Mergers, or Non-interacting. The mergers are sub-divided into three groups called Type 1, Type 2a, and Type 2b. Mergers of Type 1 appear, in the ACS F606W image, as a single morphologically distorted remnant, rather than two individually recognizable galaxies. The remnant hosts strong *externally triggered* morphological distortions similar to those seen in simulations of mergers of mass ratio $> 1/10$, such as tidal tails, shells, ripples, warps, strongly asymmetric tidal debris, double nuclei inside a common envelope, or a ‘train-wreck’ morphology. In contrast, mergers of type 2a and 2b appear in ACS images as a very close ($d < 10$ kpc) overlapping pair of two recognizable galaxies. Mergers of type 2b are resolved into two separate galaxies by the ground-based COMBO-17 data, while mergers of type 2a are not. Since some of these type 2a and 2b systems could be due to chance line-of-sight superposition, we conservatively consider for the final analysis only those pairs where at least one member is morphologically distorted (see Table 5.2 and Figure 5.3 for details). Non-interacting systems are sub-divided into Irr-1 and Symmetric systems. Irr-1 exhibit *internally triggered* asymmetries, due to star formation typically on scales of a few hundred parsecs. Symmetric systems include galaxies, which are relatively undistorted and are not part of the very close pairs that constitute the mergers of Types 2a and 2b.

Table 5.1. Visual Classification Results for the sample of bright intermediate-mass ($M_* \geq 10^9 M_\odot$) galaxies

Visual Class (1)	N_{VC} (2)	f_{VC} (3)
Mergers of Type 1 + 2a+ 2b	13+3+4 = 20	0.023±0.007
Non-interacting Irr-1	123	0.14±0.03
Non-interacting Symmetric	743	0.80±0.16
Unclassifiable	6	-

Note. — The results of visual classification (see §Section 5.3.2 for details) for the sample of bright intermediate-mass ($M_* \geq 10^9 M_\odot$) systems. Columns: (1) Visual class (VC); (2) N_{VC} = Number of systems with a given VC.; (3) f_{VC} = Fraction of systems with a given VC.

5, 6, 7, 9), or a ‘train-wreck’ morphology (Cases 7, 10, 11, 12).

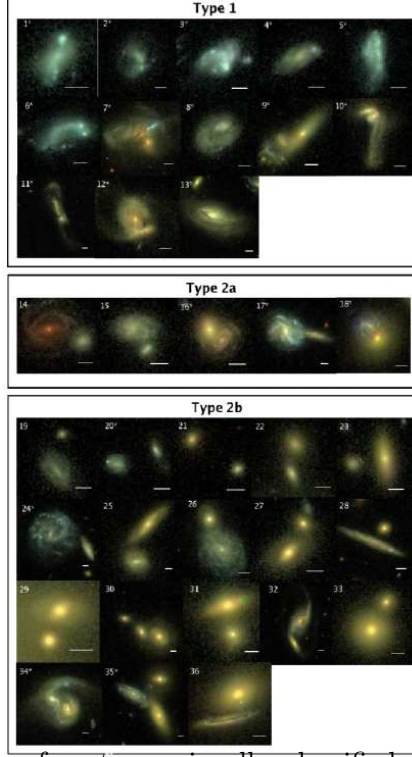


Figure 5.3 ACS images of systems visually classified as mergers of type 1 and *potential* mergers of type 2a and 2b, respectively (§Section 5.3.2). White horizontal bars denote a scale of $1''$ or 2.8 kpc at $z \sim 0.165$. **Top panel:** The 13 distorted remnants classified as type 1 mergers hosts strong *externally triggered* morphological distortions similar to those seen in simulations of mergers of mass ratio $> 1/10$, such as tidal tails (e.g., 10, 11), shells, ripples, warps, asymmetric tidal debris and distortions (e.g., 5,6,8,9), double nuclei inside a common envelope, or a ‘train-wreck’ morphology (7, 10–12). The type 1 mergers can be divided into major mergers (7, 10–12), minor mergers (Cases 8,9,13), and ambiguous ‘major or minor’ mergers (1-6; §Section 5.3.2. **Middle & Lower panels:** The 23 potential mergers of type 2a and 2b shown here include both real and projection very close ($d < 10$ kpc) pairs. The 7 likely real pairs (16–18, 20, 24, 34, 35) are denoted with a starred identification number and contain at least one galaxy with morphological distortions indicative of a galaxy-galaxy interaction. In the final analysis, only the 13 distorted mergers of Type 1 and the 7 distorted mergers of types 2a and 2b are used Type 2b pairs are resolved by COMBO-17 data into two galaxies with separate redshifts and stellar masses, and their stellar mass ratio (listed in Table 5.2) is used to divide Type 2b mergers into major mergers (20–22, 24–26, 28, 29, 23, 34) and minor mergers (19, 23, 27, 30, 31, 33, 35, 36). For the Type 2a pairs, which are unresolved by COMBO-17, the ACS-based luminosity ratio (Table 5.2) of the pair members is used to divide them into major (16, 18) and minor (14, 15, 17) mergers.

Table 5.2. Visual Classification of Mergers in the Sample of Bright Intermediate-mass ($M_* \geq 10^9 M_\odot$) galaxies

Merger ID	Merger Mass ($10^9 M_\odot$)	M_1 for Type 2b ($10^9 M_\odot$)	M_2 for Type 2b ($10^9 M_\odot$)	M_1/M_2 for Type 2b	L_1/L_2 for Type 2a	Major, Minor, or Ambiguous
(1)	(2)	(3)	(4)	(5)	(6)	(7)
Mergers of Type 1						
1*	1.22					Ambiguous
2*	1.31					Ambiguous
3*	1.62					Ambiguous
4*	1.64					Ambiguous
5*	1.64					Ambiguous
6*	2.73					Ambiguous
7*	6.66					Major
8*	8.06					Minor
9*	23.3					Minor
10*	24.4					Major
11*	46.0					Major
12*	122.1					Major
13*	191.5					Minor
Potential Mergers of Type 2a						
14	2.32				6.9	Minor
15	5.25				6.0	Minor
16*	13.0				1.4	Major
17*	36.5				5.0	Minor
18*	281.5				1.1	Major
Potential Mergers of Type 2b						
19	1.52	1.32	0.20	6.60		Minor
20*	1.95	1.12	0.83	1.35		Major
21	3.24	2.48	0.76	3.26		Major
22	7.90	5.34	2.56	2.09		Major
23	14.6	13.3	1.33	10.		Minor
24*	20.0	15.1	4.94	3.06		Major

Table 5.2 (cont'd)

Merger ID	Merger Mass ($10^9 M_\odot$)	M_1 for Type 2b ($10^9 M_\odot$)	M_2 for Type 2b ($10^9 M_\odot$)	M_1/M_2 for Type 2b	L_1/L_2 for Type 2a	Major, Minor, or Ambiguous
(1)	(2)	(3)	(4)	(5)	(6)	(7)
25	21.0	14.3	6.73	2.12		Major
26	33.6	24.1	9.45	2.55		Major
27	43.5	35.6	7.86	4.53		Minor
28	44.3	26.1	18.2	1.43		Major
29	58.9	37.4	21.5	1.74		Major
30	60.5	52.2	8.34	6.26		Minor
31	79.2	71.8	7.38	9.73		Minor
32	110.6	83.1	27.5	3.02		Major
33	126.4	113.8	12.6	9.03		Minor
34*	154.6	117.0	37.6	3.11		Major
35*	202.6	169.0	16.6	10.18		Minor
36	238.6	214.6	24.0	8.94		Minor

Note. — The table shows the visually classified mergers, which are identified in the sample of 893 bright ($R_{\text{Vega}} \leq 24$) intermediate-mass ($M_* \geq 10^9 M_\odot$) galaxies. The mergers are sub-divided into three groups: mergers of type 1 and *potential* mergers of type 2a and 2b, according to the criteria outlined in §Section 5.3.2. Table Columns: (1) Numerical identifier corresponding to the potential mergers in Figure 5.3. Note that the very close ($d < 10$ kpc) pairs listed as potential mergers of Type 2a and 2b in this table includes both real and projection pairs. The likely real pairs are marked with a star in Column 1 and contain at least one galaxy with morphological distortions indicative of a galaxy-galaxy interaction. In the final analysis, only the 13 distorted mergers of Type 1 and the 7 distorted mergers of types 2a and 2b are used; (2) The mass of the merger. For pairs of type 2b, which are resolved into two galaxies by COMBO-17 data, the mass cited is the sum ($M_1 + M_2$) of the pair members; (3) For mergers of Type 2b, the mass M_1 of one galaxy in the pair; (4) For mergers of Type 2b, the mass M_2 of the second galaxy in the pair; (5) For mergers of Type 2b, the mass ratio (M_1/M_2); (6) For mergers of Type 2a, the luminosity ratio (L_1/L_2), measured from ACS images; (7) The classification of the merger into major merger, minor merger, or ambiguous ‘major or minor’, according to the criteria outlined in §Section 5.3.2.

For mergers of type 1, a single redshift and stellar mass are available. Thus, the evidence for a merger of mass ratio $> 1/10$ does not come from a measured stellar mass ratio M_1/M_2 , but instead is inferred from the presence of the afore-mentioned morphological distortions, which are seen in simulations of mergers of mass ratio $> 1/10$.

Ideally, one would like to further separate the mergers of type 1 into major and minor mergers, as defined in §Section 5.3.1. However, without individual stellar masses M_1 and M_2 for the progenitors, and with only morphological distortions as a guide, this is not possible in every case since the morphological disturbances induced depend not only on the mass ratio of the progenitors, but also depend to some extent on the orbital geometry (prograde or retrograde), the gas mass fraction, and structural parameters (e.g., Mihos & Hernquist (1996); Struck (1997); Naab & Burkert (2001); Mihos (1995); Di Matteo et al. (2007)). Therefore, we separate the type 1 mergers into three groups: likely major mergers, likely minor mergers, and ambiguous cases of ‘major or minor’ mergers as follows:

- (i) The class of likely major mergers includes systems, which host fairly unique tell-tale morphological distortions characteristic of a major merger, such as a train-wreck morphology (e.g., Cases 7, 10, 11, 12 in Figure 5.3), or 2 nuclei of similar luminosities.
- (ii) A system is classified as a likely minor merger if the outer disk has survived a recent merger. We base this on the results of simulations of mergers involving spiral galaxies where the outer disk of the spiral survives a

minor merger, but not a major merger (§Section 5.3.1). This is not true in every case: major mergers of extremely gas-rich disks with low star formation efficiency can lead to a remnant with an extended stellar disk (Robertson et al. 2004), but such mergers are unlikely to be relevant for our study, which focuses on intermediate-mass ($M_* \geq 10^9 M_\odot$) systems at redshifts well below 1. An additional secondary criterion for classifying a system as a likely minor merger is that the light from morphological distortions, tidal debris, or accreted system in the surviving disk is a small fraction (between 1/4 and 1/10) of the total luminosity of the disk. Examples include Cases 8, 9, 13 in Figure 5.3 and Table 5.2.

- (iii) The class of ambiguous ‘major or minor’ merger is assigned to systems hosting distortions, which could be due to both a major and a minor merger. Examples are Cases 1–6 in Figure 5.3 and Table 5.2.

(B) Mergers of type 2a and 2b: Mergers of type 2a and 2b are systems, which appear in ACS images as a very close (separation $d < 10$ kpc) overlapping pair of two galaxies, and whose properties suggest they are in the very late phases of a merger of mass ratio above 1/10. The difference between mergers of type 2a and 2b is that the latter are resolved into two separate galaxies by the ground-based COMBO-17 data of resolution $\sim 1''.5$ (corresponding to ~ 4.3 kpc at $z \sim 0.165$), while the former are not. Thus, mergers of type 2a only have a single redshift and a single stellar mass for the pair, while mergers of type 2b have stellar masses (M_1, M_2) and spectrophotometric redshifts ($z_1,$

z_2) for both pair members.

We focus only on very close pairs (with $d < 10$ kpc), and ignore widely separated pairs for several reasons. First, in this work, we are interested in systems with evidence for a recent or ongoing merger of mass ratio $> 1/10$. The very close pairs represent the very late phases of such a merger, such that gravitationally bound members can coalesce into a remnant on a short timescale, comparable to the visibility timescale over which the morphological distortions in mergers of type 1 persist. Second, we expect the morphological distortions from the ongoing merger to be more prominent in close pairs than widely separated ones. These morphological signatures in turn make it easier to separate real pairs from projection pairs. Third, as shown by our Monte Carlo simulations (see below), the statistical contamination from projection pairs increases significantly for distant pairs.

When identifying potential mergers of type 2b, we consider very close pairs where one pair member has $M_* \geq 10^9 M_\odot$, and its companion satisfies the following two conditions. First, the companion has a mass such that the mass ratio is in the range $1/10 < M_1/M_2 \leq 1/1$. Note that this condition allows for pairs where the companion can be of higher, as well as lower mass (see Table 5.2). Second, the companion has similar spectrophotometric redshift, such that the absolute value of $(z_1 - z_2)$ is less than or equal to the 1-sigma redshift error σ_z . The latter criterion helps to remove some of the false projection pairs. However, there is still residual contamination by false pairs as σ_z is fairly large (see §Section 5.2 ; $\sigma_z \sim 0.028$ at $R_{\text{Vega}} = 23.0$).

We identified 5 and 18 potential candidate mergers of type 2a and 2b, respectively, in our final sample of 886 systems. They are shown in Figure 5.3 and Table 5.2. We use the term “potential mergers of type 2a and 2b” when describing the 23 very close ($d < 10$ kpc) galaxy pairs listed in Table 5.2 (Cases 14–36), because these pairs could be a mix of real pairs and false projection pairs caused by chance line-of-sight superposition. In order to minimize the contamination from false projection pairs, we only include in our final analysis those pairs where at least one galaxy shows morphological distortions indicative of a galaxy-galaxy interaction. Such pairs are most likely to be real pairs, as opposed to projection pairs, and we will use these systems to set a firm lower limit to the merger fraction in §Section 5.4.1. We find 7 such pairs (Cases 16–18, 20, 24, 34,35), which are marked with a star in column 1 of Table 5.2. This suggests that the remaining 16/23 or up to 70% of the types 2a and 2b could potentially be pairs in projection, due to the dense cluster environment.

As a second step to gauge the level of contamination from projection pairs, we performed a Monte Carlo simulation. We generated a random galaxy distribution which has an identical redshift distribution to that of our sample of intermediate-mass ($M_* \geq 10^9 M_\odot$) galaxies, over the STAGES $0.5^\circ \times 0.5^\circ$ field. We ran 100 realizations of this Monte Carlo simulation. For each realization, we took the ratio ($N_{\text{obs}}/N_{\text{mc}}$) of observed to simulated Monte Carlo pairs at different separations (d) out to 140 kpc. The same criteria outlined in §Section 5.3.2 to identify the pairs in the observations are applied to the

simulated galaxies. Namely, we apply the condition that the absolute value of the difference in spectrophotometric redshifts of the galaxies in a pair must be less than or equal to the 1-sigma redshift error σ_z , in order for the galaxies to be counted as a pair. Figure 5.4 shows the ratio $(N_{\text{obs}}/N_{\text{mc}})$ plotted as a function of d , with the four panels showing the mean, median, minimum, and maximum values of $(N_{\text{obs}}/N_{\text{mc}})$. Our results are qualitatively similar to those found by Kartaltepe et al. (2007). At large separations of $d > 50$ kpc, $(N_{\text{obs}}/N_{\text{mc}})$ is below 1, and false projection pairs can dominate the statistics. At small separations of $d < 20$ kpc, $(N_{\text{obs}}/N_{\text{mc}})$ is well above 1, suggesting that random chance superposition cannot fully account for all the observed pairs. Thus, by picking pairs with a separation of $d < 20$ kpc, one can reduce the contamination from false pairs. For $d < 20$ kpc, the mean value of the contamination level (defined as the fraction of observed pairs that are false) ranges from 16% to 55% and has a median value of 36%. The maximum contamination level is a factor of ~ 1.3 lower than the factor of 70%, which we derived in the preceding paragraph, by assuming that all pairs without morphological distortions are projection pairs. One possible explanation for the difference is that the afore-described Monte Carlo simulations do not take into account the large-scale structure and possible overdensity of galaxies associated with the central parts of the supercluster.

We next attempt to separate the mergers of type 2a and 2b into major and minor mergers. For mergers of type 2b, where stellar masses (M_1 , M_2) are available for each pair member, we can use the stellar mass ratio M_1/M_2

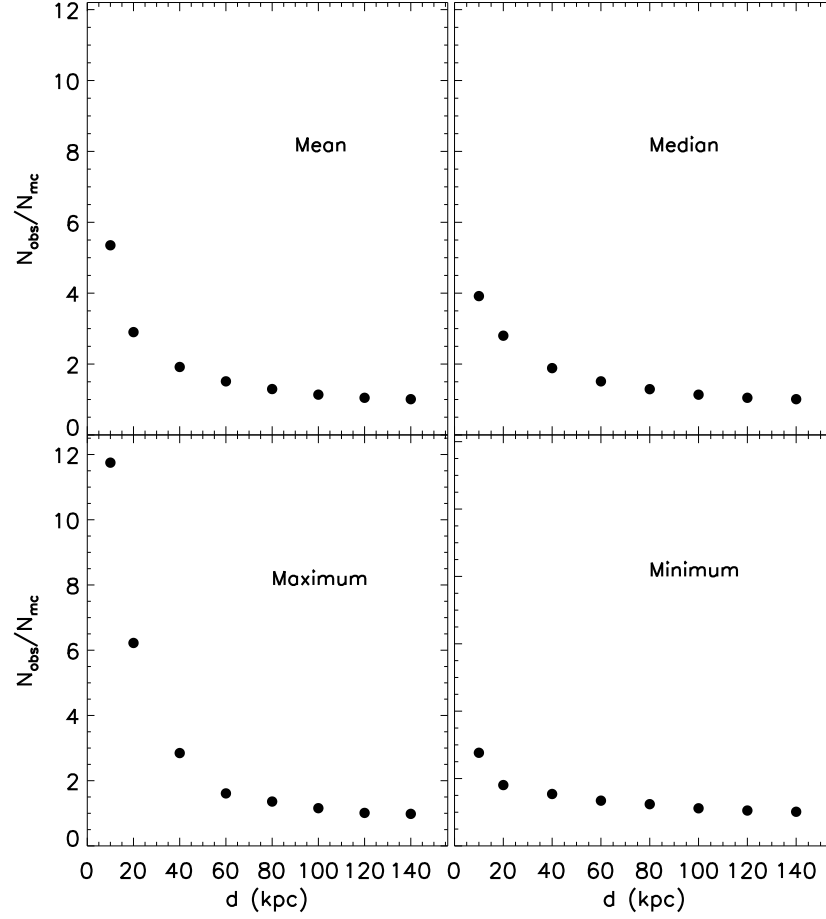


Figure 5.4 The ratio ($N_{\text{obs}}/N_{\text{mc}}$) for pairs of different projected separations d , where N_{obs} and N_{mc} are the number of pairs measured in the observations and random pairs from the Monte Carlo simulations, respectively. See §Section 5.3.2 for details. The four panels represent the mean, median, minimum and maximum distribution as labeled. At smaller separations of $d < 50$ kpc, ($N_{\text{obs}}/N_{\text{mc}}$) is above 1, suggesting that random chance superposition cannot fully account for all the observed pairs.

(see Table 5.2). By definition, systems with $1/10 < M_1/M_2 \leq 1/4$ and $1/4 < M_1/M_2 \leq 1$ are classified, respectively, as minor and major mergers. As shown in Table 5.2, potential major mergers of type 2b are Cases 20-22, 24-26, 28, 29, 32, and 34, while Cases 19, 23, 27, 30, 31, 33, 35, and 36 are potential minor mergers of type 2b.

Mergers of type 2a, however, only have a single redshift and a single stellar mass, and hence the stellar mass ratio of the pair is not directly measurable. Instead, we use the stellar light ratio L_1/L_2 , measured from the ACS images, as an approximate proxy (see Table 5.2). Examples of likely major mergers of type 2a are Cases 16 and 18 in Figure 5.3, while Cases 14, 15, and 17 are examples of likely minor mergers of type 2a.

(C) Non-interacting systems of type Symmetric and Irr-1 : The remaining systems, which show no indication of a recent merger, according to the criteria outlined in sections A and B above, are classified as non-interacting systems. They are subdivided into two groups called ‘Non-interacting Irr-1’ and ‘Non-interacting Symmetric’. ‘Non-interacting Irr-1’ systems exhibit *internally triggered* asymmetries, typically on scales of a few hundred parsecs. These asymmetries are generally due to stochastic star formation and/or low ratios of rotational to random velocities. They can impart a clumpy morphology to a galaxy and are different from externally-driven distortions, such as tails and ripples, which are often correlated on scales of several kpc. The class of ‘Non-Interacting Symmetric’ consists of galaxies, which are relatively

undistorted. Note that this class includes the undistorted galaxies, which are part of these type 2a and 2b pairs identified as projection pairs in Section B. Examples of ‘Non-interacting Irr-1’ and ‘Non-interacting Symmetric’ galaxies are shown in Figure 5.5.

In summary after performing the visual classification of the 893 bright ($R_{\text{Vega}} \leq 24$) intermediate mass ($M_* \geq 10^9$) galaxies, we find the following results. We identify 13 merger remnants of type 1 (Cases 1–13 in Table 5.2 and Figure 5.3), and 7 close pairs of type 2a and 2b (Cases 16–18, 20, 24, 34, 35 in Table 5.2 and Figure 5.3) where at least one galaxy in the close pair shows morphological distortions indicative of a galaxy-galaxy interaction. Such pairs are most likely to be real pairs, as opposed to projection pairs. We discount those very close pairs where none of the members are morphologically distorted. Our final sample includes 20 mergers and 866 non-interacting galaxies (123 Irr-1 + 743 Symmetric; see Table 5.1).

5.3.3 Tests on the Visual Classes

Several tests were performed on the visual classes described in A, B, and C in §Section 5.3.2. The visual classifications were calibrated by having three classifiers (AH, IM, SJ) train on a set of ~ 100 nearby field galaxies. The full supercluster sample was then classified by AH and IM, with all ambiguous cases and interacting galaxies discussed by all three classifiers for final determination. Random checks on sub-samples of galaxies were performed by SJ. We denote as f_{VC} the fraction of intermediate-mass ($M_* \geq 10^9 M_{\odot}$) systems with

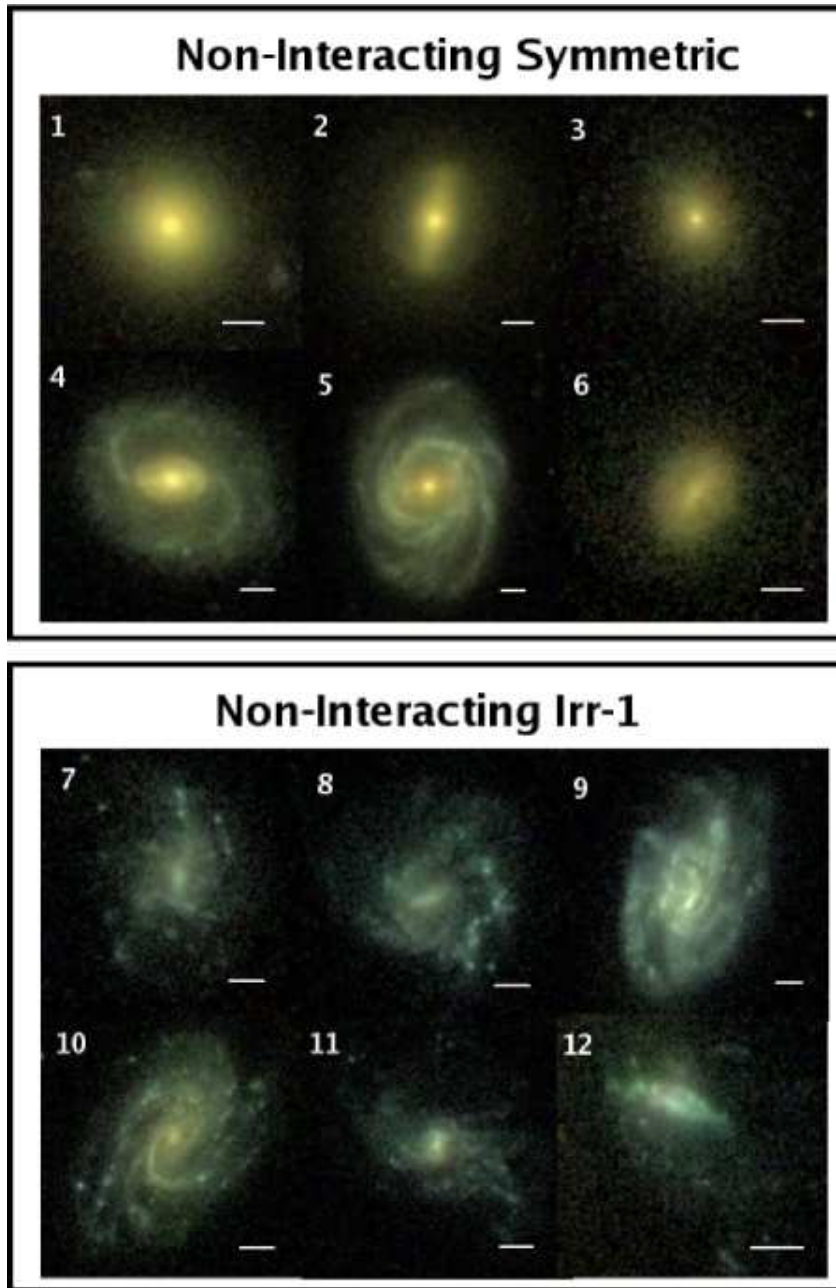


Figure 5.5 ACS F606W images of some of the systems visually classified as Non-interacting Symmetric (Cases 1-6) and Non-interacting Irr-1 (Cases 7-12). See §Section 5.3.2 for details.

different visual classes (e.g., mergers of types 1, 2a, and 2b, and non-interacting systems of type Symmetric and Irr-1). In order to gauge the subjectivity inherent in any visual classification scheme, we estimate the maximum difference in the value of f_{VC} across the classifiers (δf_{VC}). The maximum percentage difference P defined as $(100 \times \delta f_{\text{VC}}/f_{\text{VC}})$ is 4%, 19%, and 16% respectively for the visual classes of Non-interacting Symmetric, Non-interacting Irr-1, and Mergers. We conservatively adopt a value of 20% for P on the mean merger fraction, as a measure of the inherent subjectivity in the visual classification. When citing the final error bar on f_{VC} , we combine in quadrature the term δf_{VC} , which represents the subjectivity across classifiers, and the binomial error term ($\sqrt{f_{\text{VC}}(1 - f_{\text{VC}})/N}$), where N is the sample size of 886 systems. The raw values for f_{VC} are shown in Table 5.1.

It is also interesting to explore any systematic effects affecting the mergers we identified visually. The criteria we used, based on morphological distortions, might beg the question of whether these mergers are biased toward a gas-rich population. The extent to which a galaxy develops morphological distortions in an interaction depends on whether the encounter is prograde or retrograde, the interaction phase, the gas content, and the mass ratio (M_1/M_2). Di Matteo et al. (2007) found that the most influential parameters are the mass ratio and orbital geometry, and not the gas content alone. The visibility timescale (t_{vis}) on which the morphological signatures persist also depend on the orbital geometry, gas content, and the mass ratio. We do not have a direct measurement of the gas content of galaxies in A901/902, so we attempt an in-

direct first-order test in order to verify whether our methodology preferentially picks gas-rich mergers. We visually classify sample galaxies into three broad classes: ‘highly smooth’, ‘highly clumpy’, and ‘other’. If a system shows a high degree of clumpiness (i.e. very patchy regions that are likely associated with significant amounts of gas, dust, and SF), it is classified as ‘highly clumpy’. Conversely, systems with a very smooth non-clumpy appearance are classified as ‘highly smooth’.

Out of the 20 mergers and 866 non-interacting galaxies, we find that 6/20 (30%) and 210/866 (24%) are classified as ‘highly clumpy’, respectively. The comparable fraction of ‘highly clumpy’ systems among non-interacting systems and mergers suggests that our method for identifying mergers does not show a strong bias toward preferentially selecting mergers, which are highly clumpy, gas-rich, and star-forming. It is also interesting to recall here that our visual classification scheme takes special care to distinguish between Non-interacting Irr-1 and mergers (§Section 5.3.2). The Non-interacting Irr-1 galaxies were defined as those where internally triggered small-scale asymmetries, often due to SF, are present. Thus, as expected, if we separate our non-interacting galaxies into Irr-1 and Symmetric, we find that a large fraction of the Non-interacting Irr-1 (111/123 or 90%) are ‘highly clumpy’, compared to 99/713 (14%) of the Non-interacting Symmetric systems.

5.3.4 CAS: Quantitative method for capturing interacting galaxies

Using the CAS code (Conselice et al. 2000, 2003), quantitative structural parameters measuring the concentration (C), asymmetry (A), and clumpiness (S) were derived for the supercluster galaxies. CAS was run on the F606W images and the segmentation maps produced during the original source extraction (Caldwell et al. 2008) were used to mask neighboring galaxies.

The CAS concentration index C (Bershady et al. 2000) is proportional to the logarithm of the ratio of the 80%–20% curve of growth radii within 1.5 times the Petrosian inverted radius at $r(\eta = 0.2)$:

$$C = 5 \times \log \left(\frac{r_{80\%}}{r_{20\%}} \right). \quad (5.3)$$

The CAS code derives the asymmetry index A (Conselice et al. 2003) by rotating a galaxy image by 180 deg, subtracting the rotated image from the original image, summing the absolute intensities of the residuals, and normalizing the sum to the original galaxy flux. CAS improves the initial input center with the IRAF task ‘imcenter’ and then performs a further refinement within a 3×3 grid, picking the center that minimizes A .

The clumpiness parameter S is a quantitative measure of the high spatial frequency patchiness of a galaxy. It is defined as the summation of the difference of the galaxy’s original flux and the flux of an image with the high frequency structures muted by smoothing over a filter on order of the clumpiness, taking into account the background flux over that same area. This mea-

surement is then divided by the summation of the original flux of the galaxy to obtain the clumpiness parameter S .

Conselice et al. (2000) argue that the CAS merger criterion ($A > S$ and $A > 0.35$) at $\lambda_{\text{rest}} > 4500 \text{ \AA}$ can be used to capture galaxies which have strong asymmetries indicative of major mergers. However, calibrations of the asymmetry value with N-body simulations (Conselice 2006; Lotz et al. 2008) have shown that for galaxies involved in major mergers of mass ratios 1:1–1:3, the asymmetries vary as a function of time during the merger. The A value reaches a peak near the midpoint of the merger and falls off both before and after this time to less than 0.35. The criterion $A > 0.35$ is fulfilled only $\sim 1/3$ of the time for major mergers in these simulations, while minor mergers of mass ratios below 1:5 have A values significantly lower than 0.35.

Furthermore, in intermediate mass ($M_* \geq 10^9 M_\odot$) field galaxies at $z \sim 0.24\text{--}0.80$, recent work (Jogee et al. 2008, 2009; Miller et al. 2008) has shown that the CAS criterion typically only picks up 50%–70% of galaxies visually typed as being disturbed or interacting. These results caution against using CAS without complementary visual classifications in field galaxies.

The effectiveness of the CAS criterion has not been explored in cluster environments where the dominant galaxy population is more gas-poor than in the field. In §Section 5.4.2, we present the merger fraction (f_{CAS}) from CAS and perform one of the first systematic comparisons to date between CAS-based and visual classification results in clusters.

5.4 Results and Discussion

5.4.1 Merger fraction in A901/902 from visual classification

Next we discuss how to define and estimate the merger fraction. Our goal is to estimate the fraction of f_{merge} of systems with stellar mass above an appropriately chosen mass cut M_{cut} , which are involved in mergers of mass ratio $\geq 1/10$. The merger fraction f_{merge} is computed as $(N_{\text{merge}}/N_{\text{tot}})$, where N_{merge} is the number of major and minor mergers involving galaxies with $M_* \geq M_{\text{cut}}$, and N_{tot} is the total number of galaxies with $M_* \geq M_{\text{cut}}$.

It is important to determine the minimum stellar masses of the major and minor mergers involving galaxies with $M_* \geq M_{\text{cut}}$ and thereby assess for what value of M_{cut} we can trace such mergers. Major merger pairs (defined as having mass ratio $1/4 < M_1/M_2 \leq 1$) of mass ratio 1:1 to 1:3 will have minimum stellar masses ranging from $2 \times M_{\text{cut}}$ to $4 \times M_{\text{cut}}$, in cases where galaxies of mass $M_* \geq M_{\text{cut}}$ merge with systems at least as massive as themselves. However, if galaxies of mass $M_* \geq M_{\text{cut}}$ merge with lower mass systems, the minimum mass of 1:1 to 1:3 mergers will range from $2 \times M_{\text{cut}}$ to $(4 \times M_{\text{cut}}/3)$. Taken together, the above constraints imply that we are complete for major mergers involving galaxies with $M_* \geq M_{\text{cut}}$, as long as we can trace 1:3 major mergers with a minimum stellar mass of $(4 \times M_{\text{cut}}/3)$.

Repeating the exercise for minor mergers (defined as having $1/10 < M_1/M_2 \leq 1/4$), it follows that the minimum stellar mass for 1:4 to 1:9 mergers ranges from $5 \times M_{\text{cut}}$ to $9 \times M_{\text{cut}}$ or from $(5 \times M_{\text{cut}}/4)$ to $(10 \times M_{\text{cut}}/9)$, depending on whether galaxies of mass $M_* \geq M_{\text{cut}}$ merge with systems of higher mass or

lower mass. Thus, we are complete for minor mergers involving galaxies with $M_* \geq M_{\text{cut}}$, as long as we can trace 1:9 minor mergers with a minimum stellar mass of $(10 \times M_{\text{cut}}/9)$.

For what value of M_{cut} are these conditions satisfied by the mergers of Types 1, 2a, and 2b, which we visually identified in the final sample (§Section 5.3.2)? Since our final sample is complete for $M_* \geq 10^9 M_\odot$, it follows that we can identify all mergers of type 1 and 2a with $M_* \geq 10^9 M_\odot$ from this sample. If we impose this value to the afore-defined criteria of $(10 \times M_{\text{cut}}/9)$ and $(4 \times M_{\text{cut}}/3)$, it implies that a mass cut $M_{\text{cut}} \geq 0.9 \times 10^9 M_\odot$ would allow us to be complete for major and minor mergers of type 1 and 2a. However, the situation is different for the mergers of type 2b (close pairs resolved into two galaxies by COMBO-17) because the individual galaxies making up the pair are complete only for $M_* \geq 10^9 M_\odot$. As a result, we can only completely trace 1:3 major mergers of type 2b with total mass $\geq 4.0 \times 10^9 M_\odot$. If we impose this value to the afore-defined criterion of $(4 \times M_{\text{cut}}/3)$, it implies that a mass cut of $M_{\text{cut}} \geq 3.0 \times 10^9 M_\odot$ is needed to ensure completeness for major mergers of type 2b. Similarly, we can only completely trace 1:9 minor mergers of type 2b with total mass $\geq 9.0 \times 10^9 M_\odot$, which implies that a mass cut $M_{\text{cut}} \geq 9.0 \times 10^9 M_\odot$ is needed to completely trace all minor mergers of type 2b.

Using a mass cut $M_{\text{cut}} \geq 9.0 \times 10^9 M_\odot$ for computing the merger fraction f_{merge} would allow us to be complete for major and minor mergers of types 1, 2a, and 2b. However, it leads to very small number statistics and is not

viable. We therefore explore the value of f_{merge} for the less severe cut of $M_{\text{cut}} \geq 3.0 \times 10^9 M_{\odot}$, as well as for $M_{\text{cut}} \geq 10^9 M_{\odot}$. The cut of $M_{\text{cut}} \geq 3.0 \times 10^9 M_{\odot}$ ensures that we are complete for major and minor mergers of type 1, 2a, but leaves us incomplete for mergers of type 2b. It is encouraging that both cuts yield similar values for the merger fraction f_{merge} , as illustrated in Table 5.3: the merger fraction is 0.023 ± 0.007 and 0.021 ± 0.007 , respectively, for $M_{\text{cut}} \geq 10^9 M_{\odot}$ and $M_{\text{cut}} \geq 3.0 \times 10^9 M_{\odot}$. Note that in computing the merger fraction, we only include the 20 distorted mergers listed in Table 5.2, and avoid the potential projection pairs of type 2a and 2b without signs of morphological distortions ².

²Even if we included all pairs of type 2a and 2b, the merger fraction would still have similar values (0.041 ± 0.01 and 0.033 ± 0.01) for both mass cuts (Table 5.3).

Table 5.3. Merger fraction for different mass cuts

M_{cut} (M_{\odot}) (1)	N_{tot} (2)	N_1 (3)	N_{2a} (all) (4)	N_{2b} (all) (5)	N_{merge} (all) (6)	f_{merge} (all) (7)	f_{major} (all) (8)	f_{minor} (all) (9)	f_{ambig} (all) (10)
1×10^9	886	13	3(5)	4(18)	20(36)	0.023 \pm 0.007 (0.041 \pm 0.01)	9/886 (16/886)	5/886 (14/886)	6/886 (6/886)
3×10^9	609	7	3(4)	3(16)	13(27)	0.021 \pm 0.007 (0.033 \pm 0.01)	8/609 (15/609)	3/609 (12/609)	0 (0)

Note. — The merger fraction f_{merge} among systems above a mass cut (M_{cut}) is computed as ($N_{\text{merge}}/N_{\text{tot}}$), where N_{merge} is the number of galaxies with $M_* \geq M_{\text{cut}}$ involved in major and minor mergers, and N_{tot} is the total number of systems with $M_* \geq M_{\text{cut}}$. This table shows the value of f_{merge} for different mass cuts. Columns: (1) Mass cut M_{cut} in units of M_{\odot} ; (2) The total number N_{tot} of systems with $M_* \geq M_{\text{cut}}$; (3) Number N_1 of mergers of type 1 for this mass cut; (4) Number N_{2a} of mergers of type 2a for this mass cut.; (5) Number N_{2b} of mergers of type 2b for this mass cut; (6) N_{merge} , the total number of mergers of types 1, 2a, and 2b for this mass cut; (7) The merger fraction f_{merge} , computed as ($N_{\text{merge}}/N_{\text{tot}}$); (8) The major merger fraction, based on the classification in column 8 of Table 5.2; (9) Same as (8), but for the minor merger fraction; (10) Same as (8), but for the fraction of ambiguous mergers, which could be either major or minor mergers. In Columns 4–10, the first number without brackets apply to the case we only consider the 13 type 1 mergers and the subset of 7 reliable type 2a and 2b mergers, which are likely to be real pairs as they contain at least one member galaxy with morphological distortions indicative of a galaxy-galaxy interaction. The value in bracket apply to the case where we include the 13 type 1 mergers and all the 23 mergers of type 2a and 2b listed in Table 5.2, even those which are likely to be projection pairs and contain galaxies without morphological distortions.

While mergers may have played an important role in the evolution of cluster galaxies at earlier times (e.g., $z > 2$), hierarchical models (e.g., Gottlöber et al. 2001; Khochfar & Burkert 2001) predict that the merger fraction in dense clusters falls more steeply at $z < 1$ than the field merger fraction. As a result, at $z < 0.3$, the merger fraction for intermediate mass cluster galaxies is predicted to be quite low (typically below 5%). The low merger fraction among intermediate mass ($M = 10^9$ to a few $\times 10^{10} M_\odot$) galaxies in the A901/902 clusters is consistent with the latter prediction.

How are the mergers distributed among major mergers, minor mergers, and ambiguous cases that could be either major or minor mergers? The results are shown in Columns 8–10 of Table 5.3, based on the classification listed in Column 8 of Table 5.2. The estimated fractions of likely major mergers, likely minor mergers, and ambiguous cases are $0.01 \pm 0.004\%$ (9/886), $0.006 \pm 0.003\%$ (5/886), and $0.007 \pm 0.003\%$ (6/886), respectively for $M_{\text{cut}} \geq 10^9 M_\odot$. For $M_{\text{cut}} \geq 3.0 \times 10^9 M_\odot$, the corresponding fractions are $0.013 \pm 0.005\%$ (8/609), $0.008 \pm 0.004\%$ (5/609), and 0.0% (0/609), respectively.

In the rest of this paper, we continue to work with a mass cut of $M_{\text{cut}} \geq 10^9 M_\odot$, and the 20 distorted mergers (Table 5.2) applicable for this mass cut. However, where relevant, we cite many of our results for both of the mass cuts ($M_{\text{cut}} \geq 10^9 M_\odot$ and $M_{\text{cut}} \geq 3.0 \times 10^9 M_\odot$) so that we can gauge the potential effect of incompleteness in tracing major and minor mergers.

Table 5.4. Visual Classes of Galaxies Satisfying the CAS Criterion
($A > 0.35$ and $A > S$)

Visual Class (1)	$N_{\text{CAS-VC}}$ (2)	$f_{\text{CAS-VC}}$ (3)
All Visual Types	18	1.00
Merger	11	$11/18=0.61\pm0.2$
Non-interacting Irr-1	5	$5/18=0.28\pm0.1$
Non-interacting Symmetric	2	$2/18=0.11\pm0.08$

Note. — The table shows the visual classes (VC) of the galaxies, which satisfy the CAS criterion ($A > 0.35$ and $A > S$), among the sample of intermediate-mass ($M_* \geq 10^9 M_\odot$) systems. Columns: (1) Visual Class (VC) of galaxies satisfying the CAS criterion; (2) $N_{\text{CAS-VC}}$: the number of galaxies with this visual class satisfying the CAS criterion; (3) $f_{\text{CAS-VC}}$: the fraction of all the galaxies satisfying the CAS criterion, which have this visual class.

5.4.2 Frequency of mergers in A901/902 from CAS

The results of running CAS on the final classified sample of 886 intermediate-mass ($M_* \geq 10^9 M_\odot$) systems are shown in Table 5.4 and Figures 5.6 and 5.7. In Figure 5.6, the 20 mergers of type 1, 2a, and 2b are plotted in different symbols. For Type 2b merger pairs, we plot the highest value of CAS A found between the two galaxies in each system. Using the CAS merger criterion ($A > 0.35$ and $A > S$) to identify mergers yields a merger fraction (f_{CAS}) in this sample of $18/886$ or 0.02 ± 0.006 . For the more conservative sample with a mass cut $M_{\text{cut}} \geq 3 \times 10^9 M_\odot$, f_{CAS} is $7/609$ or 0.011 ± 0.005 .

When citing the error on f_{CAS} , we take the largest of either the Poisson error or the systematic error (σ_{CAS}) in f_{CAS} due to the systematic errors in

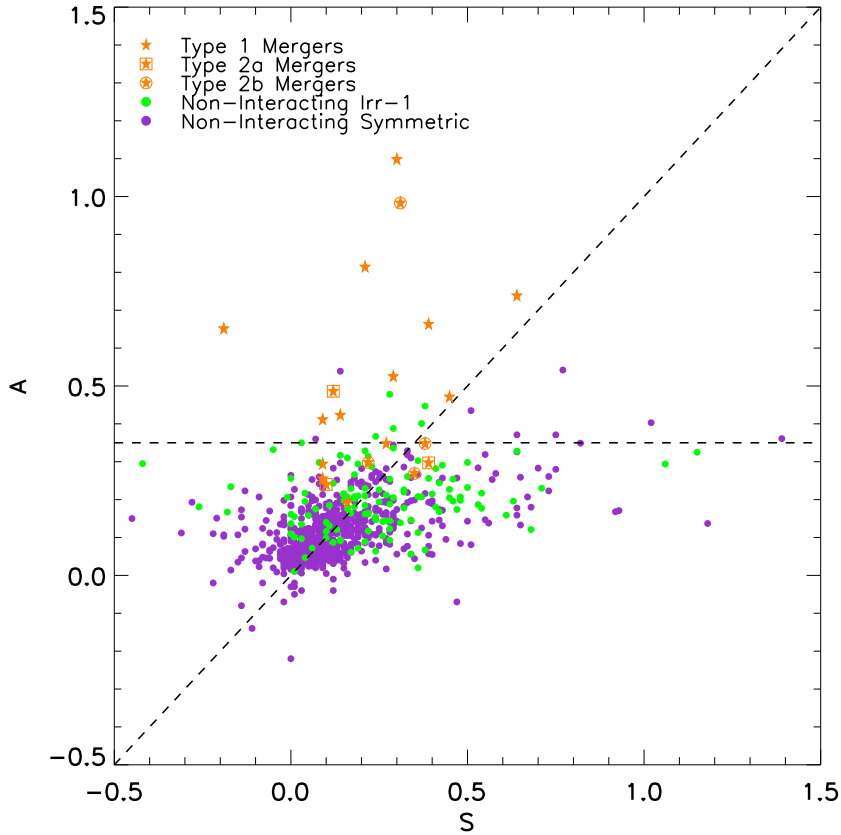


Figure 5.6 The results of running CAS on the sample of bright ($R_{\text{Vega}} \leq 24$) intermediate-mass ($M_* \geq 10^9 M_\odot$) systems are shown. Galaxies with different visual classes (Merger, Non-interacting Irr-1, and Non-interacting Symmetric) are shown in the CAS A vs. S plane. We only plot here the 20 distorted mergers of types 1, 2a, and 2b in Table 5.2. The 18 galaxies satisfying the CAS merger criterion ($A > S$ and $A > 0.35$) lie on the upper left corner of the diagram. The CAS merger criterion recovers 11 of the 20 ($61\% \pm 20\%$) of the galaxies visually classified as a merger. Furthermore, there is a significant level of contamination: 7/18 ($39\% \pm 14\%$) of the systems picked up by the CAS criterion are visually classified as Non-interacting Irr-1 and Non-interacting Symmetric.

CAS A and S . The systematic error, σ_{CAS} , is calculated by taking the upper and lower bounds of f_{CAS} based on $(A \pm \text{error in } A)$ and $(S \pm \text{error in } S)$. Specifically, these limits on f_{CAS} are found by using the criteria of $((A \pm \text{error in } A) < (S \pm \text{error in } S))$ and $((A \pm \text{error in } A) > 0.35)$.

At first sight, the CAS-based merger fractions f_{CAS} for the two mass cuts (0.020 ± 0.006 and 0.011 ± 0.005 for $M_{\text{cut}} \geq 10^9 M_{\odot}$ and $M_{\text{cut}} \geq 3 \times 10^9 M_{\odot}$, respectively) are not widely different from the merger fraction f_{merge} based on visual classification (0.023 ± 0.007 and 0.021 ± 0.007 for $M_{\text{cut}} \geq 10^9 M_{\odot}$ and $M_{\text{cut}} \geq 3 \times 10^9 M_{\odot}$, respectively; §Section 5.4.1). However, the comparison of f_{CAS} and f_{merge} does not tell the whole story because the nature of the systems picked by the two methods can be quite different. The visual classes of the 18 systems, which satisfy the CAS criterion and are considered as mergers in the CAS system, are shown in Table 5.4. It turns out 7/18 ($39 \pm 14\%$) of these “CAS mergers” are visually classified as non-interacting systems. The results are illustrated in Table 5.4 and Figure 5.6. Figure 5.7 shows examples of these “contaminants”: they tend to be dusty highly inclined systems and systems with low level asymmetries that seem to be caused by SF.

It is also useful to ask what fraction of the 20 systems visually-identified as mergers satisfy the CAS criterion. We find that for $M_{\text{cut}} \geq 10^9 M_{\odot}$, the CAS criterion only captures 11 of the 20 ($55 \pm 16\%$) of the visually-classified mergers. These results are illustrated in Figure 5.6. Figure 5.7 shows examples of merging galaxies missed by CAS. The missed mergers include galaxies with fainter outer tidal features, double nuclei where CAS puts the center between

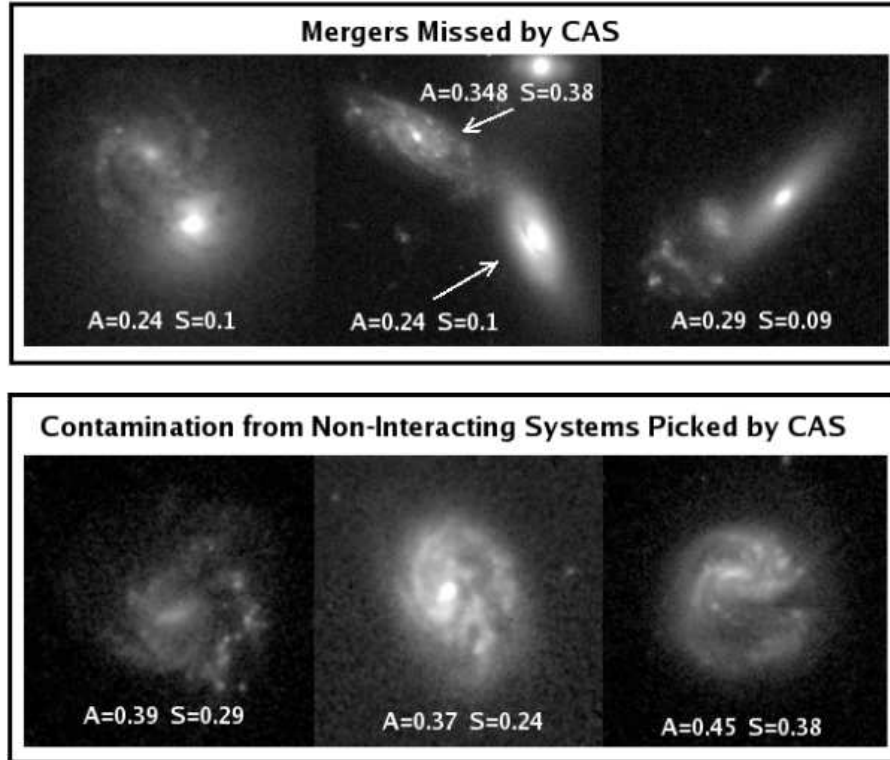


Figure 5.7 The top panel shows examples of mergers missed by the CAS merger criterion ($A > S$ and $A > 0.35$). Features of these systems include double nuclei, tidal bridges, and tidal debris. The lower panel show some non-interacting contaminants picked up by the CAS merger criterion, due to small-scale asymmetries from SF, strong patchy dust lanes, and the absence of a clear center, all leading to a larger A value.

the nuclei, and pairs of very close connected galaxies.

It is also interesting to ask what percentage of the different Types of mergers (Types 1, 2a, and 2b) does the CAS merger criterion recover. Figure 5.6 also shows the mergers divided up by merger types 1, 2a and 2b. Of the 13 mergers of type 1, CAS recovers 9/13 or $69\% \pm 18\%$. Of the 3 mergers of type 2a, CAS recovers 1/3 or $33\% \pm 28\%$. Of the 4 mergers of type 2b, CAS recovers 1/4 or $25\% \pm 22\%$.

Since the CAS criterion is widely used to pick major mergers, it is also interesting to explore how well this criterion picks up the systems that we visually classified as major mergers (Table 5.2). We find that the CAS merger criterion picks up 6/9 ($67\% \pm 20\%$) of the systems classified as major mergers. It is also interesting to note that the CAS criterion recovers 2/5 ($40\% \pm 23\%$) and 4/6 ($67\% \pm 23\%$) of the systems classified respectively as minor mergers and ambiguous mergers.

5.4.3 Distribution of mergers

In order to define different regions of the A901a, A901b, and A902 clusters, we computed the projected number density n (Figure 5.8) for intermediate-mass ($M_* \geq 10^9 M_\odot$) galaxies as a function of clustocentric radius R by assuming a spherical distribution. Note here that each galaxy is assigned to the cluster closest to it, and R is measured from the center of that cluster.

We consider the cluster core to be at $R \leq 0.25$ Mpc, as this is the region where the projected number density n rises very steeply (Figure 5.8).

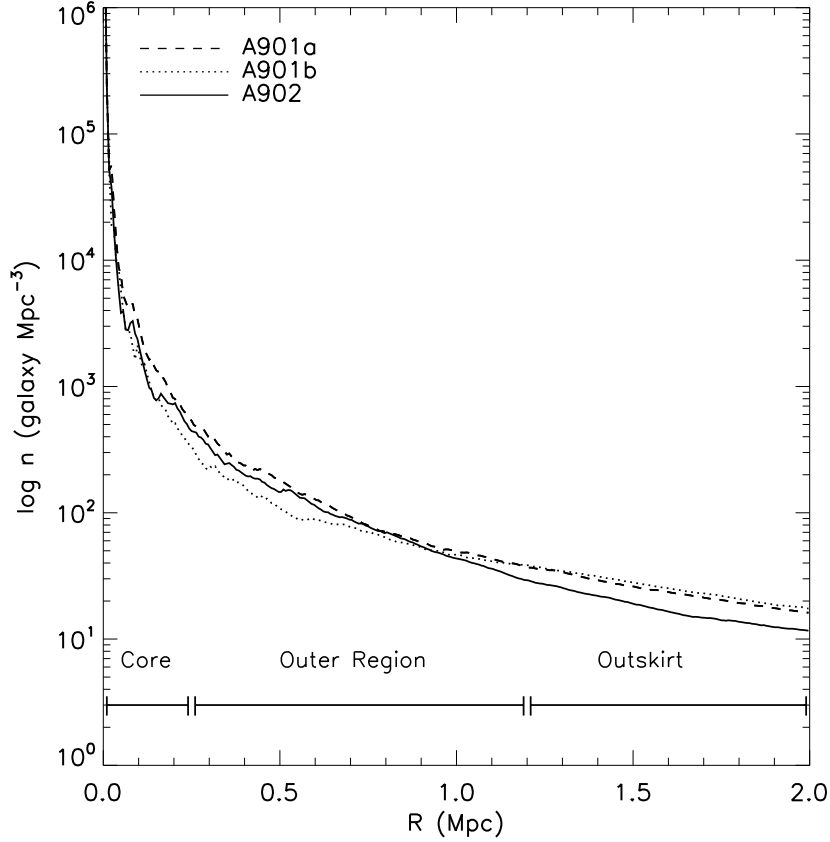


Figure 5.8 The azimuthally averaged projected number density n of bright ($R_{\text{Vega}} \leq 24$) intermediate-mass ($M_* \geq 10^9 M_\odot$) galaxies in the sample is shown as a function of clustocentric radius which is shown for each cluster A901a/b and A902. We consider the cluster core to be at $R \leq 0.25$ Mpc, as this is the region where the projected number density n rises very steeply. We refer to the region which is located at $0.25 \text{ Mpc} < R \leq 1.2 \text{ Mpc}$ between the cluster core and the cluster virial radius as the outer region of the cluster. The region outside the virial radius ($1.2 \text{ Mpc} < R \leq 2.0 \text{ Mpc}$) is referred to as the outskirts region of the cluster. The core, outer region, and outskirts region are labeled.

Table 5.5. Comparison of Projected Galaxy Number Densities n and σ_{gal}

System	Core $R \leq 0.25$ Mpc (galaxies Mpc $^{-3}$)	Outskirt $R > 1.2$ Mpc (galaxies Mpc $^{-3}$)	σ_{gal} (km s $^{-1}$)
Virgo ^a	360	75	400-750
Coma ^b	10000	400	~ 900
A901a ^c	1600	60	890 \pm 182
A901b ^c	1100	55	1189 \pm 266
A902 ^c	1000	40	792 \pm 176
Groups ^d	~ 0.01		~ 100

Note. — This table compares the projected galaxy number densities n and galaxy velocity dispersions σ_{gal} in the A901a, A901b, and A902 clusters to those of groups and other clusters, such as Coma and Virgo. For the A901 clusters, the value of n is computed using the sample of bright ($R_{Vega} \leq 24$) intermediate-mass ($M_* \geq 10^9 M_{\odot}$) galaxies. for the values cited are: a = Binggeli et al. (1988); b = The & White (1986); c = number densities are from this work, and the average local velocity dispersions are from Gray et al. (in preparation); d = Tago et al. (2008)

The cluster virial radii are taken to be ~ 1.2 Mpc, based on estimates from the DM maps derived from gravitational lensing by Heymans et al. (2008). Throughout this paper, we refer to the region at $0.25 \text{ Mpc} < R \leq 1.2 \text{ Mpc}$, between the cluster core and the cluster virial radius, as the ‘outer region of the cluster’. The region outside the virial radius ($1.2 \text{ Mpc} < R \leq 2.0 \text{ Mpc}$) is referred to as the ‘outskirt region of the cluster’. The core, outer region, and outskirts region are labeled on Figure 5.8.

As shown in Table 5.5, the A901 clusters have central galaxy number densities (n) in the core region of 1000–1600 galaxies Mpc $^{-3}$. These are lower than that of the rich Coma cluster and higher than that of the Virgo cluster.

Figure 5.9 shows the spatial distribution of the mergers visually identified among the sample of intermediate-mass ($M_* \geq 10^9 M_\odot$) galaxies in the A901a, A901b, and A902 clusters. We again consider here only the 20 distorted mergers listed in Table 5.2, for the reasons discussed in §Section 5.4.1. We find that all the 20 mergers lie outside the cluster cores. We estimate that the number density (n_{merge}) of mergers is 0, 2.09, and 0.11 galaxies Mpc^{-3} , respectively, in the core, outer region, and outskirts of the cluster (Table 5.6). When estimating n_{merge} in the three regions, we divided the number of mergers by the volume of the core region, and the volume of a spherical shell in the outer region and outskirts of the clusters.

For mergers and non-interacting galaxies, we compute the minimum distance to the nearest cluster center (A901a, A901b, and A902), and the local values of various environmental parameters, such as the local galaxy surface density Σ_{10} , the local DM mass surface density κ , and the relative local ICM density. Following Wolf et al. (2005) and Gilmour et al. (2007), we define and compute the local galaxy surface density (Σ_{10}) as the number of galaxies per $(\text{Mpc}/h)^{-2}$ that are in an annulus bracketed by two circles whose radii are equal to the average distances to the 9th and 10th nearest neighbor. The DM mass surface density (κ) is computed locally using the coordinates of each galaxy on the weak lensing map provided by Heymans et al. (2008). The relative local ICM counts are measured at each galaxy position using the X-ray map from Gray et al. (2010, in preparation) and Gilmour et al. (2007). Figure 5.10 shows these local environmental parameters as a function

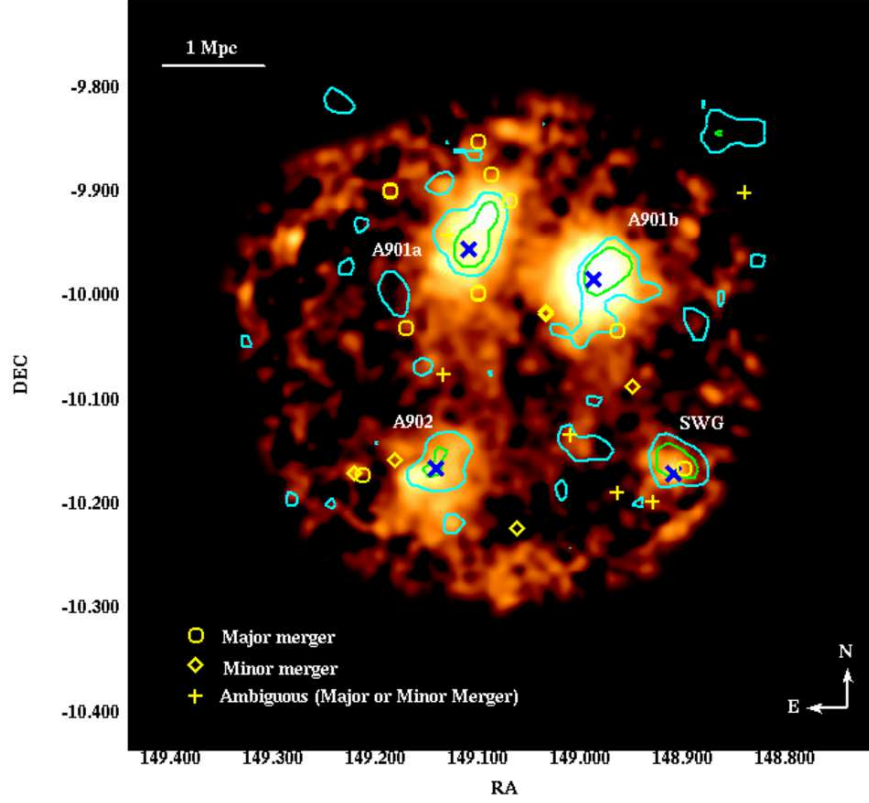


Figure 5.9 The distribution of visually-classified mergers (coded as yellow diamonds, circles, and crosses) among the final sample of bright ($R_{\text{Vega}} \leq 24$) intermediate-mass ($M_* \geq 10^9 M_\odot$) galaxies is shown, overlaid on the ICM density map (yellow-orange scale). We only plot here the final sample of 20 distorted mergers, shown with starred identification numbers in Table 5.2. Following Heymans et al. (2008) we show DM masses in terms of the signal-to-noise of the weak lensing detection. The cyan and green contours enclose roughly $6h^{-1}10^{13}M_\odot$ and $3.5h^{-1}10^{13}M_\odot$ for A901a and A901b, and roughly $3h^{-1}10^{13}M_\odot$ and $1.5h^{-1}10^{13}M_\odot$ for the lower mass A902 and South West Group (SWG). The different symbols represent major mergers (circles), minor mergers (diamonds), and ambiguous major or minor merger cases (crosses), identified in §Section 5.3.2. All mergers are located in the outer region and outskirts of each cluster ($0.25 \text{ Mpc} < R \leq 2 \text{ Mpc}$).

Table 5.6. Properties in Core, Outer Region, and Outskirt of A901/902 Clusters

	Cluster Core ($R \leq 0.25$ Mpc)	Cluster Outer Region ($0.25 \text{ Mpc} < R \leq 1.2 \text{ Mpc}$)	Outskirt ($1.2 \text{ Mpc} < R \leq 2.0 \text{ Mpc}$)
(1) N	85	533	195
(2) Volume V (Mpc ³)	0.065	7.17	26.3
(3) n (gal Mpc ⁻³)	1307	74.3	7.41
(4) $\langle B-V \rangle$	0.839	0.764	0.739
(5) $\langle U-V \rangle$	1.25	1.08	1.03
(6) t_{coll} (Gyr)	0.765	13.5	135
(7) $N_{\text{non-int}}$	84	519	192
(8) N_{merger}	0	15	3
(9) n_{merger} (merger Mpc ⁻³)	0	2.09	0.11
(10) f_{merger}	0	0.028	0.015
(11) $N_{\text{major-merger}}$	0	8	0
(12) $n_{\text{major-merger}}$ (merger Mpc ⁻³)	0	1.12	0
(13) $f_{\text{major-merger}}$	0	0.015	0.005
(14) $N_{\text{minor-merger}}$	0	5	0
(15) $n_{\text{minor-merger}}$ (merger Mpc ⁻³)	0	0.70	0
(16) $f_{\text{minor-merger}}$	0	0.009	0
(17) $N_{\text{non-int-BC}}$	7	178	81
(18) $f_{\text{non-int-BC}}$	0.08	0.34	0.42
(19) $N_{\text{merger-BC}}$	0	11	3
(20) $f_{\text{merger-BC}}$	0	0.73	1.0

Note. — This table shows galaxy properties and timescales in three different regions of the cluster: the core ($R \leq 0.25$ Mpc), the outer region ($0.25 \text{ Mpc} < R \leq 1.2 \text{ Mpc}$) between the core and the cluster, and the outskirts region ($1.2 \text{ Mpc} < R \leq 2.0 \text{ Mpc}$). The values are computed based on the sample of bright ($R_{\text{Vega}} \leq 24$) intermediate-mass ($M_* \geq 10^9 M_{\odot}$) systems. The rows are : (1) Total number of galaxies; (2) Volume of region; (3) Projected number density of galaxies; (4) Mean $B - V$ rest frame color; (5) Mean $U - V$ rest frame color; (6) Timescale for collisions or close encounters; (7) Number of non-interacting galaxies; (8) Number of mergers from Table 5.2; (9) Projected number density of mergers; (10) Fraction of mergers; (11)-(13): same as (8)-(10), but for major mergers; (14)-(16): same as (8)-(10), but for minor mergers; (17) Number of non-interacting galaxies on blue cloud; (18) Fraction of non-interacting galaxies on blue cloud; (19) Number of mergers on blue cloud; (20) Fraction of mergers on blue cloud.

of the minimum distance to the cluster center for mergers and non-interacting galaxies. Since the mergers lie outside the cluster core ($0.25 \text{ Mpc} < R \leq 2 \text{ Mpc}$), they are associated with low values of κ and intermediate values of Σ_{10} , and ICM density (Figure 5.10).

5.4.4 What accounts for the distribution of mergers?

The timescale for collisions and close encounters is given by:

$$t_{\text{coll}} = \frac{1}{n\sigma_{\text{gal}}A}, \quad (5.4)$$

where n is the galaxy number density, σ_{gal} is the galaxy velocity dispersion, A is the collisional cross section ($\pi f(2r_{\text{gal}})^2$), r_{gal} is a typical galaxy radius, and f is the gravitational focusing factor (Binney & Tremaine 1987). Since the average velocity dispersion in clusters is high, the value for f will be low and we will assume it to be on the order of unity. Thus,

$$t_{\text{coll}} \sim 800 \times \left(\frac{n}{10^3 \text{ Mpc}^{-3}} \right)^{-1} \times \left(\frac{\sigma}{10^3 \text{ km s}^{-1}} \right)^{-1} \times \left(\frac{r_{\text{gal}}}{10 \text{ kpc}} \right)^{-2} \text{ Myr} \quad (5.5)$$

We compute n using the same method as in §Section 5.4.3 for the core, and use spherical shells to compute n in the outer region and cluster outskirts for our sample of $R_{\text{Vega}} \leq 24$, intermediate mass ($M_* \geq 10^9 M_{\odot}$) galaxies. The local galaxy velocity dispersion profiles for A901a/b, A902, and the South West Group (SWG) from kinematic modeling using ~ 420 2dF

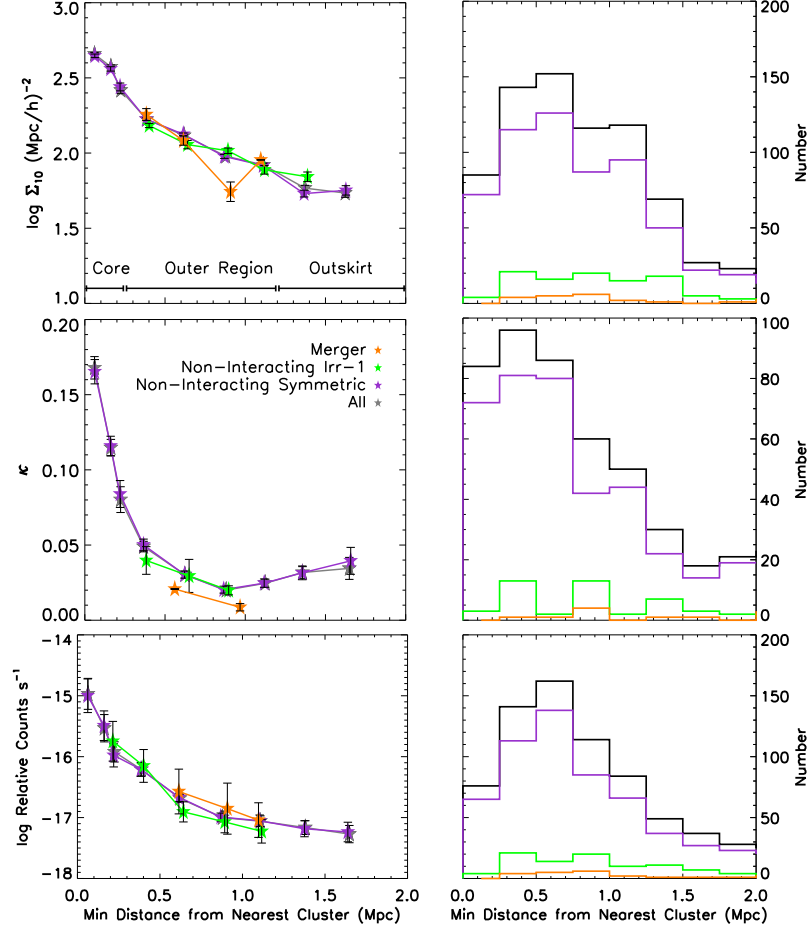


Figure 5.10 For mergers and non-interacting galaxies, the minimum distance to the nearest cluster center (A901a, A901b, A902) is plotted against the values of various local environmental parameters, such as the local galaxy surface density (Σ_{10}) (**top left**), the local DM mass surface density (κ) (**middle left**), and the relative local ICM density (**bottom left**). The panels on the right-hand side show the number of mergers and non-interacting galaxies which are found at different for each parameter. Mergers lie in the outer region and outskirts of the cluster ($0.25 \text{ Mpc} < R \leq 2 \text{ Mpc}$) and are associated with low values of κ and intermediate values of Σ_{10} , and ICM density.

redshifts (Meghan Gray, private communication) are shown in Figure 5.11, and the average velocity dispersions σ_{gal} are shown in Table 5.5.

The central galaxy velocity dispersion within the cores ($R < 0.25$ Mpc) of A901a,b and A902 typically range from 700 to 1000 km s⁻¹. Beyond the cluster core, in the outer region ($0.25 \text{ Mpc} < R \leq 1.2 \text{ Mpc}$), the small number statistics leads to large error bars on the galaxy velocity dispersion, making it not viable to determine whether it remains high, drops, or rises. To estimate timescales, we take the average σ_{gal} for A901/902 to be ~ 800 km s⁻¹ in three regions of the cluster. The timescales (t_{coll}) for close encounters are shown in Table 5.6 and range from 0.765 to 13.5 to 135 Gyrs from the core ($R \leq 0.25$ Mpc), to the outer region ($0.25 \text{ Mpc} < R \leq 1.2 \text{ Mpc}$), to the outskirts region ($1.2 \text{ Mpc} < R \leq 2.0 \text{ Mpc}$) of the cluster.

It may at first seem surprising that mergers do not preferentially lie in the cluster core, where the probability for close encounters is high due to the associated short value of the timescale t_{coll} for collisions and close encounters. However, if σ_{gal} is large, a close encounter is unlikely to lead to a merger or a large amount of tidal damage (i.e. to strong morphological and kinematical distortions). This is because a large galaxy velocity dispersion will likely cause the energy E of the reduced particle in a binary encounter to be positive, causing the orbit to become unbound (Binney & Tremaine, 1987).

All merging systems lie at a projected clustocentric radius of $0.25 \text{ Mpc} < R \leq 2 \text{ Mpc}$, between the core and cluster outskirts, although in this region the timescale for collisions and close encounters is quite large. We sug-

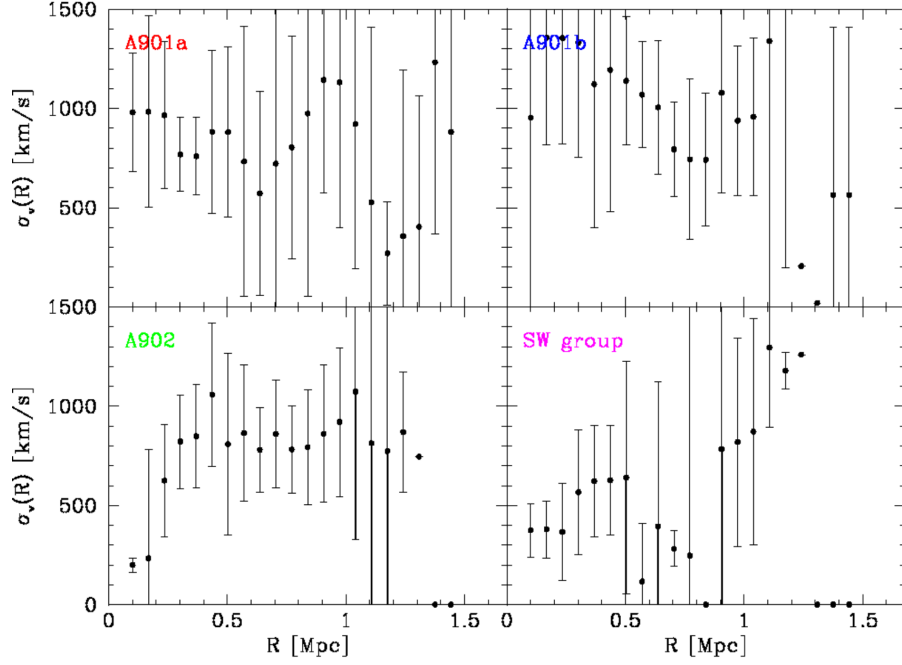


Figure 5.11 Local velocity dispersion profiles for A901a, b and A902 clusters, and associated SWG from kinematic modeling using the ~ 420 2dF redshifts (Gray et al. in preparation). The central galaxy velocity dispersion within the cores ($R < 0.25$ Mpc) of A901a,b and A902 typically range from 700 to 1000 km s^{-1} . Outside the cluster core, in the outer region ($0.25 \text{ Mpc} < R \leq 1.2 \text{ Mpc}$), the small number statistics leads to large error bars on the galaxy velocity dispersion, making it not viable to determine whether it remains high or drops.

gest two possible reasons why strong interactions and mergers might populate the outer region and cluster outskirts. The first possibility is that the velocity dispersion of galaxies falls between the core and outskirts, due to the *intrinsic* velocity dispersion profile of the clusters. Many clusters show a flat velocity dispersion profile from 1 Mpc outward, but several also show a declining profile (den Hartog & Katgert 1996; Carlberg et al. 1997). In the latter cases, the velocity dispersions can fall from 1500 to 100 km s⁻¹ from the cluster core to cluster outskirts. Since the local velocity dispersion profiles in the regions of interest in A901/902 (Figure 5.11) are based on a small number of galaxies and therefore large errors in σ_{gal} , we cannot determine if the velocity dispersion profile falls or remains flat. An additional difficulty is that the member galaxies of the neighboring clusters influence σ_{gal} at ~ 0.5 Mpc for A901a/b and ~ 1 Mpc for A902.

The second possibility is that the mergers are part of groups or field galaxies that are being accreted along filaments by the A901/902 clusters. This would be in line with the idea that clusters continuously grow by mergers and accretion of groups (e.g., Zabludoff & Franx (1993); Abraham et al. (1996); Balogh & Morris (2000)). Groups have lower galaxy velocity dispersion (typically below 300 km s⁻¹) than clusters, as shown in Table 5.6. Furthermore simulations show that merger rates are highest as field and group galaxies accrete into cluster along cosmological filaments (see below; van Kampen & Katgert (1997); Figure 5.12).

To further quantify the possibility of groups accreting into the A901/A902

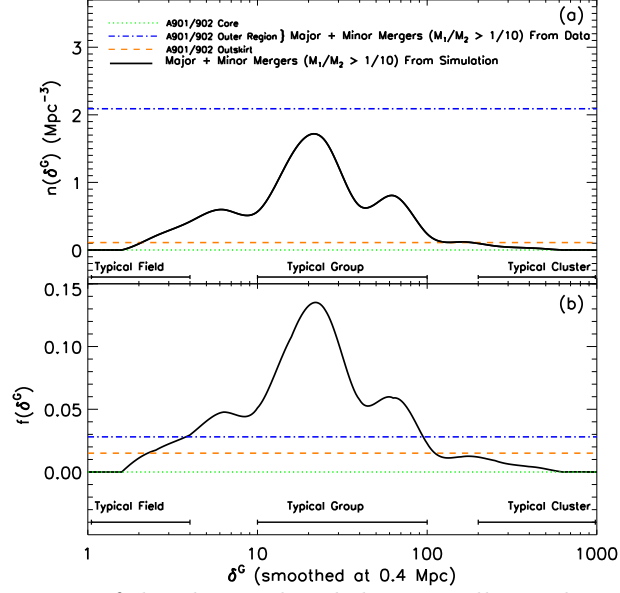


Figure 5.12 Comparison of the observed and theoretically predicted number density of mergers (**top panel**) and fraction of mergers (**lower panel**), §Section 5.4.4. The solid curve shows the *predicted model* number density of mergers ($n(\delta^G)$) and the fraction of mergers ($f(\delta^G)$) as a function of local overdensity (δ^G), in the N -body simulations of the STAGES A901/902 supercluster. Typical values of δ^G are ~ 10 – 100 for group overdensities, ~ 200 at the cluster virial radius, and $\gtrsim 1000$ in core of rich clusters. In the models, as field and group galaxies fall into a cluster along filaments, the bulk flow enhances the galaxy density and causes galaxies to have small relative velocities, thus leading to a high probability for mergers at typical group overdensities. Closer to the cluster core, model galaxies show large random motions, producing a sharp drop in the probability of mergers. The three dashed lines show the *observed* number density (n_{merge}) and fraction (f_{merge}) of mergers in three different regions of the A901/902 clusters: the core, the outer region, and the outskirts. A stellar mass cut of $M > 10^9 M_\odot$ is applied to both model and data. The points at which the three dashed lines cross or approach the solid curve tell us the typical overdensities at which we expect to find such merger fraction or merger number densities in the simulations. It can be seen that the low merger density seen in the core region (green dashed line) of the cluster correspond to those expected at typical cluster core overdensities. On the other hand, the larger merger fraction we observe between the cluster core and outer region ($0.25 \text{ Mpc} < R \leq 2 \text{ Mpc}$; blue dashed line) is close to those seen in typical *group overdensities*, in agreement with the scenario of cluster growth via accretion of group and/or field galaxies.

clusters, we compare the data to model predictions from simulations of the STAGES A901/A902 supercluster (van Kampen et al. in preparation). The simulation aims to reproduce the environment as observed for A901/A902 by using constrained initial conditions that produce clusters with overall properties similar to those of A901, A902, and the neighboring A907 and A868. The simulation box is large enough to contain all these, and hence reproduce the overall large-scale density and velocity fields similar to what is observed. A phenomenological galaxy formation model is then used to simulate the galaxy population in the same box, allowing us to select mock galaxies above a certain luminosity or stellar mass cut, as done in the observed dataset. A stellar mass cut of $M_* \geq 10^9 M_\odot$ is applied in the simulations, corresponding to the mass cut in the observational sample. The solid lines in Figure 5.12 show the predicted number density (n) and fraction (f) of galaxy mergers with mass ratio $M_1/M_2 > 1/10$, as a function of environment, as characterized by the local overdensity (δ^G). The latter is calculated by smoothing the density of DM halos with a Gaussian of width 0.4 Mpc to take out the effect of individual galaxies. Typical values of δ^G are ~ 10 -100 for group overdensities, ~ 200 at the cluster virial radius, and $\gtrsim 1000$ in the core of rich clusters.

Typically, in the simulations, as field and group galaxies fall into a cluster along filaments, the coherent bulk flow enhances the galaxy density and causes galaxies to have small relative velocities, thus leading to a high probability for mergers at typical group overdensities. Closer to the cluster core, galaxies show large random motions rather than bulk flow motion, leading

to a large galaxy velocity dispersion, and a sharp drop in the probability of mergers.

In order to compare the data to simulation results, we use the number (N_{merge}) and fraction (f_{merge}) of mergers of mass ratio $\geq 1/10$, which we computed in §Section 5.4.1. The solid curve in Figure 5.12 shows the merger fraction and number density predicted by the simulations as a function of overdensity. The three dashed lines in Figure 5.12 show the estimated range in the observational number density (n_{merge}) and fraction (f_{merge}) of mergers in the three different regions (the core, the outer region, and the outskirts) of the A901/902 clusters, as defined in §Section 5.4.3. The points at which the dashed lines cross or approach the solid curve tell us the typical overdensities at which we expect to find such merger fraction or merger number densities in the simulations. It can be seen that the low merger density seen in the core region of the cluster correspond to those expected at typical cluster core overdensities. On the other hand, the larger merger fraction we observe between the cluster core and outer region ($0.25 \text{ Mpc} < R \leq 2 \text{ Mpc}$) is close to those seen in typical *group overdensities*. Our results are in agreement with the above scenario, whereby the accretion of group and/or field galaxies along filaments, where they have low relative velocities and enhanced overdensities, leads to enhanced merger rates. We note that similar conclusions are reached if we perform the comparisons between data and simulations using the more conservative mass cut of $M_* \geq 3 \times 10^9 M_\odot$, discussed in §Section 5.4.1.

However, there are a couple of caveats when comparing our data with

simulations. One caveat is that we directly compare the projected values of the number density or fraction of mergers from two dimensional observations, to the predicted number density of mergers from three dimensional simulations. Projection effects can introduce uncertainties in our observational estimate. The magnitude of the uncertainties due to projection effects depends on the detailed environment and will be investigated in the full STAGES supercluster simulation dataset (van Kampen et al. , in preparation).

A further indirect evidence for group accretion stems from comparing semi-analytic galaxy catalogs to STAGES observations. Rhodes et al. (in preparation) finds an overabundance in galaxies in A902 compared to its mass. This could be explained by two or more galaxy groups in projection, consistent with the idea of group accretion.

5.4.5 Comparison with groups and clusters at different epochs

We first recapitulate our results on the visually-based merger fraction (f_{merge}) in the A901/902 clusters (§Section 5.4.1). Among intermediate-mass ($M_* \geq 10^9 M_\odot$) systems, we find that the fraction f_{merge} of systems which show evidence of a recent or ongoing merger of mass ratio $> 1/10$ is 0.023 ± 0.007 (Table 5.3). Most of these mergers have $M_V \sim -19$ to -22 and $L \leq L^*$ (see Figure 5.1). We also estimated that the fraction of likely major mergers, likely minor mergers, and ambiguous cases to be $0.01 \pm 0.004\%$ (9/886), $0.006 \pm 0.003\%$ (5/886), and $0.007 \pm 0.003\%$ (6/886), respectively.

Next, we compare our merger fraction in the A901/902 clusters with the

published merger fraction in other clusters and group galaxies out to $z \sim 0.8$, over the last 7 Gyr (Figure 5.13). These comparisons are difficult to make as different studies apply different luminosity or mass cuts. Furthermore, some studies consider only major mergers, while others consider all interacting galaxies, which are likely candidates for both major and minor interactions.

The variation in galaxy populations sampled at different epochs must also be kept in mind when comparing results at lower redshift with those out to $z \sim 0.8$. Low redshift samples typically sample a small volume and therefore tend to host only a small number of the brightest and most massive systems. Conversely, higher redshift magnitude-limited samples will suffer from Malmquist bias and tend to under-represent the faint ($L < L^*$) galaxies.

There have been several studies of galaxy mergers and interactions in intermediate redshift clusters (Lavery & Henry 1988; Lavery et al. 1992; Dressler et al. 1994; Oemler et al. 1997; Couch et al. 1998), but only few to date with high resolution *HST* imaging. Couch et al. (1998) used WFPC/WFPC2 observations and spectroscopy of two clusters at $z \sim 0.3$ and ~ 0.4 , focusing on galaxies with $R \sim 22.5$ or $L < L^*$. In their study, they classified $\sim 7/200$ or $\sim 3.5\%$ galaxies to be merging based on separations and visible distortions. The merger fractions of these two intermediate redshift clusters are plotted in Figure 5.13.

It is also interesting to note that the merging systems in these two intermediate redshift clusters tend to be blue and preferentially located in the outskirts of the clusters. In fact, in the Couch et al. (1998) sample, $\sim 60\%$ of

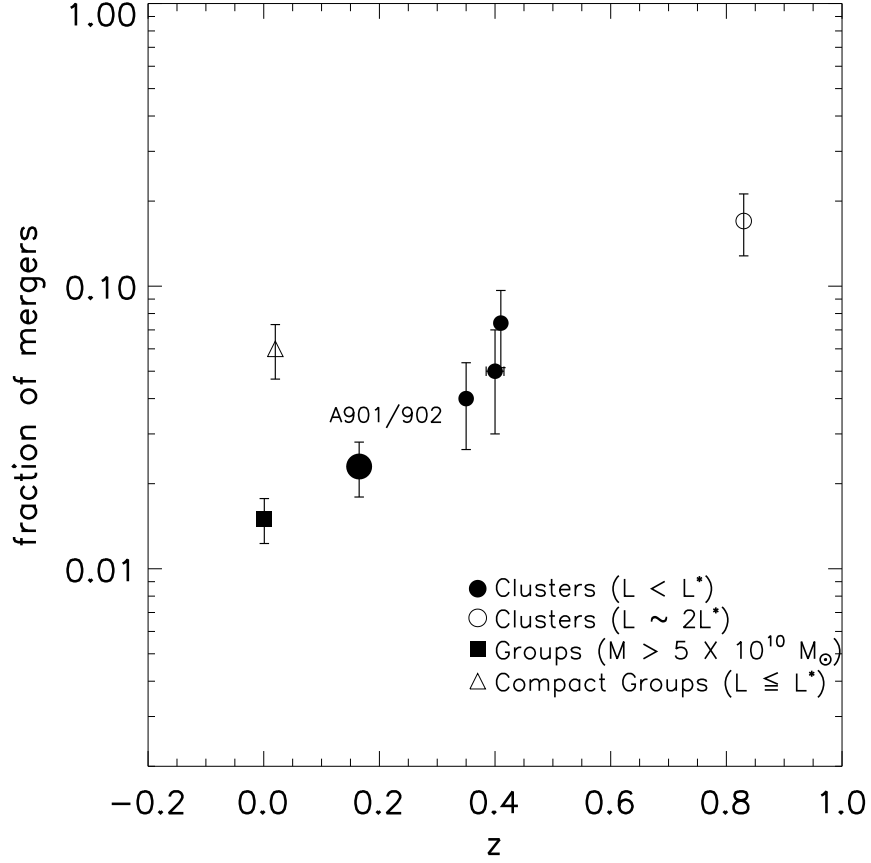


Figure 5.13 Comparisons of our observed fraction of mergers among intermediate mass systems in the A901/902 clusters (large filled solid circle) with the results from other studies of clusters and groups. Filled circles are for cluster data points of intermediate luminosity ($L < L^*$ and/or $M = 10^9$ to a few $\times 10^{10} M_\odot$), and include the following studies in order of increasing redshift: this study of A901/902 (most systems have $M_V \sim -19$ to -22 and $M_* = 10^9$ to a few $\times 10^{10} M_\odot$); Couch et al. 1998 ($L < 2L^*$), Oemler et al. 1997; lower limit of f for $M_V < -19$), Dressler et al. 1994 ($M_V < -18.5$). The van Dokkum et al. (1999) point at $z = 0.83$ (open circle) is for a cluster sample of luminous ($M_B \sim -22$ and $L \sim 2L^*$) galaxies. The group point (filled square) is from McIntosh et al. (2008) for galaxy masses above $5 \times 10^{10} M_\odot$. The Hickson compact group point (open triangle), from Zepf (1993), is for galaxies of luminosities $L \leq L^*$.

the merging galaxies among $L < L^*$ systems are blue. The mergers in these two intermediate redshift clusters are similar in many ways to the mergers in the A901/902 clusters: the latter mergers lie in between the cluster core and outskirts ($0.25 \text{ Mpc} < R \leq 2 \text{ Mpc}$; §Section 5.4.3) of the A901/902 clusters, and for the absolute magnitude range of $M_V \sim -19$ to -22 , 16/20 or $80 \pm 18\%$ of these mergers lie on the blue cloud (§Section 5.4.6).

In a study by Dressler et al. (1994), based on WFPC images of a $z \sim 0.4$ cluster, the fraction of bright ($M_V < -18.5$) galaxies identified as mergers was 10/135. Another WFPC study of four clusters at $z = 0.37 - 0.41$ by Oemler et al. (1997) placed a lower limit of 5% on the fraction of merging galaxies with $M_V < -19$ or $L \leq L^*$.

A high redshift ($z = 0.83$) cluster was studied by van Dokkum et al. (1999) using *HST* WFPC2 images and spectroscopic redshifts for 80 confirmed members. They found a high fraction (17%) of luminous ($M_B \sim -22$; $L \sim 2L^*$) systems, which exhibit signatures of ongoing mergers. These mergers were found to be red, bulge-dominated, and located in the outskirts of the cluster. A later study by Tran et al. (2005) used spectroscopic followup to confirm that $15.7\% \pm 3.6\%$ of these galaxies were bound pairs with separations $\lesssim 30h^{-1} \text{ kpc}$ and relative velocities $\lesssim 300 \text{ km s}^{-1}$. These merging pairs are located outside the cluster centers, similar to the mergers in A901/902. However, the galaxy sample at high redshift is dominated by more luminous galaxies ($M_B \sim -22$; $L \sim 2L^*$) than the A901/902 sample where most galaxies have $M_V \sim -19.5$ to -22 (Figure 5.1). The number statistics for bright ($\sim 2L^*$) mergers in

A901/902 are not robust enough to allow a direct comparison with the merger fraction cited in van Dokkum et al. (1999).

Finally, we look at the merger fraction in *groups*. A study by McIntosh et al. (2008) finds that $\sim 1.5\%$ of massive ($M \geq 5 \times 10^{10} M_{\odot}$) galaxies in SDSS groups (with $M_{\text{halo}} > 2.5 \times 10^{13} M_{\odot}$) are major mergers at z of 0.01–0.12. Most of the mergers involve two red sequence galaxies and they are located between 0.2 and 0.5 Mpc from the group center. A study by McGee et al. (2008) also finds an enhancement in asymmetric bulge-dominated galaxies in groups, consistent with a higher probability for merging in the group environment. Additional evidence for mergers in groups is shown in a study of a supergroup at $z \sim 0.37$ by Tran et al. (2008), who report dry dissipationless mergers and signatures thereof in three of four brightest group galaxies.

A merger fraction of 6% was found by Zepf (1993) in Hickson compact groups at $z < 0.05$, among systems with luminosities $L \leq L^*$. The merger fraction is significantly higher than that in SDSS groups. The increased merger fraction is expected since Hickson compact groups are different from loose groups: they have high number densities comparable to those in cluster cores, but low galaxy velocity dispersions. These two conditions provide an environment most favorable to strong tidal interactions and mergers, as argued in §Section 5.4.4.

It is not straightforward to draw conclusions about the evolution of the merger fraction in cluster galaxies over $z \sim 0.05$ –1.0 from the above studies because they sample different types of systems and different luminosity ranges.

If we conservatively restrict ourselves to only studies of $L \leq L^*$ cluster galaxies, then we have 4 data points over $z \sim 0.17\text{--}0.4$, shown as solid filled circles in Figure 5.13. The mean value of the data points allows for evolution by a factor of ~ 3.2 , in the merger fraction of $L \leq L^*$ cluster galaxies over $z \sim 0.17\text{--}0.4$. However, if one uses the full range of merger fractions allowed by the error bars on the data points, then we can admit a wider spectrum of scenarios, ranging from no evolution to evolution by a factor of ~ 5 over $z \sim 0.17\text{--}0.4$. Having additional deep, large-volume, high resolution studies, which are based on larger samples with smaller error bars would help to separate between these scenarios, and thereby test hierarchical models of galaxy evolution.

As mentioned in §Section 5.4.1, hierarchical models (e.g., Gottlöber et al. (2001); Khochfar & Burkert (2001)) predict that the merger fraction in dense clusters falls more steeply at $z < 1$ than the field merger fraction, such that at $z < 0.3$, the predicted merger fraction is quite low (typically below 5%) among intermediate mass cluster galaxies. The low merger fractions among intermediate mass (10^9 to a few $\times 10^{10} M_\odot$) or intermediate luminosities ($L < L^*$) galaxies in the A901/902 clusters and other low redshift clusters are consistent with these predictions, but we cannot yet test the predicted rate of evolution of the merger fraction in clusters with redshift.

5.4.6 Galaxies on the blue cloud and red sample

We explore the properties of galaxies on the blue cloud and in the red sample among the final sample of 886 systems (20 mergers and 866 non-

interacting galaxies; §Section 5.3.2). The red sample was defined in Wolf et al. (2009) and contains both passively evolving spheroidal galaxies on the red sequence, as well as dusty red galaxies that lie between the red sequence and the blue cloud.

Figure 5.14 shows the rest-frame $U - V$ color plotted against stellar masses for galaxies of different visual classes: Mergers, Non-interacting Irr-1, and Non-interacting Symmetric (§Section 5.3.2). The visual classes of galaxies on the blue cloud and in the red sample are shown in Table 5.7. As described in §Section 5.4.1, we only consider the 20 distorted mergers listed in Table 5.2, and avoid the potential projection pairs without signs of morphological distortions. The 20 mergers are divided into 13 mergers of type 1, 3 mergers of type 2a, and 4 mergers of type 2b. For mergers of type 2b, which are resolved into two galaxies with separate COMBO-17 colors, we plot the average $U - V$ color of the galaxies in the pair.

Out of the 886 visually classified systems in our sample, we find that 310/886 or $35\% \pm 7\%$ lie on the blue cloud. Out of the 20 visually classified mergers with distortions, 16/20 or $80\% \pm 18\%$ lie on the blue cloud (Table 5.7). Conversely, out of 866 non-interacting galaxies, 294/866 or $34\% \pm 7\%$ are on the blue cloud. Thus, the fraction of mergers, which lie on the blue cloud ($f_{\text{merg-BC}}$) is over two times larger than the fraction of non-interacting galaxies ($f_{\text{non-int-BC}}$), which lie on the blue cloud. This implies that mergers and interacting galaxies are preferentially blue, compared to non-interacting galaxies.

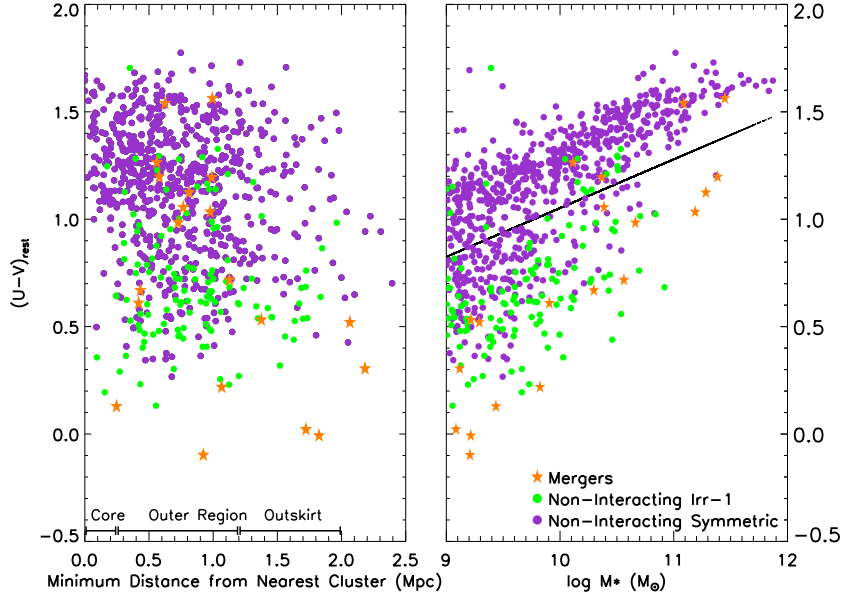


Figure 5.14 **Left:** the rest-frame $U - V$ color is plotted against the minimum distance from the nearest cluster center, for systems of different visual classes (Merger, Non-interacting Irr-1, and Non-interacting Symmetric). We only consider here the 20 distorted mergers in Table 5.2, split into 13 mergers of type 1, 3 mergers of type 2a, and 4 mergers of type 2b. For mergers of type 2b, which are resolved into two galaxies with separate COMBO-17 colors, we plot the average $U - V$ color of the galaxies in the pair. **Right:** the rest-frame $U - V$ color is plotted against stellar masses. The black solid lines separate the blue cloud and red sample. For $M \geq 10^9 M_\odot$ systems, we find that $80\% \pm 18\%$ (16/20) of mergers lie on the blue cloud, compared to (294/866) or $34\% \pm 7\%$ of the non-interacting galaxies. Thus, mergers and interacting galaxies are preferentially blue compared to non-interacting galaxies.

Table 5.7. Visual Classes of Galaxies on the Blue Cloud and Red Sample

Visual Class (1)	N_{blue} (2)	f_{blue} (3)	N_{red} (4)	f_{red} (5)
(1) All	310	1.00	576	1.00
(2) Mergers	16	$16/310 = 0.052 \pm 0.02$	4	$4/576 = 0.007 \pm 0.004$
(2a) Likely Major Mergers	6	$6/310 = 0.02 \pm 0.009$	3	$3/576 = 0.005 \pm 0.003$
(2b) Likely Minor Mergers	4	$4/310 = 0.01 \pm 0.007$	1	$1/576 = 0.002 \pm 0.002$
(2c) Ambiguous Major/Minor	6	$6/310 = 0.02 \pm 0.009$	0	0
(3) Non-interacting Irr-1	105	$105/310 = 0.34 \pm 0.07$	18	$18/576 = 0.033 \pm 0.01$
(4) Non-interacting Symmetric	189	$189/310 = 61 \pm 13$	554	$554/576 = 0.96 \pm 19$

Note. — Results are shown for the sample of 886 bright ($R_{\text{Vega}} \leq 24$) intermediate-mass ($M_* \geq 10^9 M_{\odot}$) visually classifiable systems. The table shows how galaxies in the blue cloud and red sample are split among the different visual classes (Mergers, Non-interacting Irr-1, and Non-interacting Symmetric) discussed in §Section 5.4.6. Columns: (1) Visual Classes: These include Mergers, Non-interacting Irr-1, Non-interacting Symmetric, listed in rows 2, 3, and 4. We only consider the 20 morphologically distorted mergers listed in Table 5.2. These include 13 mergers of type 1, 3 mergers of type 2a, and 4 mergers of type 2b. Rows 2a, 2b, and 2c show how the mergers are split into likely major mergers, likely minor mergers, and ambiguous cases that could be either (§Section 5.3.2). (2) N_{blue} : Number of galaxies on the blue cloud; (3) f_{blue} : Fraction of blue cloud galaxies, which belong to a given visual class; (4) N_{red} : Number of galaxies in the red sample; (5) f_{red} : Fraction of red sample galaxies, which belong to a given visual class.

The observed higher fraction of blue galaxies among mergers compared to non-interacting galaxies may be caused by several factors. It may be due to enhanced levels of unobscured star formation in mergers (see §Section 5.4.7), translating to bluer colors on average. It may also in part be the result of the mergers being part of accreted field and group galaxies (§Section 5.4.4), which are bluer than the average cluster galaxy. It is also relevant to ask whether we are overestimating the fraction of blue galaxies among interacting systems due to the visibility timescale t_{vis} of morphological distortions induced by interactions being longer in bluer galaxies than redder ones. While this is possible, it is non-trivial to correct for this effect because no direct unique relation exists between t_{vis} and color. As discussed in § 5.4.1, t_{vis} depends on the mass ratio of an interaction as well as the gas content. A higher gas content may result in a longer t_{vis} for certain gas distributions, but it can lead to either redder colors (e.g., enhanced level of dusty SF) or bluer colors (enhanced level of unobscured SF), compared to interacting systems.

5.4.7 Star formation properties of interacting galaxies

This work uses SFRs based on UV data from COMBO-17 (Wolf et al. 2004) and *Spitzer* 24 μ m imaging (Bell et al. 2007). The unobscured SFR_{UV} is derived using the 2800 Å rest frame luminosity ($L_{\text{UV}} = 1.5\nu l_{\nu,2800}$) as described in Bell et al. (2005, 2007) (2005). The UV spectrum is dominated by continuum emission from massive stars and provides a good estimate of the integrated SFR from the younger stellar population in the wavelength range

of 1216-3000 Å. The SFR_{IR} is derived using the $24\mu\text{m}$ flux to construct the integrated IR luminosity (L_{IR}) over 8-1000 μm following the methods of Papovich & Bell (2002). The total SFR is derived using identical assumptions of Kennicutt (1998a) from PEGASE assuming a 100 Myr old stellar population with constant SFR and a Chabrier (2003) IMF:

$$\text{SFR}_{\text{UV+IR}} = 9.8 \times 10^{-11} (L_{\text{IR}} + 2.2L_{\text{UV}}). \quad (5.6)$$

The factor of 2.2 on the UV luminosity accounts for light being emitted longward of 3000 Å and shortward of 1216 Å by young stars. The total SFR accounts for both the dust-reprocessed (IR) and unobscured (UV) star formation.

We work with our final sample of 886 classifiable bright massive ($M_* \geq 10^9 M_\odot$) systems, and only consider here the 20 distorted mergers in Table 5.2. All of these systems have UV-based SFR from COMBO-17 observations. Of this sample, $\sim 11\%$ (94/886) were not observed with *Spitzer*, $\sim 23\%$ (206/886) were observed and detected at $24\mu\text{m}$, while the rest had no detection at the $\sim 4\sigma$ depth of $83 \mu\text{Jy}$.

The UV-based SFR (SFR_{UV}) versus stellar mass is plotted in Figure 5.15 for all 886 systems. The SFR_{UV} ranges from ~ 0.01 to $14 M_\odot \text{ yr}^{-1}$. The UV-based SFR represents a lower limit to the total SFR for galaxies on the blue cloud and most star-forming galaxies on the red sample. However, for some old red galaxies, the SFR_{UV} may overestimate the true SFR as the UV light from such systems may not trace massive OB stars, but rather low

to intermediate mass stars.

Figure 5.16 shows the UV+IR-based SFR ($\text{SFR}_{\text{UV+IR}}$), which ranges from ~ 0.2 to $9 M_{\odot} \text{ yr}^{-1}$. For the 206 galaxies that were observed and detected at $24\mu\text{m}$, the implied UV+IR-based SFR is plotted as stars in the lower panel of Figure 5.16. For the 586 galaxies that are observed but undetected with *Spitzer*, we use the $24\mu\text{m}$ detection limit as an upper limit on the $24\mu\text{m}$ flux. The corresponding upper limit on the UV+IR-based SFR is plotted as inverted triangles in the lower panel of Figure 5.16, and included in the calculation of the average UV+IR-based SFR, plotted in the middle panel.

In a cluster environment, the competition between processes that enhance the SFR and those that depress the SFR, ultimately determine the average SFR of cluster galaxies. The first class of processes are strong close interactions: tidal and mergers (e.g., Toomre & Toomre 1972), and harassment (e.g., Moore et al. (1996)), which refers to the cumulative effect of weak interactions. The second class of processes include ram pressure stripping of cold gas out of the galaxy by the hot ICM (e.g., Gunn & Gott (1972)), and strangulation (e.g., Larson et al. (1980); Balogh & Morris (2000)).

For the few mergers (orange line) present, the average SFR_{UV} is typically enhanced by an average modest factor of ~ 2 compared to the both Non-interacting Symmetric and Irr-1 galaxies (purple, green and black lines). Similarly, the UV+IR-based SFR ($\text{SFR}_{\text{UV+IR}}$; and Figure 5.16) of merging galaxies is typically enhanced by only an average factor of ~ 1.5 compared to the Non-interacting Symmetric galaxies (purple line) and to all Non-interacting galaxies

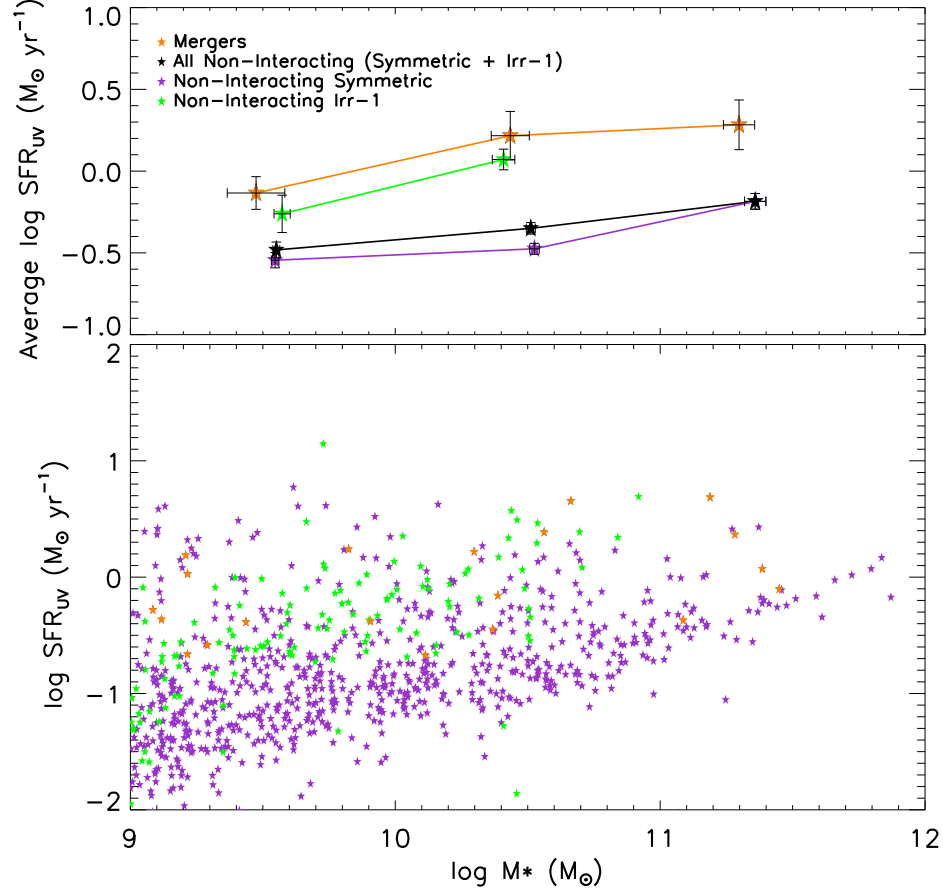


Figure 5.15 **Bottom panel:** The UV-based SFR is plotted against stellar mass for the sample of 886 bright intermediate-mass ($M_* \geq 10^9 M_{\odot}$) visually classifiable systems. Systems are coded according to their visual classes: Merger, Non-interacting Irr-1, and Non-interacting Symmetric. We only consider here the 20 distorted mergers in Table 5.2. **Top panel:** The average UV-based SFR is plotted against stellar mass for galaxies of different visual classes. For the few mergers galaxies present (orange line), the average SFR_{UV} is enhanced by at most an average factor of ~ 2 compared to the Non-interacting Symmetric galaxies (purple line) and to all Non-interacting galaxies (i.e Symmetric + Irr-1; black line). No enhancement is seen with respect to the Non-interacting Irr-1 galaxies (green line).

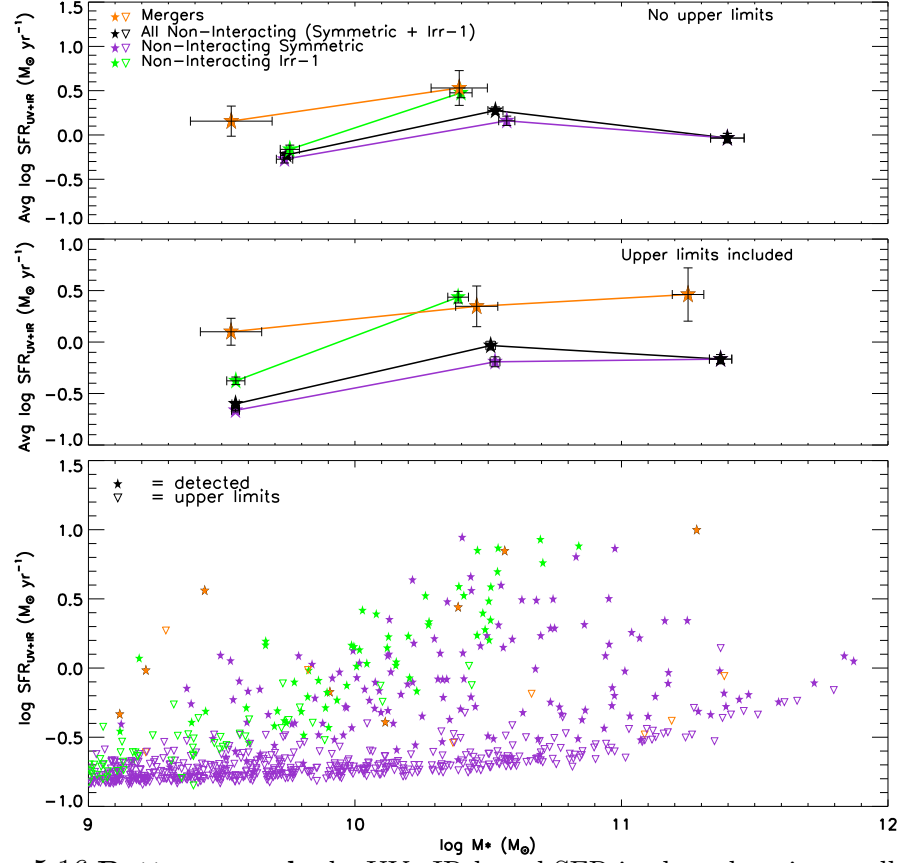


Figure 5.16 **Bottom panel:** the UV+IR-based SFR is plotted against stellar mass for the sample of bright intermediate-mass ($M_* \geq 10^9 M_\odot$) systems. Galaxies are coded according to their visual classes: Merger, Non-interacting Irr-1, and Non-interacting Symmetric. We only consider here the 20 distorted mergers in Table 5.2. For galaxies that were observed and detected at $24\mu\text{m}$, the UV+IR-based SFR is plotted as stars. For galaxies that were observed but undetected at $24\mu\text{m}$, we use the detection limit as an upper limit for the UV+IR-based SFR, and plot this limit as inverted triangles. **Middle panel:** the average UV+IR-based SFR is plotted against stellar mass for galaxies of different visual classes. We include galaxies with a $24\mu\text{m}$ detection, as well as those with only upper limits on the $24\mu\text{m}$ flux. **Top panel:** same as middle panel, except that we only include galaxies with a $24\mu\text{m}$ detection and exclude those with upper limits. In both top and middle panels, we find that for the few mergers present (orange line), the average $\text{SFR}_{\text{UV+IR}}$ is typically enhanced by only a factor of ~ 1.5 compared to the Non-interacting Symmetric galaxies (purple line) and to all Non-interacting galaxies (i.e Symmetric + Irr-1; black line).

(i.e Symmetric + Irr-1; black line). We note that a similar modest enhancement in the average SFR, by a factor of 1.5–2 is also found in mergers in the field over $z \sim 0.24$ – 0.80 by Jogee et al. (2008, 2009). This modest enhancement is consistent with the theoretical predictions of Di Matteo et al. (2007) (see their Figure 10), based on a recent statistical study of several hundred simulated galaxy collisions. Modest SFR enhancements are also seen in galaxy pair studies in the field (Barton et al. 2000; Barton Gillespie et al. 2003; Lin et al. 2004; Ellison et al. 2008) and in mixed environments (Robaina et al. 2009; Alonso et al. 2004).

While mergers in the A901/902 clusters enhance the SFR of individual galaxies, it is clear that they do not contribute much to the total SFR of the cluster. We compute the SFR density of mergers to non-interacting galaxies in the same volume of A901/902 by taking the ratio of the total SFR in each class. If we include only the 20 distorted mergers in Table 5.2, we find that the contribution of mergers to the SFR density of the clusters to be 10%. Alternatively, if we include all of the 36 visually classified mergers in Table 5.2, before accounting for false projection pairs, we find the contribution of mergers to the SFR density to be 15%. Thus, we find that mergers contribute only a small fraction (between 10% and 15%) of the total SFR density of the A901/902 clusters compared to non-interacting galaxies. The small contribution of mergers to the total cluster SFR density is likely due to the low number of mergers in A901/902, and the fact that these mergers only cause a modest SFR enhancement.

5.5 The Morphology-Density relation in A901/02

The assumed correlation implicit in the Hubble sequence, between a high bulge to disk ratio (B/D) and a low gas and dust content, can often fail in cluster environments, where systems of low B/D may have smooth featureless disks (e.g., Koopmann & Kenney 2004). This begs the question of whether the classical morphology-density relation, which claims a larger fraction of early-type galaxies in dense environments, is driven by a larger fraction of gas-poor galaxies in such environments, or a larger fraction of bulge-dominated systems, or both. In order to address this question, we visually classify the clumpiness and B/D ratio of galaxies separately, classifying galaxies into five categories: pure bulge (pB), bulge plus disk (B+D) clumpy or smooth, and pure disk (pD) clumpy or smooth.

I find that Smooth (gas-poor) galaxies cluster in regions of high ICM density while clumpy (gas-rich) systems dominate at low ICM densities (Figure 5.17). The ratio of smooth (gas-poor) galaxies to very clumpy (gas-rich) galaxies within the central 0.3 Mpc is (89%:11%), (75%:25%), and (86%:14%), respectively, for A901a, A901b, and A902. These values are comparable to the ratio of (80%:20%) for early-type to late-type galaxies in the classical morphology-density relation (Dressler 1980).

I also find that the fraction of bulge-dominated galaxies increases at higher local galaxy surface density (Σ_{10}) compared to disk-dominated galaxies which prefer lower local galaxy number density (Figure 5.18).

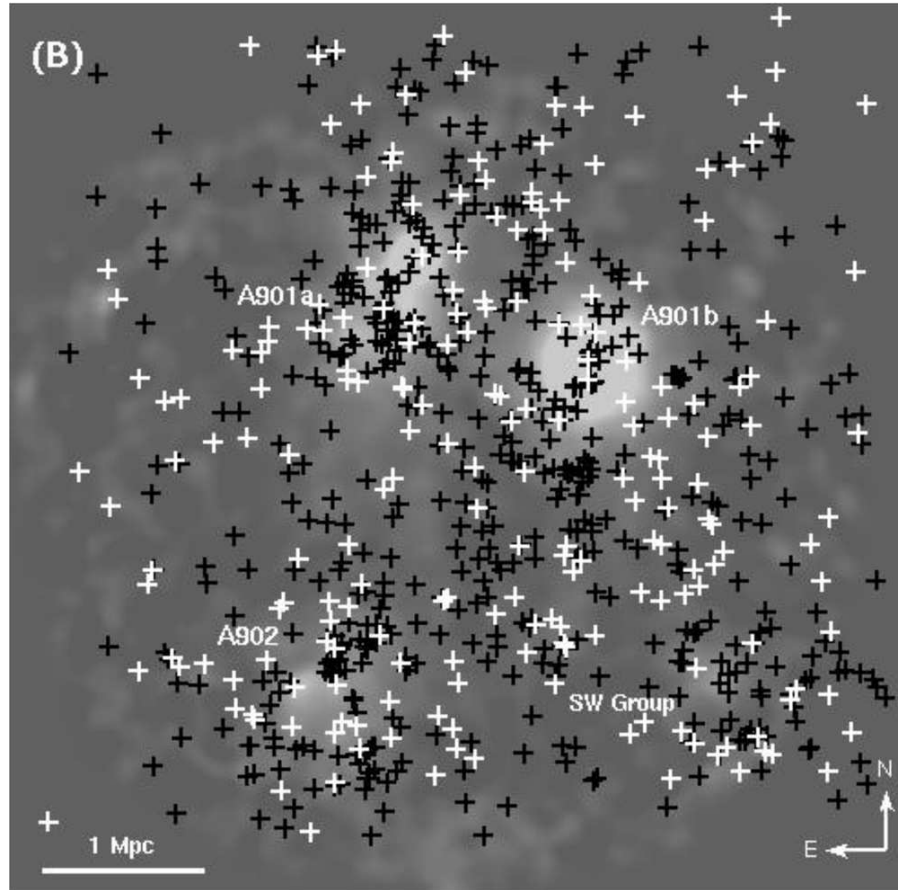


Figure 5.17 We revisit the morphology-density relation by overplotting the distribution of bright ($M_V \leq -18$) smooth (gas-poor) galaxies (black crosses) and clumpy (gas-rich) galaxies (white crosses) on the ICM density. Smooth (gas-poor) galaxies populate the highest density regions.

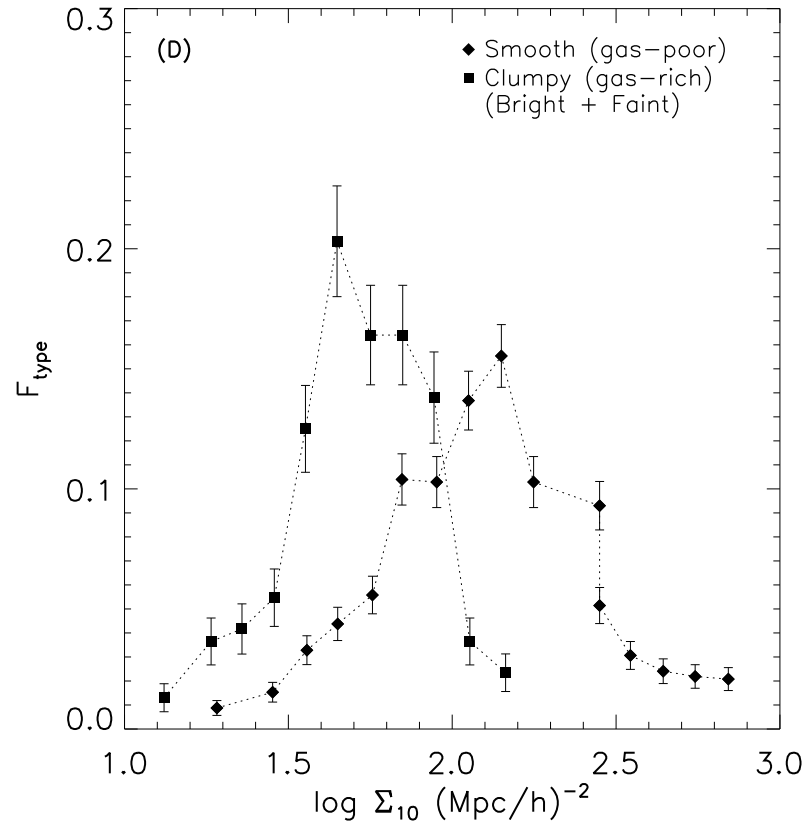


Figure 5.18 The morphology-density relation as a function of local galaxy surface density (Σ_{10}). Smooth, bulge-dominated galaxies are found to lie preferentially at higher Σ_{10} compared to clumpy, gas-rich galaxies.

5.6 The depression of star formation in A901/902 cluster galaxies

In this section, we explore some of the factors that impact star formation in clusters, and in particular account for the depression in A901/902 compared to the field. In § 5.4.7, we saw that UV-based SFR for most galaxies with $M \geq 1 \times 10^9 M_\odot$, the UV-based SFRs (Fig. 5.15) were below $0.5 M_\odot \text{ yr}^{-1}$ and the UV+IR-based SFR (Fig. 5.16) had SFRs below $3 M_\odot \text{ yr}^{-1}$. These cluster SFRs are *significantly lower* than the corresponding SFRs at a given stellar mass for field galaxies of similar redshift. For instance, in the study by (Jogee et al. 2009; Fig 14a), for field galaxies with mass $M \geq 1 \times 10^9 M_\odot$ at $z \sim 0.24$ to 0.34 , the SFR_{UV} ranges mainly from 0.1 to $3 M_\odot \text{ yr}^{-1}$, with a mean and median value of 0.47 and $0.33 M_\odot \text{ yr}^{-1}$ (Fig. 14a), while the $\text{SFR}_{\text{UV+IR}}$ ranges mainly from 6.0 to $15 M_\odot \text{ yr}^{-1}$, with a mean and median value of 4.2 and $2.1 M_\odot \text{ yr}^{-1}$ (Fig 14b).

The range of mean field values are overplotted as grey regions or hashed lines on the cluster values in Fig. 5.15, Fig. 5.16 and Fig. 5.19 (Balogh et al. 1998; Jogee et al. 2009). It is clear from Fig. 5.15 and Fig. 5.16 that most of the cluster galaxies have a UV-based SFR and a UV+IR-based SFR, *which is depressed compared to field galaxies*. Likewise, Gallazzi et al. (2009) find massive galaxies in A901/902 to have suppressed star forming activity. Similar depressions have also been reported in other clusters at $0.18 < z < 0.55$ by Balogh et al. (1998).

Possible reasons for this depression will be explored using by looking at

the how the SFR changes as a function of clustocentric radius, relative ICM densities, and local galaxy densities. The UV+IR based SFR ($\text{SFR}_{\text{UV+IR}}$) as a function of clustocentric radius R and other environmental parameters is shown in Fig. 5.19. The SFR is severely depressed in the core ($R \leq 0.25$ Mpc) compared to field values, but the SFR is also depressed out to large radii (Fig. 5.19a), in the region between the core and cluster virial radius ($0.25 \text{ Mpc} < R \leq 1.2 \text{ Mpc}$), as well as the outskirts region ($1.2 \text{ Mpc} < R \leq 2.0 \text{ Mpc}$). This suggests that the processes responsible for the depression must be effective both in the core and out to large radii. One possibility is ram pressure stripping by the hot ICM, which removes diffuse atomic gas from a galaxy, thereby causing star formation to cease gradually as the existing molecular gas reservoir is used up over a few Gyr. The criteria for a galaxy to be stripped of its gas (Gunn & Gott 1972) is given by the equation:

$$\rho_{\text{ICM}} v_{\text{rel}}^2 > 2\pi G \Sigma_{\text{ISM}} \Sigma_{\star} \quad (5.7)$$

$$> \Sigma_{\text{ISM}} \frac{V_{\text{rot}}^2}{r_{\text{gal}}} \quad (5.8)$$

The timescale $t_{\text{ram-pressure}}$ for a galaxy to be stripped of its gas by ram pressure is then:

$$t_{\text{ram-pressure}} \sim \left(\frac{2r_{\text{gal}}}{\text{kpc}} \right) \left(\frac{v_{\text{rel}}}{1000 \text{ km s}^{-1}} \right)^{-1} \left(\frac{2\rho_{\text{ISM}}}{\rho_{\text{ICM}}} \right)^{0.5}, \quad (5.9)$$

where ρ_{ISM} is the density of gas in the galaxy, ρ_{ICM} is the ICM density, r_{gal} is the galaxy radius, and v_{rel} is the galaxy speed relative to the ICM. We assume a galaxy of radius 10 kpc, and an average ρ_{ISM} of $\sim 1 \text{ cm}^{-3}$, similar to that of the Milky Way. This yields:

$$t_{\text{ram-pressure}} \sim 20 \times \left(\frac{r_{\text{gal}}}{10 \text{kpc}} \right) \left(\frac{v_{\text{rel}}}{1000 \text{kms}^{-1}} \right) \left(\frac{\rho_{\text{ICM}}}{\text{cm}^{-3}} \right)^{-0.5} \text{Myr} \quad (5.10)$$

Using the mass of ICM in A901 from Schindler (2000) of $M(r < 430 \text{ kpc}) = 1.3 \times 10^{13} M_{\odot}$ and assuming a spherical distribution, the density of ICM (ρ_{ICM}) in the core of A901 is roughly $3 \times 10^{-3} \text{ cm}^{-3}$. The corresponding timescale t_{ram} for ram pressure stripping in the cluster core is $\sim 400 \text{ Myr}$, for $v_{\text{rel}} \sim 1000 \text{ km s}^{-1}$. This suggests ram pressure stripping is quite efficient in the core – a suggestion supported by the drop in SFR at high ICM counts in Fig. 5.19c.

In order to estimate t_{ram} at larger radii outside the core, we need the radial profile of the ICM density ρ_{ICM} . This is being derived from new X-ray data by Grey et al. (in prep), and is not yet available. For now, we use the radial profile of the ICM counts (Fig. 5.19c) as a guide to estimate the change in ρ_{ICM} with radius. This yields $t_{\text{ram}} \sim 800 \text{ Myr}$ in the outer region, and $t_{\text{ram}} \sim \text{few Gyr}$ in the cluster outskirts. Thus, we suggest that ram pressure stripping may play a role in depressing star formation to the cluster virial radius of 1.2 Mpc

5.7 Summary and Conclusions

We present a study of the frequency, distribution, color, and SF properties of galaxy mergers in the A901/902 supercluster at $z \sim 0.165$, using a sample of 893 bright ($R_{\text{Vega}} \leq 24$) intermediate mass ($M_* \geq 10^9 M_{\odot}$) galax-

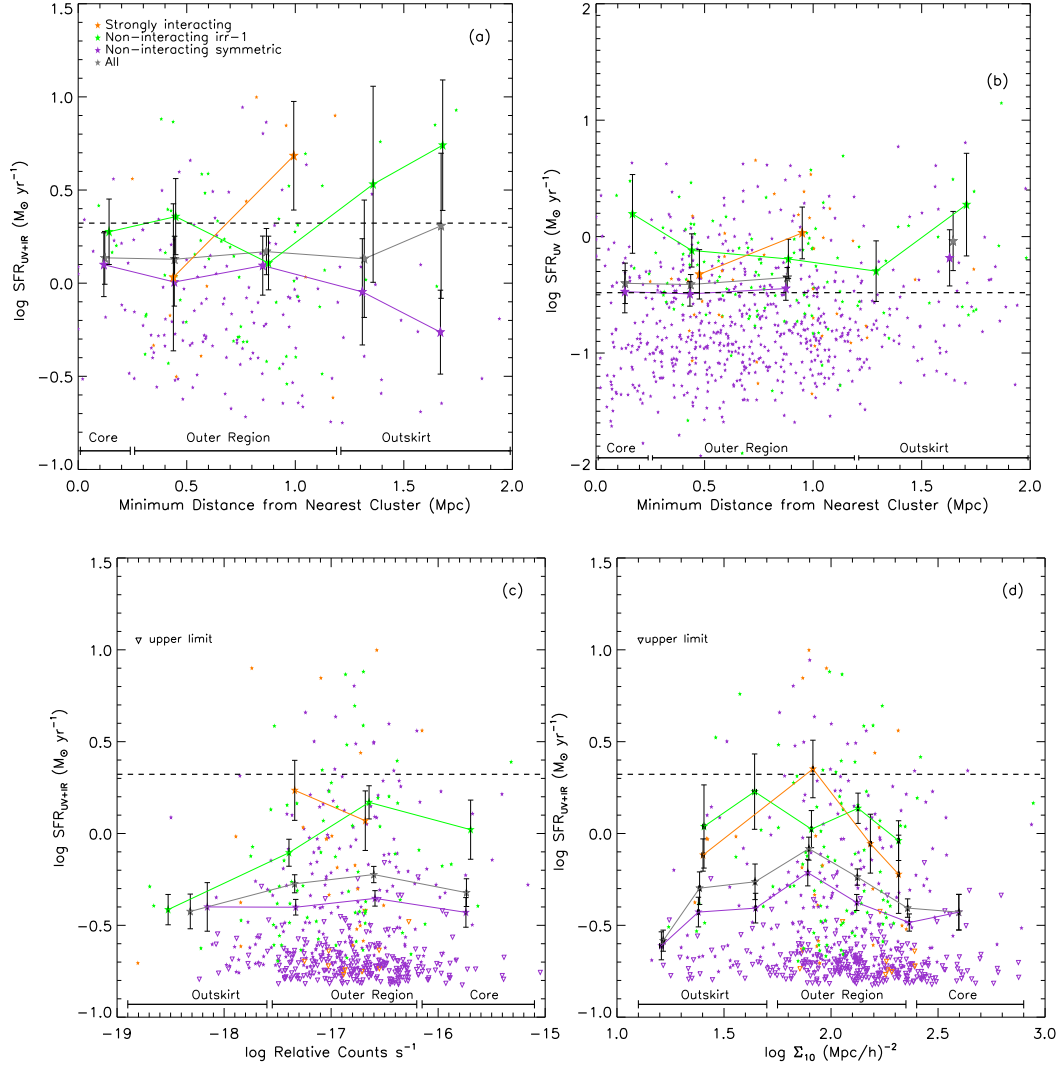


Figure 5.19 **(a)** The UV+IR based SFR ($\text{SFR}_{\text{UV+IR}}$) is plotted versus clustocentric radius R . Each galaxy is assigned to the cluster closest to it, and R is measured from the center of that cluster. **(b)** The UV based SFR (SFR_{UV}) is shown versus clustocentric radius R . **(c)** $\text{SFR}_{\text{UV+IR}}$ is shown against the local relative ICM density. The inverted triangles denote upper limits to the $\text{SFR}_{\text{UV+IR}}$ and apply to galaxies where there was no $24\mu\text{m}$ detection. **(d)** The variation of $\text{SFR}_{\text{UV+IR}}$ as a function of local galaxy surface density (Σ_{10}). The horizontal dashed line marks the median SFR value for field galaxies.

ies. The sample is complete in stellar mass down to $10^9 M_{\odot}$. We use *HST* ACS F606W data from the STAGES survey, COMBO-17, *Spitzer* 24 μ m, and *XMM-Newton* X-ray data. Our results are as follows:

- We visually classify the ACS F606W images of the sample galaxies into five main visual classes: Mergers of types 1, 2a, and 2b, and Non-Interacting systems of type Symmetric and Irr-1 (§Section 5.3.2; Tables 5.1–5.3; Figures 5.2, 5.3, and 5.5) and obtain a final sample of 886 systems. We classify the systems as mergers if they show evidence of a recent or ongoing merger of mass ratio $> 1/10$. Mergers of type 1 essentially appear as an advanced merger remnant, which hosts morphological distortions similar to those produced in simulations of mergers of mass ratio $> 1/10$. Mergers of type 2a and 2b appear in ACS images as a very close ($d < 10$ kpc) overlapping pair of two galaxies. The main difference between them is that mergers of type 2b are resolved into two separate galaxies by the ground-based COMBO-17 data, while mergers of type 2a are not.

We perform Monte Carlo simulations to gauge the level of contamination from projection pairs. In the final analysis, we minimize the contamination from false projection pairs by considering only mergers of type 1 and morphologically distorted systems of type 2a and 2b as reliable merger candidates. We identify 20 morphologically distorted mergers (13 of type 1, 3 of type 2a, and 4 of type 2b) in the sample. The fraction f_{merge} of

systems with $M_* \geq 10^9 M_\odot$, which show evidence of a recent or ongoing merger of mass ratio $> 1/10$ is 0.023 ± 0.007 . The estimated fractions of likely major mergers, likely minor mergers, and ambiguous cases are 0.01 ± 0.004 (9/886), 0.006 ± 0.003 (5/886), and 0.007 ± 0.003 (6/886), respectively. Similar merger fractions are obtained among systems with $M_* \geq 3.0 \times 10^9 M_\odot$.

- We also estimate the merger fraction using the automated CAS merger criterion ($A > 0.35$ and $A > S$; §Section 5.4.2 and Figure 5.6). Among systems with $M_* \geq 10^9 M_\odot$, we find the merger fraction to be $\sim 18/886$ or 0.02 ± 0.006 . While the CAS-based merger fraction may not be widely different from the visually-based merger fraction, the two methods pick different systems. The CAS criterion only captures 11 of the 20 ($55\% \pm 20\%$) visually classified mergers. Furthermore, the remaining 7/18 ($39\% \pm 14\%$) of the systems captured by CAS turn out to be non-interacting systems (Table 5.4). These contaminants tend to be dusty or highly inclined galaxies and systems with low level asymmetries, which are probably due to star formation (Figure 5.7).
- We compare our visually-based merger fraction in the A901/902 clusters with those reported in other clusters and groups out to $z \sim 0.8$ (§Section 5.4.5 and Figure 5.13). The low merger fractions among intermediate mass (10^9 to a few $\times 10^{10} M_\odot$) or intermediate luminosities ($L < L^*$) galaxies in the A901/902 clusters and other low redshift clusters are consistent with predictions from hierarchical models. However,

we cannot yet test the predicted rate of evolution of the merger fraction with redshift. Data on the merger fraction among $L \leq L^*$ cluster galaxies, based on our study and three other published studies, allow for a wide spectrum of scenarios, ranging from no evolution to evolution by a factor of ~ 5 over $z \sim 0.17$ to 0.4 .

- Throughout this paper, I consider the core of each cluster to be at a projected clustocentric radius of $R \leq 0.25$ Mpc. We refer to the region between the cluster core and the virial radius as the outer region of the clusters ($0.25 \text{ Mpc} < R \leq 1.2 \text{ Mpc}$). We refer to the region outside the virial radius ($1.2 \text{ Mpc} < R \leq 2.0 \text{ Mpc}$) as the outskirts region of the clusters. The mergers are found to lie outside the cluster core (§Section 5.4.3 and Figure 5.9), although the timescale for collisions and close encounters is shortest in the core (< 1 Gyr). I suggest that this is due to the large velocity dispersion ($700\text{--}900 \text{ km s}^{-1}$) of galaxies in the core. Such a dispersion makes it less likely that a close encounter between two galaxies culminates into a merger or a disruptive interaction associated with a large amount of tidal heating.

All of the galaxy mergers lie in the region ($0.25 \text{ Mpc} < R \leq 2 \text{ Mpc}$), between the core and cluster outskirts, although the timescale for collisions and close encounters is quite large ($\gg 1$ Gyr) in this region. One possible explanation might be that the galaxy velocity dispersion drops in the outer region, hence favoring mergers. However, limited number statistics of current spectroscopic data do not allow us to assess this pos-

sibility. Another possible scenario is that the interacting galaxies in the outer region and cluster outskirts are part of groups or field galaxies that are being accreted along cosmological filaments by the A901/902 clusters. We find that our estimated number density and fraction of mergers to be similar to that predicted at typical group overdensities in N -body simulations of groups and field galaxies accreting into the A901/902 clusters (Figure 5.12). This suggests the ongoing growth of the clusters via accretion of group and field galaxies. The preferentially blue color of the mergers (see below) also supports this scenario.

- Out of the 20 morphologically distorted merger remnants and merging pairs in the sample, 16 lie on the blue cloud and 4 are in the red sample (§Section 5.4.6 and Figure 5.14). The fraction of mergers, which lie on the blue cloud is $80\% \pm 18\%$ (16/20). This is over a factor of 2 higher than the fraction (294/866 or $34\% \pm 7\%$) of non-interacting galaxies, which lie on the blue cloud, suggesting that mergers are preferentially blue compared to non-interacting galaxies. This effect may be due to the enhanced recent star formation in mergers and/or due to the possibility that the mergers are part of group and field galaxies, which are accreting into the cluster.
- Among intermediate mass $M_* \geq 10^9 M_\odot$ systems, the average SFR_{UV} and $\text{SFR}_{\text{UV+IR}}$ of mergers are typically enhanced by only a modest factor of ~ 2 (Figure 5.15) and ~ 1.5 (Figure 5.16), respectively, compared

to the non-interacting galaxies (i.e., Symmetric + Irr-1). This modest enhancement is consistent with the theoretical predictions of Di Matteo et al. (2007), based on a recent statistical study of several hundred simulated galaxy collisions. Our results of a modest enhancement and a low merger fraction culminate in our finding that mergers contribute only a small fraction (between 10% and 15%) of the total SFR density of the A901/902 clusters.

- I find that Smooth (gas-poor) galaxies cluster in regions of high ICM density while clumpy (gas-rich) systems dominate at low ICM densities (Figure ??). The ratio of smooth (gas-poor) galaxies to very clumpy (gas-rich) galaxies within the central 0.3 Mpc is (89%:11%), (75%:25%), and (86%:14%), respectively, for A901a, A901b, and A902. These values are comparable to the ratio of (80%:20%) for early-type to late-type galaxies in the classical morphology-density relation (Dressler 1980). I also find that the fraction of bulge-dominated galaxies increases at higher local galaxy surface density (Σ_{10}) compared to disk-dominated galaxies which prefer lower local galaxy number density (Figure ??).
- I consider the depression of star formation in cluster galaxies via ram pressure stripping, which removes diffuse atomic gas from a galaxy, thereby gradually causing star formation to cease, once the existing molecular gas reservoir is used up over a few Gyr (§ 5.6). We estimate the timescale $t_{\text{ram-pressure}}$ for ram pressure stripping to ~ 300 Myr

in the core and ~ 600 Myr and ~ 1 Gyr in outer region. This suggests that ram pressure stripping may play a role in depressing star formation out to the cluster virial radius of 1.2 Mpc.

A.H. and S.J. gratefully acknowledge support from NSF grant AST-0607748, LTSA grant NAG5-13063, as well as programs HST-GO-10395, HST-GO-10861, and HST GO-11082, which were supported by NASA through a grant from the Space Telescope Science Institute, which is operated by the Association of Universities for Research in Astronomy, Incorporated, under NASA contract NAS5-26555. We thank Christopher Conselice for his assistance with CAS. E.vK. and M.B. were supported by the Austrian Science Foundation FWF under grant P18416, C.Y.P. by STScI and NRC-HIA Fellowship programmes, C.H. by European Commission Programme Sixth Framework Marie Curie Outgoing International Fellowship under contract MOIF-CT-2006-21891 and a CITA National fellowship, M.E.G. and C.W. by an STFC Advanced Fellowship, E.F.B. and K.J. by the DFG's Emmy Noether Programme, A.B. by the DLR (50 OR 0404), S.F.S. by the Spanish MEC grants AYA2005-09413-C02-02 and the PAI of the Junta de Andaluc as research group FQM322, L.V.W. by NSERC, Cifar and CFI, and D.H.M. by NASA under LTSA Grant NAG5-13102. The STAGES team thanks Hans-Walter Rix for providing essential support contributing to the success of the STAGES project. This research made use of NASA's Astrophysics Data System and NASA/IPAC Extragalactic Database.

Chapter 6

Summary

In this thesis I have explored the evolution of the rate at which molecular gas is converted into stars through detailed studies of Galactic low and high mass star forming regions, through multi-wavelength observations of gas-rich nearby starburst/interacting galaxies, and as a function of galaxy environment. This work provided a foundation for interpreting studies of star formation and gas content in external galaxies by directly comparing relations between star formation rate and gas surface densities in Galactic star forming regions to established extragalactic relations (Heiderman et al. 2010) as well as spatially resolved kpc regions in extreme star forming environments of starburst galaxies (Heiderman et al. 2011, 2012) and star formation in different environments (Heiderman et al. 2009). In this chapter, I summarize the main conclusions from this dissertation and refer the reader to each chapter summary and conclusions for further details.

In Chapter 2, I investigate the relation between star formation rate SFR and gas surface densities in Galactic star forming regions using a sample of young stellar objects (YSOs) and massive dense clumps. The YSO sample consists of objects located in 20 large molecular clouds from the *Spitzer* cores

to disks (c2d) and Gould’s Belt (GB) surveys. I find that c2d and GB clouds lie above the extragalactic SFR-gas relations (e.g., Kennicutt–Schmidt Law) by factors up to 17. Accounting for only the youngest YSOs, cloud regions with high Σ_{gas} lie above extragalactic relations up to a factor of 54 and overlap with high-mass star forming regions. Comparing ^{12}CO and ^{13}CO gas maps of the Perseus and Ophiuchus clouds to estimate gas surface densities and compare to measurements from A_V maps, I find that ^{13}CO , with the standard conversions to total gas, underestimates the A_V -based mass by factors of ~ 4 –5 and ^{12}CO may underestimate the total gas mass at $\Sigma_{\text{gas}} \gtrsim 200 M_{\odot} \text{ pc}^{-2}$ by $\gtrsim 30\%$. This small difference in mass estimates does not explain the large discrepancy between Galactic and extragalactic relations. I find evidence for a threshold of star formation (Σ_{th}) at $129 \pm 14 M_{\odot} \text{ pc}^{-2}$. At $\Sigma_{\text{gas}} > \Sigma_{\text{th}}$, the Galactic SFR-gas relation is linear. A possible reason for the difference between Galactic and extragalactic relations is that much of Σ_{gas} is below Σ_{th} in extragalactic studies, which detect all the CO-emitting gas. If the Kennicutt–Schmidt relation ($\Sigma_{\text{SFR}} \propto \Sigma_{\text{gas}}^{1.4}$) and a linear relation between dense gas and star formation is assumed, the fraction of dense star forming gas (f_{dense}) increases as $\sim \Sigma_{\text{gas}}^{0.4}$. A maximal starburst is created when Σ_{gas} reaches $\sim 300 \Sigma_{\text{th}}$ and the fraction of dense gas is ~ 1 .

I present the VIRUS-P Investigation of the eXtreme Environments of Starbursts (VIXENS) survey, sample of interacting galaxies, and integral field unit observations in Chapter 4.2. The VIXENS project is a large IFU survey of 15 nearby IR bright ($L_{\text{IR}} > 3 \times 10^{10} L_{\odot}$) interacting/starburst galaxies

that range from early stage (close pairs) to late stage mergers (single system with multiple nuclei) and span a wide range of SFRs and Σ_{gas} . The sample galaxies have a full suite of archival *Spitzer* 24 μm , GALEX far-UV, and existing $\text{CO}J = 1 \rightarrow 0$ and HI maps. In addition, I have single dish line survey of dense gas as traced by molecules such as $\text{HCN}(1-0)$, $\text{HCO}^+(1-0)$, and $\text{HNC}(1-0)$ from Nobeyama 45m and IRAM 30m telescopes for the sample, as well as $\text{HCN}(1-0)$ maps for a subset of our sample from CARMA. While starburst and interacting galaxies are relatively rare in the low- z universe, they are the dominant mode of star formation in the distant universe. Understanding the physics of star formation in nearby interacting/starburst systems is therefore paramount and will provide key insight to the physical processes of star formation in high- z interacting galaxies. The VIXENS observational program will provide the required constraints on theoretical models for galaxy evolution as well as a comparison sample for multi-wavelength observational studies of high- z interacting galaxies.

In Chapter 4, I investigate the relationship between star formation and gas content in late interaction phase galaxy merger Arp 299 from the VIXENS integral field unit (IFU) survey. By comparing IFU $\text{H}\alpha$ and $\text{Pa}\alpha$ hydrogen recombination line and 24 μm data to $\text{CO}J = 2 \rightarrow 1$, $\text{CO}J = 3 \rightarrow 2$, $\text{HCN}J = 1 \rightarrow 0$, $\text{HCO}^+J = 1 \rightarrow 0$, and HI maps, we explore the relation between the star formation rate (SFR) and gas surface densities on spatially resolved kpc scales. Extinction laws for a diffuse interstellar medium ($R_V = 3.1$) and in molecular clouds ($R_V = 5.5$) are considered and I find the latter to

recover the intrinsic $\text{H}\alpha/\text{Pa}\alpha$ ratio within a factor of ~ 2 , indicating $\text{H}\alpha$ and $\text{Pa}\alpha$ are heavily extinguished and do not reliably trace star formation. Visual extinctions (A_V) from $\text{H}\alpha/\text{H}\beta$ and $\text{H}\alpha/\text{Pa}\alpha$ line ratios are a factor of ~ 10 below A_V from CO maps. No evidence is found in our IFU data for an AGN in the nuclear regions of IC 694 or near the X-ray confirmed AGN in the nucleus of NGC 3690, however I find high $[\text{OI}]/\text{H}\alpha$ and $[\text{SII}]/\text{H}\alpha$ extranuclear line ratios which could be attributed to either a Seyfert-like ionization cone or shocked outflow from a superwind. The system average $\text{SFR}_{[\text{H}\alpha+24\mu\text{m}]}$ ($90 \pm 10 \text{ M}_\odot \text{ yr}^{-1}$) agrees well with the total infrared (IR) SFR from IRAS ($77 \pm 5 \text{ M}_\odot \text{ yr}^{-1}$), while $\text{SFR}_{[\text{H}\alpha]}$ and $\text{SFR}_{[24\mu\text{m}]}$ underestimate the total SFR by factors of ~ 4 and 2, respectively. SFRs derived from $\text{Pa}\alpha$ centered on the nuclear 1.3 kpc regions are found to be a factor of ~ 2 below that derived from $\text{SFR}_{[\text{H}\alpha+24\mu\text{m}]}$. I explore relations between the $\text{SFR}_{[\text{H}\alpha+24\mu\text{m}]}$ and molecular (SFR–Mol) gas surface density using $\text{CO}J = 2 \rightarrow 1$ and $\text{CO}J = 3 \rightarrow 2$ and find nuclear regions and integrated values to lie on the SFR–Mol gas surface density seen in high- z mergers (Daddi et al. 2010), while regions throughout the merger lie above the high- z relation which is likely due to the choice of CO–to- H_2 conversion factor. The SFR–Dense gas surface density relation in nuclear regions agrees well with the Gao & Solomon (2004b) relation for normal spirals and (U)LIRGs, however integrated and spatially resolved points lie above this relation with the differences being the choice of $\text{HCN}J = 1 \rightarrow 0$ and $\text{HCO}^+J = 1 \rightarrow 0$ to dense gas conversion factor. I compare $\Sigma_{\text{SFR} [\text{H}\alpha]}$ and Σ_{HI} in extranuclear regions and find the SFR–HI surface density relation on

4.7 kpc scales in Arp 299 follows similar trends seen in the outer disks of normal spirals and dwarf galaxies. The average star formation efficiency in extranuclear regions is a factor of ~ 6 compared to spirals and dwarfs, which may indicate star formation is being driven by turbulent motions compressing the gas to dense clumps. Using $[\text{NII}]/\text{H}\alpha$ strong line ratio, I find a mean metallicity for Arp 299 to be $12 + \log(\text{O}/\text{H})$ of 8.57 and see lower or diluted metallicities in the nuclear region compared to outer regions in agreement with the merger scenario in which galaxy interactions drive gas from outer regions inward. Using the relation between metallicity and CO integrated intensity, I find the median CO-to- H_2 conversion factor for Arp 299 to be $\sim 3.2\text{--}3.6 \text{ M}_\odot \text{ pc}^{-2} (\text{K km s}^{-1})^{-1}$ which lowers the dispersion in the SFR-Mol relation and moves 1.3 kpc regions in Arp 299 to lie in between the Kennicutt (1998b) normal spiral and starburst and Daddi et al. (2010) high- z SFR-gas relations. A relation between IRAS $F_{60}/F_{100} - \alpha_{\text{CO}}$ and $T_{\text{dust}} - \alpha_{\text{CO}}$ gives a range in α_{CO} of 0.67-0.99 $\text{M}_\odot \text{ pc}^{-2} (\text{K km s}^{-1})^{-1}$. This indicates a Galactic α_{CO} may be more suitable, however α_{CO} likely varies as a function of interaction phase based on whether the system is in starburst mode and region by region in galaxy mergers.

I investigated galaxy mergers and the influence of environment in the Abell 901/902 supercluster at $z \sim 0.165$ in Chapter 5. This investigation uses a sample of 893 bright ($R_{\text{Vega}} \leq 24$) intermediate mass ($M_* \geq 10^9 \text{ M}_\odot$) supercluster galaxies. I use *HST* ACS F606W data from the Space Telescope A901/902 Galaxy Evolution Survey (STAGES), COMBO-17, *Spitzer* $24\mu\text{m}$, and *XMM-Newton* X-ray data. The analysis utilizes both a physi-

cally driven visual classification system, and quantitative CAS parameters to identify systems which show evidence of a recent or ongoing merger of mass ratio $> 1/10$ (i.e., major and minor mergers). I find the merger fraction f_{merge} to be 0.023 ± 0.007 and estimate the fractions of likely major mergers, likely minor mergers, and ambiguous cases are 0.01 ± 0.004 , 0.006 ± 0.003 , and 0.007 ± 0.003 , respectively. I find that *all* mergers lie outside the cluster core of radius $R < 0.25$ Mpc and populate the region ($0.25 \text{ Mpc} < R \leq 2 \text{ Mpc}$) between the core and the cluster outskirts. The lack of mergers in the innermost regions of the cluster is likely due to the large galaxy velocity dispersion in the core. The frequency of mergers in the supercluster outer region is similar to that seen at typical group overdensities in N-body simulations. This can be attributed to the ongoing growth of clusters via accretion of group and field galaxies. I also compare the merger fraction in the Abell 901/902 supercluster with those reported in other clusters and groups out to $z \sim 0.4$ and find a wide spectrum of scenarios, ranging from no evolution to evolution by a factor of ~ 5 over $z \sim 0.17$ to 0.4 . I find galaxy mergers are preferentially blue and the average SFR is enhanced by a factor of ~ 1.5 to 2 compared to non-interacting normal galaxies, however Abell 901/902 mergers only contribute a small fraction 10%–15% of the total supercluster SFR density.

This thesis presents a study of star formation and relation to gas content from star forming regions in the Milky Way to nearby interacting galaxies that span a range of environments from isolated pairs to galaxy groups and clusters. The results of this study suggest that studying SFR–gas relations in

our Galaxy and in nearby galaxies may be useful and necessary for interpreting star formation observed in high- z galaxies. Connecting scaling relations across all star forming regimes will allow us to better understand if there exists a universal relation between star formation and gas content that could describe the process of star formation throughout cosmic time.

Bibliography

- Aalto, S., Radford, S. J. E., Scoville, N. Z., & Sargent, A. I. 1997, *ApJL*, 475, L107
- Abraham, R. G., van den Bergh, S., Glazebrook, K., Ellis, R. S., Santiago, B. X., Surma, P., & Griffiths, R. E. 1996, *ApJS*, 107, 1
- Adams, J. J., Blanc, G. A., Hill, G. J., Gebhardt, K., Drory, N., Hao, L., Bender, R., Byun, J., Ciardullo, R., Cornell, M. E., Finkelstein, S. L., Fry, A., Gawiser, E., Gronwall, C., Hopp, U., Jeong, D., Kelz, A., Kelzenberg, R., Komatsu, E., MacQueen, P. J., Murphy, J., Odoms, P. S., Roth, M., Schneider, D. P., Tufts, J. R., & Wilkinson, C. P. 2011, *ApJS*, 192, 5
- Alonso, M. S., Tissera, P. B., Coldwell, G., & Lambas, D. G. 2004, *MNRAS*, 352, 1081
- Alonso-Herrero, A., Rieke, G. H., Rieke, M. J., & Scoville, N. Z. 2000, *ApJ*, 532, 845
- André, P., Men'shchikov, A., Bontemps, S., Könyves, V., Motte, F., Schneider, N., Didelon, P., Minier, V., Saraceno, P., Ward-Thompson, D., di Francesco, J., White, G., Molinari, S., Testi, L., Abergel, A., Griffin, M., Henning, T., Royer, P., Merín, B., Vavrek, R., Attard, M., Arzoumanian, D., Wilson, C. D., Ade, P., Aussel, H., Baluteau, J., Benedettini, M., Bernard, J.,

- Blommaert, J. A. D. L., Cambr  sy, L., Cox, P., di Giorgio, A., Hargrave, P., Hennemann, M., Huang, M., Kirk, J., Krause, O., Launhardt, R., Leeks, S., Le Penne  , J., Li, J. Z., Martin, P. G., Maury, A., Olofsson, G., Omont, A., Peretto, N., Pezzuto, S., Prusti, T., Roussel, H., Russeil, D., Sauvage, M., Sibthorpe, B., Sicilia-Aguilar, A., Spinoglio, L., Waelkens, C., Woodcraft, A., & Zavagno, A. 2010, *A&A*, 518, L102
- Asplund, M., Grevesse, N., Sauval, A. J., & Scott, P. 2009, *ARAA*, 47, 481
- Baan, W. A. & Haschick, A. 1990, *ApJ*, 364, 65
- Bachiller, R. & Cernicharo, J. 1986, *A&A*, 166, 283
- Baldwin, A., Phillips, M. M., & Terlevich, R. 1981, *PASP*, 93, 817
- Ballo, L., Braito, V., Della Ceca, R., Maraschi, L., Tavecchio, F., & Dadina, M. 2004, *ApJ*, 600, 634
- Balogh, M. L. & Morris, S. L. 2000, *MNRAS*, 318, 703
- Balogh, M. L., Morris, S. L., Yee, H. K. C., Carlberg, R. G., & Ellingson, E. 1999, *ApJ*, 527, 54
- Balogh, M. L., Schade, D., Morris, S. L., Yee, H. K. C., Carlberg, R. G., & Ellingson, E. 1998, *ApJL*, 504, L75
- Barnes, J. E. 1992, *ApJ*, 393, 484
- Barnes, J. E. & Hernquist, L. E. 1991, *ApJL*, 370, L65

- Barton, E. J., Geller, M. J., & Kenyon, S. J. 2000, *ApJ*, 530, 660
- Barton Gillespie, E., Geller, M. J., & Kenyon, S. J. 2003, *ApJ*, 582, 668
- Bell, E. F., Papovich, C., Wolf, C., Le Floch, E., Caldwell, J. A. R., Barden, M., Egami, E., McIntosh, D. H., Meisenheimer, K., Pérez-González, P. G., Rieke, G. H., Rieke, M. J., Rigby, J. R., & Rix, H.-W. 2005, *ApJ*, 625, 23
- Bell, E. F., Zheng, X. Z., Papovich, C., Borch, A., Wolf, C., & Meisenheimer, K. 2007, *ApJ*, 663, 834
- Bershady, M. A., Jangren, A., & Conselice, C. J. 2000, *AJ*, 119, 2645
- Bertin, E. & Arnouts, S. 1996, *A&A Suppl.*, 117, 393
- Bigiel, F., Leroy, A., Walter, F., Blitz, L., Brinks, E., de Blok, W. J. G., & Madore, B. 2010, *AJ*, 140, 1194
- Bigiel, F., Leroy, A., Walter, F., Brinks, E., de Blok, W. J. G., Madore, B., & Thornley, M. D. 2008, *AJ*, 136, 2846
- Bigiel, F., Leroy, A. K., Walter, F., Brinks, E., de Blok, W. J. G., Kramer, C., Rix, H. W., Schrubba, A., Schuster, K.-F., Usero, A., & Wiese Meyer, H. W. 2011, *ApJL*, 730, L13
- Binggeli, B., Sandage, A., & Tammann, G. A. 1988, *ARAA*, 26, 509
- Binney, J. & Tremaine, S. 1987, *Galactic dynamics*

- Blanc, G. A., Heiderman, A., Gebhardt, K., Evans, N. J., & Adams, J. 2009, *ApJ*, 704, 842
- Blanton, M. R., Eisenstein, D., Hogg, D. W., Schlegel, D. J., & Brinkmann, J. 2005, *ApJ*, 629, 143
- Blitz, L., Fukui, Y., Kawamura, A., Leroy, A., Mizuno, N., & Rosolowsky, E. 2007, *Protostars and Planets V*, 81
- Bloemen, J. B. G. M., Strong, A. W., Mayer-Hasselwander, H. A., Blitz, L., Cohen, R. S., Dame, T. M., Grabelsky, D. A., Thaddeus, P., Hermsen, W., & Lebrun, F. 1986, *A&A*, 154, 25
- Boissier, S., Prantzos, N., Boselli, A., & Gavazzi, G. 2003, *MNRAS*, 346, 1215
- Borch, A., Meisenheimer, K., Bell, E. F., Rix, H.-W., Wolf, C., Dye, S., Kleinheinrich, M., Kovacs, Z., & Wisotzki, L. 2006, *A&A*, 453, 869
- Bournaud, F., Elmegreen, B. G., Teyssier, R., Block, D. L., & Puerari, I. 2010, *MNRAS*, 409, 1088
- Braun, R., Thilker, D. A., Walterbos, R. A. M., & Corbelli, E. 2009, *ApJ*, 695, 937
- Butcher, H. & Oemler, Jr., A. 1978, *ApJ*, 219, 18
- Caldwell, J. A. R., McIntosh, D. H., Rix, H.-W., Barden, M., Beckwith, S. V. W., Bell, E. F., Borch, A., Heymans, C., Häußler, B., Jahnke, K.,

- Jogee, S., Meisenheimer, K., Peng, C. Y., Sánchez, S. F., Somerville, R. S., Wisotzki, L., & Wolf, C. 2008, *ApJS*, 174, 136
- Calzetti, D., Armus, L., Bohlin, R. C., Kinney, A. L., Koornneef, J., & Storchi-Bergmann, T. 2000, *ApJ*, 533, 682
- Calzetti, D., Liu, G., & Koda, J. 2012, *ApJ*, 752, 98
- Cappellari, M. & Emsellem, E. 2004, *PASP*, 116, 138
- Carlberg, R. G., Yee, H. K. C., Ellingson, E., Morris, S. L., Abraham, R., Gravel, P., Pritchet, C. J., Smecker-Hane, T., Hartwick, F. D. A., Hesser, J. E., Hutchings, J. B., & Oke, J. B. 1997, *ApJL*, 476, L7
- Carpenter, J. M., Snell, R. L., & Schloerb, F. P. 1995, *ApJ*, 445, 246
- Caselli, P., Walmsley, C. M., Tafalla, M., Dore, L., & Myers, P. C. 1999, *ApJL*, 523, L165
- Casoli, F., Willaime, M.-C., Viallefond, F., & Gerin, M. 1999, *A&A*, 346, 663
- Chabrier, G. 2003, *PASP*, 115, 763
- Cole, S., Lacey, C. G., Baugh, C. M., & Frenk, C. S. 2000, *MNRAS*, 319, 168
- Cole, S., Norberg, P., Baugh, C. M., Frenk, C. S., Bland-Hawthorn, J., Bridges, T., Cannon, R., Colless, M., Collins, C., Couch, W., Cross, N., Dalton, G., De Propriis, R., Driver, S. P., Efstathiou, G., Ellis, R. S., Glazebrook, K., Jackson, C., Lahav, O., Lewis, I., Lumsden, S., Maddox, S., Madgwick,

- D., Peacock, J. A., Peterson, B. A., Sutherland, W., & Taylor, K. 2001, MNRAS, 326, 255
- Conselice, C. J. 2006, ApJ, 638, 686
- Conselice, C. J., Bershadsky, M. A., Dickinson, M., & Papovich, C. 2003, AJ, 126, 1183
- Conselice, C. J., Bershadsky, M. A., & Jangren, A. 2000, ApJ, 529, 886
- Couch, W. J., Barger, A. J., Smail, I., Ellis, R. S., & Sharples, R. M. 1998, ApJ, 497, 188
- Coziol, R., Torres, C. A. O., Quast, G. R., Contini, T., & Davoust, E. 1998, ApJS, 119, 239
- Crutcher, R. M. 1999, ApJ, 520, 706
- Daddi, E., Elbaz, D., Walter, F., Bournaud, F., Salmi, F., Carilli, C., Dannerbauer, H., Dickinson, M., Monaco, P., & Riechers, D. 2010, ApJL, 714, L118
- De Propris, R., Colless, M., Driver, S. P., Couch, W., Peacock, J. A., Baldry, I. K., Baugh, C. M., Bland-Hawthorn, J., Bridges, T., Cannon, R., Cole, S., Collins, C., Cross, N., Dalton, G. B., Efstathiou, G., Ellis, R. S., Frenk, C. S., Glazebrook, K., Hawkins, E., Jackson, C., Lahav, O., Lewis, I., Lumsden, S., Maddox, S., Madgwick, D. S., Norberg, P., Percival, W., Peterson, B., Sutherland, W., & Taylor, K. 2003, MNRAS, 342, 725

- Della Ceca, R., Ballo, L., Tavecchio, F., Maraschi, L., Petrucci, P. O., Bassani, L., Cappi, M., Dadina, M., Franceschini, A., Malaguti, G., Palumbo, G. G. C., & Persic, M. 2002, *ApJL*, 581, L9
- den Hartog, R. & Katgert, P. 1996, *MNRAS*, 279, 349
- Di Matteo, P., Combes, F., Melchior, A.-L., & Semelin, B. 2007, *A&A*, 468, 61
- Diaferio, A., Kauffmann, G., Balogh, M. L., White, S. D. M., Schade, D., & Ellingson, E. 2001, *MNRAS*, 323, 999
- Dickman, R. L., Snell, R. L., & Schloerb, F. P. 1986, *ApJ*, 309, 326
- Dopita, M. A. & Sutherland, R. S. 1995, *ApJ*, 455, 468
- Downes, D. & Solomon, P. M. 1998, *ApJ*, 507, 615
- Draine, B. T. 2003, *ARAA*, 41, 241
- Dressler, A. 1980, *ApJ*, 236, 351
- Dressler, A., Oemler, Jr., A., Couch, W. J., Smail, I., Ellis, R. S., Barger, A., Butcher, H., Poggianti, B. M., & Sharples, R. M. 1997, *ApJ*, 490, 577
- Dressler, A., Oemler, Jr., A., Sparks, W. B., & Lucas, R. A. 1994, *ApJL*, 435, L23
- Duvert, G., Cernicharo, J., & Baudry, A. 1986, *A&A*, 164, 349

- Dzib, S., Loinard, L., Mioduszewski, A. J., Boden, A. F., Rodríguez, L. F., & Torres, R. M. 2010, *ApJ*, 718, 610
- Ellison, S. L., Patton, D. R., Simard, L., & McConnachie, A. W. 2008, *AJ*, 135, 1877
- Elmegreen, B. G. 1994, *ApJL*, 425, L73
- . 2002, *ApJ*, 577, 206
- Enoch, M. L., Glenn, J., Evans, II, N. J., Sargent, A. I., Young, K. E., & Huard, T. L. 2007, *ApJ*, 666, 982
- Evans, N. J., Dunham, M. M., Jørgensen, J. K., Enoch, M. L., Merín, B., van Dishoeck, E. F., Alcalá, J. M., Myers, P. C., Stapelfeldt, K. R., Huard, T. L., Allen, L. E., Harvey, P. M., van Kempen, T., Blake, G. A., Koerner, D. W., Mundy, L. G., Padgett, D. L., & Sargent, A. I. 2009, *ApJS*, 181, 321
- Evans, II, N. J. 1999, *ARAA*, 37, 311
- Evans, II, N. J. 2008, in *Astronomical Society of the Pacific Conference Series*, Vol. 390, *Pathways Through an Eclectic Universe*, ed. J. H. Knapen, T. J. Mahoney, & A. Vazdekis, 52
- Evans, II, N. J., Allen, L. E., Blake, G. A., Boogert, A. C. A., Bourke, T., Harvey, P. M., Kessler, J. E., Koerner, D. W., Lee, C. W., Mundy, L. G., Myers, P. C., Padgett, D. L., Pontoppidan, K., Sargent, A. I., Stapelfeldt,

- K. R., van Dishoeck, E. F., Young, C. H., & Young, K. E. 2003, *PASP*, 115, 965
- Falcón-Barroso, J., Sánchez-Blázquez, P., Vazdekis, A., Ricciardelli, E., Cardiel, N., Cenarro, A. J., Gorgas, J., & Peletier, R. F. 2011, *A&A*, 532, A95
- Forbrich, J., Lada, C. J., Muench, A. A., Alves, J., & Lombardi, M. 2009, *ApJ*, 704, 292
- Frerking, M. A., Langer, W. D., & Wilson, R. W. 1982, *ApJ*, 262, 590
- Gallais, P., Charmandaris, V., Le Floch, E., Mirabel, I. F., Sauvage, M., Vigroux, L., & Laurent, O. 2004, *A&A*, 414, 845
- Gallazzi, A., Bell, E. F., Wolf, C., Gray, M. E., Papovich, C., Barden, M., Peng, C. Y., Meisenheimer, K., Heymans, C., van Kampen, E., Gilmour, R., Balogh, M., McIntosh, D. H., Bacon, D., Barazza, F. D., Böhm, A., Caldwell, J. A. R., Häußler, B., Jahnke, K., Jogee, S., Lane, K., Robaina, A. R., Sanchez, S. F., Taylor, A., Wisotzki, L., & Zheng, X. 2009, *ApJ*, 690, 1883
- Gao, Y. & Solomon, P. M. 2004a, *ApJS*, 152, 63
- . 2004b, *ApJ*, 606, 271
- García-Burillo, S., Usero, A., Alonso-Herrero, A., Graciá-Carpio, J., Pereira-Santaella, M., Colina, L., Planesas, P., & Arribas, S. 2012, *A&A*, 539, A8

- García-Marín, M., Colina, L., Arribas, S., Alonso-Herrero, A., & Mediavilla, E. 2006, *ApJ*, 650, 850
- Gavazzi, G. & Jaffe, W. 1985, *ApJL*, 294, L89
- Gehrz, R. D., Sramek, R. A., & Weedman, D. W. 1983, *ApJ*, 267, 551
- Genzel, R., Tacconi, L. J., Gracia-Carpio, J., Sternberg, A., Cooper, M. C., Shapiro, K., Bolatto, A., Bouché, N., Bournaud, F., Burkert, A., Combes, F., Comerford, J., Cox, P., Davis, M., Schreiber, N. M. F., Garcia-Burillo, S., Lutz, D., Naab, T., Neri, R., Omont, A., Shapley, A., & Weiner, B. 2010, *MNRAS*, 407, 2091
- Gilmour, R., Gray, M. E., Almaini, O., Best, P., Wolf, C., Meisenheimer, K., Papovich, C., & Bell, E. 2007, *MNRAS*, 380, 1467
- Giovanelli, R., Haynes, M. P., & Chincarini, G. L. 1986, *ApJ*, 300, 77
- Gnedin, O. Y. 2003, *ApJ*, 582, 141
- Goldsmith, P. F., Heyer, M., Narayanan, G., Snell, R., Li, D., & Brunt, C. 2008, *ApJ*, 680, 428
- Gottlöber, S., Klypin, A., & Kravtsov, A. V. 2001, *ApJ*, 546, 223
- Graciá-Carpio, J., García-Burillo, S., Planesas, P., & Colina, L. 2006, *ApJL*, 640, L135
- Gray, M. E., Taylor, A. N., Meisenheimer, K., Dye, S., Wolf, C., & Thommes, E. 2002, *ApJ*, 568, 141

- Gray, M. E., Wolf, C., Barden, M., Peng, C. Y., Häußler, B., Bell, E. F., McIntosh, D. H., Guo, Y., Caldwell, J. A. R., Bacon, D., Balogh, M., Barazza, F. D., Böhm, A., Heymans, C., Jahnke, K., Jogee, S., van Kampen, E., Lane, K., Meisenheimer, K., Sánchez, S. F., Taylor, A., Wisotzki, L., Zheng, X., Green, D. A., Beswick, R. J., Saikia, D. J., Gilmour, R., Johnson, B. D., & Papovich, C. 2009, MNRAS, 393, 1275
- Greene, T. P., Wilking, B. A., Andre, P., Young, E. T., & Lada, C. J. 1994, ApJ, 434, 614
- Gunn, J. E. & Gott, III, J. R. 1972, ApJ, 176, 1
- Gutermuth, R. A., Pipher, J. L., Megeath, S. T., Myers, P. C., Allen, L. E., & Allen, T. S. 2011, ApJ, 739, 84
- Harvey, P. M., Huard, T. L., Jørgensen, J. K., Gutermuth, R. A., Mamajek, E. E., Bourke, T. L., Merín, B., Cieza, L., Brooke, T., Chapman, N., Alcalá, J. M., Allen, L. E., Evans, II, N. J., Di Francesco, J., & Kirk, J. M. 2008, ApJ, 680, 495
- Heckman, T. M., Armus, L., Weaver, K. A., & Wang, J. 1999, ApJ, 517, 130
- Heiderman, A., Evans, II, N. J., Allen, L. E., Huard, T., & Heyer, M. 2010, ApJ, 723, 1019
- Heiderman, A., Jogee, S., Marinova, I., van Kampen, E., Barden, M., Peng, C. Y., Heymans, C., Gray, M. E., Bell, E. F., Bacon, D., Balogh, M.,

- Barazza, F. D., Böhm, A., Caldwell, J. A. R., Häußler, B., Jahnke, K., Lane, K., McIntosh, D. H., Meisenheimer, K., Sánchez, S. F., Somerville, R. S., Taylor, A., Wisotzki, L., Wolf, C., & Zheng, X. 2009, *ApJ*, 705, 1433
- Heiderman, A. L., Evans, N. J., Gebhardt, K., Blanc, G. A., Davis, T. A., Iono, D., Papovich, C., van den Bosch, R., & Yun, M. 2012, *ApJ*, submitted
- Heiderman, A. L., Evans, II, N. J., Gebhardt, K., Blanc, G., Davis, T. A., Papovich, C., Iono, D., & Yun, M. S. 2011, in *New Horizons in Astronomy, Proceedings of the Frank N. Bash Symposium 2011*, held October 9-11, 2011. Austin, Texas, USA. Edited by S. Salviander, J. Green, and A. Pawlik. Published online at <http://pos.sissa.it/cgi-bin/reader/conf.cgi?confid=149><http://pos.sissa.it/cgi-bin/reader/conf.cgi?confid=149>, id.29
- Heiles, C. & Crutcher, R. 2005, in *Lecture Notes in Physics*, Berlin Springer Verlag, Vol. 664, *Cosmic Magnetic Fields*, ed. R. Wiełebinski & R. Beck, 137
- Helou, G. 1986, *ApJL*, 311, L33
- Hernquist, L. & Mihos, J. C. 1995, *ApJ*, 448, 41
- Heyer, M., Krawczyk, C., Duval, J., & Jackson, J. M. 2009, *ApJ*, 699, 1092
- Heyer, M. H., Carpenter, J. M., & Ladd, E. F. 1996, *ApJ*, 463, 630
- Heyer, M. H., Carpenter, J. M., & Snell, R. L. 2001, *ApJ*, 551, 852

- Heyer, M. H., Corbelli, E., Schneider, S. E., & Young, J. S. 2004, *ApJ*, 602, 723
- Heyer, M. H. & Ladd, E. F. 1995, *ApJ*, 439, 269
- Heymans, C., Gray, M. E., Peng, C. Y., van Waerbeke, L., Bell, E. F., Wolf, C., Bacon, D., Balogh, M., Barazza, F. D., Barden, M., Böhm, A., Caldwell, J. A. R., Häußler, B., Jahnke, K., Jogee, S., van Kampen, E., Lane, K., McIntosh, D. H., Meisenheimer, K., Mellier, Y., Sánchez, S. F., Taylor, A. N., Wisotzki, L., & Zheng, X. 2008, *MNRAS*, 385, 1431
- Hibbard, J. E. & Yun, M. S. 1999, *AJ*, 118, 162
- Hildebrand, R. H. 1983, *QJRAS*, 24, 267
- Ho, L. C., Filippenko, A. V., & Sargent, W. L. W. 1997, *ApJS*, 112, 315
- Hopkins, P. F., Cox, T. J., Younger, J. D., & Hernquist, L. 2009, *ApJ*, 691, 1168
- Imanishi, M. & Nakanishi, K. 2006, *PASJ*, 58, 813
- Jogee, S. 2006, in *Lecture Notes in Physics*, Berlin Springer Verlag, Vol. 693, *Physics of Active Galactic Nuclei at all Scales*, ed. D. Alloin, 143
- Jogee, S., Kenney, J. D. P., & Smith, B. J. 1999, *ApJ*, 526, 665
- Jogee, S., Miller, S., Penner, K., Bell, E. F., Conselice, C., Skelton, R. E., Somerville, R. S., Rix, H.-W., Barazza, F. D., Barden, M., Borch, A., Beckwith, S. V., Caldwell, J. A. R., Häußler, B., Heymans, C., Jahnke, K.,

- McIntosh, D., Meisenheimer, K., Papovich, C., Peng, C. Y., Robaina, A., Sanchez, S., Wisotzki, L., & Wolf, C. 2008, in *Astronomical Society of the Pacific Conference Series*, Vol. 396, *Formation and Evolution of Galaxy Disks*, ed. J. G. Funes & E. M. Corsini, 337
- Jogee, S., Miller, S. H., Penner, K., Skelton, R. E., Conselice, C. J., Somerville, R. S., Bell, E. F., Zheng, X. Z., Rix, H.-W., Robaina, A. R., Barazza, F. D., Barden, M., Borch, A., Beckwith, S. V. W., Caldwell, J. A. R., Peng, C. Y., Heymans, C., McIntosh, D. H., Häußler, B., Jahnke, K., Meisenheimer, K., Sanchez, S. F., Wisotzki, L., Wolf, C., & Papovich, C. 2009, *ApJ*, 697, 1971
- Johnstone, D., Di Francesco, J., & Kirk, H. 2004, *ApJL*, 611, L45
- Juneau, S., Narayanan, D. T., Moustakas, J., Shirley, Y. L., Bussmann, R. S., Kennicutt, Jr., R. C., & Vanden Bout, P. A. 2009, *ApJ*, 707, 1217
- Kartaltepe, J. S., Sanders, D. B., Scoville, N. Z., Calzetti, D., Capak, P., Koekemoer, A., Mobasher, B., Murayama, T., Salvato, M., Sasaki, S. S., & Taniguchi, Y. 2007, *ApJS*, 172, 320
- Kauffmann, G., Heckman, T. M., Tremonti, C., Brinchmann, J., Charlot, S., White, S. D. M., Ridgway, S. E., Brinkmann, J., Fukugita, M., Hall, P. B., Ivezić, Ž., Richards, G. T., & Schneider, D. P. 2003, *MNRAS*, 346, 1055
- Kauffmann, J., Bertoldi, F., Bourke, T. L., Evans, II, N. J., & Lee, C. W. 2008, *A&A*, 487, 993
- Kennicutt, R. C. & Evans, N. J. 2012, *ARAA*, 50, 531

Kennicutt, Jr., R. C. 1989, *ApJ*, 344, 685

—. 1998a, *ARAA*, 36, 189

—. 1998b, *ApJ*, 498, 541

Kennicutt, Jr., R. C., Calzetti, D., Walter, F., Helou, G., Hollenbach, D. J., Armus, L., Bendo, G., Dale, D. A., Draine, B. T., Engelbracht, C. W., Gordon, K. D., Prescott, M. K. M., Regan, M. W., Thornley, M. D., Bot, C., Brinks, E., de Blok, E., de Mello, D., Meyer, M., Moustakas, J., Murphy, E. J., Sheth, K., & Smith, J. D. T. 2007, *ApJ*, 671, 333

Kennicutt, Jr., R. C. & Kent, S. M. 1983, *AJ*, 88, 1094

Kewley, L. J., Dopita, M. A., Sutherland, R. S., Heisler, C. A., & Trevena, J. 2001, *ApJ*, 556, 121

Kewley, L. J., Groves, B., Kauffmann, G., & Heckman, T. 2006, *MNRAS*, 372, 961

Kewley, L. J., Rupke, D., Zahid, H. J., Geller, M. J., & Barton, E. J. 2010, *ApJL*, 721, L48

Khochfar, S. & Burkert, A. 2001, *ApJ*, 561, 517

Kirk, J. M., Ward-Thompson, D., Di Francesco, J., Bourke, T. L., Evans, N. J., Merín, B., Allen, L. E., Cieza, L. A., Dunham, M. M., Harvey, P., Huard, T., Jørgensen, J. K., Miller, J. F., Noriega-Crespo, A., Peterson, D., Ray, T. P., & Rebull, L. M. 2009, *ApJS*, 185, 198

- Komugi, S., Sofue, Y., Nakanishi, H., Onodera, S., & Egusa, F. 2005, PASJ, 57, 733
- Koopmann, R. A. & Kenney, J. D. P. 2004, ApJ, 613, 866
- Kroupa, P. 2001, MNRAS, 322, 231
- . 2002, Science, 295, 82
- Kroupa, P., Tout, C. A., & Gilmore, G. 1993, MNRAS, 262, 545
- Krumholz, M. R., McKee, C. F., & Tumlinson, J. 2009, ApJ, 693, 216
- Krumholz, M. R. & Tan, J. C. 2007, ApJ, 654, 304
- Krumholz, M. R. & Thompson, T. A. 2007, ApJ, 669, 289
- Kuno, N., Nakai, N., Handa, T., & Sofue, Y. 1995, PASJ, 47, 745
- Lada, C. J. & Lada, E. A. 2003, ARAA, 41, 57
- Lada, E. A. 1992, ApJL, 393, L25
- Langer, W. D., Wilson, R. W., Goldsmith, P. F., & Beichman, C. A. 1989, ApJ, 337, 355
- Larson, R. 1992, in Star Formation in Stellar Systems, ed. G. Tenorio-Tagle, M. Prieto, & F. Sanchez, 125
- Larson, R. B. & Tinsley, B. M. 1978, ApJ, 219, 46
- Larson, R. B., Tinsley, B. M., & Caldwell, C. N. 1980, ApJ, 237, 692

- Lavery, R. J. & Henry, J. P. 1988, *ApJ*, 330, 596
- Lavery, R. J., Pierce, M. J., & McClure, R. D. 1992, *AJ*, 104, 2067
- Le Floch, E., Papovich, C., Dole, H., Bell, E. F., Lagache, G., Rieke, G. H., Egami, E., Pérez-González, P. G., Alonso-Herrero, A., Rieke, M. J., Blaylock, M., Engelbracht, C. W., Gordon, K. D., Hines, D. C., Misselt, K. A., Morrison, J. E., & Mould, J. 2005, *ApJ*, 632, 169
- Lin, L., Koo, D. C., Willmer, C. N. A., Patton, D. R., Conselice, C. J., Yan, R., Coil, A. L., Cooper, M. C., Davis, M., Faber, S. M., Gerke, B. F., Guhathakurta, P., & Newman, J. A. 2004, *ApJL*, 617, L9
- Lombardi, M., Alves, J., & Lada, C. J. 2006, *A&A*, 454, 781
- Lombardi, M., Lada, C. J., & Alves, J. 2008, *A&A*, 489, 143
- . 2010, *A&A*, 512, A67
- Lotz, J. M., Jonsson, P., Cox, T. J., & Primack, J. R. 2008, *MNRAS*, 391, 1137
- Magnelli, B., Saintonge, A., Lutz, D., Tacconi, L. J., Berta, S., Bournaud, F., Charmandaris, V., Dannerbauer, H., Elbaz, D., Förster-Schreiber, N. M., Graciá-Carpio, J., Ivison, R., Maiolino, R., Nordon, R., Popesso, P., Rodighiero, G., Santini, P., & Wuyts, S. 2012, *ArXiv e-prints*
- Margoniner, V. E., de Carvalho, R. R., Gal, R. R., & Djorgovski, S. G. 2001, *ApJL*, 548, L143

- Martin, C. L. & Kennicutt, Jr., R. C. 2001, *ApJ*, 555, 301
- Massey, P., Strobel, K., Barnes, J. V., & Anderson, E. 1988, *ApJ*, 328, 315
- McGee, S. L., Balogh, M. L., Henderson, R. D. E., Wilman, D. J., Bower, R. G., Mulchaey, J. S., & Oemler, Jr., A. 2008, *MNRAS*, 387, 1605
- McIntosh, D. H., Guo, Y., Hertzberg, J., Katz, N., Mo, H. J., van den Bosch, F. C., & Yang, X. 2008, *MNRAS*, 388, 1537
- McKee, C. F. 1989, *ApJ*, 345, 782
- Mihos, J. C. 1995, *ApJL*, 438, L75
- Mihos, J. C. & Hernquist, L. 1996, *ApJ*, 464, 641
- Miller, S. H., Jogee, S., Conselice, C., Penner, K., Bell, E., Zheng, X., Papovich, C., Skelton, R., Somerville, R., Rix, H.-W., Barazza, F., Barden, M., Borch, A., Beckwith, S., Caldwell, J., Häussler, B., Heymans, C., Robaina, A., Sanchez, S., Zheng, X., Borch, A., Peng, C., Papovich, C., Beckwith, S., McIntosh, D., Caldwell, J., Conselice, C., Haeussler, B., Rix, H., Wolf, C., Somerville, R., Meisenheimer, K., & Wisotzki, L. 2008, in *Astronomical Society of the Pacific Conference Series*, Vol. 393, *New Horizons in Astronomy*, ed. A. Frebel, J. R. Maund, J. Shen, & M. H. Siegel, 235
- Moore, B., Katz, N., Lake, G., Dressler, A., & Oemler, A. 1996, *Nature*, 379, 613
- Moore, B., Lake, G., & Katz, N. 1998, *ApJ*, 495, 139

- Mouschovias, T. C. & Spitzer, Jr., L. 1976, ApJ, 210, 326
- Murphy, E. J., Condon, J. J., Schinnerer, E., Kennicutt, R. C., Calzetti, D., Armus, L., Helou, G., Turner, J. L., Aniano, G., Beirão, P., Bolatto, A. D., Brandl, B. R., Croxall, K. V., Dale, D. A., Donovan Meyer, J. L., Draine, B. T., Engelbracht, C., Hunt, L. K., Hao, C.-N., Koda, J., Roussel, H., Skibba, R., & Smith, J.-D. T. 2011, ApJ, 737, 67
- Naab, T. & Burkert, A. 2001, ApJL, 555, L91
- Narayanan, D., Krumholz, M. R., Ostriker, E. C., & Hernquist, L. 2012, MNRAS, 421, 3127
- Neff, S. G., Ulvestad, J. S., & Teng, S. H. 2004, ApJ, 611, 186
- Negroponte, J. & White, S. D. M. 1983, MNRAS, 205, 1009
- Nikolic, B., Cullen, H., & Alexander, P. 2004, MNRAS, 355, 874
- Ninkovic, S. & Trajkovska, V. 2006, Serbian Astronomical Journal, 172, 17
- Oemler, Jr., A., Dressler, A., & Butcher, H. R. 1997, ApJ, 474, 561
- Onishi, T., Mizuno, A., Kawamura, A., Ogawa, H., & Fukui, Y. 1998, ApJ, 502, 296
- Osterbrock, D. E. & Ferland, G. J. 2006, Astrophysics of gaseous nebulae and active galactic nuclei

- Papadopoulos, P. P., van der Werf, P., Xilouris, E., Isaak, K. G., & Gao, Y. 2012, *ApJ*, 751, 10
- Papovich, C. & Bell, E. F. 2002, *ApJL*, 579, L1
- Pettini, M. & Pagel, B. E. J. 2004, *MNRAS*, 348, L59
- Pineda, J. E., Caselli, P., & Goodman, A. A. 2008, *ApJ*, 679, 481
- Pineda, J. L., Goldsmith, P. F., Chapman, N., Snell, R. L., Li, D., Cambresy, L., & Brunt, C. 2010, *ArXiv e-prints*
- Plume, R., Jaffe, D. T., Evans, II, N. J., Martin-Pintado, J., & Gomez-Gonzalez, J. 1997, *ApJ*, 476, 730
- Postman, M. & Geller, M. J. 1984, *ApJ*, 281, 95
- Quilis, V., Moore, B., & Bower, R. 2000, *Science*, 288, 1617
- Quinn, P. J., Hernquist, L., & Fullagar, D. P. 1993, *ApJ*, 403, 74
- Rahman, N., Bolatto, A. D., Xue, R., Wong, T., Leroy, A. K., Walter, F., Bigiel, F., Rosolowsky, E., Fisher, D. B., Vogel, S. N., Blitz, L., West, A. A., & Ott, J. 2012, *ApJ*, 745, 183
- Rebull, L. M., Padgett, D. L., McCabe, C., Hillenbrand, L. A., Stapelfeldt, K. R., Noriega-Crespo, A., Carey, S. J., Brooke, T., Huard, T., Terebey, S., Audard, M., Monin, J., Fukagawa, M., Güdel, M., Knapp, G. R., Menard, F., Allen, L. E., Angione, J. R., Baldwin-Saavedra, C., Bouvier, J., Briggs,

- K., Dougados, C., Evans, N. J., Flagey, N., Guieu, S., Grosso, N., Glauser, A. M., Harvey, P., Hines, D., Latter, W. B., Skinner, S. L., Strom, S., Tromp, J., & Wolf, S. 2010, *ApJS*, 186, 259
- Reiter, M., Shirley, Y. L., Wu, J., Brogan, C., Wootten, A., & Tatematsu, K. 2011, *ApJS*, 195, 1
- Ridge, N. A., Di Francesco, J., Kirk, H., Li, D., Goodman, A. A., Alves, J. F., Arce, H. G., Borkin, M. A., Caselli, P., Foster, J. B., Heyer, M. H., Johnstone, D., Kosslyn, D. A., Lombardi, M., Pineda, J. E., Schnee, S. L., & Tafalla, M. 2006, *AJ*, 131, 2921
- Robaina, A. R., Bell, E. F., Skelton, R. E., McIntosh, D. H., Somerville, R. S., Zheng, X., Rix, H.-W., Bacon, D., Balogh, M., Barazza, F. D., Barden, M., Böhm, A., Caldwell, J. A. R., Gallazzi, A., Gray, M. E., Häussler, B., Heymans, C., Jahnke, K., Jogee, S., van Kampen, E., Lane, K., Meisenheimer, K., Papovich, C., Peng, C. Y., Sánchez, S. F., Skibba, R., Taylor, A., Wisotzki, L., & Wolf, C. 2009, *ApJ*, 704, 324
- Robertson, B., Yoshida, N., Springel, V., & Hernquist, L. 2004, *ApJ*, 606, 32
- Robitaille, T. P. & Whitney, B. A. 2010, *ApJL*, 710, L11
- Rohlfs, K. & Wilson, T. L. 1996, *Tools of Radio Astronomy (XVI)* (Springer-Verlag Berlin Heidelberg New York)
- Roy, A. L., Goss, W. M., & Anantharamaiah, K. R. 2008, *A&A*, 483, 79

- Salim, S., Rich, R. M., Charlot, S., Brinchmann, J., Johnson, B. D., Schiminovich, D., Seibert, M., Mallery, R., Heckman, T. M., Forster, K., Friedman, P. G., Martin, D. C., Morrissey, P., Neff, S. G., Small, T., Wyder, T. K., Bianchi, L., Donas, J., Lee, Y.-W., Madore, B. F., Milliard, B., Szalay, A. S., Welsh, B. Y., & Yi, S. K. 2007, *ApJS*, 173, 267
- Sánchez-Blázquez, P., Peletier, R. F., Jiménez-Vicente, J., Cardiel, N., Cenarro, A. J., Falcón-Barroso, J., Gorgas, J., Selam, S., & Vazdekis, A. 2006, *MNRAS*, 371, 703
- Sanders, D. B. & Mirabel, I. F. 1996, *ARAA*, 34, 749
- Sarzi, M., Falcón-Barroso, J., Davies, R. L., Bacon, R., Bureau, M., Cappellari, M., de Zeeuw, P. T., Emsellem, E., Fathi, K., Krajnović, D., Kuntschner, H., McDermid, R. M., & Peletier, R. F. 2006, *MNRAS*, 366, 1151
- Schmidt, M. 1959, *ApJ*, 129, 243
- Schuster, K. F., Kramer, C., Hitschfeld, M., Garcia-Burillo, S., & Mookerjee, B. 2007, *A&A*, 461, 143
- Shetty, R., Kelly, B. C., & Bigiel, F. 2012, *ArXiv e-prints*
- Shirley, Y. L., Evans, II, N. J., Young, K. E., Knez, C., & Jaffe, D. T. 2003, *ApJS*, 149, 375
- Sliwa, K., Wilson, C. D., Petitpas, G. R., Armus, L., Juvela, M., Matsushita, S., Peck, A. B., & Yun, M. S. 2012, *ApJ*, 753, 46

- Smith, B. J. & Madden, S. C. 1997, *AJ*, 114, 138
- Solomon, P. M., Rivolo, A. R., Barrett, J., & Yahil, A. 1987, *ApJ*, 319, 730
- Spezzi, L., Alcalá, J. M., Covino, E., Frasca, A., Gandolfi, D., Oliveira, I., Chapman, N., Evans, II, N. J., Huard, T. L., Jørgensen, J. K., Merín, B., & Stapelfeldt, K. R. 2008, *ApJ*, 680, 1295
- Stanford, S. A. & Wood, D. O. S. 1989, *ApJ*, 346, 712
- Steinmetz, M. & Navarro, J. F. 2002, *Nature*, 7, 155
- Straizys, V., Cernis, K., & Bartasiute, S. 1996, *Baltic Astronomy*, 5, 125
- Struck, C. 1997, *ApJS*, 113, 269
- Tacconi, L. J., Genzel, R., Smail, I., Neri, R., Chapman, S. C., Ivison, R. J., Blain, A., Cox, P., Omont, A., Bertoldi, F., Greve, T., Förster Schreiber, N. M., Genel, S., Lutz, D., Swinbank, A. M., Shapley, A. E., Erb, D. K., Cimatti, A., Daddi, E., & Baker, A. J. 2008, *ApJ*, 680, 246
- Tago, E., Einasto, J., Saar, E., Tempel, E., Einasto, M., Vennik, J., & Müller, V. 2008, *A&A*, 479, 927
- Teyssier, R., Chapon, D., & Bournaud, F. 2010, *ApJL*, 720, L149
- The, L. S. & White, S. D. M. 1986, *AJ*, 92, 1248
- Thilker, D. A., Boissier, S., Bianchi, L., Calzetti, D., Boselli, A., Dale, D. A., Seibert, M., Braun, R., Burgarella, D., Gil de Paz, A., f, G., Walter, F.,

- Kennicutt, Jr., R. C., Madore, B. F., Martin, D. C., Barlow, T. A., Forster, K., Friedman, P. G., Morrissey, P., Neff, S. G., Schiminovich, D., Small, T., Wyder, T. K., Donas, J., Heckman, T. M., Lee, Y., Milliard, B., Rich, R. M., Szalay, A. S., Welsh, B. Y., & Yi, S. K. 2007, *ApJS*, 173, 572
- Toomre, A. & Toomre, J. 1972, *ApJ*, 178, 623
- Tran, K.-V. H., Moustakas, J., Gonzalez, A. H., Bai, L., Zaritsky, D., & Kautsch, S. J. 2008, *ApJL*, 683, L17
- Tran, K.-V. H., van Dokkum, P., Franx, M., Illingworth, G. D., Kelson, D. D., & Schreiber, N. M. F. 2005, *ApJL*, 627, L25
- Troland, T. H. & Crutcher, R. M. 2008, *ApJ*, 680, 457
- Urban, A., Martel, H., & Evans, N. J. 2010, *ApJ*, 710, 1343
- van Dokkum, P. G. 2001, *PASP*, 113, 1420
- van Dokkum, P. G., Franx, M., Fabricant, D., Kelson, D. D., & Illingworth, G. D. 1999, *ApJL*, 520, L95
- van Dokkum, P. G., Franx, M., Kelson, D. D., Illingworth, G. D., Fisher, D., & Fabricant, D. 1998, *ApJ*, 500, 714
- van Kampen, E. & Katgert, P. 1997, *MNRAS*, 289, 327
- van Kampen, T. A., van Dishoeck, E. F., Salter, D. M., Hogerheijde, M. R., Jørgensen, J. K., & Boogert, A. C. A. 2009, *A&A*, 498, 167

- Vázquez-Semadeni, E., Gómez, G. C., Jappsen, A., Ballesteros-Paredes, J., & Klessen, R. S. 2009, *ApJ*, 707, 1023
- Verley, S., Corbelli, E., Giovanardi, C., & Hunt, L. K. 2010, *A&A*, 510, A64
- Weingartner, J. C. & Draine, B. T. 2001, *ApJ*, 548, 296
- Whitmore, B. C., Gilmore, D. M., & Jones, C. 1993, *ApJ*, 407, 489
- Wilson, C. D., Petitpas, G. R., Iono, D., Baker, A. J., Peck, A. B., Krips, M., Warren, B., Golding, J., Atkinson, A., Armus, L., Cox, T. J., Ho, P., Juvela, M., Matsushita, S., Mihos, J. C., Pihlstrom, Y., & Yun, M. S. 2008, *ApJS*, 178, 189
- Wolf, C., Aragón-Salamanca, A., Balogh, M., Barden, M., Bell, E. F., Gray, M. E., Peng, C. Y., Bacon, D., Barazza, F. D., Böhm, A., Caldwell, J. A. R., Gallazzi, A., Häußler, B., Heymans, C., Jahnke, K., Jogee, S., van Kampen, E., Lane, K., McIntosh, D. H., Meisenheimer, K., Papovich, C., Sánchez, S. F., Taylor, A., Wisotzki, L., & Zheng, X. 2009, *MNRAS*, 393, 1302
- Wolf, C., Gray, M. E., & Meisenheimer, K. 2005, *A&A*, 443, 435
- Wolf, C., Meisenheimer, K., Kleinheinrich, M., Borch, A., Dye, S., Gray, M., Wisotzki, L., Bell, E. F., Rix, H.-W., Cimatti, A., Hasinger, G., & Szokoly, G. 2004, *A&A*, 421, 913
- Wong, T. & Blitz, L. 2002, *ApJ*, 569, 157
- Wu, J., Evans, N. J., Shirley, Y. L., & Knez, C. 2010, *ApJS*, 188, 313

- Wu, J., Evans, II, N. J., Gao, Y., Solomon, P. M., Shirley, Y. L., & Vanden
Bout, P. A. 2005, ApJL, 635, L173
- Zabludoff, A. I. & Franx, M. 1993, AJ, 106, 1314
- Zepf, S. E. 1993, ApJ, 407, 448
- Zezas, A., Ward, M. J., & Murray, S. S. 2003, ApJL, 594, L31
- Zhang, Q., Fall, S. M., & Whitmore, B. C. 2001, ApJ, 561, 727
- Zuckerman, B. & Evans, II, N. J. 1974, ApJL, 192, L149

Index

Abstract, viii
Acknowledgments, v
Bibliography, 287
Dedication, iv
*Galactic Star Formation Rate and
Gas Surface Density Relations*, 11
*Interacting Galaxies in the A901/902
Supercluster*, 173
Introduction, 1
*Star Formation Rate and Gas Re-
lations in Arp 299 Merger
from VIXENS*, 89
Summary, 255
VIXENS Survey, 79

Vita

Amanda Lea Heiderman was born on September 23, 1981 in Carson City, Nevada to parents Frank and Yolanda (Lonnie) Heiderman. She attended Western Nevada Community College from August 2000 to May 2002 where she studied physics under the guidance of Professor Robert Collier and was a teaching assistant in both math and physics lab courses. She transferred to the University of California at Berkeley in August of 2002 where she graduated with a Bachelor of Arts in Astrophysics in May of 2005.

During her time at the University of California at Berkeley, Amanda worked on a multitude of research projects both on and off the Berkeley Campus. In August of 2002, she worked with Dr. Gerson Goldhaber, graduate student Michael Wood-Vasey, and the Supernova Cosmology Project's Supernova Factory team at the Lawrence Berkeley National Lab (LBNL). She developed code to perform a photometric calibration of Near Earth Asteroid Tracking (NEAT) data using standard stars. She searched through consecutive images in the Supernova Factory data to find potential supernovae, checking them against the calibrated NEAT data, variable stars, and quasars in their host galaxies. During her time at LBNL she was awarded a research scholarship from the UC Berkeley campus UC Leadership Excellence through Advanced Degrees (UCLEADS) diversity research program. With the aid of her UCLE-

ADs scholarship she began a summer project In May of 2003 working with Dr. Marc Davis, graduate student Michael Cooper, and the DEEP2 Redshift Survey team at UC Berkeley. She developed an routine to measure the equivalent widths of ionized oxygen (a proxy for star formation activity) and compared that to galaxy properties and environment for a subset of the DEEP2 Redshift Survey galaxies. In April of 2004, she started working with Dr. Crystal Martin and graduate student Colleen Schwartz in the Physics Department at the University of California at Santa Barbara. She collected observations of a sample nearby starburst galaxies using the 40 inch Nickel Telescope at Lick Observatory. In May of 2004, she worked at UC Santa Barbara and wrote routines to reduced, flux calibrate, and perform photometry on the Lick Observatory data to investigate the star formation properties in the starburst galaxies.

After graduating from UC Berkeley, Amanda was accepted into the Summer 2005 Graduate Research Program (GRP/REU) at the National Radio Astronomy Observatory (NRAO) in Charlottesville, Virginia. There, she explored the star formation and neutral hydrogen gas properties of Hickson Compact Groups of galaxies (HCGs) with Dr. John Hibbard at NRAO and Dr. Kelsey Johnson in the Astronomy Department at the University of Virginia (UVa). In order to understand how the cold gas content and star formation activity evolve in compact groups, she reduced and calibrated archival Very Large Array (VLA) neutral hydrogen data and wrote routines to measure the gas masses and perform photometry on *Spitzer* Space Telescope infrared images. She then was invited to stay on through the academic year and work

as a student research assistant in the Extragalactic Star Formation group at UVa. She continued her work on HCGs and also began a project studying star formation by looking at the young stellar object population in a Galactic star forming region in collaboration with Dr. Remy Indebetouw and the *Spitzer* Galactic Legacy Infrared Mid-Plane Survey (GLIMPSE) team.

In August of 2006 Amanda joined the Astronomy Department at University of Texas at Austin to pursue graduate studies. Upon matriculation into the graduate program, she started working as a research assistant with Dr. Shardha Jogee. She studied interacting galaxies and environmental dependence in a galaxy supercluster and obtained her Masters of Arts in August of 2008. In January of 2009 she began working with her two doctoral thesis advisors Dr. Neal J. Evans II and Dr. Karl Gebhardt. During her thesis research program she worked with Dr. Neal Evans and investigated the relations between the star formation rate and gas content in nearby Milky Way clouds and implications for extragalactic studies. She was also the principle investigator, leading and managing, the VIRUS-P Investigation of the eXtreme ENvironments of Starbursts (VIXENS) survey in collaboration with her thesis advisors and an international research team. Amanda received a Doctorate of Philosophy in Astronomy from the University of Texas at Austin in November of 2012. In January of 2013 Amanda will begin her postdoctoral research program bridging the gap between Galactic and extragalactic star formation as a postdoctoral fellowship in the newly formed group “Star Formation throughout the Milky-Way Galaxy” in the Planet and Star Formation Department at

the Max Planck Institute for Astronomy in Heidelberg, Germany.

Permanent address: The University of Texas
Department of Astronomy
2515 Speedway, Stop C1400
Austin, Texas 78712-1205

This dissertation was typeset with \LaTeX^\dagger by the author.

[†] \LaTeX is a document preparation system developed by Leslie Lamport as a special version of Donald Knuth's \TeX Program.